

IntechOpen

Vortex Structures in Fluid Dynamic Problems

Edited by Hector Perez-de-Tejada



WEB OF SCIENCE™

VORTEX STRUCTURES IN FLUID DYNAMIC PROBLEMS

Edited by **Héctor Pérez-de-Tejada**

Vortex Structures in Fluid Dynamic Problems

<http://dx.doi.org/10.5772/67197>

Edited by Hector Perez-de-Tejada

Contributors

Ali Serkan Soydan, Gizem Karakan Günaydin, Michael Allen, Norihiko Sugimoto, Gunraj Prasad, Alejandro Aguilar, Jaime Hernández, Ismael Pérez García, Tomoaki Watanabe, Sergio Pedraza, Jose R. Toro, Omar D Lopez Mejia, Ivan Salmerón, René Oswaldo Vargas-Aguilar, Eduardo Valente Gómez-Benítez, Ildebrando Pérez-Reyes, Boris Malomed, Jianhua Zeng, Gary Matthew Wysin, Ken Sawada, Takashi Suzuki, Zhongxun Liu, Xuesong Wang, Jianbing Li, Hector Perez-De-Tejada

© The Editor(s) and the Author(s) 2017

The moral rights of the and the author(s) have been asserted.

All rights to the book as a whole are reserved by INTECH. The book as a whole (compilation) cannot be reproduced, distributed or used for commercial or non-commercial purposes without INTECH's written permission.

Enquiries concerning the use of the book should be directed to INTECH rights and permissions department (permissions@intechopen.com).

Violations are liable to prosecution under the governing Copyright Law.



Individual chapters of this publication are distributed under the terms of the Creative Commons Attribution 3.0 Unported License which permits commercial use, distribution and reproduction of the individual chapters, provided the original author(s) and source publication are appropriately acknowledged. If so indicated, certain images may not be included under the Creative Commons license. In such cases users will need to obtain permission from the license holder to reproduce the material. More details and guidelines concerning content reuse and adaptation can be found at <http://www.intechopen.com/copyright-policy.html>.

Notice

Statements and opinions expressed in the chapters are those of the individual contributors and not necessarily those of the editors or publisher. No responsibility is accepted for the accuracy of information contained in the published chapters. The publisher assumes no responsibility for any damage or injury to persons or property arising out of the use of any materials, instructions, methods or ideas contained in the book.

First published in Croatia, 2017 by INTECH d.o.o.

eBook (PDF) Published by IN TECH d.o.o.

Place and year of publication of eBook (PDF): Rijeka, 2019.

IntechOpen is the global imprint of IN TECH d.o.o.

Printed in Croatia

Legal deposit, Croatia: National and University Library in Zagreb

Additional hard and PDF copies can be obtained from orders@intechopen.com

Vortex Structures in Fluid Dynamic Problems

Edited by Hector Perez-de-Tejada

p. cm.

Print ISBN 978-953-51-2943-1

Online ISBN 978-953-51-2944-8

eBook (PDF) ISBN 978-953-51-4106-8

We are IntechOpen, the world's leading publisher of Open Access books Built by scientists, for scientists

3,650+

Open access books available

114,000+

International authors and editors

118M+

Downloads

151

Countries delivered to

Our authors are among the
Top 1%

most cited scientists

12.2%

Contributors from top 500 universities



WEB OF SCIENCE™

Selection of our books indexed in the Book Citation Index
in Web of Science™ Core Collection (BKCI)

Interested in publishing with us?
Contact book.department@intechopen.com

Numbers displayed above are based on latest data collected.
For more information visit www.intechopen.com



Meet the editor



Professor Héctor Pérez-de-Tejada obtained a bachelor's degree in science from the National Autonomous University of Mexico (UNAM) and later received his PhD degree from the University of Colorado (Boulder, Colorado). He has been a full researcher at the Institute of Geophysics of UNAM and participated in various academic functions first at the Ensenada (Baja California) campus and later at the Mexico City campus of that Institution. He was president of the Mexican Geophysical Union and has been a fellow of the National Research System in Mexico (level 3). Currently, he is the head of the Space Science Department of the Institute of Geophysics of UNAM, has participated in numerous research projects including as a guest investigator of the Pioneer Venus Orbiter mission of NASA at Venus, and has been involved in the analysis of plasma data of the Mars and Venus Express spacecraft of ESA. His academic activities have been related to studies of the interaction of the solar wind with planetary ionospheres and he has participated in many scientific publications where he has been the main author in most of them. He has been responsible for activities in the ionospheric sounder station near Mexico City and has been the supervisor of many graduate students at the Ensenada and at the Mexico City campuses of UNAM.

Contents

Preface XI

- Section 1 Vortices in Earth and Planetary Sciences 1**
- Chapter 1 **Vortex Structure in the Plasma Flow Channels of the Venus Wake 3**
Héctor Pérez-de-Tejada, Rickard Lundin and Devrie S. Intriligator
- Chapter 2 **Interaction of Tropical Cyclones with a Dipole Vortex 15**
Ismael Perez-Garcia, Alejandro Aguilar-Sierra and Jaime Hernández
- Chapter 3 **Nonlinear Interaction Between Vortex and Wave in Rotating Shallow Water 33**
Norihiro Sugimoto
- Section 2 Vortices in Fluid Dynamic Problems 53**
- Chapter 4 **Modelling of Temporal-Spatial Distribution of Airplane Wake Vortex for Scattering Analysis 55**
Jianbing Li, Zhongxun Liu and Xuesong Wang
- Chapter 5 **Vorticity Evolution near the Turbulent/Non-Turbulent Interfaces in Free-Shear Flows 75**
Tomoaki Watanabe, Koji Nagata and Carlos B. da Silva
- Chapter 6 **Simulation of Axisymmetric Flows with Swirl in Vorticity-Stream Function Variables Using the Lattice Boltzmann Method 95**
Omar D. Lopez, Sergio Pedraza and Jose R. Toro

- Chapter 7 **Thickness and Thermal Conductivities of the Walls and Fluid Layer Effects on the Onset of Thermal Convection in a Horizontal Fluid Layer Heated from Below 115**
Ildebrando Pérez-Reyes, René Osvaldo Vargas-Aguilar, Eduardo Valente Gómez-Benítez and Iván Salmerón-Ochoa
- Chapter 8 **Role of Vortex Dynamics in Relativistic Fluids 129**
Gunraj Prasad
- Chapter 9 **Statistics of Gyrotropic Vortex Dynamics in Submicron Magnetic Disks 147**
Gary Matthew Wysin
- Chapter 10 **Two-Dimensional Solitons and Vortices in Linear and Nonlinear Lattice Potentials 179**
Jianhua Zeng and Boris A. Malomed
- Chapter 11 **Relaxation Theory for Point Vortices 205**
Ken Sawada and Takashi Suzuki
- Section 3 Vortices in General Physical Problems 225**
- Chapter 12 **Development of Vortex Bioreactor Technology for Decentralised Water Treatment 227**
Andrew Landels, Neil Cagney, Lisa Bauer, Tracey A. Beacham, Stavroula Balabani and Michael J. Allen
- Chapter 13 **Vortex Spinning System and Vortex Yarn Structure 247**
Gizem Karakan Günaydin and Ali Serkan Soydan

Preface

The contents of this book are related to studies of vortices measured in the earth and planetary sciences together with vortex dynamics related to different fluid problems. The 13 chapters that are presented in the book are directed to the detailed analysis of vortex dynamics in general flow problems together with studies of the presence, evolution, and dynamics of vortices in physical processes of general knowledge. The book is intended to serve as a reference guide to scientists, engineers, and students with an interest on the advances in those areas of research.

The book first provides information on vortices measured in the plasma wake of planet Venus and then on the interaction of tropical cyclones with a dipole vortex in the Earth. In addition, a study on vortices and waves in rotating shallow water applying to the earth's atmosphere is also presented. Studies on vortex dynamics in fluid problems first describe the modeling of the distribution of airplane wake vortex and then on interfaces in free-shear layer flows. Axisymmetric flows with swirl in vorticity stream functions are then described, and thermal conductivities and fluid layer effects are examined. The dynamics of vortices in relativistic fluids are also examined together with a study of the gyrotropic dynamics of magnetic vortices. Two-dimensional solitons and vortices are at the same time discussed together with a relaxation theory for point vortices. Contributions related to the dynamics of vortices observed in other fields of observation are also presented by discussing the development of the vortex bio-reactor and also vortex spinning systems in vortex yarn structures.

Much of what is described in the book is updated information on issues that further improve the importance of vorticity to the understanding of problems in fluid dynamics and also the application of those problems to many scientific goals. This statement is primarily directed to emphasize the advantages of fluid dynamics in the mathematical follow-up of basic matters in science. The edition of the book was conducted through the initiative of InTech with the professional work of its staff. The contribution of many scientists and researchers in various areas included in the book provides a substantial amount of innovative information that improves our understanding of vortex dynamics.

Much of the revision of the contents of this book was derived from the participation of the editor on the application of fluid dynamics to various physical problems. The initiative to carry out that effort in response to the invitation by the editorial board of InTech originated from contact with various colleagues who provided useful information in various areas of research in fluid dynamics. Important participation was first contributed by Dr. A. Poveda at UNAM, by Dr. M. Dryer at NOAA, and later by Prof. E. N. Parker at the University of Chicago. Encouragement has been available from Guadalupe Hernandez Ramos and other family members and remains in memory from that of his late parents (Jesus Pérez-de-Tejada and Rogelia Jaime).

Professor Héctor Pérez-de-Tejada
Institute of Geophysics, UNAM
Ciudad Universitaria, Mexico City, Mexico

Vortices in Earth and Planetary Sciences

Vortex Structure in the Plasma Flow Channels of the Venus Wake

Héctor Pérez-de-Tejada, Rickard Lundin and
Devrie S. Intriligator

Additional information is available at the end of the chapter

<http://dx.doi.org/10.5772/66762>

Abstract

An overall description of the solar wind that streams into the Venus wake and the ionospheric plasma that is driven from that planet's magnetic polar region is examined from measurements conducted with the various spacecraft that have probed the Venus plasma environment (Mariner 5, Venera 9-10, Pioneer Venus Orbiter, Venus Express). It is shown that the plasma properties in the Venus wake describe conditions that are less suitable for steady gyrotropic trajectories of the planetary particles but require the assumption that they are also subject to a fluid dynamic description that introduces structures similar to those generated through kinetic forces. Most notable is that there is evidence of decelerated solar wind proton fluxes measured within plasma channels that are mostly populated by outflowing planetary ions and that the solar wind particles moving in the wake execute trajectories that resemble motion along a vortex shape with motion directed even back toward the planet in the Venus inner wake. The plasma flow channels are mostly restricted to the vicinity of the midnight plane and extend downstream from the magnetic polar region.

Keywords: solar wind in the Venus wake, vortex structures in the Venus wake, plasma channels in the Venus ionosphere, erosion of the Venus ionosphere, acceleration of planetary ions in the Venus wake

1. Introduction

From the early measurements of the Venus plasma environment conducted with the Mariner 5 and the Venera 9-10 spacecraft it was noted that the profiles of the dynamic properties of the

solar wind particles and those of its convected magnetic field exhibit sudden fluctuations that reveal sharp variations of the particles' physical properties and that result from instabilities unrelated to steady gyrotropic trajectories. At the same time, measurements show changes in the temperature and speed of the solar wind that indicate variations different from those produced by mass loading with planetary ions. A suitable example was provided from measurements conducted with the Venera spacecraft [1] and that are reproduced in **Figure 1**. The temperature and speed profiles obtained as the vehicle probed the Venus wake show a bow shock crossing by 00:00 MT, which is marked by a brief burst in the ion temperature profile and a minor decrease in the speed profile. Further within the boundary layer of the Venus wake there is a more noticeable transition marked with a sudden increase of the ion temperature by 01:50 MT, which is followed by a subsequent rise downstream with irregular sharp changes before reaching a third transition by 03:00 MT at the outer extent of the wake. Together with such variation there is also a sharp decrease of the solar wind speed at the same transition by 01:50 MT and that is followed with subsequent lower values further downstream leading to a velocity boundary layer. The presence of that sharp transition is significant in the sense that marks a feature unexpected from mass loading processes where gradual changes in the plasma properties should be produced when approaching the planet. Most notable, however, is the fact that enhanced ion temperatures are encountered at and downstream from that transition. The higher temperatures revealed from the data in **Figure 1** at and downstream from that transition are not expected either from mass loading processes but suggest that other physical processes become dominant. At the same time, the various temperature ion peaks shown in the temperature profile downstream from the plasma transition at 01:50 MT indicate variations more accordant with instabilities than with conditions expected along a steady gyrotropic trajectory. Additional information on enhanced plasma temperatures within the boundary layer of the Venus wake and that was measured with a different experiment in the Venera spacecraft [2] was obtained from data taken in different orbits. Their results show that enhanced temperatures are measured with decreasing distance from the wake in a pattern that could not be expected from mass loading processes.

Equally significant are the kinetic and thermal speed profiles together with the magnetic field profiles that were reported from the flyby of the Mariner 5 spacecraft along and near the Venus wake as it moved towards the dayside [3, 4]. Such profiles are reproduced in **Figure 2** to show that enhanced thermal speed values U_T and hence larger ion temperatures are measured across a boundary layer located between -100 min and -40 min before closest approach throughout the crossing of that spacecraft around Venus. Strong and frequent changes in the magnitude and direction of the magnetic field are also observed (top panel). The observed fluctuating orientation of the magnetic field leads as well to question the conventional description of the motion of the planetary ions in terms of steady gyrotropic trajectories since their acceleration through the convective electric field of the solar wind will be rapidly modified to produce, instead, stochastic trajectories. Similar fluctuating variations of the magnetic field direction were also recently reported from the Venus Express measurements conducted in a comparable region of the Venus wake [5].

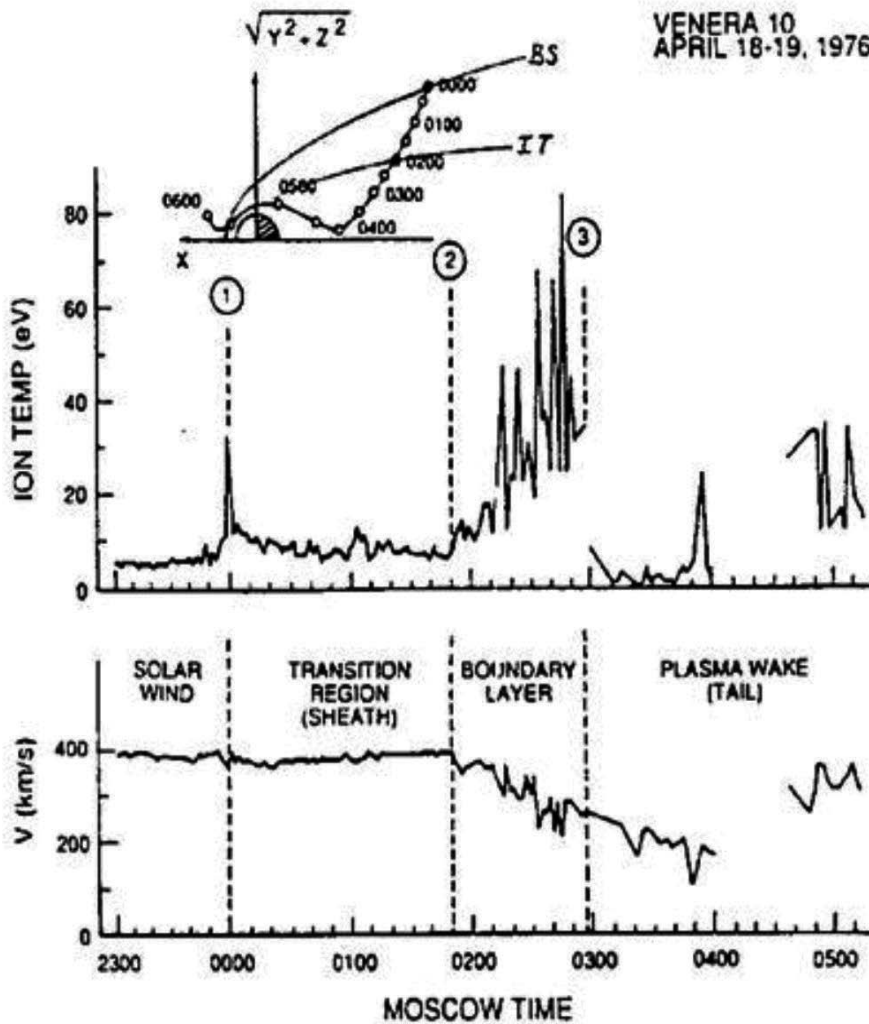


Figure 1. Ion speed and temperature measured along the orbit of Venera 10 on April 19, 1976. The orbit of Venera is shown at the top. The temperature burst was recorded during a flank crossing of the shock wave. The boundary layer is apparent by the increase in temperature and decrease in speed and is bounded by the intermediate transition at position labeled 2. The discontinuity in the boundary layer temperature profile corresponds to the boundary of the magneto-tail. Moscow time (MT) is shown along the abscissa [1].

As a whole, the experimental evidence indicates that mass loading processes and gyrotropic trajectories derived from the application of a steady convective electric field of the solar wind to the planetary ions are not sufficient to account for the observed changes in the plasma properties in the Venus magnetosheath; namely, the presence of a sharp plasma transition embedded in that region together with enhanced ion temperatures seen at and downstream from that transition.

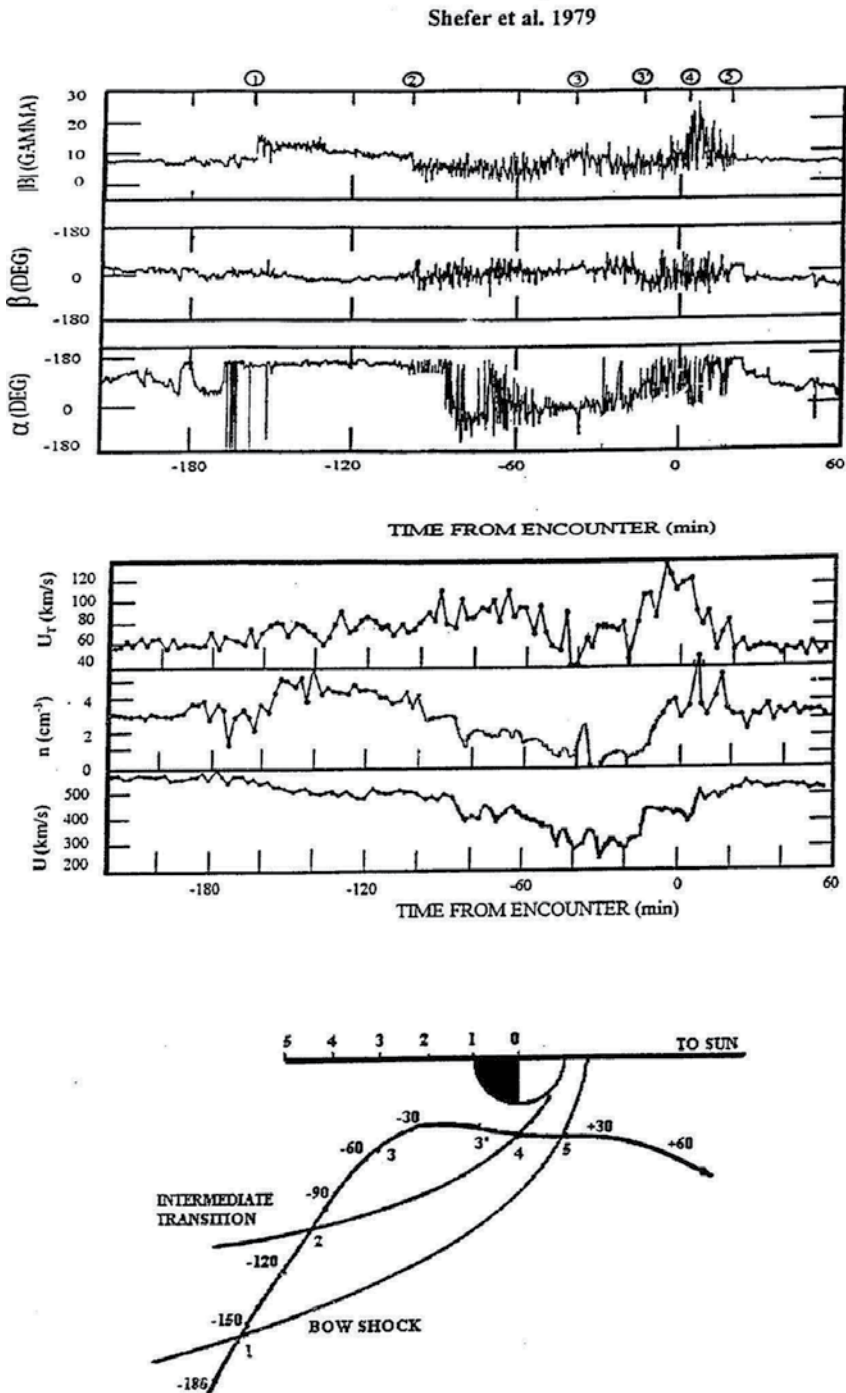


Figure 2. (Upper panel) Magnetic field signature (magnitude $|B|$ and direction angles), thermal speed U_T , density n , and kinetic speed U of the solar wind measured near Venus with the Mariner 5. (Lower panel) Flyby trajectory of the Mariner 5 near Venus in cylindrical coordinates [3].

2. Magnetic and kinetic forces

It is currently accepted that magnetic forces are sufficient to drive planetary ions away from the Venus wake. From measurements conducted with the Venus Express spacecraft it has been found, however, that conditions in the wake show the opposite since the motion of the plasma particles is super-Alfvénic [6]; namely, their kinetic energy density is larger than the local magnetic energy density. An example of this behavior is shown in **Figure 3** where the energy spectra of the solar wind and those of the O⁺ planetary ions measured in orbit 123 of the Venus Express are shown in the top panels. Their density and speed values (third, fourth, and fifth panels) together with the magnetic field intensity (bottom panel) lead to the kinetic energy density of the particle ions in the wake and the magnetic energy density profiles that are shown in **Figure 4**. Those profiles are important since they unveil that the kinetic forces in the wake are dominant in directing the motion of the planetary ions. As a result, the effects of the magnetic forces in the region where the planetary ions are measured are not dominant. In those regions the magnetic forces do not dictate the manner in which the planetary ions stream and are distributed through the wake. Much of this behavior is conducted through wave-particle interactions that enable the planetary ions to become accelerated and produce in turn the enhanced plasma temperatures that are measured at and downstream from the plasma transition in the magnetosheath as shown in **Figures 1 and 2**.

Different from the conditions encountered within the magnetic barrier in the vicinity of the dayside ionopause where the local solar wind flow is subalfvénic and thus the magnetic forces become dominant in the acceleration of the planetary ions, the recovery of the solar wind flow as it streams around Venus towards the wake leads to a plasma regime in which kinetic forces are strengthened and dominate the motion of the planetary particles. Such peculiar evolution can be appreciated in the magnetic field profile in **Figure 3** where small (≤ 5 nT) magnetic field intensity values are measured (between 01:30 UT and 01:50 UT) by the (01:45 UT - 01:55 UT) time range where the kinetic energy density of the planetary ions is large as it is shown in **Figure 4**. As a result, the trajectory of those particles is guided in a manner different from that produced by magnetic forces and their motion should be more accordant with that expected from fluid dynamics. In particular, the solar wind flow that streams over the magnetic polar regions of the Venus ionosphere where smaller magnetic field intensity values are measured may directly carve the upper ionosphere and produce plasma flow channels that extend downstream into the wake. Evidence of those features is available from measurements in the Pioneer Venus Orbiter (PVO) and in the Venus Express spacecraft (VEX). In the PVO plasma data there are regions within the nightside ionosphere where the local electron density drops to small values in the form of ionospheric holes [7]. In such regions there are enhanced magnetic field intensity values but, in the wake, the measured magnetic field decreases and the speed and density of the solar wind lead the planetary ions to move under superalfvénic flux conditions.

The data in **Figure 3** provide a good example where the speed and the density of the H⁺ and the O⁺ ions together with the low magnetic field intensity values measured in the near wake in the 01:30–01:50 UT time interval lead to a super-Alfvénic ion flow as shown in **Figure 4**.

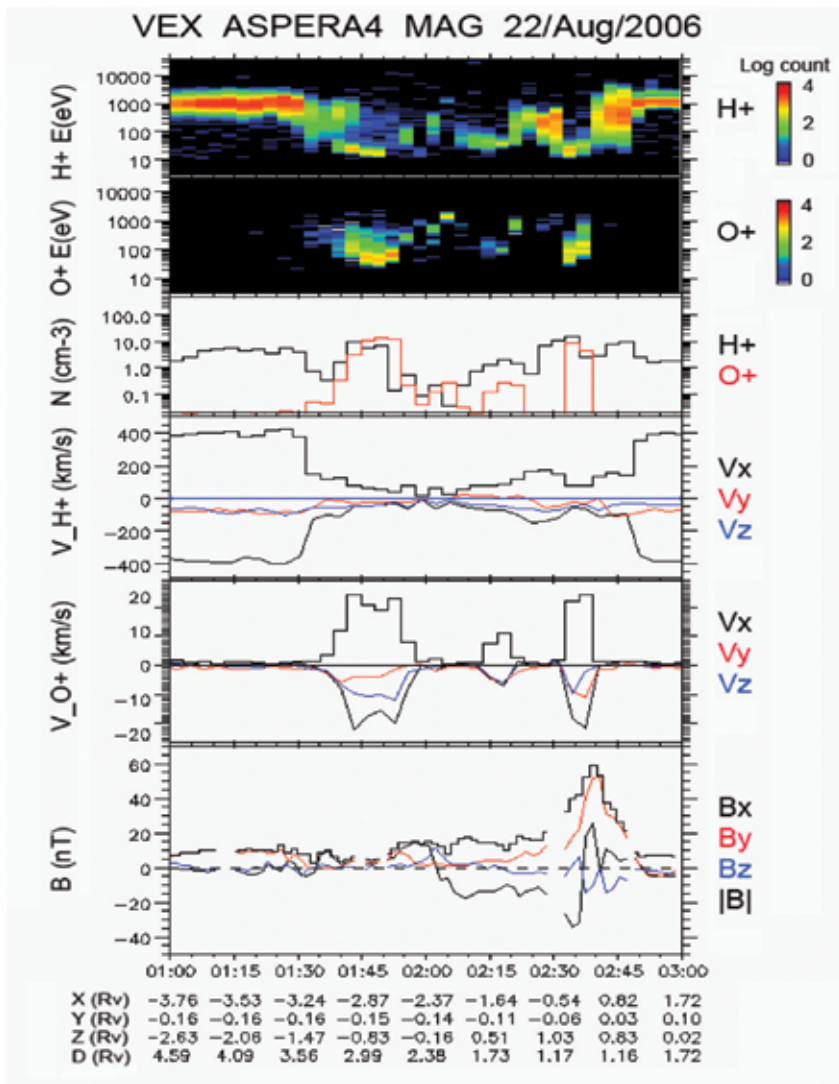


Figure 3. Energy spectra of H⁺ and O⁺ ion fluxes (first and second panels) measured in the Venus wake during orbit 123 of the Venus Express spacecraft [6]. Density and speed values of those ion components are shown the third, fourth, and fifth panels. The magnitude and the components of the magnetic field vector are shown in the bottom panel.

An important property of the plasma flow channels that have been further identified in the Venus wake from the Venus Express measurements is that they are observed mostly in the vicinity of the midnight plane as they evolve from the magnetic polar region. The plasma data reproduced in **Figure 3** is useful to stress this property since the planetary ions detected as the spacecraft approached the planet from the wake (in the 02:30–02:40 UT time interval) are located at small $Y \sim 0.05$ coordinate values and thus in the vicinity of the midnight plane. In such time interval there is evidence of O⁺ ion fluxes together with decelerated solar wind protons (with spectra in the 10–100 eV energy range) showing that a large fraction of their

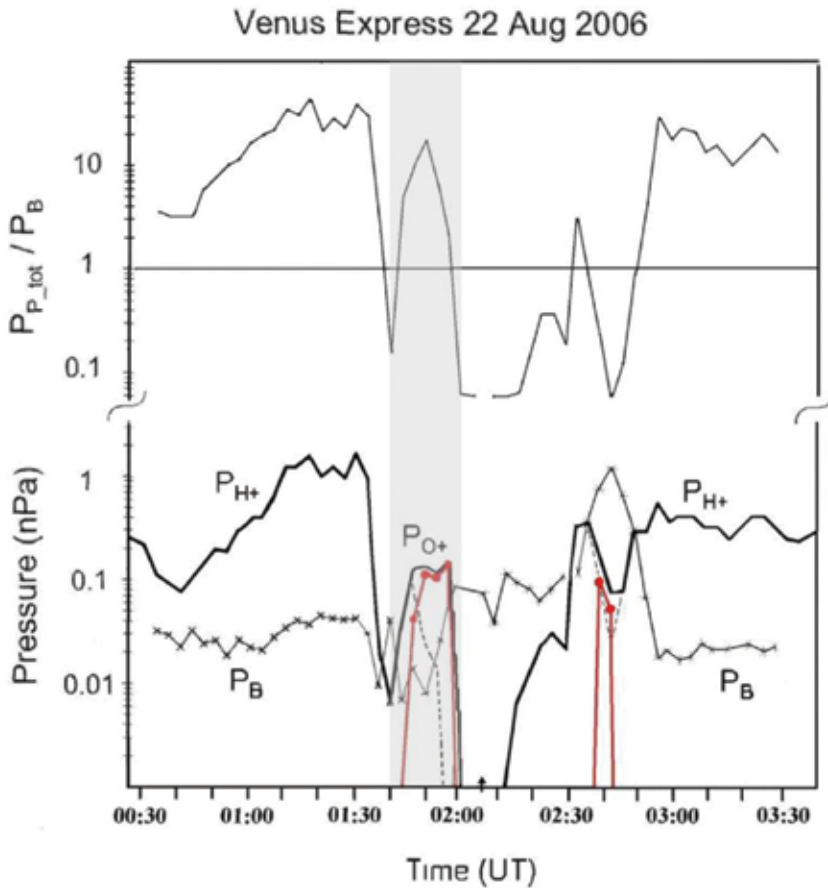


Figure 4. (Lower panel) Kinetic pressure of the O⁺ ions (profiles marked in red) and the H⁺ ions, together with the profile of the magnetic field pressure measured through the Venus wake during orbit 123 of the Venus Express spacecraft [6]. (Upper panel) Ratio values of the total kinetic pressure of the plasma to the magnetic field pressure derived from the profiles shown in the lower panel. The outbound bow shock crossing occurs at ~02:53 UT and the peak value of that ratio detected at ~01:50 UT is provided by the kinetic pressure of the O⁺ ions.

momentum has been transferred to the planetary ions. In fact, from the speed and the density profiles obtained from the spectra of both ion components it is found that at the two consecutive measurements when VEX moved across the plasma channel (at ~ 02:34 UT and at ~ 02:38 UT) the local deficiency in the value of the momentum flux of the solar wind protons is nearly equal to the momentum flux of the O⁺ ion fluxes obtained in each measurement. The outcome of this result strongly supports the view that an efficient erosion process occurs between the solar wind protons and the planetary ions.

As it is indicated schematically in **Figure 5**, the observation of outflowing planetary ion fluxes within the wake is mostly restricted within the plasma channels and in the vicinity of the magnetic polar region near the midnight plane, but the erosion process should not be dominant by the flanks of the wake. This constraint provides an explanation for the absence

of \sim keV solar wind proton fluxes in an ionospheric hole reported from VEX measurements at large angles from the midnight plane and in the vicinity of the equator [8] (see their Section 4.2). In fact, along the VEX trajectory in the 19 May 2010 orbit reported in **Figure 2** of [8] (between 05:21:37 and 05:30:15 UT) the spacecraft is located by $0.73 < Y < 0.87 R_V$ and between $Z = -0.12$ and $Z = 0.21 R_V$ and thus far from the midnight plane and close to the equatorial plane, and also far from a magnetic polar region since $1.45 < X < 1.72 R_V$. Consequently, the statement indicated in [8] in the sense that H⁺ ions fluxes are not measured at the time when the Venus Express is within an ionospheric hole is incorrect. In fact, the spectra of the decelerated solar wind protons shown in **Figure 3** were obtained as the spacecraft traveled through a plasma channel in the close vicinity of a magnetic polar region near the midnight plane.

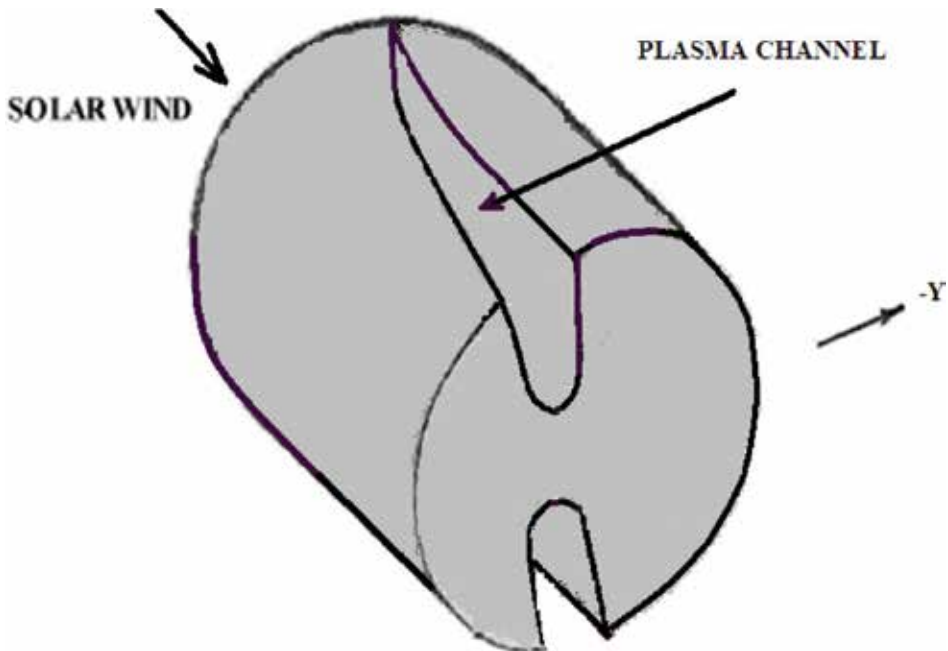


Figure 5. Schematic view of plasma flow channels that form by the magnetic polar regions of the Venus ionosphere and that are then deviated toward the dawn side (+Y) direction, together with the region above them where planetary ions are eroded by the solar wind [9].

3. Vortex structure in the Venus wake

From the early analysis of the motion of the solar wind in the Venus wake with the PVO plasma data it was noted that in specific orbits the solar wind fluxes can be directed back into the planet from the wake [10, 11]. The velocity distribution of those particles in the inner wake is reproduced in **Figure 6** (upper panel) in cylindrical coordinates to indicate that the solar wind ions are forced to execute a nearly $\sim 180^\circ$ turn in their trajectory direction following the form of a fluid dynamic vortex structure. This issue was more extensively examined using the Venus Express measurements by collecting the direction of motion of the solar wind

particles observed in many orbits across the Venus wake [12]. A summary of those results is reproduced in **Figure 6** (lower panel) where the solar wind velocity vectors are also presented in cylindrical coordinates. The figure applies to the Venus inner wake where the velocity vectors clearly show a gradual deviation away from the incident solar wind direction until they become oriented back into the planet (R. Lundin, personal communication 2016). An alternative interpretation of the sunward directed motion of the solar wind particles in that region in terms of magnetic forces is not consistent with the measured super-Alfvénic flow conditions in which the kinetic energy density of the plasma in the wake is larger than the local magnetic field energy density [6].

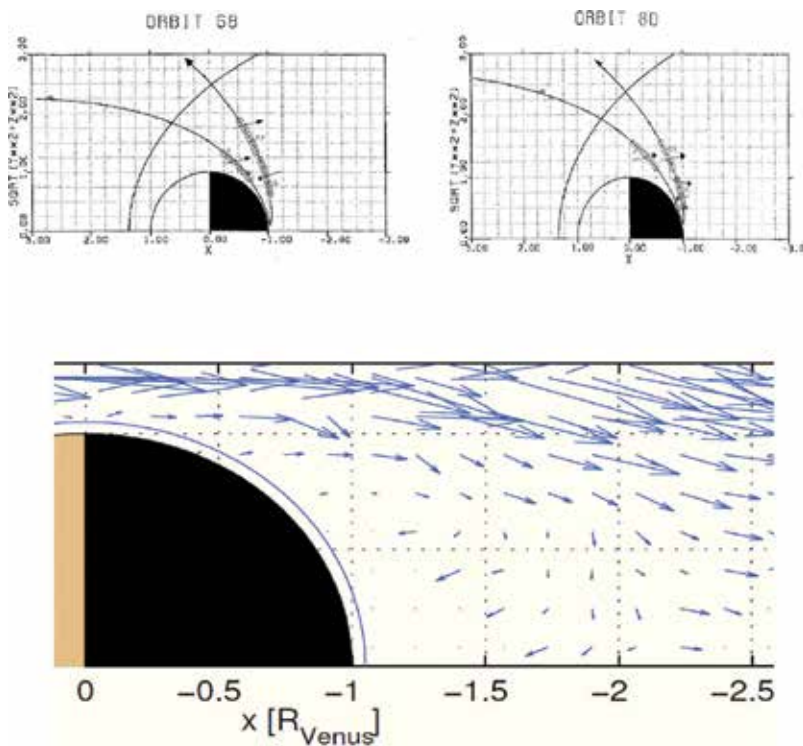


Figure 6. (Upper panel) Velocity vectors of the solar wind ion fluxes measured during different energy cycles marked with rectangles in two PVO orbits projected on one quadrant across the Venus wake in cylindrical coordinates [10, 11]. (Lower panel) Average updated direction of solar wind ion fluxes collected from many VEX orbits projected on cylindrical coordinates (Lundin, R, personal communication, 2016).

A useful configuration of the velocity vectors in a vortex flow structure is also available from their projection on the YZ plane (perpendicular to the solar wind direction) which is reproduced in **Figure 7** [13]. While the region of observation mostly extends over the southern hemisphere in the near wake ($X < -1.5 R_V$) there is a clear rotation of the velocity vectors centered around a position located north from the ecliptic plane (at $Z = 0$) and east from the midnight plane (at $Y = 0$). Also peculiar is that the magnitude of the velocity

vectors directed toward positive Y values by the upper part of the diagram is larger than that of the velocity vectors directed toward negative Y values in the lower part of the diagram. This difference may imply that the velocity vectors of the solar wind particles have a larger component along the Sun-Venus direction (away from the figure) in the Southern Hemisphere thus producing a more extended vortex structure along the X -axis in that hemisphere. Further studies are required to examine the rotation period of the solar wind as it moves in the vortex structure together with its evolution and extent in the YZ plane. Much of what has been addressed here stresses the value of fluid dynamic concepts to the interpretation of the plasma data and that has been obtained in measurements around Venus and in its wake [14]. However, the physical principles that substantiate the fluid response of the solar wind as it streams around the Venus ionosphere and that should be related to wave-particle interactions among the particle populations have not yet been properly identified.

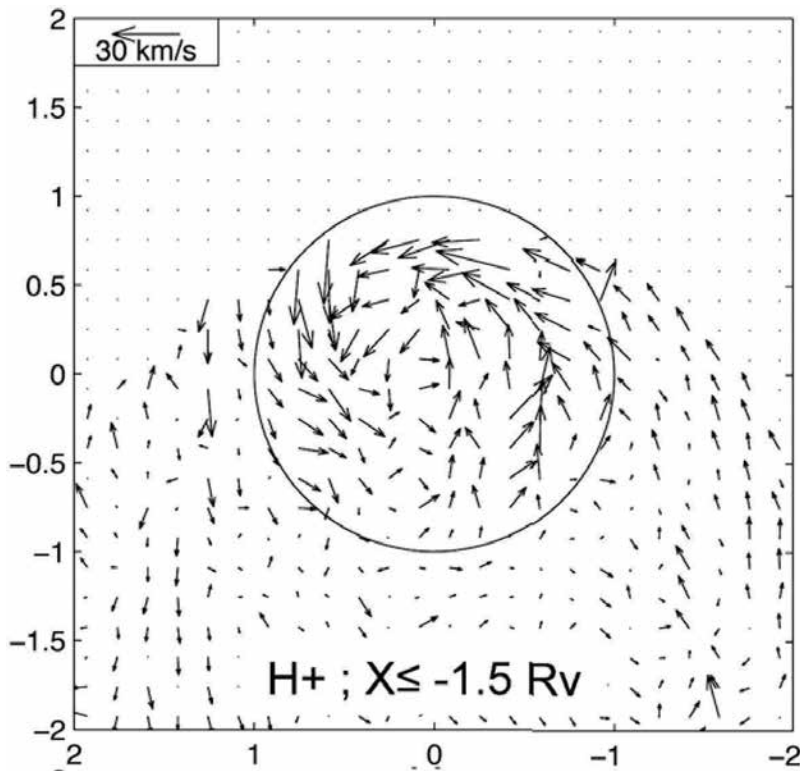


Figure 7. Velocity vectors of the solar wind H⁺ ions (1-300 eV) measured with the Venus Express spacecraft in the Venus near wake when projected on the YZ plane transverse to the solar wind direction (Y and Z are the horizontal and the vertical axis). Data are averaged in 1000×1000 km columns at $X < -1.5 R_v$ [13].

In summary, from the analysis of the plasma and magnetic field measurements conducted with various spacecraft across the Venus wake it has been learned that planetary ions that stream in the vicinity of the midnight plane are mostly seen to be accelerated by the kinetic

energy of the solar wind rather than by the local magnetic field forces. Plasma channels with decelerated solar wind ion fluxes are mostly detected near the midnight plane, and contrary to the claims made in Ref. [8], there should not be a conflict when they are not encountered by the equatorial flanks of the wake and far from the midnight plane [15]. Under such conditions the decelerated solar wind ions follow trajectories that are consistent with fluid dynamic motion and that lead them to produce vortex structures in the Venus wake.

Acknowledgements

Financial support was provided through Project: IN108814-3 of DGAPA at UNAM.

Author details

Héctor Pérez-de-Tejada^{1*}, Rickard Lundin² and Devrie S. Intriligator³

*Address all correspondence to: perezdet@geofisica.unam.mx

1 Institute of Geophysics, UNAM, Mexico, D.F., Mexico

2 Swedish Space Research Institute, Kiruna, Sweden

3 Carmel Research Center, Santa Monica, CA, USA

References

- [1] Romanov, S. A., et al., Interaction of the solar wind with Venus, *Cosmic Research*, 1979, 16, 603, see Fig. 5.
- [2] Verigin, M., et al., Plasma near Venus from the Venera 9 and 10 wide-angle analyzer data, *Journal of Geophysical Research*, 1978, 83, 3721, see Fig 8.
- [3] Bridge, H., A. et al., Plasma and magnetic fields observed near Venus, *Science*, 1967, 158, 1669–1673.
- [4] Shefer, R., et al., A re-examination of plasma measurements from the Mariner 5 Venus encounter, *Journal of Geophysical Research.*, 1979, 84, 2109–2114.
- [5] Vörös, Z., et al., Intermittent turbulence, noisy fluctuations, and wavy structures in the Venusian magnetosheath and wake, *Journal of Geophysical Research*, 2008, 113, ED0B21, doi: 10.2929/2008JE003159.
- [6] Pérez-de-Tejada, H., et al., Solar wind driven plasma fluxes from the Venus ionosphere, *Journal of Geophysical Research*, 2013, 118, 1–10, doi: 10.1002/2013JA019029.
- [7] Brace, L., et al., Holes in the nightside ionosphere of Venus, *Journal of Geophysical Research*, 1982, 87, 19921.

- [8] Collinson, G., et al., The extension of ionospheric holes into the tail of Venus, *Journal of Geophysical Research*, 2014, 119, 6940, doi: 10.1002/2014JA019851.
- [9] Pérez-de-Tejada, H. Plasma channels and electron density profiles near the midnight plane in the Venus ionosphere, *Journal of Geophysical Research*, 2004, 109, A04106, doi: 10.1029/2002JA009811.
- [10] Pérez-de-Tejada, H., et al., Plasma vortex in Venus wake, *EOS, American Geophysical Union Publications*, Washington D. C. 1982, 63(18), 368.
- [11] Pérez-de-Tejada, H., R. Lundin, D. Intriligator, Plasma vortices in planetary wakes, Chapter 13, in: *Open Questions in Cosmology*, G. Olmo, Ed., INTECH Pub., Dec. 2012 (ISBN 978-953-51-0880-1).
- [12] Lundin, R., et al., Ion flow and momentum transfer in the Venus plasma environment, *ICARUS*, 2011, 215, 7.
- [13] Lundin, R., et al., A large scale vortex in the Venus plasma tail and its fluid dynamic interpretation, *Geophysical Research Letters*, 2013, 40(7), 273.
- [14] Pérez-de-Tejada, H., et al., Plasma transition at the flanks of the Venus ionosheath: Evidence from the Venus Express plasma data, *Journal of Geophysical Research*, 2011, 116, A01103, doi: 10.1029/2009/JA015216.
- [15] Pérez-de-Tejada, H., et al., Measurements of a plasma channel in the Venus wake (in revision) *Journal of Geophysical Research*.

Interaction of Tropical Cyclones with a Dipole Vortex

Ismael Perez-Garcia, Alejandro Aguilar-Sierra and
Jaime Hernández

Additional information is available at the end of the chapter

<http://dx.doi.org/10.5772/65953>

Abstract

The purpose of this chapter is to discuss certain disturbances around the pole of a Venus-type planet that result as a response to barotropic instability processes in a zonal flow. We discuss a linear instability of normal modes in a zonal flow through the barotropic vorticity equations (BVEs). By using a simple idealization of a zonal flow, the instability is employed on measurements of the upper atmosphere of Venus. In 1998, the tropical cyclone Mitch gave way to the observational study of a dipole vortex. This dipole vortex might have helped to intensify the cyclone and moved it towards the SW. In order to examine this process of interaction, the nonlinear BVE was integrated in time applied to the 800–200 hPa average layer in the previous moment when it moved towards the SW. The 2-day integrations carried out with the model showed that the geometric structure of the solution can be calculated to a good approximation. The solution HLC moves very fast westwards as observed. On October 27, the HLA headed north-eastward and then became quasi-stationary. It was also observed that HLA and HLC as a coupled system rotates in the clockwise direction.

Keywords: polar vortices Venus, barotropic vorticity equation, normal mode instability, tropical cyclone, American monsoon system.

1. Introduction

The air at the equatorial regions rises when heated by the sun and as it does, it cools down and sinks. Rising air creates low pressure, sinking air creates high pressure. High altitude winds move towards the poles and surface winds move towards the equator, creating a simple convective motion known as the Hadley cells. These Hadley cells are the atmospheric circulation system driven by solar heated ground. On Earth, the Coriolis effect breaks each circulation

cell into several separate cells, which are easily visible from space. Global circulation or local weather systems moves from West to East at mid-latitudes in the Northern Hemisphere (NH). Two main factors that cause these patterns are atmospheric heating and planetary rotation.

Vortices are structures observed in planets with atmospheres. Earth, Mars, Venus, Jupiter and Saturn. On Earth, these atmospheric vortices are called cyclones and anticyclones. A cyclone or “Low” is a storm or a system of winds that rotates around a centre of low atmospheric pressure. An anticyclone or “High” is a system of winds that rotates around a centre of high atmospheric pressure.

Winds in a cyclone blow counterclockwise in the NH while they move clockwise in the Southern Hemisphere (SH). Winds in an anticyclone blow in the opposite direction. Cyclones that form over tropical regions are called tropical cyclones. The semi-permanent and transient cyclones or anticyclones are associated with weather systems. Polar vortex, Bermuda High, the Siberian High and the Aleutian Low are examples of semi-permanent systems. The subtropical high pressure belts that exist in the atmosphere overlaps with the descending legs of the Hadley cells. These semi-permanent subtropical centres of high pressure develop as direct responses to solar heating produced by the differential heating of continents and oceans. The role of the cyclones and anticyclones in the general circulation of the atmosphere is to exchange heat and moisture between the equator and the poles.

The polar vortex, also called “Circumpolar vortex”, is an upper level low-pressure zone, with a prevailing wind pattern that circulates in the Arctic, flowing from west to east lying near the Earth’s pole, that is usually kept in place by the jet stream that divides cold air from warm air. The jet stream is a relatively narrow band of strong winds in the upper levels of the atmosphere that blow from West to East; however, it often shifts to the North or South. The strongest occurrence of jet stream takes place during both the Northern and Southern Hemisphere winters. The 50° – 60° N/S region is where the polar jet is located with the subtropical jet near 30° N. The interface between the cold dry air mass from the pole and the warm moist air mass from the south, defines the location of the polar front, extending from the surface up to the troposphere. An upper-level front on Earth is usually associated with the mid-latitude jet [1], while the cold collar on Venus is a ring of cooler air that surrounds the polar vortex and which denotes a darker area between 60° and 80° [2].

The Earth and Venus are about the same size. Venus has a radius of $a_v = 6051.8\text{km}$ and the Earth has a mean radius $a = 6371\text{ km}$. Venus moves around the Sun, completing one orbit in every 224 earth days. Most of the planets and the sun in our solar system rotate in the counterclockwise direction when viewed from above their North Poles. Venus, however, rotates in the opposite direction. Venus spins extremely slowly, completing one rotation every 243 earth days, so on Venus the Coriolis effect is very weak. It is also weak in Earth’s tropics. A day in Venus is longer than its year. Venus’s retrograde turn means that the planet’s North Pole actually lies below the ecliptic plane.

The atmosphere on Venus is extremely dense, the temperature increases downwards from 100 to 40 km except in an inversion layer about 60–70km. The range of 1–360mbar have altitudes of 55–85 km, with surface pressures of 90 mbar and clouds beginning at 43 km [3]. In 1974, a

hemispheric vortex centred at the South Pole of Venus was observed at the time of Mariner 10. In 1979, images of Venus from Pioneer showed a similar vortex at North Pole. The winds were stronger at the equator, and slowed down towards the poles, creating a visible “V” shape on images of the cloud layers. In fact, the Venus clouds upper-deck rotates around the planet in just 4–5 days, which is in a much faster pace than in the underlying surface [4]. This is called super-rotation, because it is in the same direction as the rotation of the planet, but much stronger. The super-rotation is not that of an actual rigid body. Two essential questions remain to be answered: what are these eddies at the polar region? Where do they come from? They come from the processes of barotropic instability [5]. In Section 2, the fact that certain disturbances around the Venus pole arise as a response to barotropic instability processes of a zonal flow is demonstrated.

On Earth, tropical cyclones originate over tropical or subtropical regions in the Indian Ocean, western North Pacific and South Pacific Ocean, forming between 5° and 30° N and typically move westwards, north and north-westwards. When tropical cyclones reach subtropical latitudes, they often move north-eastwards. Also, the coasts of Mexico and Central America are influenced by the presence of the northern Atlantic and north-eastern Pacific tropical cyclones. A question remains to be answered on the movement of tropical cyclones: what pushes them south-westward. In particular, tropical cyclone Mitch moved south-westward by October 26–30, [6]. The overall motion of Mitch was slow, less than 5mph, this resulted in a tremendous amount of rainfall, primarily over Central America, which killed thousands of people. Section 3 of this present chapter, provides an observational study of a dipole vortex associated with the tropical cyclone Mitch, and the barotropic vorticity equations (BVEs) used to study the movement toward Southwest. The dipole vortex is an interesting feature that occurs during the intersection of the local summer months (September–November), formed in coupled monsoon systems: the late North American monsoon system (NAMS) and early South American monsoon system (SAMS).

2. Polar vortices in planetary atmosphere

A polar vortex, also known as the “Circumpolar Whirl”, is a large-scale circulation in the middle and upper troposphere, generally centred in the Polar Regions. These polar vortices form when heated air from equatorial latitudes rises, and then spirals towards the poles. In fact, the upper deck of clouds on Venus rotates around the planet much faster than the underlying surface. This is also called super-rotation, because the rotation is in the same direction as the rotation of the planet, but faster [4].

At the cloud top altitude of 67–72km, the main properties of the mean zonal velocity profile are well known. Hueso and Sanchez-Lavega [3] presented an update on the average zonal and meridional mean profile wind of the upper cloud at 66–73km for Venus SH from -90° to near -5° as observed with VIRTIS-M UV day-side data. Comparing with previous results by Sanchez-Lavega [7] and Moissl [8], they present the same general behaviour at all altitudes. Moissl [8] showed that a profile zonal wind from -85° to 20° with a zonal wind speed of

85° -90m/s almost constant with latitude is observed at low latitudes. The latitude zonal wind profile shows a gradually increase reaching 100m/s near 45° S, indicating the presence of a weak midlatitude jet. South of this latitude the wind speed decreases to zero towards the poles.

We assume that there is a similar circulation in the Northern Hemisphere in Venus, as observed in the "V" shaped clouds that move westwards. Therefore, we may be reconstructing a simple idealization of a symmetric zonal flow around Venus' equator based on the measurements taken from the upper atmosphere of Venus broadly consistent with the work of Refs. [3, 7, 8, 9]. This latitude profiles of symmetric zonal wind at the upper cloud layer at $66\text{--}73\text{km}$ is shown in **Figure 1**.

In latitudes between -50° and 50° , strong winds of up to 100 m/s with -10 m/s oscillations were observed. In latitudes between -4° and 4° strong winds of up to -108 m/s were observed, indicating the presence of a weak jet near the equator. Zonal winds closer to the poles gradually slowdown at latitude of about 48° on Venus. In both the Northern and Southern Hemispheres a small jet stream was found along with a meridional shear of $\frac{\partial u}{\partial y} = -0.027\text{ms}^{-1}\text{km}^{-1}$ [3].

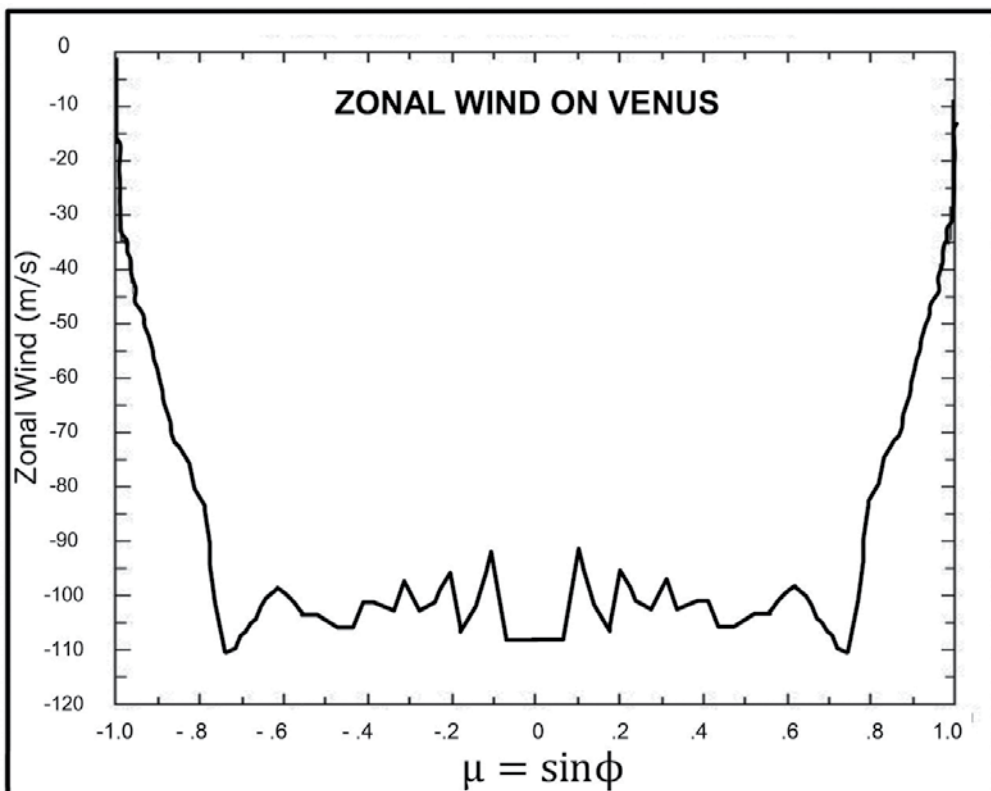


Figure 1. Zonal wind profiles idealized at the upper cloud layer of Venus taken and adapted from Ref. [3]. The horizontal axis is $\mu = \sin\phi$.

Venus' atmosphere can be divided into two broad layers. The first layer rotates in 4 Earth days and the second one is underneath. Let the height of Venusian atmosphere be H_v , we may consider that the Venusian atmosphere resides between two concentric spheres with different radii a_v and $a_{v_t} = a_v + H_v$. Assuming that the mean level of this spherical shell rotated around the planet in just 4 Earth days or at an angular velocity $\Omega_{v_t} = -2.893 \times 10^{-6} \text{ s}^{-1}$, it would be much faster than the underlying surface or Venus angular velocity $\Omega_v = -3 \times 10^{-7} \text{ s}^{-1}$.

Widely used to understand many features of the large scale dynamics of the barotropic Earth atmosphere, we might consider the vertical component of the barotropic vorticity equation (BVE) for an ideal fluid non-divergent on a unit sphere S , which can be written in the non-dimensional form as follows [10]:

$$\frac{\partial \Delta \Psi}{\partial t} + J(\Psi, \Delta \Psi + 2\mu) = 0 \quad (1)$$

where $\Psi(\lambda, \mu)$ denotes the stream function. The spherical coordinates are longitude λ , latitude ϕ or $\mu = \sin \phi$, $-\pi \leq \lambda \leq \pi$, $-\frac{\pi}{2} \leq \phi \leq \frac{\pi}{2}$. Δ is the Laplace operator on a sphere and $J(\Psi, \eta)$ is the Jacobian operator. The equation is non-dimensionalized with the Earth radius a as the length scale and the inverse of the Earth angular velocity $7.292 \times 10^{-5} \text{ s}^{-1}$ as the timescale. The relative vorticity is $\xi = \Delta \Psi$ and the absolute vorticity is $\eta = \xi + 2\mu$. On Venus, the Coriolis parameter would be neglected, since it is two orders of magnitude lower than the Earth's one. The relative vorticity expressed in terms of wind vector (u, v) :

$$\xi(\lambda, \mu) = \frac{1}{\sqrt{1-\mu^2}} \frac{\partial v}{\partial \lambda} - \sqrt{1-\mu^2} \frac{\partial u}{\partial \mu} + \frac{\mu u}{\sqrt{1-\mu^2}} \quad (2)$$

Where

$$u = -\sqrt{1-\mu^2} \frac{\partial \Psi}{\partial \mu}, \quad v = \frac{1}{\sqrt{1-\mu^2}} \frac{\partial \Psi}{\partial \lambda} \quad (3)$$

are the velocity components that relates to the stream function.

Eq. (1) captures many features of the large scale dynamics of the barotropic Earth's atmosphere, providing better understanding of the low-frequency variability, teleconnection patterns and the synoptic blocking events [11–15]. A mechanism that generates low-frequency variability is the instability of non-zonal basic flow as proposed by Simmons et al. [11]. The four classes of BVE (for ideal flow) solutions known by now are the simple zonal flows $\tilde{\Psi}(\mu)$ and more complicated flows called Rossby–Haurwitz (RH) waves, Wu–Verkley waves [16] and modons [17–21].

The temperature and pressure on Earth are similar to those above 50 km on Venusian atmosphere. This implies that Earth's BVE can be applied to Venus middle atmosphere [2, 5]. The instability caused by the existence of a sufficiently large horizontal shear in the wind field of a basic flow is known as barotropic instability [22]. In continuation with the study of that polar

dipole vortex might result from the barotropic and baroclinic instabilities of the Venusian atmosphere [5, 23–25]. We were interested in exploring the instability of a zonal flow in super-rotation and the instability of zonal basic flow as shown in **Figure 1**.

In order to examine the resulting perturbation in the linear barotropic model, Skiba and Perez–Garcia [26] developed a numerical spectral method for normal mode stability study of ideal flows on a rotating sphere, which was tested on zonal flows [27].

The linearized equation for ξ' is:

$$\frac{\partial \xi'}{\partial t} + J(\tilde{\Psi}, \xi' + 2\mu) + J(\Delta^{-1}\xi', \tilde{\xi} + 2\mu) = 0, \quad (4)$$

Where $\xi' = \Delta\psi'$ is relative vorticity of the perturbation, the wide tilde mark represents basic flow, and primes refer to infinitesimal perturbation. In the form of a normal mode

$$\psi'(\lambda, \mu, t) = \hat{\Psi}(\lambda, \mu)e^{\omega t}, \quad \xi'(\lambda, \mu, t) = \Delta\hat{\Psi}(\lambda, \mu)e^{\omega t} = G(\lambda, \mu)e^{\omega t}, \quad (5)$$

leads to the spectral problem

$$LG = \omega G \quad (6)$$

For the linearized operator $LG = J(\tilde{G}, \Delta^{-1}G) - J(\tilde{\Psi}, G)$, $\omega = \omega_r + i\omega_i$, is the eigenvalue, G the eigenfunction and $\hat{\Psi}(\lambda, \mu) = \hat{\Psi}_r(\lambda, \mu) + i\hat{\Psi}_i(\lambda, \mu) = |\hat{\Psi}(\lambda, \mu)|e^{i\theta}$ is the amplitude. Here $\theta(\lambda, \mu) = \arg \theta(\lambda, \mu) = \arctan\left\{\frac{\hat{\Psi}_r(\lambda, \mu)}{\hat{\Psi}_i(\lambda, \mu)}\right\}$ is the initial phase of the mode. In the normal mode (linear) stability analysis, the basic state must be regarded as a steady state. A mode ψ' is unstable if $\omega_r > 0$, decaying if $\omega_r < 0$, neutral if $\omega_r = 0$, and stationary if $\omega_i = 0$.

A zonal basic flow with horizontal shear can be constructed analytically by $\tilde{\Psi}(\mu) = w P_n(\mu)$ in which $P_n(\mu)$ is a Legendre Polynomial (LP), with $\mu = \sin\phi$, and w , an arbitrary constant. The simplest super-rotation zonal flow is analytically constructed so that the equatorial easterly jet streams (the mean zonal wind in the equatorial latitude is -105 m/s decreasing to zero at the pole) are preserved with a weak easterly wind around poles: $\tilde{\Psi}(\mu) = -wP_1(\mu) = -w\mu$ ($w = -0.226$ is the rotation velocity). We used the Rayleigh-Kuo necessary condition for the instability [28, 29]: Let $\tilde{\Psi}(\mu)$ be a zonal flow on the sphere, then a normal mode may be unstable only if the derivative $\frac{\partial \tilde{\eta}}{\partial \mu}$ of the absolute vorticity $\tilde{\eta} = \tilde{\Psi}(\mu) + 2\mu$ changes its sign at least in one point of the interval $(-1, +1)$. Since in the mean level of Venus' atmosphere the absolute vorticity $\tilde{\eta} = \tilde{\Psi}(\mu) + 2r\mu$, where $r = -3.96 \times 10^{-2}$, then in our case, $\frac{\partial \tilde{\eta}}{\partial \mu} = 2(w + r)$ is a constant and hence there is no unstable normal mode, this is neutral. However for the zonal flow $\tilde{\Psi}(\mu) = wP_n(\mu)$, $\frac{\partial \tilde{\eta}}{\partial \mu} = 2r - w\chi_n \frac{\partial P_n}{\partial \mu}$ where $\chi_n = n(n+1)$, then there is a critical amplitude w for developing the instability, due to the sphere rotation [26, 27].

Rossby-Haurwitz wave has proved to be very useful in interpreting the large-scale wave structures in the Earth atmospheric circulation of middle latitudes. Not only should the zonal wind profile be consistent with Venusian climatology (**Figure 1**), but attention must also be given to the absolute vorticity of the zonal flow in the equatorial region. The effect of the mean flow, given by a linear combination Legendre polynomials and a Rossby-Haurwitz wave, was provided by Refs. [15, 27]. The zonal basic flow, demonstrated in **Figure 2**, can be approximated by the following,

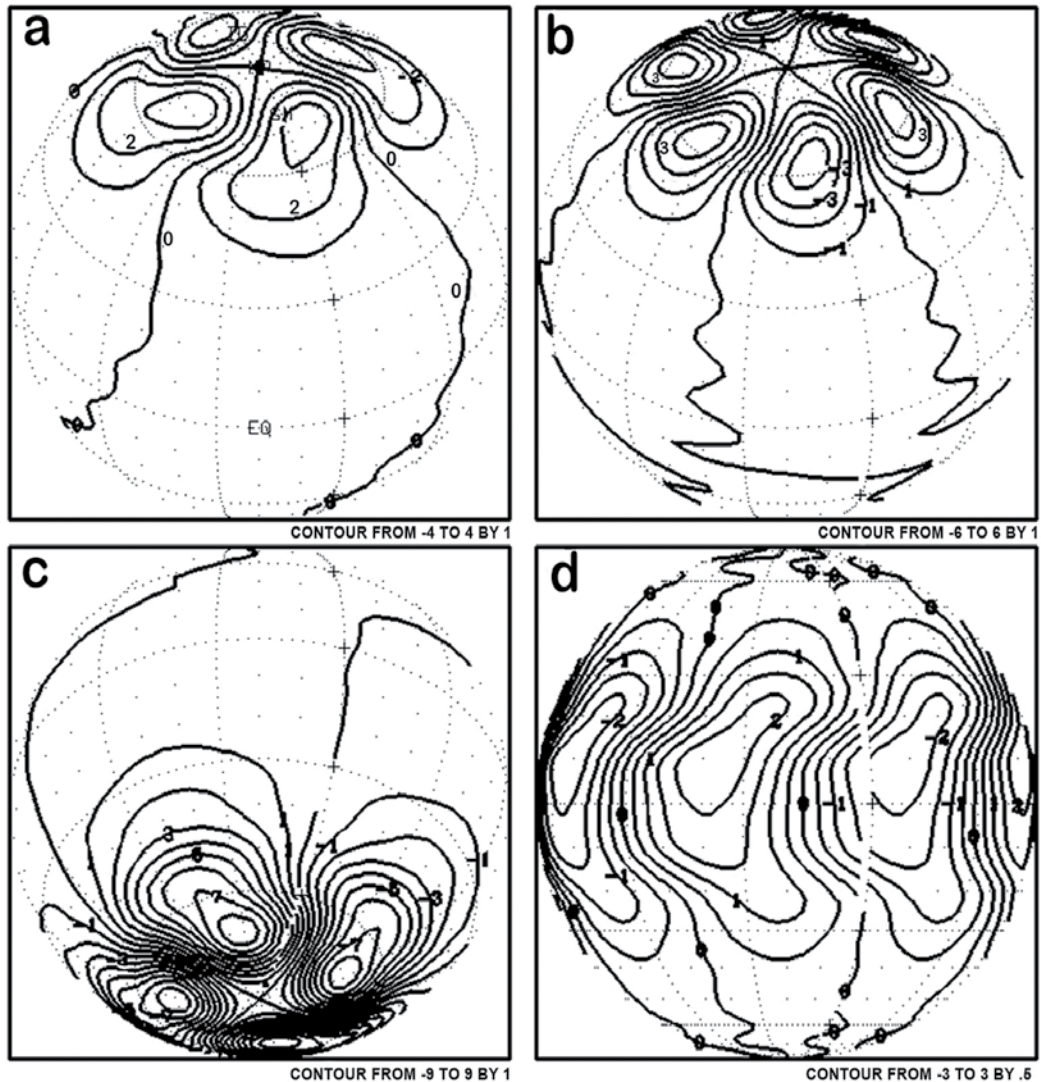


Figure 2. Isolines of the amplitudes $\hat{\Psi}_r(\lambda, \mu)$ of four most unstable modes corresponding to: $\omega_r = 86.08$ (a), $\omega_r = 64.31$ (b), $\omega_r = 67.23$ (c) and $\omega_r = 47.61$ (d).

$$\tilde{\Psi}(\mu) = \sum_{j=0}^5 w_{2j+1} P_{2j+1}^0(\mu) + \sum_{j=1}^2 w_{2j} P_{2j}^0(\mu), \tag{7}$$

where $P_n^m(\mu)$ is the associated Legendre function of degree n and zonal wave number m , and w' are constants and w_5 is very small. Then,

$$\frac{\partial \tilde{\eta}}{\partial \mu} = 2r - \sum_{j=0}^5 \chi_{2j+1} w_{2j+1} \frac{\partial P_{2j+1}^0}{\partial \mu} - \sum_{j=1}^2 \chi_{2j} w_{2j} \frac{\partial P_{2j}^0}{\partial \mu} \tag{8}$$

changes its sign at least in one point of the interval $(-1, +1)$, and thus Eq. (7) may have unstable normal modes.

Observational evidence indicates that the zonal flow pattern on the Earth can be approximately represented by a linear combination of seven Legendre polynomials of odd parity [15, 30]. The zonal flow has the maximum westerly of 33m/s at 35° North and South, and an easterly wind of 5m/s at the equator. This zonal wind field resembles the upper troposphere during the northern winter. The stability analysis showed that unstable perturbations are observed in the neighbourhood of subtropical jets, and the dominant zonal wave number of the modes are $m = 7$ and $m = 5$ (see **Figure 3** of [15]).

However, Skiba [31] showed that for a zonal flow PL and a RH wave, the amplitude $\hat{\Psi}$, of each unstable or decaying mode must satisfy the condition,

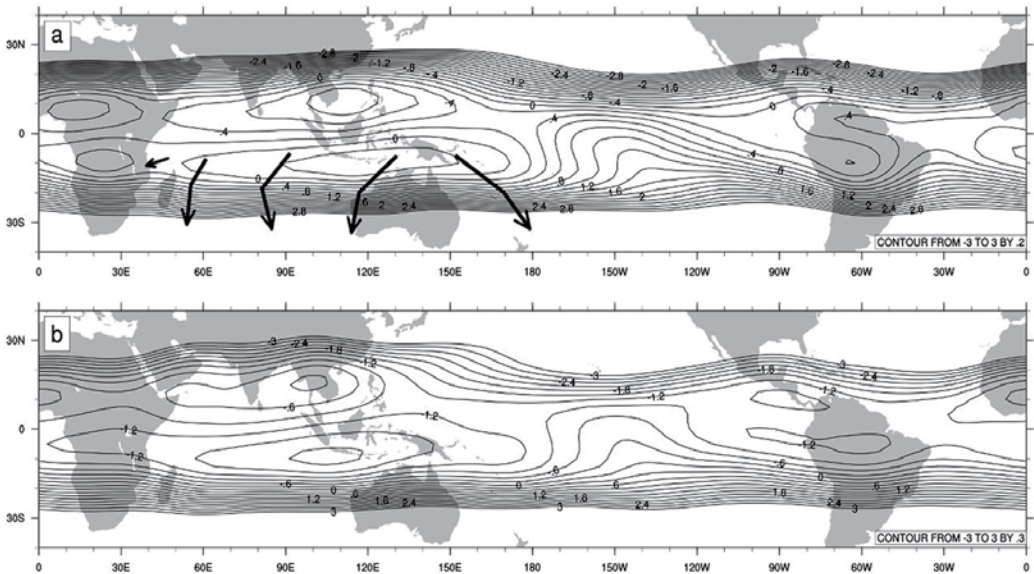


Figure 3. Isolines of the monthly stream function multiplied by 10^7 for April (a) and May (b) mean 200-250 mbar respectively. Tropical cyclone tracks in (a) are adapted from Ref. [36].

Modes	ω_r	ω_i	$\chi_{\hat{\Psi}}$	τ_e	T
1	86.03	215.53	86.26	1.84×10^{-3} ,	4.63×10^{-3} ,
2	64.28	-309.52	89.39	2.47×10^{-3} ,	3.23×10^{-3} ,
3	57.16	236.45	76.94	2.78×10^{-3} ,	4.22×10^{-3} ,
4	47.63	66.01	56.55	3.34×10^{-3} ,	1.51×10^{-2} ,

Table 1. The most unstable mode of the Venus' polar zonal flow described by **Figure 2**.

$$\chi_{\hat{\Psi}} = \frac{E(\hat{\Psi})}{k(\hat{\Psi})} \tag{9}$$

where $\chi_{\hat{\Psi}}$ is the square of Fjörtoft's [32] average spectral number of the mode amplitude $\hat{\Psi}$, and $K(\hat{\Psi}) = \frac{1}{2} \|\nabla \hat{\Psi}\|^2 = \frac{1}{2} \sum_{n=1}^{\infty} \chi_n \sum_{m=-n}^n |\hat{\Psi}_n^m|^2$ and $E(\hat{\Psi}) = \frac{1}{2} \|\Delta \hat{\Psi}\|^2 = \frac{1}{2} \sum_{n=1}^{\infty} \chi_n^2 \sum_{m=-n}^n |\hat{\Psi}_n^m|^2$ are the total kinetic energy, and entropy of $\hat{\Psi}$, and $\hat{\Psi}_n^m$ is the Fourier coefficient.

In this part of our chapter we shall study the normal mode numerical stability, in the case of zonal flow in **Figure 1**, then Eq. (6) is solved by representing all variables as series of spherical harmonics, by employing triangular truncation T21 and by taking the Coriolis parameter as $2r\mu$. The main parameters of the first four most unstable modes, $\omega = \omega_r + i\omega_i$, spectral number $\chi_{\hat{\Psi}}$ of the mode amplitude, e-folding time $\tau_e = \frac{1}{2\pi|\omega_i|}$ and period $T = \frac{1}{|\omega_r|}$ of the mode are given in **Table 1**.

As shown in **Figure 2**, for the first two most unstable modes, disturbances are located at the northern side of the largest jet stream of the North Hemisphere and for the third most unstable mode the disturbances are generated at the southern side of the largest jet stream in the South Hemisphere. From Ref. [26] we get the equation that describes the evolution of the total kinetic energy $K(\psi')$ of an infinitesimal perturbation ψ' to a zonal flow $\tilde{\Psi}(\mu)$ on sphere S ,

$$\frac{dK(\psi')}{dt} = -\int \sqrt{1-u^2} (u'v') \cdot \frac{\partial \tilde{u}}{\partial \mu} ds - \int \frac{\mu}{\sqrt{1-\mu^2}} (u'v') \cdot \tilde{u} ds \tag{10}$$

The sign of $\frac{dK(\psi')}{dt}$ depends on the signs of the products $(u'v') \cdot \tilde{u}$ and $(u'v') \cdot \frac{\partial \tilde{u}}{\partial \mu}$ in various regions of the sphere. In regions of generation of the energy of perturbations, the inclination of main axes of localized perturbations in the stream function field must be opposite to the inclination of zonal velocity profile, that is, in the regions where product $(u'v') \cdot \frac{\partial \tilde{u}}{\partial \mu}$ is positive [11]. Whereas the first integral dominates principally at the sides of the jets located in the tropics and mid-latitudes, the second integral can be significant in the central parts of strong jets, especially when such jets are located in the polar regions, where $\frac{\mu}{\sqrt{1-\mu^2}}$ is large [26, 27]).

Figure 2(d) shows the four modes most unstable with the V shapes, along the equatorial region. Data from the Vertis on Venus Express [33], also near the equator, show that similar

“V” structure of cloud layers were observed, as shown in this chapter, which could be associated with the barotropic instability processes. Further experiments were performed with different values for $r = \frac{\Omega_0}{\Omega} = 0$ (the Coriolis parameter neglected). The results proved to be similar to those presented in **Table 1**. So the generated unstable disturbances are due to intense zonal wind shear.

Unstable perturbation or vortices behaviour develops in the polar regions of Venus as a response to processes of barotropic instability of a zonal flow. These results are consistent with earlier studies of barotropic instability on Venus given in Refs. [24, 34, 35] and others, who were seeking a possible origin for the Venus polar dipole features observed by Pioneer Venus.

New data of zonal wind of the middle atmosphere to cover a wide range of latitudes in the NH will help to know about the unstable perturbation that develops in the polar regions of Venus NH as a response to processes of barotropic instability. It has been shown that the Venus polar dipole is a permanent feature in the Venusian atmosphere and that it is confined to latitudes higher than 75° S [25, 33].

Simmons et al. [11] showed that barotropic instability can be responsible for a low-frequency variability of Earth's atmosphere, and Perez-Garcia [15] demonstrated that unstable perturbations are observed in the neighbourhood of subtropical jets on the Earth. Then an analytic dipole vortex may be constructed on the Venus Polar Regions. This would be called a Verkleij's polar modon [17] with different dynamical configurations. Venusian atmosphere has given us not just the opportunity to learn from this initial work, but also to continue research on this topic. Our next challenge is to analyse the barotropic instability of the Zonal Flow seen in **Figure 1**, coupled with Verkleij's polar modon.

3. Global monsoon system, tropical dipole vortices and tropical cyclones

NCAR-ds627.0 and NCEP/NCAR Reanalysis data were used. In particular, we used the relative humidity, the zonal (u) and meridional (v) components of the wind field at different pressure levels. These wind components are further used in the calculation of their corresponding velocity potential and stream function.

Figure 3 shows the mean of 200–250mbar stream function monthly and tropical cyclone tracks for April. A noticeable feature in **Figure 3(a)** is the basic patterns of the circulation associated with monsoon land heating at the equator in the African region monsoon, 10° – 40° E, Asian-Australian monsoon, 60° – 180° E and South-American monsoon, 80° – 40° W. The Australian summer monsoon influences the climate of the Australian tropics during the period of December–March [37]. The onset of the Australian summer monsoon occurs in late December and typically retreats in April [38].

The early arrival of the Indian summer monsoon and North American early summer monsoon are shown in **Figure 3(b)**. The wet season of the Asian monsoon system begins in May and ends in October and the dry phase occurs in the other half of the year [39]. The set of these local monsoon systems is called the global monsoon system [40]. Liu and Zorita [41] defined the

local summer as May through September (MJJAS) in NH and November through March (NDJFM) for SH.

The American monsoon is determined by the dynamic processes of the interaction between the American continent, the eastern Pacific, the Atlantic Ocean and the overlying atmosphere [42]. The intense heat from the land creates rising of air and a surface low pressure, with low-level air flowing towards the convective regions and divergence in the upper troposphere, then the tropical cyclone moves towards the convective regions of the heated continents (**Figures 3(a)** and **4(b)**).

An important feature of the upper troposphere of a monsoon system is the high-level anticyclone (HLA) located above and to the north of the monsoon trough. The clockwise flow around this anticyclone contains an easterly jet stream in its southern flank called tropical easterly jet [43] and in the lower troposphere, for example, in North America late summer contains a maritime-continental thermal low (**Figure 5**).

In the Indian Ocean, the tropical cyclones mainly occur during pre-monsoon and post-monsoon seasons. In western North Pacific, TC most generally begins from June and ends in November [44]. Gray [45] estimates that the majority of TCs originate in or are just polewards of the Intertropical Convergence Zone [ITCZ] or monsoon trough. The upper tropospheric flow patterns over the region of storm formation control their formation and movement. Some storms recurve under the influence of a high-level anticyclone or an approaching westerly troughs of middle latitudes that extends into the upper levels of lower latitudes where east winds occur in the surface layers.

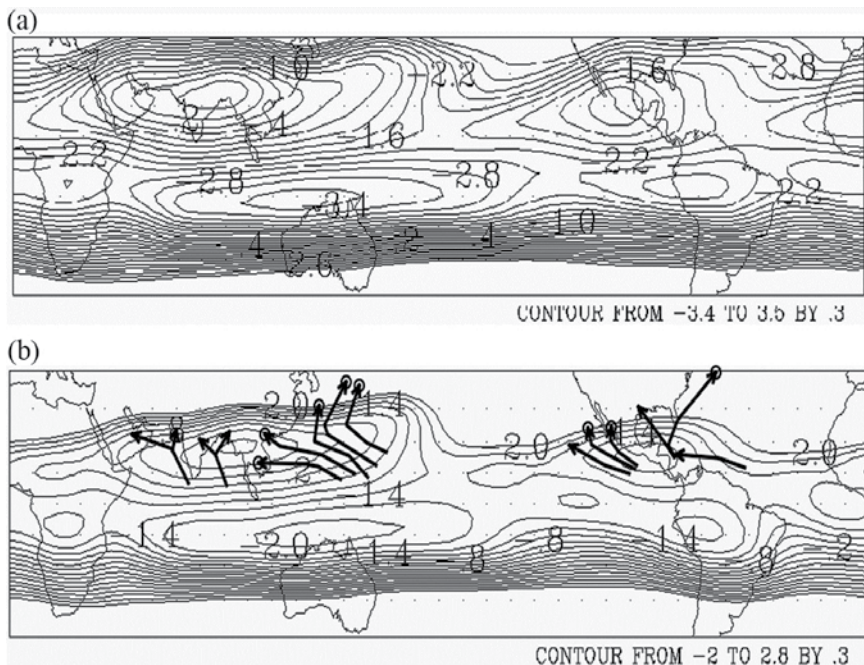


Figure 4. Isolines of the monthly stream function multiplied by 10^7 for September (a) and October (b) mean 200–250 mbar, respectively. Tropical cyclone tracks in (b) are adapted from Ref. [36].

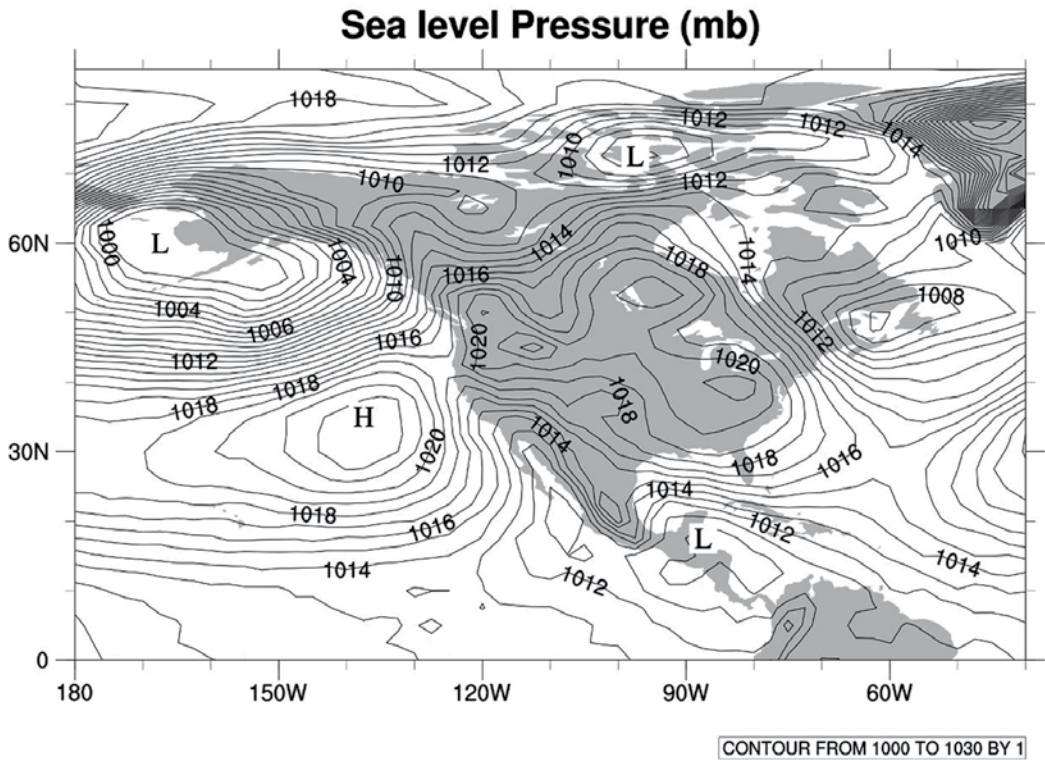


Figure 5. Sea level pressure composite, mean October 17–November 04, 1998, adapted from NOAA/ESRL.

In the Atlantic Ocean, the tropical cyclones mainly occur during May–October. In the lower troposphere, westward traveling tropical wave disturbances move in the trade wind flow across the Atlantic Ocean. They begin appearing as early as April/May and continue until October/November. Burpee [46] documented a mechanism for the origins of these waves, the instability of the African easterly jet.

An interesting feature occurs during months of May, September–November in the American monsoon system, in which its upper levels are formed with an anticyclone HLA on the northern side and an anticyclone HLC (high-level cyclone at NH) on its southern side. As a result, in certain periods, for example between September and November, the HLC and HLA remain coupled and then form a bipolar vortex or coupled monsoon system North American monsoon system (NAMS) late, and South American monsoon system (SAMS) early [6]. This bipolar vortex has a similar configuration to the Gill–Matsuno wave [47].

The genesis of Mitch was given by Refs. [6, 48–50]. In this chapter, we are interested in studying its trajectory. Why did it change its direction south-westward during the period of October 26–28, 1998? And how the interaction with HLA and HLC may have contributed to change its path south-westward? Due to the variation of the Coriolis parameter, a cyclone embedded in a resting atmosphere moves north-westwards [51].

In **Figure 6(a)** and **(c)** we get a general idea that the trajectory HLA and HLC took. By October 26–27, 00Z, HLA acquired a movement almost axi-symmetric with a north-eastern flow on its southeast side. HLC was moving west-north-westward very quickly, while HLA headed north-eastward, merging together as a coupled system (Bipolar Vortex), apparently starting an anticyclonic rotation (**Figure 6(a–c)**). Because Mitch was much closer to HLA, it was guided by the HLA circulation.

On October 26th HLA was situated on the Mexican plateau along with three other anticyclone disturbances, while HLC also had three more perturbations involved with it. The tracks of HLA and HLC and their multiple disturbances by October 27 are shown in **Figure 6(b)**, merging together, demonstrating their clockwise rotation.

During October 27–28, HLA changed direction, returning south-westward; however, HLC dispersed in a westward direction. In order to examine these interaction processes, the numer-

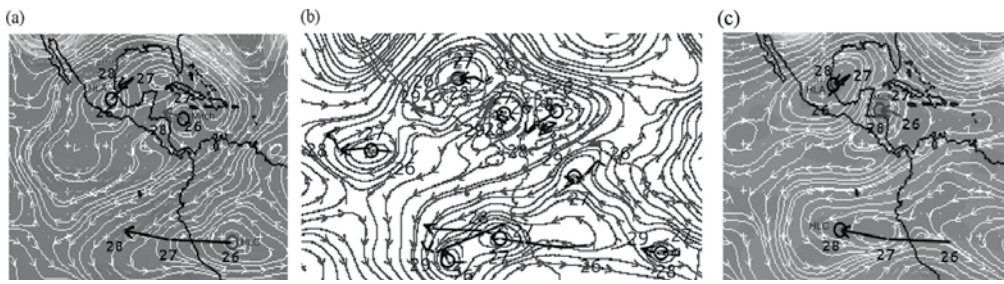


Figure 6. Streamline mean 850–200 mbar and tracks (wide lines) of vortices HLC, HLA and tropical cyclone Mitch, the maps is for days 26 (a), 27 (b) and 28 (c) of October 1998-00Z respectively. The small circle in (b) indicates the dates 00Z (white) and 12Z (black).

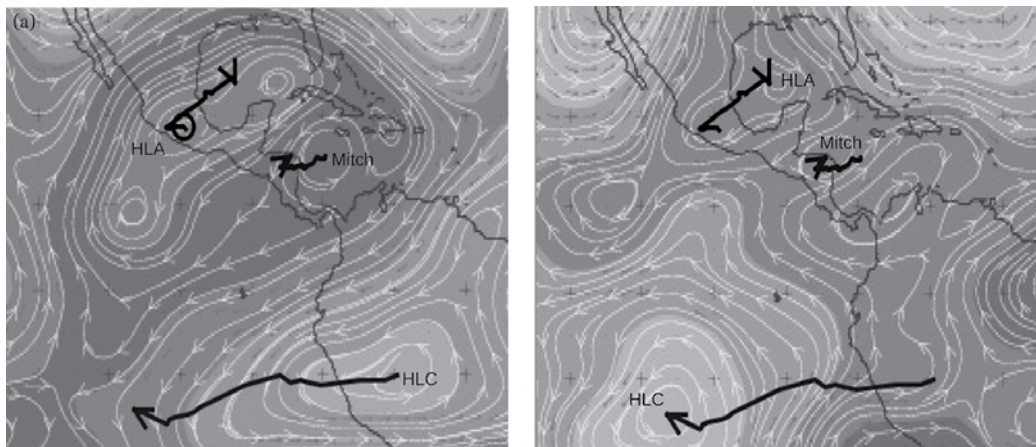


Figure 7. Streamline mean 850–200 mbar of non-divergent wind for October 26, 1998-00Z (a), and streamlines mean 850–200 mbar calculated for October 28-00Z in the integration of BVE (b). Wide lines represent tracks of vortices HLC, HLA and Mitch in the period October 26–28, 1998-00Z.

ical spectral of nonlinear barotropic model (1), in truncation T31, was integrated in the time, with the initial stream-function corresponding to October 26th-00Z, 800–200 mbar mean layer (see **Figures 6(a)** and **7(a)**).

The 2-day integrations carried out with the model show that the geometric structure (comparing **Figures 6** and **7**) of the solution can be calculated to a good approximation. On October 27th, the solution HLC moved westward very fast, while HLA headed north-eastward and then became quasi-stationary. Also, HLA and HLC as a coupled system rotated in a clockwise direction as given in **Figure 6(c)**.

The formation, development and evolution of the tropical cyclone Mitch was not a process by which isolated vortices were solely involved, but rather a result of a very complicated and precise conditions, which interacted among themselves and by nearby flows. In the case described here, these nearby flows were associated with the bipolar vortex formed by late NAMS and early SAMS.

Acknowledgements

The authors are grateful to A. Salas, E. Azpra, F. Villacaña, O. Delgado, R. Patiño and L. Meza for the map analysis. We thank Nat Aguilar and an anonymous reviewer for their useful comments that helped to improve the manuscript. The data was provided by NCAR's Data Support Section (DSS). The National Science Foundation is NCAR's sponsor.

Author details

Ismael Perez-Garcia*, Alejandro Aguilar-Sierra and Jaime Hernández

*Address all correspondence to: ismael@unam.mx

Laboratory of Modeling of Atmospheric Processes, Atmospheric Science Center UNAM, (Mexican National Autonomous University), Mexico City, Mexico

References

- [1] R. J. Reed, "A study of a characteristic type of upper-level frontogenesis," *J. Meteorol.*, vol. 12, pp. 226–237, 1955.
- [2] Garate-Lopez, I. R. Hueso, A. Sanchez-Lavega, and A. G. Munoz, "Potential vorticity of the south polar vortex of Venus," *J. Geophys. Res.*, vol. 121, pp. 574–593, 2016.
- [3] J. Peralta, R. Hueso, and A. Sanchez-Lavega, "Assessing the long-term variability of Venus winds at cloud level from Virtis–Venus express," *Icarus*, vol. 217, no. 2, pp. 585–598, 2012.

- [4] C. B. Leovy, "Rotation of the upper atmosphere of Venus," *J. Atmos. Sci.* Vol. 30, pp. 1218-1220, 1973.
- [5] S. S. Limaye, J. P. Kossin, C. Rozo, G. Piccioni, D. V. Titov, and W. J. Markiewicz, "Vortex circulation on Venus: Dynamical similarities with terrestrial hurricanes," *Geophys. Res. Lett.*, vol. 36, L04204, 2009.
- [6] I. Perez-Garcia, A. Aguilar, and J. Hernandez, "Patterns that led to the development of tropical cyclone Mitch (1988): A tribute to the affected," in preparation for publication, 2016.
- [7] A. Sanchez-Lavega, "Variable winds on Venus mapped in three dimensions," *Geophys. Res. Lett.*, vol. 35, L13204, 2008.
- [8] R. Moissl, et al., "Venus cloud top winds from tracking uv features in Venus monitoring camera images," *J. Geophys. Res.*, vol. 114, 2009.
- [9] S. S. Limaye, C. G. Grasotti, and M. J. Kuetemeyer, "Venus: Cloud level circulation during 1982 as determined from pioneer clout photo-Polari meter images time and zonally averaged circulation," *Icarus*, vol. 73, pp. 193-211, 1988.
- [10] I. Perez-Garcia and Y. N. Skiba, "Simulation of exact barotropic vorticity equation solutions using a spectral model," *Atmósfera*, vol. 12, pp. 223-243, 1999.
- [11] A. J. Simmons, J. M. Wallace, and G. W. Branstator, "Barotropic wave propagation and instability, and atmospheric teleconnection patterns," *J. Atmos. Sci.*, vol. 40, pp. 1363-1392, 1983.
- [12] J. S. Frederiksen, "A unified three-dimensional instability theory of the onset of blocking and cyclogenesis," *J. Atmos. Sci.*, vol. 39, pp. 969-982, 1982.
- [13] G. J. Shutts, "The propagation of eddies in diffluent jet streams: Eddy vorticity forcing of 'blocking' flow fields," *Quart. J. Roy. Meteor. Soc.*, vol. 109, pp. 737-761, 1983.
- [14] H. Nakamura, M. Nakamura, and J. L. Anderson, "The role of high and low-frequency dynamics in blocking formation," *Mon. Wea. Rev.*, vol. 125, pp. 2074-2093, 1997.
- [15] I. Perez-Garcia, "Rossby-Haurwitz perturbation under tropical forcing," *Atmósfera*, vol. 27, pp. 239-249, 2014.
- [16] P. Wu and W. T. M. Verkley, "Non-linear structures with multivalued relationships – exact solutions of the barotropic vorticity equation on a sphere," *Geophys. Astro. Fluid*, vol. 69, pp. 77-94, 1993.
- [17] W. T. M. Verkley, "The construction of barotropic modons on a sphere," *J. Atmos. Sci.*, vol. 41, pp. 2492-2504, 1984.
- [18] W. T. M. Verkley, "Stationary barotropic modons in westerly background flows," *J. Atmos. Sci.*, vol. 44, pp. 2383-2398, 1987.
- [19] W. T. M. Verkley, "Modons with uniform absolute vorticity," *J. Atmos. Sci.*, vol. 47, pp. 727-745, 1990.

- [20] J. J. Tribbia, "Modons in spherical geometry," *Geophys. Astro. Fluid*, vol. 30, pp. 131–168, 1984.
- [21] E. C. Neven, "Quadrupole modons on a sphere," *Geophys. Astro. Fluid*, vol. 65, pp. 105–126, 1992.
- [22] J. Pedlosky, "Finite-amplitude baroclinic waves in a continuous model of the atmosphere," *J. Atmos. Sci.*, vol. 36, pp. 1908–1924, 1979.
- [23] R. Young and J. Pollack, "A three-dimensional model of dynamical processes in the Venus atmosphere," *Atmos. Sci.*, vol. 34, pp. 1315–1351, 1977.
- [24] L. S. Elson, "Wave instability in the polar region of Venus," *J. Atmos. Sci.*, vol. 39, pp. 2356–2362, 1982.
- [25] I. Garate-Lopez, R. Hueso, A. Sanchez-Lavega, J. Peralta, G. Piccioni, and P. Drossart, "A chaotic long-lived vortex at the southern pole of Venus," *Nat. Geosci.*, vol. 6, pp. 254–257, 2013.
- [26] Y. N. Skiba and I. Perez-Garcia, "Numerical spectral method for normal-mode stability study of ideal ows on a rotating sphere," *Int. Jour. Appl. Mat.*, vol. 22, pp. 725–758, 2009.
- [27] I. Perez-Garcia and Y. N. Skiba, "Tests of a numerical algorithm for the linear instability study of ows on a sphere," *Atmosfera*, vol. 14, pp. 95–112, 2001.
- [28] L. Rayleigh, "On the stability of certain fluid motions," *Proc. London Math. Soc.*, vol. 11, pp. 57–70, 1880.
- [29] H. L. Kuo, "Dynamic instability of two-dimensional non-divergent flow in a barotropic atmosphere," *J. Meteor.*, vol. 6, pp. 105–122, 1949.
- [30] F. Baer, "Studies in low-order spectral systems," Tech. rep., Colorado State University, Department of Atmospheric Physics, 1968.
- [31] Y. N. Skiba, "On the normal mode instability of harmonic waves on a sphere," *Geophys. Astro. Fluid*, vol. 92, pp. 115–127, 2000.
- [32] R. Fjortoft, "On the changes in the spectral distribution of kinetic energy for two-dimensional non-divergent ow," *Tellus*, vol. 5, pp. 225–230, 1953.
- [33] G. Piccioni, "The many faces of the Venus polar vortex," *European Planetary Science Congress*, vol. 5, pp. 2010–2480, 2010.
- [34] D. V. Michelangeli, R. Zurek, and L. S. Elson, "Barotropic instability of midlatitude zonal jets on Mars, Earth and Venus," *J. Atmos. Sci.*, vol. 44, pp. 2031–2041, 1987.
- [35] A. R. Dobrovolskis and D. J. Diner, "Barotropic instability with divergence: Theory and applications to Venus," *J. Atmos. Sci.*, vol. 47, no. 3, pp. 1578–1588, 1990.
- [36] H. L. Crutcher and R. G. Quayle, "Mariners worldwide climatic guide to tropical storms at sea," Tech. rep., US Navy, 1974.

- [37] Carvalho, Leila Maria Véspoli de; Jones, Charles, *The Monsoons and Climate Change: Observations and Modeling*, Springer climate, ISBN 978-3-319-21650-8, 2016.
- [38] C. W. Hung and M. Yanai, "Factors contributing to the onset of the Australian summer monsoon," *Quart. J. Roy. Meteor. Soc.*, vol. 130, pp. 739–758, 2004.
- [39] P. J. Webster, T. Palmer, M. Yanai, R. Tomas, V. Magaña, J. Shukla, and A. Yasunari, "Monsoons: Processes, predictability and the prospects for prediction," *J. Geophys. Res.* (TOGA special issue), vol. 7, p. 14, 1998.
- [40] C. P. Chan, B. Wang, and G. Lau. (Eds.). *The Global Monsoon System: Research and Forecast*. Report of the International Committee of the Third 22 International Workshop on Monsoons (IWM-III). WMO/TD, No. 1266. Tropical Meteorology Research Programme (TMRP). Report No. 70. November 2004.
- [41] J. Liu and E. Zorita, "Centennial variations of the global monsoon precipitation in the last millennium: results from echo-g model," *J. Climate*, vol. 22, pp. 2356–2371, 2009.
- [42] A. Chakraborty and T. N. Krishnamurti, "Numerical simulation of the North American monsoon system," *Meteorol Atmos Phys*, vol. 84, pp. 57–82, 2003.
- [43] B. Hoskins and B. Wang, *The Asian Monsoon*, Ch. Large-Scale Atmospheric Dynamics, Springer, Berlin Heidelberg, pp. 357–415, 2006.
- [44] L. Chen and Y. Ding, *An Introduction to the Typhoon Over Western Pacific*. Science Press, Beijing, 1979.
- [45] W. M. Gray, "Global view of the origin of tropical disturbances and storms," *Mon. Wea. Rev.*, vol. 96, pp. 669–700, 1968.
- [46] R. W. Burpee, "The origin and structure of easterly waves in the lower troposphere of North Africa," *J. Atmos. Sci.*, vol. 29, pp. 77–90, 1972.
- [47] A. E. Gill, "Some simple solutions for heat induced tropical motion," *Quart. J. Roy. Meteor. Soc.*, vol. 449, pp. 447–462, 1980.
- [48] J. L. Guiney and M. B. Lawrence, "Hurricane Mitch 22 October–05 November 1998," *Tech. rep.*, National Hurricane Center, NOAA, 1999.
- [49] L. A. Avila, R. J. Pasch, and J. L. Guiney, "Atlantic hurricane season of 1998," *Mon. Wea. Rev.*, vol. 129, pp. 3085–3123, 2001.
- [50] Hernández, J. (2016). *Interaction of North American summer anticyclone and tropical cyclones: study of specific cases*. (M. Sc. thesis), Autonomous National University of Mexico, Mexico City.
- [51] J. Adem, "A series solution for the barotropic vorticity equation and its application in the study of atmospheric vortices," *Tellus*, vol. 8 (3), pp. 364–372, 1956.

Nonlinear Interaction Between Vortex and Wave in Rotating Shallow Water

Norihiko Sugimoto

Additional information is available at the end of the chapter

<http://dx.doi.org/10.5772/65431>

Abstract

This chapter is primarily concerned with the generation of inertia-gravity wave by vortical flows (spontaneous emission) in shallow water system on an f -plane. Sound waves are generated from vortical flows (aeroacoustics). There are many theoretical and numerical works regarding this subject. A shallow water system is equivalent to a two-dimensional adiabatic gas system, if the effect of Earth's rotation is negligibly small. Then gravity waves are analogous to sound waves. While it is widely known that the effect of the Earth's rotation suppresses inertia-gravity wave radiation, there are few studies about spontaneous emission in rotating shallow water. Here, the generation of inertia-gravity waves by unsteady vortical flows is investigated analytically and numerically as an extension of aeroacoustics. A background of this subject is introduced briefly and several recent works including new results are reviewed. Main findings are cyclone-anticyclone asymmetry in spontaneous emission and a local maximum of intensity of gravity waves emitted from anticyclones at intermediate value of the Coriolis parameter f , which are caused by the source originating in the Coriolis acceleration. All different experimental settings show the similar results, suggesting the robustness of these features.

Keywords: geophysical fluid dynamics, inertia-gravity wave, spontaneous emission, shallow water flows, aeroacoustics

1. Introduction

Sound waves are generated from vortical flows (aeroacoustics). After the pioneering work of Lighthill [1], many theoretical and numerical works regarding this subject have been done. There are several good review papers and text books, for example, see [2–5].

Inertia-gravity waves, in which buoyancy and Coriolis force provide the restoring force, are important in the atmosphere and ocean, because they drive general circulation in the middle

atmosphere [6] and contribute to the ocean energy budget [7, 8]. Traditionally, rotating shallow water system has been used to study nonlinear interactions between vortex and wave [9] because this system is the simplest system in which both vortical flows and inertia-gravity waves can exist. One of the typical examples is the Rossby adjustment process [10, 11], in which initial unbalanced state is assumed. Then inertia-gravity waves (hereafter inertia-gravity waves are referred to gravity waves) are radiated from unbalanced state toward balanced state. However, there are few works regarding the generation of gravity waves by unsteady motions of nearly balanced vortical flows in rotating shallow water system.

Ford's pioneering work [12] has shown that gravity waves are radiated from unsteady vortical flows. This type of gravity wave radiation is referred to as "spontaneous emission" [13], because initial balanced flows radiate gravity waves spontaneously during the time evolution. Since a shallow water system is equivalent to a two-dimensional adiabatic gas system if the effect of Earth's rotation is negligibly small, gravity waves are analogous to sound waves. Using the acoustic analogy of Lighthill [1], Ford [12, 13] introduced a source of gravity waves. For the purpose of practical motivation, this new paradigm of spontaneous emission is intensively investigated; for example, see [14] and references therein. Recently, the theory of generation mechanism has been proposed [15, 16]. While it is pointed out that spontaneous emission in the shallow water system is different from that in the continuous stratified system [17], fundamental works from a viewpoint of geophysical fluid dynamics are nevertheless important [18].

As an extension of Ford's works [12, 13], several numerical works are performed in shallow water system on an f -plane [19, 20] and a sphere [21]. While it is widely known that the effect of the Earth's rotation suppresses inertia-gravity wave radiation, previous studies [20, 21] have reported that the effect of the Earth's rotation intensify gravity wave radiation in some parameter space. In this chapter, recent results of the inertia-gravity wave radiation from nearly balanced vortical flows as an extension of sound wave generation from vortical flows are reviewed. Inertia-gravity wave radiation from various types of vortical flows, such as a corotating vortex pair [22], elliptical vortex (Kirchhoff vortex) [23] and merging of (equal or unequal) vortices [24, 25], are investigated in a wide range of parameter space. All these works have reported that cyclone-anticyclone asymmetry in spontaneous emission and a local maximum of intensity of gravity waves emitted from anticyclones at intermediate value of the Coriolis parameter f .

This chapter is organized as follows. In Section 2, the analytical derivation of the far fields of gravity waves is introduced for the cases of a corotating point vortex pair and an almost circular Kirchhoff vortex. The derived forms are verified quite well by the numerical simulation (Section 3). In addition, the results of gravity wave radiation from the merging of (equal or unequal) vortices are also introduced. Section 4 gives brief summary points and future issues.

2. Analytical estimate

In this section, the analytical derivation of the far fields of gravity waves from vortical flows is introduced. The derived form includes the effect of Earth's rotation in the source term, which

causes the cyclone-anticyclone asymmetry. Two examples of the corotating point vortex pair and Kirchhoff vortex are shown. See Refs. [22] and [23] for details.

2.1. Basic equation

Basic equations are the shallow water equations on an f -plane, written as

$$\frac{\partial u_c}{\partial t} + u_c \frac{\partial u_c}{\partial x} + v_c \frac{\partial u_c}{\partial y} - f v_c = -g \frac{\partial h}{\partial x}, \tag{1}$$

$$\frac{\partial v_c}{\partial t} + u_c \frac{\partial v_c}{\partial x} + v_c \frac{\partial v_c}{\partial y} + f u_c = -g \frac{\partial h}{\partial y}, \tag{2}$$

$$\frac{\partial h}{\partial t} + u_c \frac{\partial h}{\partial x} + v_c \frac{\partial h}{\partial y} + h \left(\frac{\partial u_c}{\partial x} + \frac{\partial v_c}{\partial y} \right) = 0, \tag{3}$$

where $\mathbf{u} = (u_c, v_c)$ is the horizontal velocity vector, where u_c and v_c are the velocity components in the x and y directions in the Cartesian coordinates, respectively. The total depth of the fluid $h = \eta + h_0$, in which η is the surface displacement from the average depth of the fluid h_0 . The Coriolis parameter and gravitational acceleration are f and g , respectively.

Eqs. (1)–(3) are the same as for vortex sound (aeroacoustics) if the effect of the Earth's rotation is negligibly small. From Eqs. (1)–(3), Lighthill-Ford equation is obtained [1, 12]:

$$\left(\frac{\partial^2}{\partial t^2} + f^2 - c_0^2 \nabla^2 \right) \frac{\partial h}{\partial t} = \frac{\partial^2}{\partial x_i \partial x_j} T_{ij}, \tag{4}$$

where $x_1 = x, x_2 = y$ and the Einstein summation convention is used. Note that $c_0 = \sqrt{gh_0}$ and ∇^2 are the phase speed of the fastest gravity wave and the horizontal Laplacian, respectively. Here, T_{ij} is written as

$$T_{ij} = \frac{\partial(hu_i u_j)}{\partial t} + \frac{f}{2} (\epsilon_{ik} h u_j u_k + \epsilon_{jk} h u_i u_k) + \frac{g}{2} \frac{\partial}{\partial t} (h - h_0)^2 \delta_{ij}, \tag{5}$$

where $\epsilon_{12} = -\epsilon_{21} = 1, \epsilon_{11} = \epsilon_{22} = 0, u_1 = u_c, u_2 = v_c$ and δ_{ij} is the Kronecker delta. Since the left-hand side of Eq. (4) is the wave operator of a linear gravity wave, the right-hand side can be regarded as the source of gravity waves under the assumption in the limit of small Froude number [12, 13], Fr (where $Fr \equiv U/c_0$ is the ratio of the flow velocity U to the phase speed of gravity waves). Note that Fr corresponds to Mach number (the ratio of the flow velocity to the phase speed of sound waves) in the field of aeroacoustics.

2.2. Source and far field

In the source T_{ij} , the primary source of gravity waves for the nonrotating case is the first term on the right-hand side of Eq. (5), which is associated with the vortical flows. Then, for the relevant term on the right-hand side of Eq. (4), the following approximation holds

$$\frac{\partial^2(hu_i u_j)}{\partial x_i \partial x_j} \approx h_0 \nabla \cdot (\boldsymbol{\omega} \times \mathbf{u}) + h_0 \nabla^2 \left(\frac{1}{2} u^2 \right), \quad (6)$$

for nondivergent flow ($\nabla \cdot \mathbf{u} = 0$ and $h \approx h_0$) under the assumption of $Fr \ll 1$ with compact source of the vortical motion. The second term on the right-hand side of Eq. (6) can be neglected, because this term is $O(Fr^2)$ smaller than that from the first term for $Fr \ll 1$.

For the rotating case, on the other hand, the second term on the right-hand side of Eq. (5) becomes also important for relatively larger f [20, 21]. Then, for the relevant term on the right-hand side of Eq. (4), the following approximation holds

$$\frac{\partial^2}{\partial x_i \partial x_j} \frac{f}{2} (\epsilon_{ik} h u_j u_k + \epsilon_{jk} h u_i u_k) = \frac{\partial^2}{\partial x_i \partial x_j} f h \epsilon_{ik} u_j u_k \approx -f h_0 \nabla \cdot [\mathbf{k} \times (\boldsymbol{\omega} \times \mathbf{u})], \quad (7)$$

for nondivergent flow ($\nabla \cdot \mathbf{u} = 0$ and $h \approx h_0$). This is the source originating in the Coriolis acceleration.

The Green's function of Eq. (4) in the two-dimensional domain incorporating time variation is defined from the Klein-Gordon equation:

$$\left(\nabla^2 - \frac{1}{c_0^2} \frac{\partial^2}{\partial t^2} - \mu^2 \right) G_2(\mathbf{x}, t, \mathbf{x}', t') = -\delta(\mathbf{x} - \mathbf{x}') \delta(t - t'), \quad (8)$$

where $\mu = f/c_0$. The form of Green's function is

$$G_2(\mathbf{x}, t, \mathbf{x}', t') = \frac{c_0}{2\pi} \frac{\cos\left(\mu \sqrt{c_0^2(t-t')^2 - |\mathbf{x} - \mathbf{x}'|^2}\right)}{\sqrt{c_0^2(t-t')^2 - |\mathbf{x} - \mathbf{x}'|^2}} \theta_s\left(c_0(t-t') - |\mathbf{x} - \mathbf{x}'|\right), \quad (9)$$

where θ_s is the Heaviside function. Finally, by analogy with the derivation of the far field of sound waves, the integral form of far field of gravity waves is formally expressed as

$$\frac{\partial h(\mathbf{x}, t)}{\partial t} = \frac{h_0}{c_0^2} \iiint_{-\infty}^{\infty} G_2 \left[\frac{\partial}{\partial t'} \nabla \cdot (\boldsymbol{\omega} \times \mathbf{u}) - f \nabla \cdot [\mathbf{k} \times (\boldsymbol{\omega} \times \mathbf{u})] \right] d\mathbf{x}' dt'. \quad (10)$$

2.3. Typical examples

To solve Eq. (10) analytically, two cases of a corotating point vortex pair and an almost circular Kirchhoff vortex are introduced as examples. **Figure 1** shows the schematics of these experimental configurations.

A point vortex pair with the same sign and strength corotates. For aeroacoustics, analytical [4] and numerical [26] studies are performed in this configuration. Zeitlin [9] also derived an analytical solution in nonrotating shallow water. A vortex pair with a circulation Γ positioned at distance $2l$ corotates at an angular velocity $\Omega = \Gamma/4\pi l^2$. The positions are

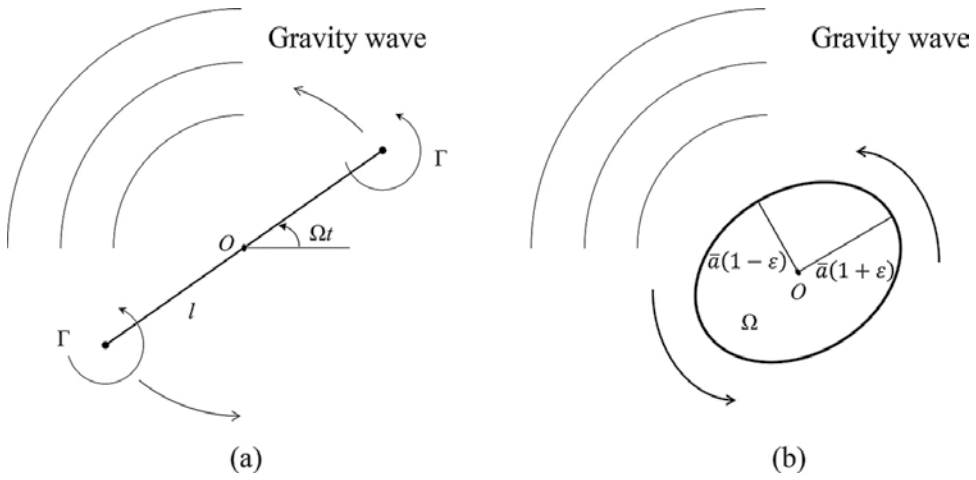


Figure 1. Schematics of experimental configurations for the cases of (a) a corotating point vortex pair and (b) an almost circular Kirchhoff vortex.

$$\mathbf{x} = (x_1, x_2) = \mathbf{s} \equiv (s_1(t), s_2(t)) = \pm l (\cos(\Omega t), \sin(\Omega t)). \quad (11)$$

Then the vorticity $\boldsymbol{\omega}$ and velocity $\mathbf{u} = (u_1, u_2)$ associated with the vortices are written as

$$\boldsymbol{\omega} = \Gamma \mathbf{k} [\delta(\mathbf{x} - \mathbf{s}) + \delta(\mathbf{x} + \mathbf{s})], \quad (12)$$

$$\mathbf{u} = \pm \Omega \mathbf{k} \times \mathbf{s} \text{ at } \mathbf{x} = \pm \mathbf{s}, \quad (13)$$

where \mathbf{k} is a unit vector in the z direction and δ is a delta function. Assuming that the characteristic velocity scale $U = \Omega l \ll c_0$, then,

$$\boldsymbol{\omega} \times \mathbf{u} = -\Gamma \Omega \mathbf{s} [\delta(\mathbf{x} - \mathbf{s}) - \delta(\mathbf{x} + \mathbf{s})]. \quad (14)$$

From Eq. (6) the source associated with vortical flows is equivalent to the two-dimensional quadrupole

$$\nabla \cdot (\boldsymbol{\omega} \times \mathbf{u}) \approx \frac{\partial^2}{\partial x_i \partial x_j} (S_{ij} \delta(\mathbf{x})), \quad (15)$$

where

$$S_{ij} = \Gamma \Omega^2 \begin{pmatrix} 1 + 2 \cos 2\Omega t & \sin 2\Omega t \\ \sin 2\Omega t & 1 - \cos 2\Omega t \end{pmatrix}. \quad (16)$$

Similarly, from Eq. (7) the source originating in the Coriolis acceleration is expressed as

$$-f \nabla \cdot [\mathbf{k} \times (\boldsymbol{\omega} \times \mathbf{u})] \approx f \frac{\partial^2}{\partial x_i \partial x_j} (\epsilon_{ik} S_{kj} \delta(\mathbf{x})). \quad (17)$$

As for the case of the Kirchhoff vortex, the derivation is in the same line as a corotating point vortex pair. The Kirchhoff vortex has a patch of constant vorticity, Ω , inside an ellipse and zero vorticity outside. It is an exact solution of the two-dimensional, incompressible and inviscid flow equations [27]. Howe [4] derived far field of sound waves from the Kirchhoff vortex analytically. An almost circular Kirchhoff vortex with a small aspect ratio is the ellipse defined by the polar equation for $\varepsilon \ll 1$

$$r = \bar{a} \left[1 + \varepsilon \cos \left(2\theta - \frac{\Omega t}{2} \right) \right], \quad (18)$$

where the semimajor axis of the ellipse is $a = \bar{a}(1 + \varepsilon)$, the semiminor axis is $b = \bar{a}(1 - \varepsilon)$. The ellipse rotates at angular velocity $\Omega/4$. The velocity within the core is

$$\mathbf{u} = (u_1, u_2) = -\frac{1}{2}\Omega r \left(\sin \theta + \varepsilon \sin \left(\theta - \frac{\Omega t}{2} \right), -\cos \theta + \varepsilon \cos \left(\theta - \frac{\Omega t}{2} \right) \right). \quad (19)$$

Then, to first order in ε , the source associated with vortex and the source originating in the Coriolis acceleration are again expressed as Eqs. (15) and (17), respectively, where

$$S_{ij} = \frac{\varepsilon \pi \Omega^2 \bar{a}^4}{8} \begin{pmatrix} \cos(\Omega t/2) & \sin(\Omega t/2) \\ \sin(\Omega t/2) & -\cos(\Omega t/2) \end{pmatrix}. \quad (20)$$

After substituting Eqs. (15) and (17) in Eq. (10), the delta function can be integrated

$$\frac{\partial h(\mathbf{x}, t)}{\partial t} = \frac{h_0}{c_0^2} \frac{\partial^2}{\partial x_i \partial x_j} \int_{-\infty}^{\infty} G_2 \left[\frac{\partial}{\partial t'} (S_{ij}) + f \epsilon_{ik} S_{kj} \right] dt'. \quad (21)$$

Recalling that the following approximation in the far field ($r = \sqrt{x_1^2 + x_2^2} \gg 1$),

$$\frac{\partial^2}{\partial x_i \partial x_j} = \left(\frac{\delta_{ij}}{r} - \frac{x_i x_j}{r^3} \right) \frac{\partial}{\partial r} + \frac{x_i x_j}{r^2} \frac{\partial^2}{\partial r^2} \approx \frac{x_i x_j}{r^2} \frac{\partial^2}{\partial r^2}, \quad (22)$$

then it follows from Eq. (21):

$$\begin{aligned} \frac{\partial h(\mathbf{x}, t)}{\partial t} &= \frac{h_0}{c_0^2} \frac{\partial^2}{\partial r^2} \int_{-\infty}^{\infty} G_2 \frac{x_i x_j}{r^2} \left[\frac{\partial}{\partial t'} (S_{ij}) + f \epsilon_{ik} S_{kj} \right] dt' \\ &= \begin{cases} \frac{2\Gamma \Omega^2 l^2 h_0}{c_0^2} \left(1 - \frac{f}{2\Omega} \right) \frac{\partial^2}{\partial r^2} \int_{-\infty}^{\infty} G_2 \sin(2\theta - 2\Omega t') dt', & \text{for } a \text{ corotating vortex pair} \\ \frac{\varepsilon \pi \Omega^3 \bar{a}^4 h_0}{16c_0^2} \left(1 - \frac{2f}{\Omega} \right) \frac{\partial^2}{\partial r^2} \int_{-\infty}^{\infty} G_2 \sin \left(2\theta - \frac{\Omega t'}{2} \right) dt', & \text{for the Kirchhoff vortex.} \end{cases} \quad (23) \end{aligned}$$

With the form of Green's function Eq. (9), Eq. (23) for a corotating vortex pair is written as

$$\frac{\partial h(x, t)}{\partial t} = \left(1 - \frac{f}{2\Omega}\right) \frac{\Gamma \Omega^2 l^2 h_0}{\pi c_0} \frac{\partial^2}{\partial r^2} \underbrace{\int_{-\infty}^t \frac{\sin(2\theta - 2\Omega t') \cos(\mu \sqrt{\tau})}{\sqrt{\tau}} \theta_s(c_0(t-t') - r) dt'}_B, \quad (24)$$

where $\tau = c_0^2(t - t')^2 - r^2$. The integral in Eq. (24), labeled as B , can be calculated by changing variables, $t - t' = (r/c_0)\cosh \varphi$ and $\sqrt{\tau} = \sinh \varphi$. By using the integral form of Hankel's function $H_0(x)$, B is expressed as

$$B = \frac{1}{2c_0} \operatorname{Re} \left[i\pi H_0^{(1)} \left(r \sqrt{\left(\frac{2\Omega}{c_0}\right)^2 - \mu^2} \right) \right] \sin(2\theta - 2\Omega t) - \operatorname{sgn}(f) \operatorname{sgn}(\Omega) \frac{1}{2c_0} \operatorname{Im} \left[i\pi H_0^{(1)} \left(r \sqrt{\left(\frac{2\Omega}{c_0}\right)^2 - \mu^2} \right) \right] \cos(2\theta - 2\Omega t), \quad (25)$$

where the sign function $\operatorname{sgn}(x)$ is defined so that $\operatorname{sgn}(0) = 1$. $H_2^{(1)}(ax) \approx -H_0^{(1)}(ax)$ for $ax \gg 1$ are also used for $(r/c_0)\sqrt{\Omega^2/4 - f^2} \gg 1$. Then the following approximation can be used

$$\frac{\partial^2 B}{\partial r^2} \approx \left[\left(\frac{\Omega}{2c_0}\right)^2 - \mu^2 \right] B, \quad (26)$$

because $d^2 H_0^{(1)}(ax)/dx^2 = \alpha^2/2(H_2^{(1)}(ax) - H_0^{(1)}(ax)) \approx -\alpha^2 H_0^{(1)}(ax)$. Finally, the following form for the far field of gravity waves is obtained for a corotating point vortex pair,

$$\frac{\partial h(x, t)}{\partial t} = \frac{2\Gamma \Omega^4 l^2 h_0}{c_0^4} \left(1 - \frac{f}{2\Omega}\right) \left[1 - \left(\frac{f}{2\Omega}\right)^2\right] \left[Y_0\left(\frac{r}{c_0} \sqrt{4\Omega^2 - f^2}\right) \sin(2\theta - 2\Omega t) - \operatorname{sgn}(f) \operatorname{sgn}(\Omega) J_0\left(\frac{r}{c_0} \sqrt{4\Omega^2 - f^2}\right) \cos(2\theta - 2\Omega t) \right], \quad (27)$$

where $H_0^{(1)}(ax) = J_0(ax) + iY_0(ax)$ is used, in which J_0 and Y_0 are the zeroth-order Bessel functions of the first and second kind, respectively. The similar procedure from Eqs. (24) to (27) can be applied for the Kirchhoff vortex, then

$$\frac{\partial h(x, t)}{\partial t} = \frac{\varepsilon \pi \Omega^5 \bar{a}^4 h_0}{256c_0^4} \left(1 - \frac{2f}{\Omega}\right) \left[1 - \left(\frac{2f}{\Omega}\right)^2\right] \left[Y_0\left(\frac{r}{c_0} \sqrt{\frac{\Omega^2}{4} - f^2}\right) \sin\left(2\theta - \frac{\Omega}{2}t\right) - \operatorname{sgn}(f) \operatorname{sgn}(\Omega) J_0\left(\frac{r}{c_0} \sqrt{\frac{\Omega^2}{4} - f^2}\right) \cos\left(2\theta - \frac{\Omega}{2}t\right) \right]. \quad (28)$$

Eqs. (27) and (28) are applicable for both cyclone ($\Omega > 0$) and anticyclone ($\Omega < 0$) vortices regardless of the signs of f . In the absence of the Earth's rotation for $f \rightarrow 0$, Eqs. (27) and (28) correspond to the analytical form of the vortex sound [4, 26]. In contrast, there are several important effects for finite f . First, spontaneous emission is suppressed for large f because of a small value in the square root and second parentheses. Second, the source Eq. (7) originating in the Coriolis acceleration acts oppositely to the gravity wave radiation caused by the second term in the first parentheses. Meanwhile, the source Eq. (7) originating in the Coriolis acceleration cancels out the source Eq. (6) associated with vortex, since the same signs of Ω and f for cyclone. In contrast, those two sources magnify each other for anticyclone. Then, gravity waves are intensely radiated from anticyclone. Simple explanations for the suppression of gravity wave radiation at large f are reported [9]. Note also that it is possible to derive analytical estimate in the case of evanescent gravity waves for $\Omega^2/4 \leq f^2$ [22].

Examples of the far field of gravity waves ($d\Phi/dt$, where $\Phi \equiv gh$ is the geopotential height) from the corotating point vortex pair and Kirchhoff vortex are shown in **Figure 2**. Here, the Rossby number ($Ro \equiv U_l/fL$) and Froude number ($Fr \equiv U_l/\sqrt{\Phi_0}$) are defined by the typical values, where the velocity U_l and the length L scales are chosen as the velocity and the length of each vortex configuration. The values of $\Omega = 0.1$, $U_l = 0.5$, $l = 1.0$ and $\Phi_0 = 25/36$ for the corotating vortex pair and those of $U_l = 0.2$, $L = a = 1.0$ and $\Phi_0 = 4/9$ for the Kirchhoff vortex are fixed to be consistent with those of numerical simulations. The value of $\Omega = 0.449 - 0.025(0.95 - b)$ for the Kirchhoff vortex is also chosen for different values of b in order to keep $U_l = 0.2$ as a constant value. The double spiral patterns for both cases clearly show the rotating quadrupole features of the radiated gravity waves. The wave patterns depend on the vortical flows and their parameter values, namely, Ω , Ro , Fr and the aspect ratio. Anticyclone radiates gravity waves more intensely than cyclone at relatively large f (**Figure 2a** and **b**) and there is no cyclone-anticyclone asymmetry in spontaneous emission for the nonrotating case of $f = 0$ (**Figure 2c**).

The intensity of gravity waves for both cases of the corotating vortex pair, I_{vp} and the Kirchhoff vortex, I_{kv} , are defined by

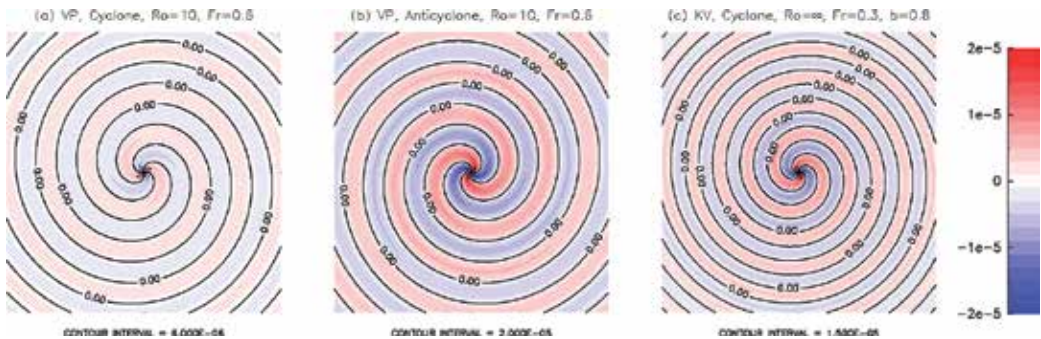


Figure 2. Snapshots of the far fields ($r \leq 100$) of gravity waves ($d\Phi/dt$, where $\Phi \equiv gh$) radiated from the corotating point vortex pair and Kirchhoff vortex: (a) cyclone, (b) anticyclone corotating vortex pair with $Ro = 10$ ($f = 1/10$) and $Fr = 0.6$ ($gh_0 = 25/36$) and (c) cyclone Kirchhoff vortex with $Ro = \infty$ ($f = 0$), $b = 0.8$ ($\bar{a} = 0.9$, $\varepsilon = 1/9$) and $Fr = 0.3$ ($gh_0 = 4/9$).

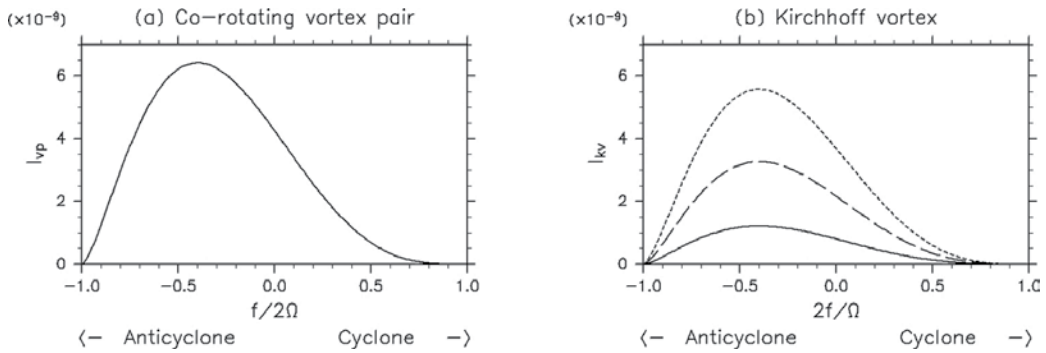


Figure 3. Analytical estimates of the dependence on f of the intensity of gravity waves: (a) the corotating vortex pair, I_{vp} , calculated from Eq. (29) and (b) the Kirchhoff vortex, I_{kv} , calculated from Eq. (30) with $b = 0.95$ ($\bar{a} = 0.975, \varepsilon = 1/39$; solid line), $b = 0.9$ ($\bar{a} = 0.95, \varepsilon = 1/19$; broken line) and $b = 0.8$ ($\bar{a} = 0.9, \varepsilon = 1/9$; dotted line).

$$I_{vp} = \int_0^{2\pi} \left(\frac{\partial \Phi}{\partial t} \right)^2 r d\theta \approx \frac{64\pi^2 \Omega^9 l^8}{c_0^3} \left(1 - \frac{f}{2\Omega} \right)^2 \left[1 - \left(\frac{f}{2\Omega} \right)^2 \right]^{\frac{3}{2}}, \quad (29)$$

$$I_{kv} \approx \frac{\varepsilon^2 \pi^2 \Omega^9 \bar{a}^8}{16384 c_0^3} \left(1 - \frac{2f}{\Omega} \right)^2 \left[1 - \left(\frac{2f}{\Omega} \right)^2 \right]^{\frac{3}{2}}, \quad (30)$$

to estimate the dependence on f of gravity waves from both cyclone and anticyclone. Here, $J_0(ax) \approx \sqrt{2/\pi ax} \cos(ax - \pi/4)$ and $Y_0(ax) \approx \sqrt{2/\pi ax} \sin(ax - \pi/4)$ for $ax \gg 1$ are used to derive Eqs. (29) and (30). These values are the same at any r in the field. **Figure 3** shows I_{vp} (Eq. 29) and I_{kv} (Eq. 30) for three b cases ($b = 0.95, 0.9$, and 0.8). For anticyclone vortex, a local maximum appears at $f/2\Omega = -0.4$ ($Ro \sim 12.5, f \sim 2/25$) for the corotating point vortex pair and $2f/\Omega = -0.4$ ($Ro \sim 1, f \sim 1/10$) for the Kirchhoff vortex. The cyclone-anticyclone asymmetry is similar to both cases, though vortical flows are completely different. Note that Ro is different among the vortices for the same value of f because the velocity and length scales depend on the vortical configuration.

3. Numerical simulation

To verify the analytical solution, a numerical simulation with a newly developed spectral method in an unbounded domain has been performed. The numerical results are in excellent agreement with the analytical results of Eqs. (27) and (28) [22, 23]. Furthermore, additional numerical simulations have been performed for the cases of merging of (equal or unequal) vortices, in which analytical solution cannot be derived [24, 25]. In this section, the results of numerical simulation as well as model settings are introduced.

3.1. Model settings

Shallow water equations on an f -plane in polar coordinates are used for the numerical simulation. The equations of relative vorticity ζ , divergence δ and geopotential height Φ are

$$\frac{\partial \zeta}{\partial t} = -\frac{1}{r} \frac{\partial (rv\zeta_a)}{\partial r} - \frac{1}{r} \frac{\partial (u\zeta_a)}{\partial \theta}, \quad (31)$$

$$\frac{\partial \delta}{\partial t} = \frac{1}{r} \frac{\partial (ru\zeta_a)}{\partial r} - \frac{1}{r} \frac{\partial (v\zeta_a)}{\partial \theta} - \Delta(E + \Phi), \quad (32)$$

$$\frac{\partial \Phi}{\partial t} = -\frac{1}{r} \frac{\partial (rv\Phi)}{\partial r} - \frac{1}{r} \frac{\partial (u\Phi)}{\partial \theta}, \quad (33)$$

where u and v are the velocities in the azimuthal (θ) and radial (r) directions, respectively and

$$\text{relative vorticity } \zeta = \frac{1}{r} \frac{\partial (ru)}{\partial r} - \frac{1}{r} \frac{\partial v}{\partial \theta} = \Delta\psi, \quad (34)$$

$$\text{divergence } \delta = \frac{1}{r} \frac{\partial (rv)}{\partial r} + \frac{1}{r} \frac{\partial u}{\partial \theta} = \Delta\chi, \quad (35)$$

$$\text{Laplacian } \Delta = \frac{1}{r} \frac{\partial}{\partial r} \left(r \frac{\partial}{\partial r} \right) + \frac{1}{r^2} \frac{\partial^2}{\partial \theta^2}, \quad (36)$$

$$\text{kinetic energy } E = \frac{1}{2} (u^2 + v^2), \quad (37)$$

$$\text{absolute vorticity } \zeta_a = f + \zeta, \quad (38)$$

where ψ and χ are the stream function and velocity potential, respectively.

Eqs. (31)–(33) are solved by a conformal mapping from a sphere $P_i(\lambda, \phi)$ with radius R to a plane $Q_i(r, \theta)$ in the numerical simulation [28]. **Figure 4** shows a schematic of this mapping. With the aid of the following relation,

$$r = 2R \tan \left(\frac{\phi}{2} + \frac{\pi}{4} \right), \quad (39)$$

the transformation of the coordinates is expressed as

$$\frac{\partial}{\partial r} = \frac{1 - \sin \phi}{2R}, \quad \frac{1}{r} \frac{\partial}{\partial \theta} = \frac{1 - \sin \phi}{2R \cos \phi} \frac{\partial}{\partial \lambda}. \quad (40)$$

Then the phenomena on a two-dimensional unbounded plane can be calculated on a sphere with an ordinary spectral method of spherical harmonics by this mapping. Since grid points are arranged nonuniformly (many grid points are positioned in the near field of vortical flows, while few are in the far field of gravity waves), this method enables us to simulate nonlinear interactions between vortical flows and gravity waves with high accuracy [22–25].

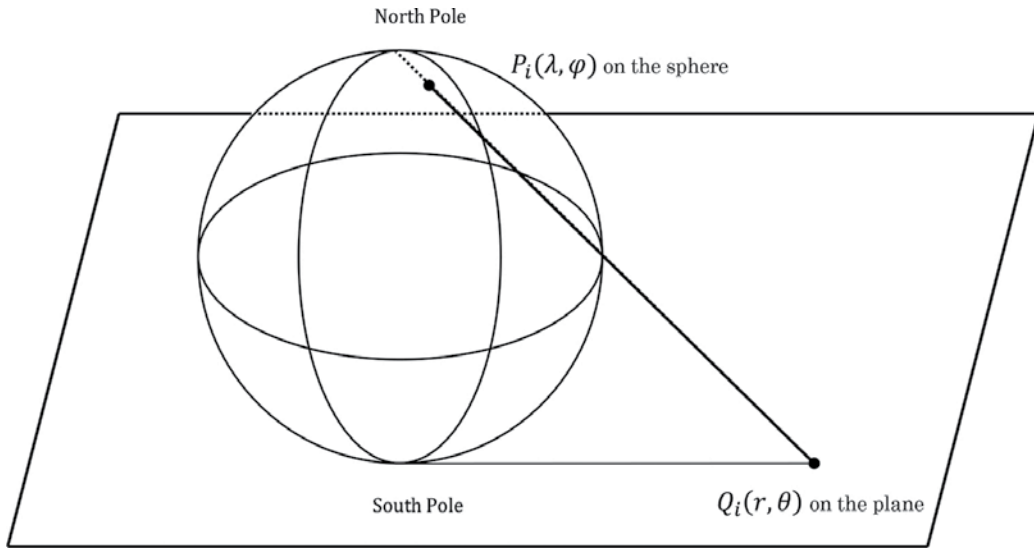


Figure 4. Schematic of the mapping method from $P_i(\lambda, \phi)$ on sphere to $Q_i(r, \theta)$ on a plane.

Additional advantage is that the term of the hyper viscosity, which is intended to dissipate unresolved small scales numerically in the spectral model, acts as a sponge layer. By the conformal mapping, the usual form of hyper viscosity can be written as

$$\nu(-1)^{p+1} \left(\frac{4\Delta}{(1 - \sin\phi)^2} \right)^p P, \tag{41}$$

where ν , p and $P = (\zeta, \delta, \Phi)$ are the viscosity coefficient, order of viscosity and physical variables, respectively. Eq. (41) acts as a usual hyper viscosity in the near field of vortical flow for small ϕ . On the other hand, the viscosity becomes large and acts as a sponge layer for large ϕ in the far field where waves are propagating. Eq. (41) is easy to code in the numerical simulation because Laplacian operator on a sphere is simply calculated by spherical harmonics.

3.2. Verification

As an initial state, a corotating Gaussian vortex pair is used to mimic a point vortices, which is expressed as

$$\zeta = \pm A_1 \exp \left\{ -\frac{(x - x_1)^2 + (y - y_1)^2}{2\sigma^2} \right\} \pm A_2 \exp \left\{ -\frac{(x - x_2)^2 + (y - y_2)^2}{2\sigma^2} \right\}, \tag{42}$$

where $(x, y) = (r\cos\theta, r\sin\theta)$. The values of A_1 , A_2 , σ , $(x_1, y_1) = (l\cos\theta_1, l\sin\theta_1)$ and $(x_2, y_2) = (l\cos(\theta_1 + \pi), l\sin(\theta_1 + \pi))$ determine the amplitudes, radius and positions of the vortices, respectively (see also **Figure 1a**). The values of $A_1 = A_2 = 20$, $\sigma = 0.05$, $l = 0.5$ and

$\theta_1 = \pi/4$ are fixed and then the maximum velocity $U_{vp} \approx 0.5$ becomes a constant value. The Rossby number $Ro \equiv U_{vp}/fl$ and the Froude number $Fr \equiv U_{vp}/\sqrt{\Phi_0}$ are defined by the basic state, where $\Phi_0 = 25/36$ determines the average depth. Then, $Fr(= 0.6)$ is fixed and Ro is reciprocal of f . The field of Φ is set to be in gradient balance with ζ .

Similarly, elliptical Gaussian vortex positioned at the origin is used to mimic the Kirchhoff vortex

$$\zeta = \pm A \exp \left\{ - \left(\frac{\sqrt{(ax)^2 + (by)^2}}{l_{kv}} \right)^n \right\}, \quad (43)$$

where A , a , b , n and l_{kv} determines the amplitude, the length of semimajor axis and semiminor axis, the steepness and the core area of elliptical vortex, respectively. The values of $a = 1.0$, $n = 10$, and $l_{kv} = 1.0$ are fixed, then the semimajor axis of elliptical vortex is fixed to ~ 1 , while b is swept to change the aspect ratio. Then, \bar{a} and ε are determined by b solely (see also **Figure 1b**). $A = 0.449 - 0.025(0.95 - b)$ is also set to keep the maximum velocity $U_{kv} \approx 0.2$ as a constant value. The Rossby number $Ro \equiv U_{kv}/fl_{kv}$ and the Froude number $Fr \equiv U_{kv}/\sqrt{\Phi_0}$ are defined by the basic state, where $\Phi_0 = 4/9$ determines the average depth. Again, $Fr(= 0.3)$ is fixed and Ro is reciprocal of f . Note again that Ro is different among the vortices for the same value of f because the velocity and length scales depend on the vortical configuration. The field of Φ is set to be in gradient balance with ζ , too. **Figure 5** shows examples of initial Gaussian vortex pair with $Ro = 10$ ($f = 1/10$) and $Fr = 0.6$ and elliptical Gaussian vortex with $Ro = 1$ ($f = 1/10$), $Fr = 0.3$ and $b = 0.9$ ($\bar{a} = 0.95$, $\varepsilon = 1/19$). The vorticity ζ velocity u in the θ direction and geopotential height Φ are shown for the corotating vortex pair (along the section of center of the vortices) and for the elliptical vortex (along the sections of semimajor axis and semiminor axis of the vortex).

The number of grid points is set to be 2048×1024 in the θ and r directions, with the truncation wavenumber of spherical harmonics $T = 682$ and $R = 8$. Then the grid interval in the r direction (Δr) in the near field ($r \leq 2$) is $\Delta r \leq 0.0249$ and the farthest grid points are positioned at $r \sim 13,632$. The viscosity coefficient and order of viscosity are set to be $\nu = 10^{-11}$ and $p = 3$, respectively. Fourth-order Runge-Kutta method is used for the time integration. For the corotating vortex pair 8,000 total time steps are conducted to the end of time 200 with a time interval $\Delta t = 0.025$, while for the elliptical vortex, 10,000 time steps are conducted with a $\Delta t = 0.02$.

In both configurations, the numerical simulations with several Ro for fixed Fr are performed for cyclone and anticyclone vortex individually, starting from above initial state. Gravity waves are spontaneously radiated from both cyclone and anticyclone vortical flows for large enough Ro , while anticyclones rotate in the opposite direction to cyclones. **Figure 6** shows line plots of radiated gravity waves $d\Phi/dt$ against r from cyclone and anticyclone for both cases of the corotating vortex pair and Kirchhoff vortex. The line plots in the $\theta = \pi/4$ section at $t = 200$ are shown for the numerical simulation (broken lines), while appropriate times are chosen for the analytical estimates (solid lines) to coincide with the numerical results. The amplitudes of

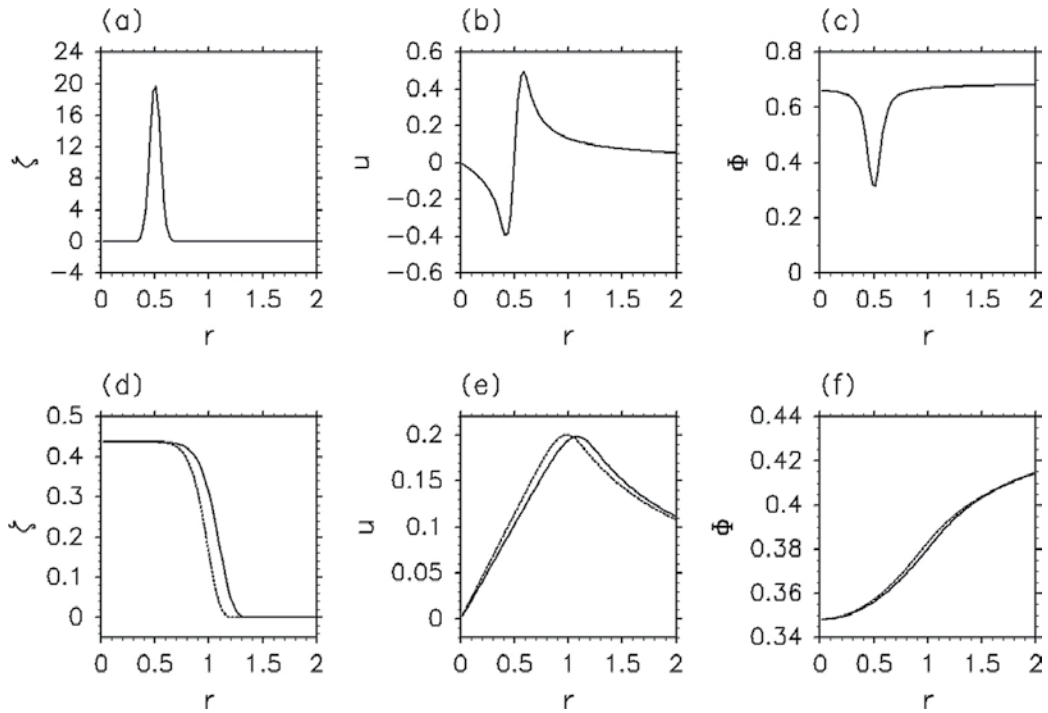


Figure 5. Initial corotating cyclone vortex pair (top panels) with $Ro = 10$ ($f = 1/10$) and $Fr = 0.6$ ($\Phi_0 = 25/36$) and elliptical cyclone vortex (bottom panels) with $Ro = 1$ ($f = 1/10$), $Fr = 0.3$ ($\Phi_0 = 4/9$) and $b = 0.9$ ($\bar{a} = 0.95$, $\varepsilon = 1/19$): ζ (a, d), u (b, e) and Φ (c, f) are shown. In the top panels, solid lines indicate the values along the section of center of vortex. In bottom panels, the solid lines indicate the values along the section of semi-major axis, while dotted lines indicate those of semi-minor axis.

gravity waves in the far field between the analytical and numerical results are almost the same for all cases. While there is no cyclone–anticyclone asymmetry for the nonrotating case ($f = 0$), the anticyclones radiate gravity waves more intensely than cyclones for relatively small Ro cases. Local maximum appears around $2f/\Omega \sim -0.4$ only for the cases of anticyclone, as expected in Section 2.3. All cases with different Ro are remarkably good overlapped between analytical estimates and numerical results, except for the elliptical vortex with for $b = 0.8$.

The intensity of gravity waves for both cases calculated from Eqs. (29) and (30) in the numerical simulation agree well with analytical estimates (not shown). The results indicate that the analytical estimates give the far fields of gravity waves quite accurately and the newly developed numerical model is well verified. Furthermore, cyclone-anticyclone asymmetry and the local maximum of gravity waves for anticyclone are also confirmed for both cases of the corotating vortex pair and Kirchhoff-like elliptical vortex. Note that for the elliptical vortex with for $b = 0.8$, the aspect ratio increases gradually in the time evolution, more elongated elliptical vortex with filaments appears. Then the amplitude of the source becomes larger than that used in the analytical estimate. Significant deviation for the shape of vortex from the ideal elliptical vortex causes the large discrepancy between the analytical and numerical results for $b = 0.8$ [23].

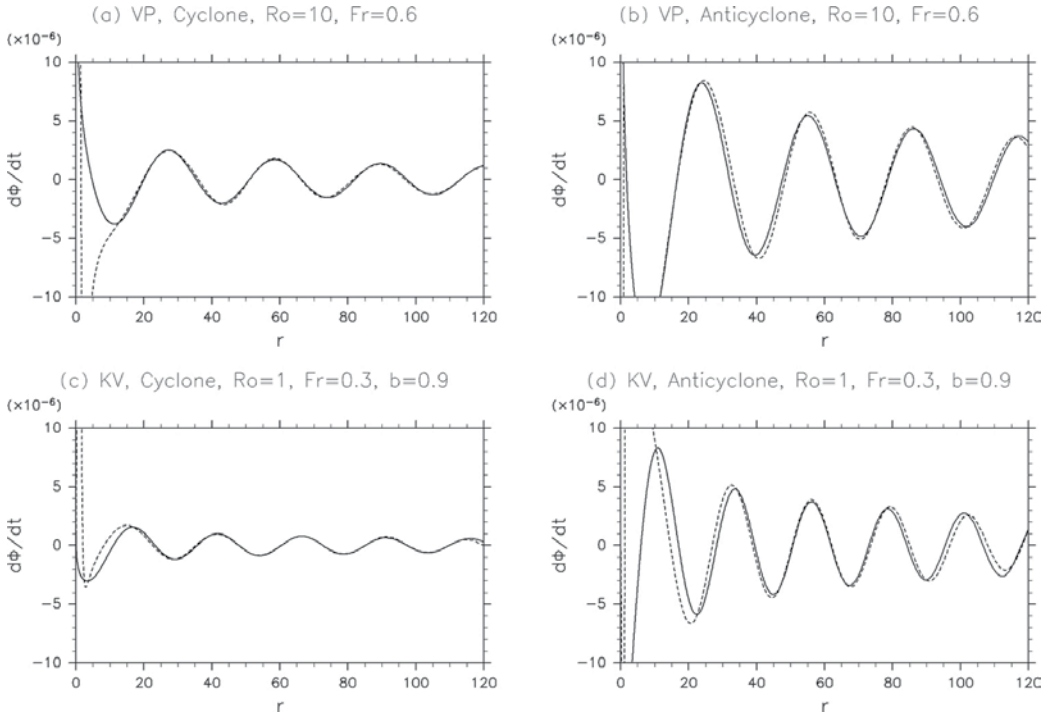


Figure 6. The far field ($r \leq 100$) of gravity waves ($d\Phi/dt$) for the corotating vortex pair (top panels) with $Ro = 10$ and $Fr = 0.6$ and elliptical vortex (bottom panels) with $Ro = 1$, $Fr = 0.3$, and $b = 0.9$. The analytical estimates Eqs. (27) and (28) (solid lines) and the numerical results in the $\theta = \pi/4$ section at $t = 200$ (broken lines) are shown for (a, c) cyclones and (b, d) anticyclones.

3.3. Extended experiments

As extended experiments, the results of the merging of (equal and unequal) vortices are introduced here [24, 25]. As an initial state, a pair of corotating Gaussian vortices expressed by Eq. (42) with different values of $A_1 = 2.165$, $\sigma = 0.16$ is used. By defining asymmetric parameter $d \equiv A_2/A_1$, $d = 1.0$ is used for the symmetric vortex merger, while $d < 1.0$ is swept for asymmetric vortex merger. The Rossby number $Ro \equiv U_{vm}/fl$ and the Froude number $Fr \equiv U_{vm}/\sqrt{\Phi_0}$ are defined by the basic state again, where $U_{vm} \approx 0.2$ is the maximum velocity (fixed). The average depth is set to $\Phi_0 = 4/9$ so that $Fr = 0.3$ (fixed). Then, again, Ro is reciprocal of f . The field of Φ is set to be in gradient balance with ζ . **Figure 7** shows initial Gaussian vortex (cyclone) with $Ro = 4$ ($f = 1/10$) and $Fr = 0.3$ for symmetric ($d = 1.0$) and asymmetric merger ($d = 0.7$). The other experimental settings are the same as Subsection 3.2.

Starting from above initial state, vortices evolve with time. The time evolutions for cyclones with $Ro = 4$ and $Fr = 0.3$ for the symmetric ($d = 1.0$) and asymmetric merger ($d = 0.7$) are shown in **Figure 8**. Vortices merge in a similar way for both cases of equal vortices and unequal vortices. Initially, vortices corotate with each other ($t \lesssim 45$) and then merge into a single vortex ($45 \lesssim t \lesssim 65$). After merging, the vortex rotates with nutation from an elliptical shape to an axisymmetric one ($65 \lesssim t$). Spontaneous emission is observed at all three stages, while amplitude

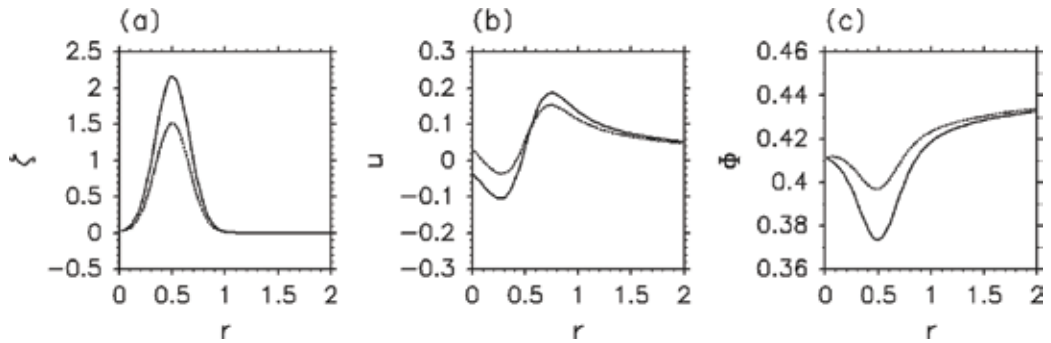


Figure 7. Initial Gaussian cyclone vortex pair with $Ro = 4$ ($f = 1/10$) and $Fr = 0.3$ for symmetric ($d = 1.0$, solid line) and asymmetric merger ($d = 0.7$, dotted line): ζ (a), u (b) and Φ (c) are shown. One (weaker) vortex is shown (for unequal vortices).

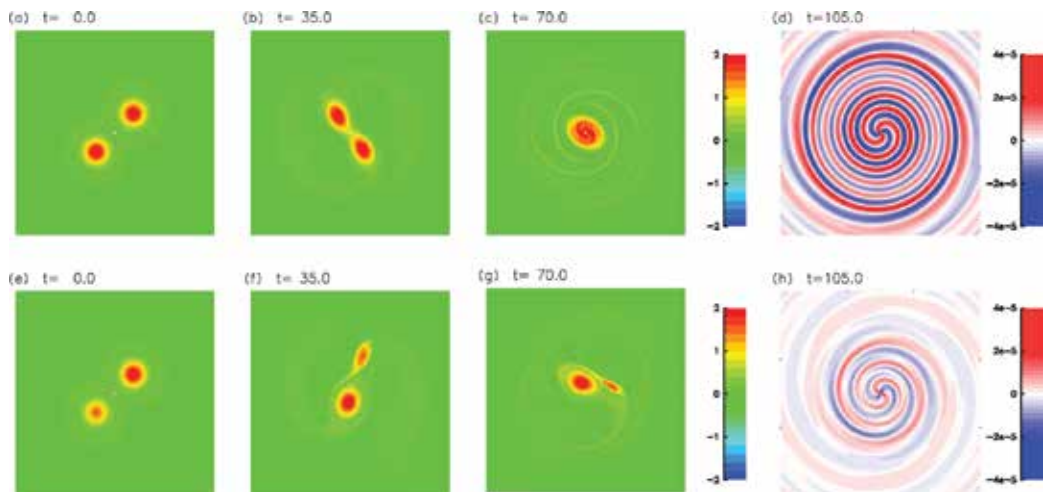


Figure 8. Snapshots of the time evolution of cyclones with $Ro = 4$ ($f = 1/10$) and $Fr = 0.3$ for symmetric merger ($d = 1.0$, top panels) and asymmetric merger ($d = 0.7$, bottom panels): ζ for (a, e) $t = 0$, (b, f) $t = 45$, (c, g) $t = 90$ and $\partial\Phi/\partial t$ for (d, h) $t = 135$ (d). ζ is shown in the near field ($r \leq 2$), while $\partial\Phi/\partial t$ is shown in the far field ($r \leq 50$).

of gravity waves for the asymmetric merger is significantly smaller than that of the symmetric merger. The wavelength of the gravity waves from the corotating vortices becomes shorter gradually with time due to an increase of the rotation rate. Then it becomes almost constant after merging into a single vortex.

A series of numerical simulations at different values of Ro ($0.5 \leq Ro \leq \infty$) is performed. The time evolutions of $\partial\Phi/\partial t$ at several r values are shown in **Figure 9** for both cyclones and anticyclones with $Ro = 4$ and $Fr = 0.3$ for the symmetric ($d = 1.0$) and asymmetric merger ($d = 0.7$). While vortical flows evolve with time in a similar manner (not shown), gravity waves radiated from them are considerably different between cyclones and anticyclones. At large $Ro (\geq 4)$, both cyclones and anticyclones radiate gravity waves in the three stages of vortical flows:

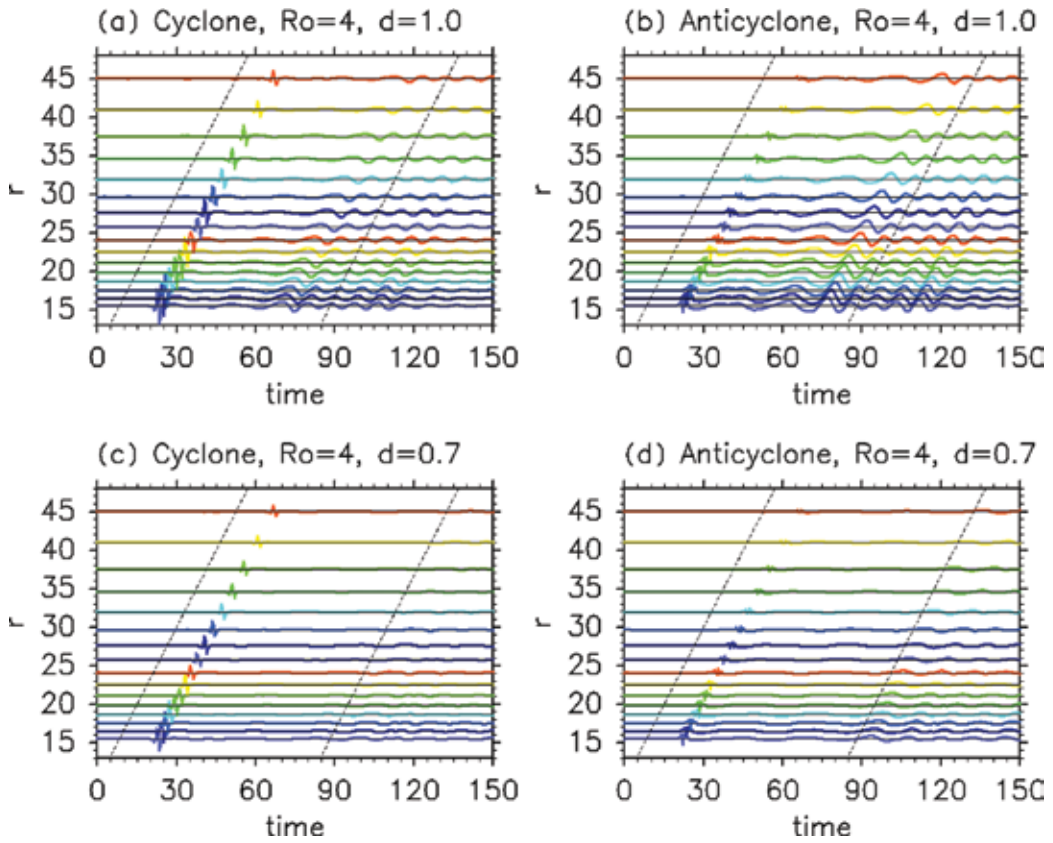


Figure 9. Time evolutions of $\partial\Phi/\partial t$ (colored lines multiplied by 10^4) from symmetric merger (top panels) and asymmetric merger (bottom panels) with $Ro = 4$ and $Fr = 0.3$: (a, c) cyclone and (b, d) anticyclone. Black dotted lines indicate the phase speed of the fastest gravity waves.

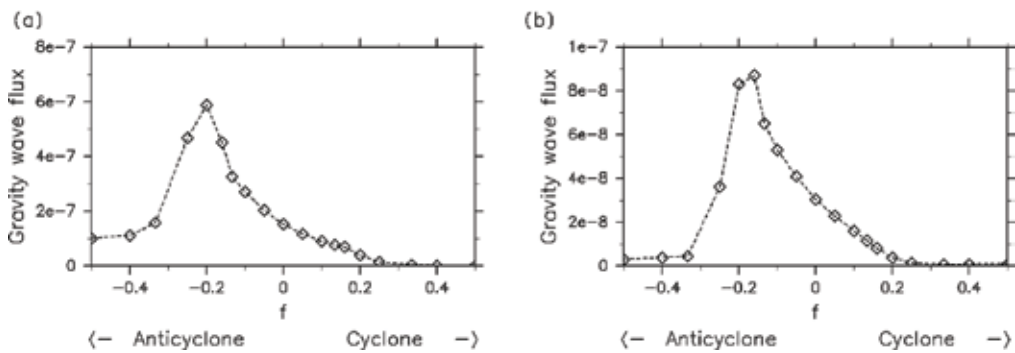


Figure 10. Dependence on f of the maximum value of the gravity wave flux averaged in the θ direction at $r = 45$ for the (a) symmetric merger and (b) asymmetric merger.

corotating ($t \lesssim 45$), merging ($45 \lesssim t \lesssim 65$) and after merging ($65 \lesssim t$). At smaller $Ro (\leq 0.8)$, however, gravity waves from cyclones decrease significantly. There are almost no gravity waves, except for the initial geostrophic adjustment. On the other hand, gravity waves from

anticyclones are radiated even when gravity waves from corotating vortices are hardly observed, namely, spontaneous emission is observed after merging into a single vortex. Therefore, significant cyclone-anticyclone asymmetry appears at small Ro .

In order to estimate the intensity of gravity waves quantitatively, a pseudo-energy flux is derived and calculated as the gravity wave flux [12, 21]. This quantity is conserved when gravity waves propagate into the far field. **Figure 10** shows the maximum values of the gravity wave flux averaged in the θ direction at $r = 45$ for several Ro values ($0.5 \leq Ro \leq \infty$). Generally, the maximum values are caused by gravity waves from the time of merging. Cyclone-anticyclone asymmetry is confirmed clearly. Anticyclones radiate gravity waves more intensely than cyclones and they have a local maximum of gravity wave flux at $f \sim 0.2$ for both cases. See Refs. [24] and [25] for details.

4. Concluding remarks

4.1. Summary points

1. Far field of inertia-gravity wave radiated from the corotating point vortex pair and Kirchhoff vortex with nearly circular shape is derived analytically in the f -plane shallow water system. Cyclone-anticyclone asymmetry in gravity waves from vortical flows and a local maximum of intensity of gravity waves from anticyclones at an intermediate f appear. This is caused by the effect of the Earth's rotation.
2. The derived analytical estimate is well verified for both cases of the corotating vortex pair and Kirchhoff vortex with a small aspect ratio by the numerical simulation with a newly developed spectral method in an unbounded domain.
3. The numerical experiments extend to the cases of symmetric and asymmetric vortex merger, in which analytical estimate cannot be derived. In both cases, cyclone-anticyclone asymmetry clearly appears and the local maximum at intermediate f exists only for anticyclones.
4. Within all parameter values and vortical flows used in the present work, there is a cyclone-anticyclone asymmetry at finite values of f . Gravity waves from anticyclones are larger than those from cyclones and have a local maximum at intermediate f . The source originating in the Coriolis acceleration has a key role in cyclone-anticyclone asymmetry in spontaneous emission. This feature would be robust and ubiquitous in the rotating shallow water system.

4.2. Future issues

1. The derived analytical forms would give useful references for testing the accuracy of the numerical model from a viewpoint of developing new numerical methods.
2. Cyclone-anticyclone asymmetry may be related with the change of the dominant balanced state from quasi-geostrophic one to gradient wind one [29].

3. There are additional effects which cause the discrepancy between analytical and numerical results, such as nutation of vortex, change of the rotation rate and filaments of the vortex.
4. More comprehensible understanding of cyclone-anticyclone asymmetry in spontaneous emission from general complicated vortical flows is needed not only in the rotating shallow water system but also in the continuous stratified system.

Acknowledgements

The work was supported by the JSPS Grant-in-Aid for Young Scientists (B) (no. 25800265). The GFD-DENNOU Library was used for drawing the figures. ISPACK-1.0.3 was used for numerical simulation and analysis. N.S. thanks K. Ishioka, H. Kobayashi, Y. Shimomura, P. D. Williams, R. Plougonven, M. E. McIntyre and the editor H. Pérez-de-Tejada for their constructive comments.

Author details

Norihiko Sugimoto

Address all correspondence to: nori@phys-h.keio.ac.jp

Department of Physics, Keio University, Yokohama, Japan

References

- [1] M. J. Lighthill. On the sound generated aerodynamically. I. general theory. *Proc. R. Soc. London*. 1952;**211A**:564–587. DOI: 10.1098/rspa.1952.0060
- [2] J. E. F. Williams. Aeroacoustics. *Annu. Rev. Fluid Mech.* 1977;**9**:447–468. DOI: 10.1146/annurev.fl.09.010177.002311
- [3] M. E. Goldstein. Aeroacoustics of turbulent shear flows. *Annu. Rev. Fluid Mech.* 1984;**16**:263–285. DOI: 10.1146/annurev.fl.16.010184.001403
- [4] M. S. Howe. *Theory of vortex sound*. Cambridge: Cambridge University Press; 2003. 216 p. DOI: 10.1017/CBO9780511755491
- [5] M. Wang, J. B. Freund, S. K. Lele. Computational prediction of flow-generated sound. *Annu. Rev. Fluid Mech.* 2006;**38**:483–512. DOI: 10.1146/annurev.fluid.38.050304.092036
- [6] D. C. Fritts, M. J. Alexander. Gravity wave dynamics and effects in the middle atmosphere. *Rev. Geophys.* 2003;**41**:1003. DOI: 10.1029/2001RG000106

- [7] R. Ferrari, C. Wunsch. Ocean circulation kinetic energy: reservoirs, sources and sinks. *Annu. Rev. Fluid Mech.* 2009;**41**:253–282. DOI: 10.1146/annurev.fluid.40.111406.102139
- [8] N. Sugimoto, R. Plougonven. Generation and backreaction of spontaneously emitted inertia-gravity waves. *Geophys. Res. Lett.* 2016;**43**(7):3519–3525. DOI: 10.1002/2016GL068219
- [9] V. Zeitlin. *Nonlinear dynamics of rotating shallow water: Methods and Advances*. Amsterdam: Elsevier; 2007. 392 p.
- [10] C. G. Rossby. On the mutual adjustment of pressure and velocity distributions in certain simple current systems. II. *J. Mar. Res.* 1938;**5**:239–263.
- [11] A. E. Gill. Adjustment under gravity in a rotating channel. *J. Fluid Mech.* 1977;**80**:641–671. DOI: 10.1017/S0022112076002280
- [12] R. Ford. Gravity wave radiation from vortex trains in rotating shallow water. *J. Fluid Mech.* 1994;**281**:81–118. DOI: 10.1017/S0022112094003046
- [13] R. Ford, M. E. McIntyre, W. A. Norton. Balance and the slow quasimanifold: some explicit results. *J. Atmos. Sci.* 2000;**57**:1236–1254. DOI: 10.1175/1520-0469(2000)057
- [14] R. Plougonven, F. Zhang. Internal gravity waves from atmospheric jets and fronts. *Rev. Geophys.* 2014;**52**:33–76. DOI: 10.1002/2012RG000419
- [15] Y. Yasuda, K. Sato, N. Sugimoto. A theoretical study on the spontaneous radiation of inertia-gravity waves using the renormalization group method. Part I: derivation of the renormalization group equations. *J. Atmos. Sci.* 2015;**72**:957–983. DOI: 10.1175/JAS-D-13-0370.1
- [16] Y. Yasuda, K. Sato, N. Sugimoto. A theoretical study on the spontaneous radiation of inertia-gravity waves using the renormalization group method. Part II: verification of the theoretical equations by numerical simulation. *J. Atmos. Sci.* 2015;**72**:984–1009. DOI: 10.1175/JAS-D-13-0371.1
- [17] J. Vanneste. Balance and spontaneous wave generation in geophysical flows. *Annu. Rev. Fluid. Mech.* 2013;**45**:147–172. DOI: 10.1146/annurev-fluid-011212-140730
- [18] M. E. McIntyre. Spontaneous imbalance and hybrid vortex-gravity structures. *J. Atmos. Sci.* 2009;**66**:1315–1325. DOI: 10.1175/2008JAS2538.1
- [19] N. Sugimoto, K. Ishioka, S. Yoden. Gravity wave radiation from unsteady rotational flow in an f-plane shallow water system. *Fluid. Dyn. Res.* 2007;**39**(11–12):731–754. DOI: 10.1016/j.fluiddyn.2007.07.001
- [20] N. Sugimoto, K. Ishioka, K. Ishii. Parameter sweep experiments on spontaneous gravity wave radiation from unsteady rotational flow in an f-plane shallow water system. *J. Atmos. Sci.* 2008;**65**:235–249. DOI: 10.1175/2007JAS2404.1
- [21] N. Sugimoto, K. Ishii. Spontaneous gravity wave radiation in a shallow water system on a rotating sphere. *J. Meteor. Soc. Japan.* 2012;**90**(1):101–125. DOI: 10.2151/jmsj.2012-106

- [22] N. Sugimoto, K. Ishioka, H. Kobayashi, Y. Shimomura. Cyclone-anticyclone asymmetry in gravity wave radiation from a co-rotating vortex pair in rotating shallow water. *J. Fluid Mech.* 2015;**772**:80–106. DOI: 10.1017/jfm.2015.209
- [23] N. Sugimoto. Inertia-gravity wave radiation from the elliptical vortex in the f-plane shallow water system. *Fluid. Dyn. Res.* Under revision.
- [24] N. Sugimoto. Inertia-gravity wave radiation from the merging of two co-rotating vortices in the f-plane shallow water system. *Phys. Fluids.* 2015;**27**:12701. DOI: 10.1063/1.4936869
- [25] N. Sugimoto. Gravity wave radiation from asymmetric vortex merger in an f-plane shallow water system. *Theor. Comput. Fluid Dyn.* Forthcoming.
- [26] B. E. Mitchell, S. K. Lele, P. Moin. Direct computation of the sound from a compressible co-rotating vortex pair. *J. Fluid Mech.* 1995;**285**:181–202. DOI: 10.1017/S0022112095000504
- [27] H. Lamb. *Hydrodynamics*. New York: Dover; 1932. 762 p.
- [28] K. Ishioka. A spectral method for unbounded domains and its application to wave equations in geophysical fluid dynamics. In: Y. Kaneda, editor. *IUTAM Symposium on Computational Physics and New Perspectives in Turbulence*; 11–14 September 2006; Nagoya, Japan: Springer; 2008. pp. 291–296. DOI: 10.1007/978-1-4020-6472-2_45
- [29] N. Sugimoto, K. Ishioka, S. Yoden. Balance regimes for the stability of a jet in an f-plane shallow water system. *Fluid. Dyn. Res.* 2007;**39**(5):353–377. DOI: 10.1016/j.fluiddyn.2006.07.004

Vortices in Fluid Dynamic Problems

Modelling of Temporal-Spatial Distribution of Airplane Wake Vortex for Scattering Analysis

Jianbing Li, Zhongxun Liu and Xuesong Wang

Additional information is available at the end of the chapter

<http://dx.doi.org/10.5772/66544>

Abstract

Aircraft wake vortex is a pair of intensive counter-rotating airflow generated by a flying aircraft. Wake vortex is one of the most dangerous hazards in aviation because it may cause a following aircraft to roll out of control, particularly during the taking off and landing phases. The real-time detection of wake vortex is a frontier scientific problem emerging from many fields like aviation safety and atmospheric physics, and the dynamics and scattering characteristics of it remain as key problems to develop corresponding detection technologies. This chapter aims at presenting a simulation scheme for the dynamics of wake vortex under different weather conditions. For wake vortex generated in clear air, changes of the atmospheric dielectric constant produced by the density variation and water vapour variation are analysed; for wake vortex generated in rainy condition, the raindrop distribution in the wake vortex is also analysed. Both of them are essential for further analysing the scattering characteristics and developing new detection algorithms.

Keywords: wake vortex, dynamics, clear air, wet weather

1. Introduction

Wake vortex is an inevitable physical phenomenon that exists in the rear zone of a flying aircraft, which rotates intensively and has a complex structure. The wake vortex generated by a large aircraft could be very hazardous to aviation safety since it might cause a following aircraft to roll out of control, particularly during the departure and landing phases.

In Air Traffic Management (ATM) field, International Civil Aviation Organization (ICAO) established a series of flight interval rules. These rules can ensure the flight safety in most time, but they are too conservative. In order to reach a good balance between avoiding the encountering

hazard of wake vortex and increasing the transport capacity of airports, much attention has been paid on the real-time monitoring and detection of wake vortex in the past decades. Some major ATM programmes like Single European Sky ATM Research (SESAR) and Next Generation Air Transportation System, USA (NextGen) have also launched many projects on this topic, and the representative research institutes include Thales, Office National d'Etudes et de Recherches Aérospatiales (ONERA), Deutsches Zentrum für Luft- und Raumfahrt e.V. (DLR), Université catholique de Louvain (UCL), National Aeronautics and Space Administration (NASA), Federal Aviation Administration (FAA), Lincoln Lab, Boeing, and so on. In all these studies, the characteristics, detection technology and parameter retrieval are the key issues, and the characteristics of wake vortex serve as the basis for the rest studies.

In aviation safety, we mainly concern the clear air condition and wet weather condition. According to the scattering theory, the scattering of wake vortex in clear air is mainly determined by the fluctuation of dielectric constant inside the wake; while under wet condition, the key scattering factor becomes the massive number of precipitation droplets carried by the velocity of wake vortex. In this chapter, we present simulation schemes for the dielectric constant distribution and droplet distribution of wake vortex. The distributions are caused by the dynamics of wake vortex and serve as the physical basis for scattering analysis.

First, we study the dielectric constant distribution of wake vortex generated in clear air.

2. Dielectric constant of wake vortex generated in clear air

2.1. Two key parameters for determining the dielectric constant of wake vortex

The relative dielectric constant of atmosphere (ϵ_r) can be well depicted by the following expression [1]:

$$\epsilon_r = \left[1 + 0.776 \times 10^{-6} \frac{p}{T} \left(1 + \frac{7780q}{T} \right) \right]^2 \quad (1)$$

where p, T, q are the pressure (pa), absolute temperature (K), and water vapour content (kg/kg), respectively. Generally, the second term in the square bracket is much smaller than 1, so the variation in dielectric constant between wake vortex and ambient air can be approximated as follows when the Taylor expansion is taken into account:

$$\Delta\epsilon_r = \epsilon_r - \epsilon_{r,a} \approx 1.552 \times 10^{-6} \left[\frac{p}{T} \left(1 + \frac{7780q}{T} \right) - \frac{p_a}{T_a} \left(1 + \frac{7780q_a}{T_a} \right) \right] \quad (2)$$

In the expression, the parameters with subscript "a" refer to the ambient parameters and those without "a" refer to the wake vortex's parameters.

As is known, an isentropic process is a process in which there is neither heat exchange nor any friction effect [2]. Typically, the wake vortex of a subsonic airplane can be assumed as an isentropic flow, and the thermodynamic parameters at different points along a streamline can be written as follows:

$$\frac{p}{p_a} = \left(\frac{\rho}{\rho_a}\right)^\gamma, \frac{T}{T_a} = \left(\frac{\rho}{\rho_a}\right)^{\gamma-1} \quad (3)$$

where $\gamma = 1.4$ is the adiabatic coefficient for air. Consequently, the variation in dielectric constant is transformed to

$$\Delta\varepsilon_r \approx 1.552 \times 10^{-6} \times \left[\frac{p_a}{T_a} (\xi-1) + 7780 \frac{p_a}{T_a^2} (\xi^{2-\gamma} q - q_a) \right] \quad (4)$$

Here we have denoted $\xi = \rho/\rho_a$, and the effects due to density and water vapour are mixed in the term $\xi^{2-\gamma}q$. In order to separate the two factors, this term is transformed to

$$\xi^{2-\gamma}q = [1 + (\xi-1)]^{2-\gamma} (q_a + \Delta q) \quad (5)$$

with $\Delta q = q - q_a$ being the water vapour variation between the local wake and the ambient air. Since the variations in density and water vapour for wake vortex are very small, say $\xi-1 \ll 1$ and $\Delta q \ll q_a$, the dielectric constant variation can be approximated as follows when the Taylor expansion is adopted:

$$\Delta\varepsilon_r \approx 1.552 \times 10^{-6} \frac{p_a}{T_a^2} \times \{ [T_a + 7780(2-\gamma)q_a](\xi-1) + 7780\Delta q \} \quad (6)$$

In this expression there are two undetermined parameters, ξ and Δq . They are separated into two different terms:

$$\Delta\varepsilon_r = \Delta\varepsilon_r^d + \Delta\varepsilon_r^v \quad (7)$$

The first term is determined by the density variation ξ :

$$\Delta\varepsilon_r^d \approx 1.552 \times 10^{-6} \frac{p_a}{T_a^2} (T_a + 4668q_a)(\xi-1) \quad (8)$$

and the second term is determined by the water vapour variation Δq :

$$\Delta\varepsilon_r^v \approx 1.207 \times 10^{-2} \frac{p_a}{T_a^2} \Delta q \quad (9)$$

In this manner, the key of modelling the dielectric constant is to determine the two parameters, ξ and Δq .

2.2. Effect of density variation on the dielectric constant

2.2.1. Velocity field of wake vortex

When the stationary phase of a subsonic wake vortex is taken into account, the dynamics can be well characterized by the steady Lamb momentum equation [2]:

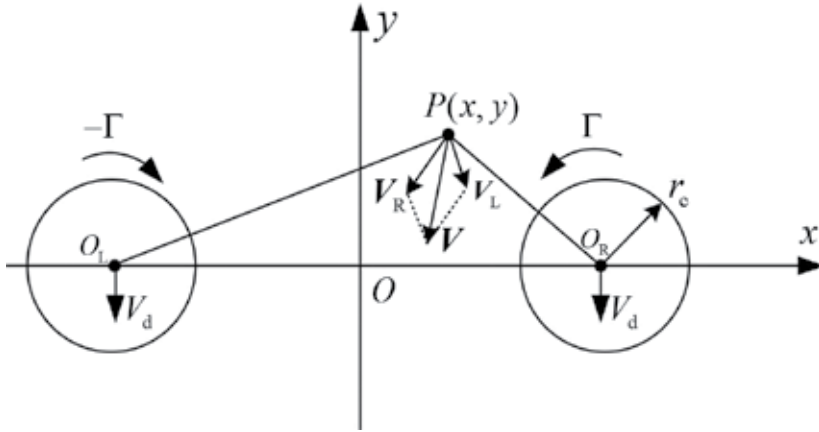


Figure 1. Velocity of counter-rotating vortices.

$$\Omega \times V + \frac{1}{2} |V|^2 = -\frac{1}{\rho} \nabla p \tag{10}$$

where V is the total velocity of wake vortex, and $\Omega = \nabla \times V$ is the vorticity. In this expression, the velocity and density are separated, which makes it convenient to work out the thermodynamics parameters according to the velocity field.

Typically, when no cross-wind is considered, a stable-stage wake is composed of two contour rotating vortices of the same strength, and they descend at a velocity V_d . In this manner, in a coordinate system descending with the vortex cores, the wake vortex is steady, and the velocity for a given point P can be written as (see Figure 1):

$$V = -V_d + V_L + V_R \tag{11}$$

where V_L and V_R are the velocities deduced by the left and right vortices, and V_d is the descending velocity. In Figure 1, the parameter Γ is the circulation which defines the strength of the wake vortex.

- In the expression, the deduced velocity of each vortex can be presented by existing velocity profile models, such as Rankine model, Lamb-Oseen model, and so on. Among them, the Rankine model is a widely used one, and the corresponding tangential velocity (V_θ) follows [3]:

$$V_\theta(r) = \frac{\Gamma_0}{2\pi r} \begin{cases} r^2/r_c^2, & r < r_c \\ 1, & r \geq r_c \end{cases} \tag{12}$$

where r is the distance of a given point to the vortex centre, $r_c \approx 0.052b_0$ the vortex core radius, and b_0 the vortex spacing. As shown in Figure 2, the velocity outside the vortex core is irrotational, while the inside part is with a uniform vorticity:

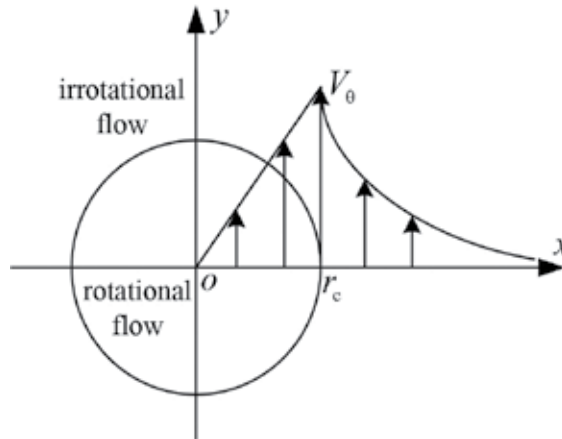


Figure 2. Rankine velocity profile.

$$\omega_0 = \frac{\Gamma_0}{\pi r_c^2} \tag{13}$$

- The descending velocity can be derived from the deduced velocity of a vortex core:

$$\mathbf{V}_d = -\frac{\Gamma_0}{2\pi b_0} \hat{y} \tag{14}$$

2.2.2. Stream function of wake vortex

When the velocity components are determined, the vorticity is finally obtained as

$$\boldsymbol{\Omega} = \nabla \times \mathbf{V} = \omega_0 H(\mathbf{r}) \tag{15}$$

In this expression, we have considered $\nabla \times \mathbf{V}_d = 0$, and $H(\mathbf{r})$ is an identification function for the left vortex core region (C_L) and right one (C_R):

$$H(\mathbf{r}) = \begin{cases} -1, & \mathbf{r} \in C_L \\ 1, & \mathbf{r} \in C_R \\ 0, & \text{otherwise} \end{cases} \tag{16}$$

As a result, we have

$$\boldsymbol{\Omega} \times \mathbf{V} = \omega_0 H(\mathbf{r})(-v\hat{x} + u\hat{y}) = \omega_0 H(\mathbf{r})\nabla\psi \tag{17}$$

where u and v are the velocity components in x and y directions, and ψ is the stream function:

$$u = \frac{\partial\psi}{\partial y}, v = -\frac{\partial\psi}{\partial x} \tag{18}$$

In this manner, the Lamb momentum equation for wake vortex is rewritten as

$$\omega_0 H(\mathbf{r}) \nabla \psi + \frac{1}{2} |\mathbf{V}|^2 = -\frac{1}{\rho} \nabla p. \quad (19)$$

Furthermore, integrating the above equation from a point \mathbf{r} to infinity gives

$$I = -\omega_0 H(\mathbf{r}) \psi + \frac{1}{2} V_d^2 - \frac{1}{2} |\mathbf{V}|^2 = -\int_r^\infty \frac{1}{\rho} dp \quad (20)$$

where we have considered $\mathbf{V}_\infty = V_d \hat{\mathbf{y}}$, and the total stream function ψ is

$$\psi = -V_d x + \psi_L + \psi_R + C \quad (21)$$

with the four terms on the right-hand side being the up-wash flow at infinity, the stream function due to the left vortex and right vortex, and a constant.

For a Rankine vortex, the stream function follows

$$\psi_{\text{Rankine}} = -\frac{\Gamma}{4\pi} \begin{cases} \frac{r^2}{r_0^2} - 1 + \ln r_0^2, & r < r_c; \\ \ln r^2, & r \geq r_c. \end{cases} \quad (22)$$

Then ψ_L and ψ_R can be obtained by replacing the circulation Γ with $-\Gamma_0$ and Γ_0 , respectively.

Also, the constant C is chosen to meet $\psi(\mathbf{r}) = 0$ when \mathbf{r} is on the vortex core boundary:

$$C = \psi_1(\mathbf{r}) = V_d x - \psi_L - \psi_R \quad (23)$$

Due to the impact between two vortices, the constant C has a very slight variation along the vortex core boundary. In practice, the average of $\psi_1(\mathbf{r})$ along one vortex core boundary is chosen as the constant.

As a result, combination of the total stream function and velocity gives the distribution of integral I as shown in Eq. (20), which is then used to calculate the density distribution of wake vortex.

2.2.3. Determination of dielectric constant due to density variation

Substituting the isentropic relationship (3) into the item on the right hand of Eq. (20) gives

$$I = -\int_r^\infty \frac{1}{\rho} dp = -\int_r^\infty \frac{\gamma}{\gamma-1} \frac{p_a}{\rho_a^\gamma} d\rho^{\gamma-1} = \frac{\gamma}{\gamma-1} \frac{p_a}{\rho_a^\gamma} (\rho^{\gamma-1} - \rho_a^{\gamma-1}) \quad (24)$$

which can then be transformed as

$$\xi = \frac{\rho}{\rho_a} = \left[1 + \frac{(\gamma-1)\rho_a}{\gamma p_a} I \right]^{\frac{1}{\gamma-1}} \quad (25)$$

For a wake vortex, the integral I has the same magnitude as V_0^2 (generally not larger than 1000). On the other hand, ρ_a and p_a are, respectively, on the magnitude of 1 and 10^5 . Therefore, the second term in Eq. (25) is much smaller than 1, and the Taylor expansion gives:

$$\xi \approx 1 + \frac{\rho_a}{\gamma p_a} I \tag{26}$$

Consequently, the effects of dielectric constant can be rewritten as

$$\Delta \epsilon_r^d(\mathbf{r}) \approx 1.552 \times 10^{-6} \frac{p_a(T_a + 4668q_a)}{\gamma R T_a^3} I(\mathbf{r}). \tag{27}$$

2.3. Effect of water vapour variation on the dielectric constant

Generally, the atmospheric water vapour inside the wake vortex can be modelled as a passive scalar, which is convected by the wake vortex velocity field and is governed by the convection-diffusion equation [4]:

$$\frac{\partial q}{\partial t} + (\mathbf{V} \cdot \nabla)q - D\nabla^2 q = 0, \tag{28}$$

where q is the water vapour concentration, D is the diffusion coefficient for an air/water vapour system, and \mathbf{V} is the velocity field of a wake.

In fluid dynamics, the Péclet number is a dimensionless number indicating the rates of convection and diffusion of a flow [5]:

$$Pe = \frac{UL}{D} \tag{29}$$

where L is the characteristic length, U is the velocity, and D is the mass diffusion coefficient. Generally, a flow is convection-dominated, if the Péclet number is large. In this study, the diffusion coefficient for air ($D = 2.42 \times 10^{-5}$) is very small, which leads to a big Péclet number and the flow is convection dominated. In this manner, neglecting the impact of diffusion leads to a simplified governing equation:

$$\frac{\partial q}{\partial t} + (\mathbf{V} \cdot \nabla)q = 0 \tag{30}$$

As is known, the initial water vapour gradient is very important to characterize the equation. Here the stratified model is adopted in this work

$$q(\mathbf{r}, t)|_{t=0} = q_a = m_q(y-y_0) + q_0 \tag{31}$$

with q_0 and m_q being the offset and gradient of water vapour content, respectively. Substituting the initial condition into the governing equation gives

$$\frac{\partial q(\mathbf{r}, 0)}{\partial t} + (\mathbf{V} \cdot \nabla)q(\mathbf{r}, 0) = V_y m_q \quad (32)$$

Therefore, Eq. (30) minus Eq. (32) leads to a new equation:

$$\frac{\partial Q}{\partial t} + (\mathbf{V} \cdot \nabla)Q = -V_y m_q \quad (33)$$

with $Q(\mathbf{r}, t) = \Delta q(\mathbf{r}, t) = q(\mathbf{r}, t) - q(\mathbf{r}, 0)$ being the water vapour variation. At the same time, the initial condition of Eq. (33) becomes $Q(\mathbf{r}, t)|_{t=0} = q(\mathbf{r}, t)|_{t=0} - q(\mathbf{r}, 0) = 0$; this is coincident with the physical image that the water vapour variation is initially zero.

Eq. (33) is a hyperbola differential equation, which is often numerically difficult to solve. In the present work, the leapfrog scheme is adopted to solve the target equation, and good convergence and stability are achieved. The scheme is as follows:

$$\frac{Q_{i,j}^{n+1} - Q_{i,j}^{n-1}}{2\Delta t} + u \frac{Q_{i+1,j}^n - Q_{i-1,j}^n}{2\Delta x} + v \frac{Q_{i,j+1}^n - Q_{i,j-1}^n}{2\Delta x} = -v_{i,j} m_q, \quad (34)$$

with u and v being the velocity components in x and y direction, respectively. In the process, the Von Neumann method leads to the following stable condition [6]:

$$\Delta t < \frac{1}{2} \frac{\Delta}{V_{\max}} \quad (35)$$

where Δt is the time step, Δ is the minimum grid spacing, and V_{\max} is the maximum velocity in the wake vortex.

In addition, non-uniform grids and symmetric condition are used to reduce computational cost. On the one hand, the velocity distribution shows that the flow in and around the vortex core is relatively complex and the flow far from the vortex core is slowly variational. Typically, sparse grids are adequate to characterize the slowly variational zones, but complex zones require dense grids. In this manner, non-uniform grid scheme can be adopted to reduce the total number of grids. On the other hand, the wake vortex is symmetric, so only half of wake vortex needs to be computed. Overall much computational cost can be saved through the above scheme.

If the water vapour variation, $Q(\mathbf{r}, t)$ is solved from Eq. (33), then $\Delta \varepsilon_i^v$ can be immediately obtained according to Eq. (9).

In this above simulation, the moving coordinate system is also used. The dielectric constant distribution can be transformed into the stationary coordinate system if the following transform is used:

$$y' = y - V_d \cdot t \tag{36}$$

where V_d is the descending velocity, t is the evolutionary time, y and y' are the coordinates in the moving coordinate system and stationary coordinate system, respectively.

2.4. Numerical examples

Here we give several numerical examples for the dielectric constant distribution due to different effects. The parameters of airplane and atmosphere are as shown in **Table 1**.

According to the parameters, the distribution of $I(\mathbf{r})$ can be worked out, and the intensity of dielectric constant due to density variation can be obtained as shown in **Figure 3**. It is observed that $\Delta\epsilon_r^d$ in the vortex cores are much larger than that outside, so the vortex core could present a big contribution to the scattering of wake vortex.

The dielectric constant due to water vapour variation ($\Delta\epsilon_r^v$) can be obtained when the given partial equation (33) is solved, and **Figure 4** presents $\Delta\epsilon_r^v$ at $t = 40s$. It is observed that the convection effect of water vapour results in a non-uniform laminar structure in and around the wake vortex cores, and these structures could be good contributor to the scattering in high frequency.

Consequently, the sum of **Figures 3** and **4** gives the total distribution of dielectric constant (see **Figure 5**). Comparing the magnitude of $\Delta\epsilon_r^d$ and that of $\Delta\epsilon_r^v$ shows that $\Delta\epsilon_r^v$ is much less than $\Delta\epsilon_r^d$, and $\Delta\epsilon_r^d$ dominates the magnitude of $\Delta\epsilon_r$. However, $\Delta\epsilon_r^d$ and $\Delta\epsilon_r^v$ have different structures; they make different contribution to the scattering in different frequency bands. Typically, the scattering of clear air wake vortex at a frequency lower than 100MHz is mainly determined by the density variation $\Delta\epsilon_r^d$; otherwise, the water vapour variation $\Delta\epsilon_r^v$ makes the major contribution.

2.5. Extrapolation of dielectric constant distribution

The extrapolation includes two parts: one is relate to the density distribution and another is related to the water vapour distribution.

Parameters	Value
Airplane mass M	250,000 kg
Wingspan B	68 m
Speed V	133 m/s
Ambient pressure p_a	100,000 pa
Ambient absolute temperature T_a	288 K
Diffusion constant D	$2.42 \times 10^{-5} \text{m}^2/\text{s}$
Water vapour content offset q_0	0.018 kg/kg
Water vapour content gradient m_q	$-8 \times 10^{-8} \text{kg}/(\text{m kg})$

Table 1. Parameters of airplane and atmosphere.

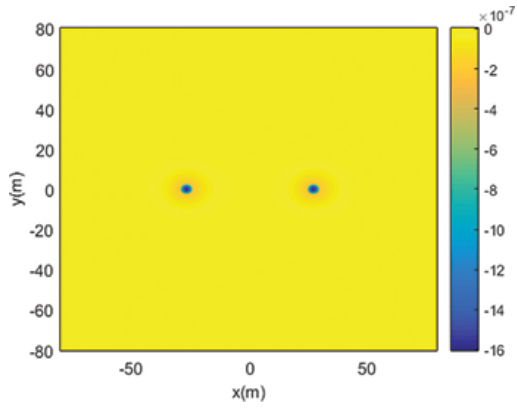


Figure 3. Dielectric constant distribution due to density variation.

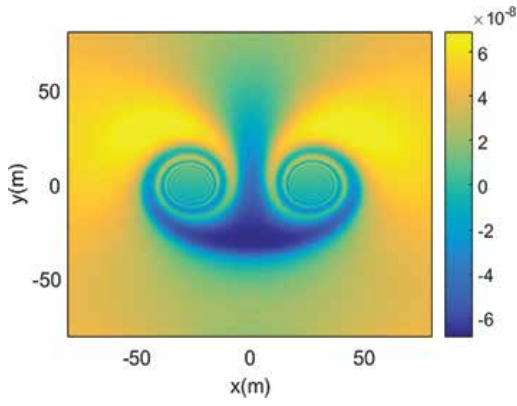


Figure 4. Dielectric constant distribution due to water vapour variation.

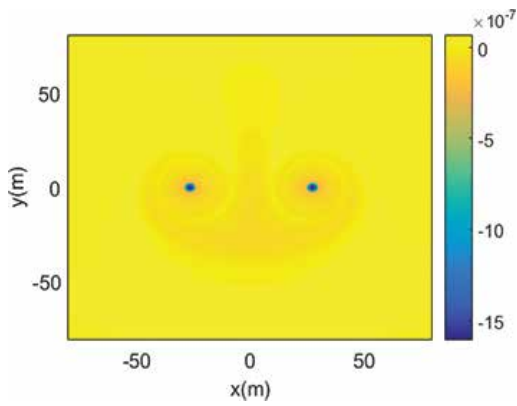


Figure 5. Total dielectric constant distribution.

2.5.1. Extrapolation of dielectric constant related to density distribution

As shown in Eq. (27), the key of density distribution is the integral $I(\mathbf{r})$; this could be obtained with the normalized parameters.

First, if the space is normalized by vortex separation b_0 , say $\tilde{r} = r/b_0$, the Rankine model can be normalized as

$$V_\theta(r) = \frac{\Gamma_0}{b_0} \tilde{V}_\theta(\tilde{r}), \tag{37}$$

with \tilde{V}_θ being the normalized velocity:

$$\tilde{V}_\theta(\tilde{r}) = \frac{1}{2\pi\tilde{r}} \begin{cases} \tilde{r}^2/0.052^2, & \tilde{r} < 0.052, \\ 1, & \tilde{r} \geq 0.052. \end{cases} \tag{38}$$

Other velocity profile models have similar expressions. Substituting the normalized velocity into the integral Eq. (20) gives

$$I(\mathbf{r}) = \left(\frac{\Gamma_0}{b_0}\right)^2 \tilde{I}(\tilde{\mathbf{r}}) \tag{39}$$

Where the normalized integral $\tilde{I}(\tilde{\mathbf{r}}) = \int_{\tilde{C}} (\tilde{\mathbf{V}} \cdot \tilde{\nabla}) \tilde{\mathbf{V}} \cdot d\tilde{\mathbf{s}}$ is only related to the velocity model, and $\tilde{\nabla} = (\partial/\partial\tilde{x} \quad \partial/\partial\tilde{y})^T = b_0 \nabla$, $\tilde{\mathbf{s}} = (\tilde{x}, \tilde{y})$.

For a stably flying airplane, the lift force balances the weight, which leads to the following initial circulation expression:

$$\Gamma_0 = \frac{Mg}{\rho_a V_a b_0} \tag{40}$$

Consequently, substituting the circulation into the integral gives

$$I(b_0\tilde{\mathbf{r}}) = \frac{M^2 g^2}{\rho_a^2 V_a^2 b_0^4} \tilde{I}(\tilde{\mathbf{r}}) \tag{41}$$

The dielectric constant related to density distribution is then rewritten as

$$\Delta \epsilon_r^d(b_0\tilde{\mathbf{r}}) \approx 1.552 \times 10^{-6} \frac{R[T_a(b_0\tilde{\mathbf{r}}) + 4668q_a(b_0\tilde{\mathbf{r}})] M^2 g^2}{\gamma p_a(b_0\tilde{\mathbf{r}}) T_a(b_0\tilde{\mathbf{r}})} \frac{\tilde{I}(\tilde{\mathbf{r}})}{V_a^2 b_0^4} \tag{42}$$

Since the normalized integral $\tilde{I}(\tilde{\mathbf{r}}) = \int_{\tilde{C}} (\tilde{\mathbf{V}} \cdot \tilde{\nabla}) \tilde{\mathbf{V}} \cdot d\tilde{\mathbf{s}}$ is only related the velocity model, the following relationship can be obtained when the different airplane parameters and air conditions are introduced:

$$\frac{\Delta \varepsilon_{r,2}^d(\mathbf{r}_2)}{\Delta \varepsilon_{r,1}^d(\mathbf{r}_1)} \approx \frac{p_{a,1}(\mathbf{r}_1) T_{a,1}(\mathbf{r}_1) [T_{a,2}(\mathbf{r}_2) + 4668q_{a,2}(\mathbf{r}_2)]}{p_{a,2}(\mathbf{r}_2) T_{a,2}(\mathbf{r}_2) [T_{a,1}(\mathbf{r}_1) + 4668q_{a,1}(\mathbf{r}_1)]} \cdot \frac{M_2^2 V_{a,1}^2 b_{0,1}^4}{M_1^2 V_{a,2}^2 b_{0,2}^4} \quad (43)$$

with $\mathbf{r}_1 = b_{0,1} \tilde{\mathbf{r}}$ and $\mathbf{r}_2 = b_{0,2} \tilde{\mathbf{r}}$.

2.5.2. Extrapolation of dielectric constant related to water vapour distribution

The key of water vapour distribution is to solve the partial differentiation equation (33).

Define some related normalized parameters as follows: $\tilde{Q} = Q/b_0$, $\tilde{t} = t/t_0$, $\tilde{\mathbf{r}} = \mathbf{r}/b_0$, $\tilde{\mathbf{V}} = \mathbf{V}/V_0$, where $V_0 = \Gamma_0/b_0$ and $t_0 = b_0/V_0$. Consequently, the target partial differentiation equation is rewritten as

$$\frac{\partial \tilde{Q}}{\partial \tilde{t}} + (\tilde{\mathbf{V}} \cdot \tilde{\nabla}) \tilde{Q} = -\tilde{V}_y m_q. \quad (44)$$

If the variable $\tilde{Q}(\tilde{\mathbf{r}}, \tilde{t})$ is solved from above equation, the dielectric constant related to water vapour distribution becomes

$$\Delta \varepsilon_r^v(b_0 \tilde{\mathbf{r}}, t_0 \tilde{t}) = 1.207 \times 10^{-2} \frac{p_a}{T_a^2} b_0 \tilde{Q}(\tilde{\mathbf{r}}, \tilde{t}). \quad (45)$$

In this manner, the dielectric constant for different airplane and air parameters is extrapolated as

$$\frac{\Delta \varepsilon_{r,2}^v(\mathbf{r}_2, t_2)}{\Delta \varepsilon_{r,1}^v(\mathbf{r}_1, t_1)} \approx \frac{p_{a,2}(\mathbf{r}_2)}{p_{a,1}(\mathbf{r}_1)} \left[\frac{T_{a,1}(\mathbf{r}_1)}{T_{a,2}(\mathbf{r}_2)} \right]^2 \frac{b_{0,2}}{b_{0,1}} \quad (46)$$

where $\mathbf{r}_1 = b_{0,1} \tilde{\mathbf{r}}$, $\mathbf{r}_2 = b_{0,2} \tilde{\mathbf{r}} = \frac{b_{0,2}}{b_{0,1}} \mathbf{r}_1$, $t_1 = t_{0,1} \tilde{t}$, and $t_2 = t_{0,2} \tilde{t} = \frac{t_{0,2}}{t_{0,1}} t_1$. For stably flying airplane, we have $t_0 = \rho_a b_0^3 V_a / (Mg)$, and then the relationship becomes

$$\frac{t_{0,2}}{t_{0,1}} = \left(\frac{b_{0,2}}{b_{0,1}} \right)^3 \frac{p_{0,2} T_{0,1} V_{0,2} M_1}{p_{0,1} T_{0,2} V_{0,1} M_2} \quad (47)$$

This is a very simple relationship.

With the combination of two extrapolation formulae, the dielectric constant distribution is then determined. This can save a lot of computation cost when different airplane wake vortices are to be analysed.

Another condition we always experience is wet weather condition (fog, rain, and snow). Here we mainly concern the rainy condition since it is the most common situation around airports.

3. Wake vortex generated in rainy weather

In still air, the raindrops fall vertically towards the ground and reach a constant terminal falling velocity. When an aircraft takes off or lands in rainy weather, the raindrops will be inevitably involved in the aircraft wake vortices. Raindrops' motion in wake vortex is modified by the vortex flow. This modification of the trajectories of the raindrops may induce changes in raindrops' number concentration and velocity distribution in wake vortices, therefore results in changes in the recorded radar signal. This section presents a modelling scheme for raindrops' motion and distribution within the wake vortex.

3.1. Parameterization of raindrops

In still air, a falling raindrop reaches its terminal fall velocity V_T with the equilibrium between the inertial force and the drag force acting on it [7]. A widely used exponential expression between V_T (m/s) and the diameter D (mm) is given by [8]

$$V_T(D) = [\alpha_1 - \alpha_2 \exp(-\alpha_3 D)] \left(\frac{\rho_0}{\rho}\right)^{0.4} \quad (48)$$

where $\alpha_1 = 9.65$ m/s, $\alpha_2 = 10.3$ m/s, $\alpha_3 = 0.6$ m/s, and $(\rho_0/\rho)^{0.4}$ is a density ratio correction factor adjusting deviation of the terminal fall velocity due to the air density change with the fall altitude.

Drop size distributions (DSD) have been widely used by radar meteorologists as they are directly related to radar reflectivity [9]. In the following analysis, a suitable model to describe the size distribution of the rainfall in Europe is adopted [10]

$$N(D) = N_0 D^2 e^{-\Lambda D} \quad (49)$$

where $N_0 = 64500 R^{-0.5}$ ($\text{m}^{-3} \text{mm}^{-3}$) with R (mm/h) being the considered rain rate, $\Lambda = 7.09 R^{-0.27}$ (mm^{-1}), $N(D)$ ($\text{m}^{-3} \text{mm}^{-1}$) represents the number of raindrops of the diameter D per unit volume per unit diameter class interval.

3.2. The motion equation of raindrops in wake vortices

Typically, the diameter of raindrops disperses between 0.5 and 4 mm. Usually their Stokes number in wake vortex flow is approximate to 1, which makes their motion trajectories significantly differ from the streamlines of total velocity field. To obtain those trajectories, the motion equation of the raindrops is studied [11].

When a raindrop enters into the wake vortex flow, its movement is governed by

$$a(t) = \frac{F_d(t)}{m_p} + g \quad (50)$$

where t is the time, a is the acceleration of the raindrop, F_d is the fluid drag force acting on the raindrop, m_p is its mass, and g is the gravity acceleration. For a raindrop moving with velocity

v_p in the fluid whose velocity field is $u[z_p(t)]$, if its diameter D ranges from 0.5 to 4 mm, the drag force F_d can be approximately considered in the Newton regime [12] and given by

$$F_d(t) = \frac{1}{2} C_d \rho_a \delta v^2 \left(\frac{\pi D}{2} \right)^2, \delta v = u[z_p(t)] - v_p(t) \quad (51)$$

where $z_p(t)$ denotes raindrops' position, δv is the relative velocity between the vortex flow and the raindrop, and C_d is the fluid drag coefficient. The impact of air density variations in the vortex flow on C_d can be neglected because the density of raindrops is much larger than that of air. Thus, C_d for a raindrop of diameter D is derived by the equilibrium equation of its weight and the drag force when falling at terminal falling velocity in still air:

$$C_d = \frac{4\rho_w g D}{3\rho_a V_T^2} \quad (52)$$

where ρ_w is the density of raindrops. Substituting Eqs. (51) and (52) into Eq. (50), the motion equation of raindrops within wake vortices can be further expressed as

$$\begin{cases} \mathbf{a}(t) = \mathbf{g} + \frac{\mathbf{g}}{V_T^2} |\delta \mathbf{v}| \delta \mathbf{v} \\ \frac{d\mathbf{v}_p(t)}{dt} = \mathbf{a}(t) \\ \frac{d\mathbf{z}_p(t)}{dt} = \mathbf{v}_p(t) \end{cases} \quad (53)$$

The instantaneous position and velocity of raindrops can be obtained from the above equations, but it is not easy to obtain a simple and closed expression. Here, a fourth-order four variables Runge-Kutta algorithm is proposed to solve the equation of motion [11].

3.3. Examples of trajectories of raindrops in wake vortices

In still air, the raindrop falls along a vertical trajectory to the ground. In presence of wake vortices, the trajectory of a raindrop is depending on its diameter and the location where it enters into the wake vortex flow. Circulation is a very important parameter to characterize wake vortex since it describes the strength of wake vortex. For raindrops moving in the vortex flow, their motion characteristics, that is, trajectory and velocity also largely depend on the vortex circulation. For simplicity, only the impacted part of the wake vortex region is shown in **Figure 6**, where four sets of trajectories are illustrated for raindrops of diameters 0.5, 1.0, 2.0, and 4.0 mm. Each set of trajectories corresponds to a given circulation value of the wake vortices. For a given circulation, the corresponding trajectory and velocity of raindrops in the wake vortices are unique. Comparisons between different trajectories give the following conclusions: (1) the smallest raindrops are much more sensitive to the vortex circulation and (2) the motion characteristic of raindrops in wake vortices is representative of the vortex strength.

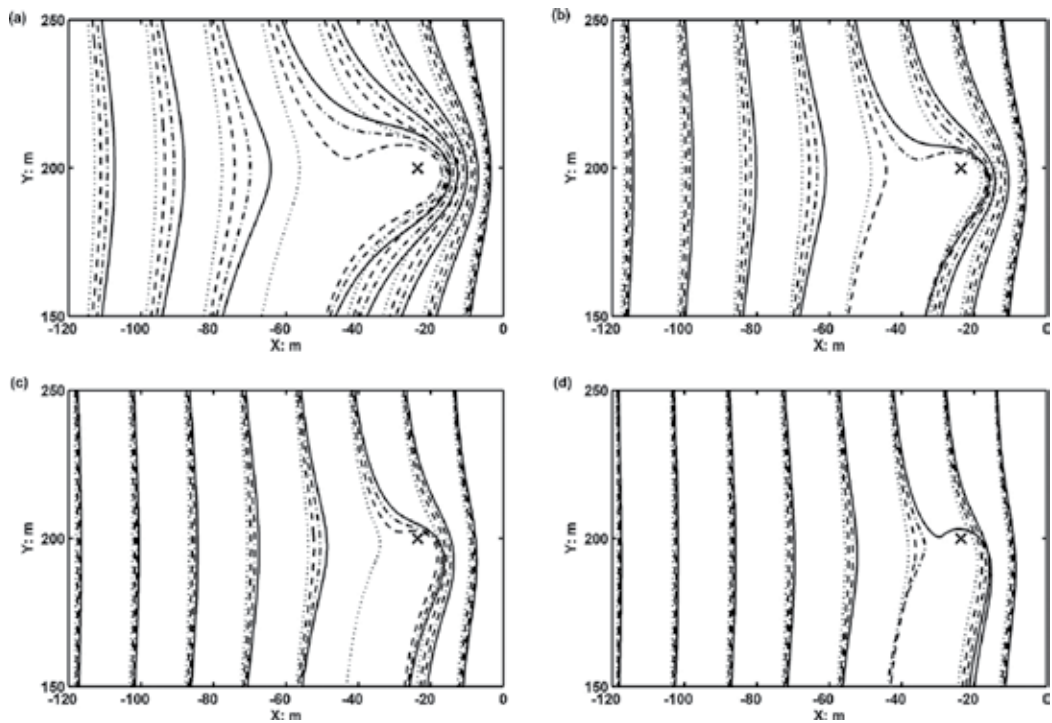


Figure 6. Raindrops' trajectories in wake vortices with different circulation: (a) $D = 0.5$ mm, (b) $D = 1.0$ mm, (c) $D = 2.0$ mm, (d) $D = 4.0$ mm. The solid line '-', the dash-dotted line '-.', the dashed line '-' and the dotted line '...', correspond to the values of vortex circulation: $490 \text{ m}^2/\text{s}$, $430 \text{ m}^2/\text{s}$, $360 \text{ m}^2/\text{s}$, and $300 \text{ m}^2/\text{s}$, respectively.

3.4. Raindrops' distribution in wake vortices

A Doppler radar will be very sensitive to raindrops' motion and possibly enable the detection of wake vortices in rain. To better understand the impact of wake vortices on the raindrops' motion, it is necessary to develop the methodology to quantitatively analyse the raindrops' distribution in wake vortices.

3.4.1. Raindrops' number concentration

The box counting method is adopted here to quantitatively compute raindrops' distribution in wake vortices. For simplification, we consider the situation where the raindrops are falling into the two dimensional rectangular region of wake vortex in stable phase. Before entering into the wake vortex region, the raindrops are falling in still air with the constant terminal falling velocity, and they are named as "initial raindrops". The number density of initial raindrops of diameter D (mm) is assumed to be $N_0(D)$ ($\text{m}^{-3} \text{ mm}^{-1}$). In the wake vortex region, the raindrops' trajectory and velocity are changed and they are denoted as "disturbed raindrops". The number density of disturbed raindrops is assumed to be $N(D, x, y)$ ($\text{m}^{-3} \text{ mm}^{-1}$), where (x, y) are the coordinates in the wake vortex region. Obviously, for a given wake vortex pair, $N(D, x, y)$ depends on both the diameters of raindrops and their locations in wake vortex. In

order to better illustrate the influence of wake vortices on the raindrops' distribution, the raindrops' relative number concentration at a point (x, y) is defined as

$$\eta_N(D, x, y) = \frac{N(D, x, y)}{N_0(D)} \quad (54)$$

where $\eta_N(D, x, y)$ depicts the change in raindrops' concentration induced by the wake vortex. If $\eta_N > 1$, the concentration of raindrops is enhanced, otherwise it is reduced.

In order to obtain the quantitative estimation of η_N , the wake vortex region is divided into $n_x \times n_y$ grid boxes with equal size. The size of each grid box in xy plane are Δx and Δy , respectively. Above the wake vortex region, there are $n_x \times 1$ grid boxes where the initial raindrops of diameter D are homogeneously distributed, and the number of initial raindrops in each grid box is recorded as $\text{Num}_0(D)$. At each time step, their positions and velocities are updated by computing the equation of motion. If some of the initial raindrops enter into the wake vortex region, the same number of new initial raindrops is added to the first row of the $n_x \times n_y$ grid boxes, say, the $n_x \times 1$ grid boxes above the wake vortex region. When all the raindrops released at initial time arrive at the bottom of wake vortex region, the number of disturbed raindrops $\text{Num}(D, x, y)$ in each grid box in wake vortex region is counted. Thus, $\eta_N(D, x, y)$ can be approximated by the

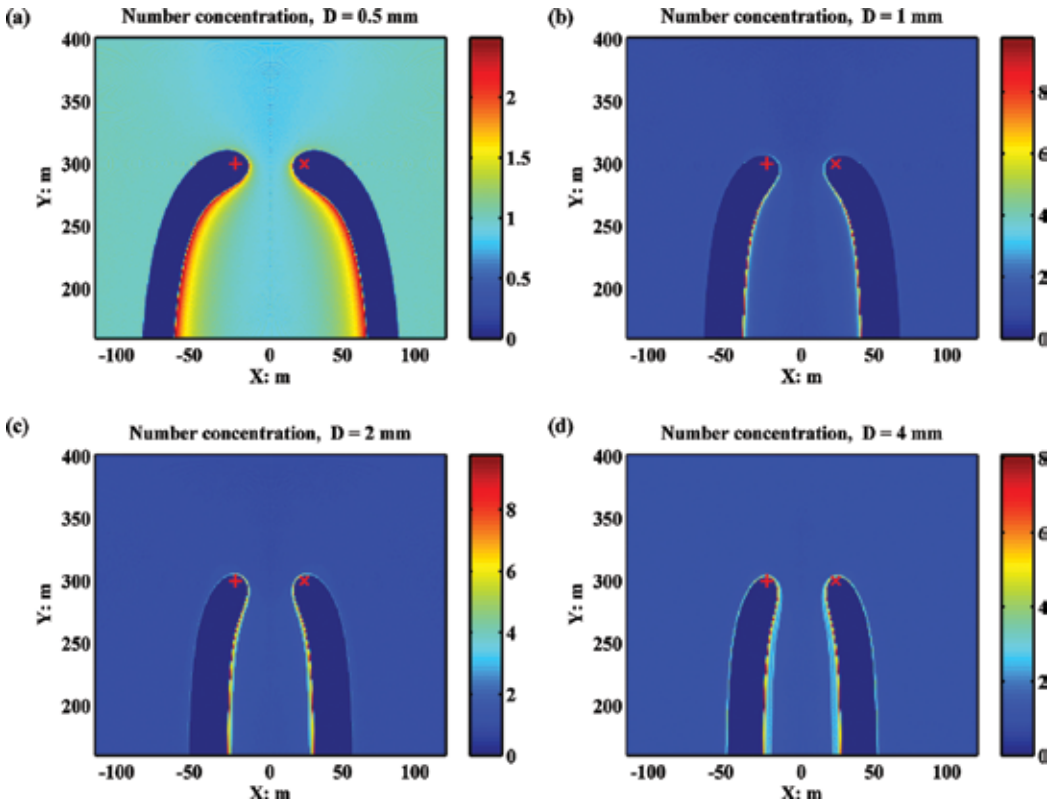


Figure 7. Raindrops' number concentration in wake vortices: (a) $D = 0.5$ mm, (b) $D = 1.0$ mm, (c) $D = 2.0$ mm, (d) $D = 4.0$ mm. The colour bar indicates the value of raindrops' number concentration in each grid box.

ratio of the number of disturbed raindrops in a grid box centred at (x, y) to the number of initial raindrops in a grid box above the wake vortex region, that is

$$\eta_N(D, x, y) = \frac{N(D, x, y)}{N_0(D)} \approx \frac{\text{Num}(D, x, y)}{\text{Num}_0(D)} \quad (55)$$

Obviously, the estimation accuracy of $\eta_N(D, x, y)$ depends on the choice of the grid box size: Δx and Δy , and the number of initial raindrops in each grid box above the wake vortex region: $\text{Num}_0(D)$.

Parameters	Values
Aircraft wingspan	60.30 m
Aircraft maximum landing weight	259,000 kg
Aircraft landing speed	290 km/h
Grid box size	1 m × 1 m
$\text{Num}_0(D)$	100
Raindrops' diameter	0.5 mm, 1.0 mm, 2.0 mm, and 4.0 mm

Table 2. Parameters for the computation of raindrops' number concentration.

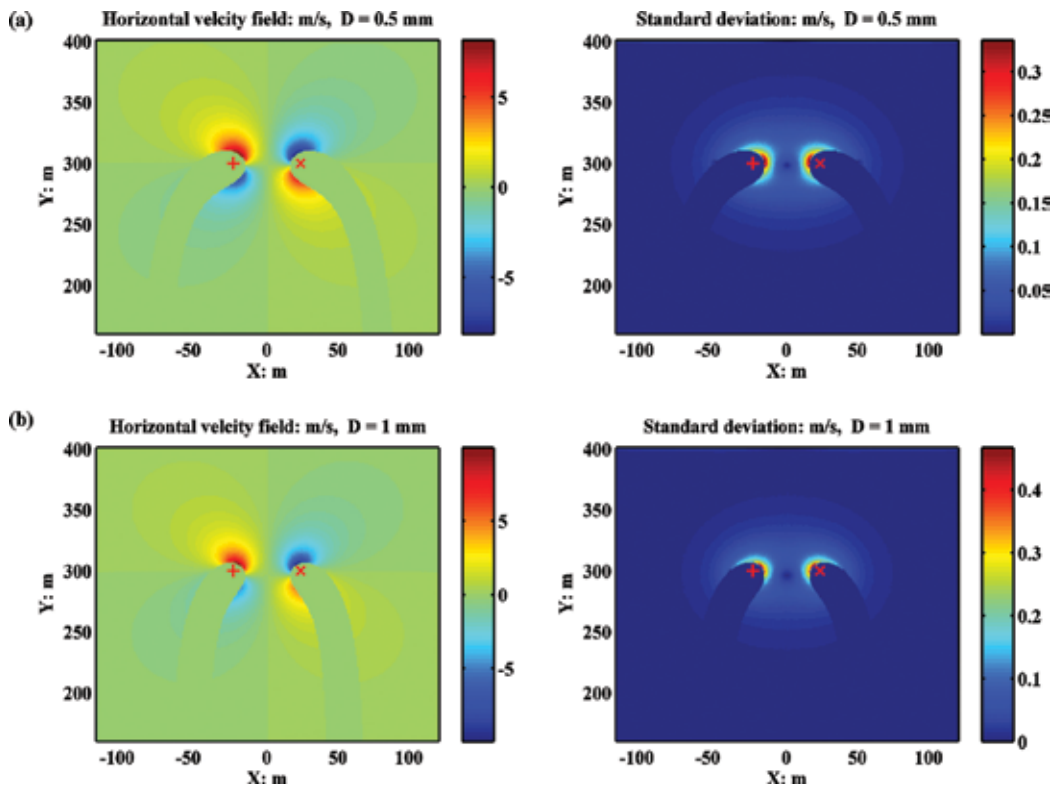


Figure 8. Raindrops' horizontal velocity distribution in wake vortices: (a) $D = 0.5$ mm and (b) $D = 1.0$ mm.

In **Figure 7**, the raindrops' number concentration in wake vortices is illustrated. The simulation parameters are listed in **Table 2**. It can be noticed that in the wake vortex region, there are two columns where the raindrops' concentration is very small, even to zero. These two columns appear symmetrically below the two vortex cores and the distance between them in (a) is much wider than the others. Between these two columns, there are two narrow regions where the number concentration of raindrops is enhanced. For the raindrops of 1 and 2 mm of diameter, the number concentration value exceeds 8 in some grid boxes.

3.4.2. Raindrops' velocity distribution

Besides the number concentration, the raindrops' velocity distribution in each grid box is of great interest. If the grid box size used for the box counting method is small enough and the number of raindrops in each grid box is large enough, the velocity components of the raindrops in one grid box can be thought to obey Gaussian distributions. The mean value and variance of the velocity of the raindrops in each grid box are computed. If the number concentration of the grid box is zero, the raindrops' velocity in this grid box is set to 0.

In **Figures 8 and 9**, the raindrops' horizontal and vertical velocity distribution in wake vortices are illustrated, respectively. From **Figure 8**, it is interesting to find that the raindrops'

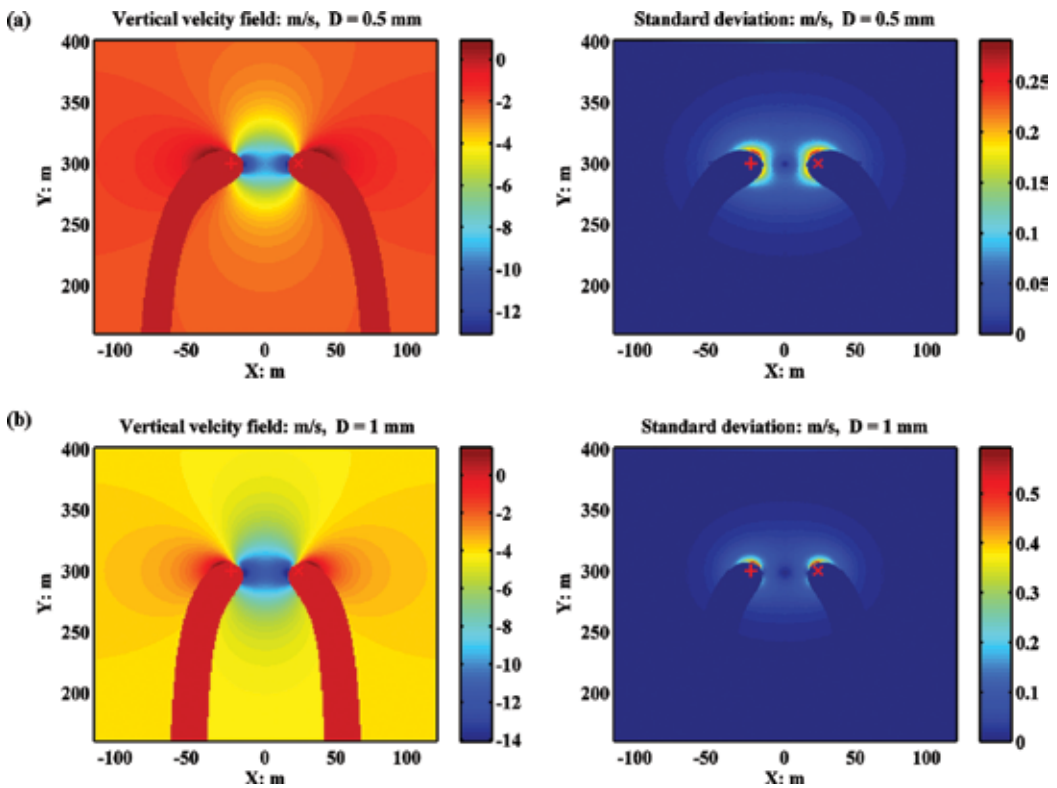


Figure 9. Raindrops' vertical velocity distribution in wake vortices: (a) $D = 0.5$ mm and (b) $D = 1.0$ mm.

horizontal velocity field is similar to the wake vortex velocity field. From **Figure 9**, it is interesting to find that between the two vortex cores, the raindrops' vertical velocity is speeded up. At the same time, the standard deviation of the raindrops' velocity distribution in a grid box is sufficiently low to consider it as constant within each grid box. In fact, in wake vortex, the raindrops' motion is affected by the vortex flow; the raindrops' velocity field is not the same as the superimposition of the vortex flow velocity and raindrops' terminal velocity, but it is representative of the wake vortex velocity characteristics.

Author details

Jianbing Li^{1*}, Zhongxun Liu² and Xuesong Wang³

*Address all correspondence to: jianbingli@nudt.edu.cn

1 College of Electronic Science and Engineering, National University of Defence Technology, Changsha, China

2 National Key Laboratory of Airspace Technology, Beijing, China

3 College of Science, National University of Defense Technology, Changsha, China

References

- [1] Thayer, G.D. An improved equation for the radio refractive index of air. *Radio Science*. 1974; **9**(10):803–807.
- [2] Anderson, J. D. *Introduction to Flight*. McGraw-Hill College; New York, 2004.
- [3] Gerz T., Holzapfel F., and Darracq D. Commercial aircraft wake vortices. *Progress in Aerospace Sciences*. 2002; **38**(3):181–208.
- [4] Myers, T. J. and Scales, W. A. Determination of aircraft wake vortex radar cross section due to coherent Bragg scatter from mixed atmospheric water vapor. *Radio Science*. 1999; **34**(1):103–111.
- [5] Streeter, V. L., Wylie, E. B., and Bedford, K. W. *Fluid Mechanics*. McGraw-Hill; New York, 1997.
- [6] Anderson, J. D. *Computational Fluid Dynamics: The Basics with Applications*. McGraw-Hill; New York, 1995.
- [7] Sauvageot, H. *Radar Meteorology*. Artech House Publishers; London, 1992.
- [8] Bringi, V. N. and Chandrasekar, V. *Polarimetric Doppler Weather Radar: Principles and Applications*. Cambridge University Press; Cambridge, 2004.

- [9] Marshall, J. S. and Palmer, W. M. The distribution of raindrops with size. *Journal of Meteorology*, **5**: 165–166, 1948.
- [10] Owolawi, P. A. Characteristics of Rain at Microwave and Millimetric Bands for Terrestrial and Satellite Links Attenuation in South Africa and Surrounding Islands. PhD thesis, University of KwaZulu-Natal, KwaZulu-Natal, South Africa, 2010.
- [11] Zhongxun, L. I. U. Modélisation des signatures radar des tourbillons de sillage par temps de pluie. PhD thesis, University of Toulouse, Toulouse, 2013.
- [12] Lovejoy, S. and Schertzer, D. Turbulence, raindrops and the 11/2 number density law. *New Journal of Physics*, **10**: 075017 (32pp), 2008.

Vorticity Evolution near the Turbulent/Non-Turbulent Interfaces in Free-Shear Flows

Tomoaki Watanabe, Koji Nagata and
Carlos B. da Silva

Additional information is available at the end of the chapter

<http://dx.doi.org/10.5772/64669>

Abstract

Vorticity dynamics is studied near the interface between turbulent and non-turbulent flows, the so-called turbulent/non-turbulent (T/NT) interface, with the direct numerical simulations of planar jets and mixing layers. The statistics near the interface confirm that the T/NT interface consists of two layers: viscous superlayer and turbulent sublayer. The viscous superlayer with the thickness of four times of Kolmogorov length scale is found at the outer edge of the interface, where the vorticity grows with the viscous diffusion. In the turbulent sublayer between the viscous superlayer and the turbulent region, the strain-vorticity interaction becomes active. In the Lagrangian statistics for the fluid particles, the different scaling laws appear in the entrained particle movement depending on the layer: a ballistic evolution in the viscous superlayer and the Richardson-like scaling for relative dispersion in the turbulent sublayer. These scalings indicate that the change in the particle position in the viscous superlayer is governed by the outward viscous diffusion of vorticity, whereas it is governed by the inviscid small-scale eddy motions in the turbulent sublayer. The flow topology on the particle path line shows that the fluid being entrained tends to circumvent the core region of intense eddies near the T/NT interface.

Keywords: jet, mixing layer, turbulent/non-turbulent interface, DNS, Lagrangian statistics

1. Introduction

Interfaces dividing turbulent and non-turbulent regions appear in various canonical turbulences, such as boundary layers, jets, and mixing layers, where turbulence is generated from the shear due to the wall friction or mean velocity difference. These interfaces are called turbulent/

non-turbulent (T/NT) interfaces. Turbulence is generated by shear motions in various circumstances, where the turbulent fluids are surrounded by non-turbulent fluids. This locally generated turbulence often plays an important role in the relevant phenomena. For example, ocean-mixing layers [1], generated in the stably stratified fluid, are sometimes responsible for the transport of heat, salinity, and plankton. The atmospheric boundary layer [2] is related to the cooling/heating of the ground surface and the transport of contaminant. In the flows with the T/NT interface, the turbulent region grows into the non-turbulent region with the mass, momentum, and energy exchanges across the T/NT interface.

Corrsin and Kistler [3], in laboratory experiments with hot-wire probes, found that the essential feature of the turbulent regions is the high vorticity, and the turbulent and non-turbulent regions can be distinguished by the vorticity. They also predicted that a very thin layer where the non-turbulent fluids acquire vorticity by the viscous diffusion is formed at the outer edge of the turbulent region. This thin layer, called the viscous superlayer, was confirmed with the recent high-resolution direct numerical simulations (DNSs) [4]. Furthermore, the statistical approach conditioned relative to the interface [5] clearly showed that the T/NT interface is the layer with a finite thickness. In addition to the viscous superlayer, an adjacent layer, turbulent sublayer, was found between the turbulent core region and the viscous superlayer [6]. One of the differences between the turbulent sublayer and the viscous superlayer is in the vorticity dynamics; the initial growth of vorticity of the non-turbulent fluid occurs by the viscous diffusion in the viscous superlayer with the absence of inviscid vortex stretching, whereas the vortex stretching plays an important role in the amplification of vorticity in the turbulent sublayer [7,8].

The T/NT interface has been studied in particular attention to the entrainment process since this is where the non-turbulent fluid acquires vorticity and results in the transition to turbulence. Turbulent flows consist of the motions in a wide range of scales, and both small and large scales can cause the entrainment by nibbling [9] and engulfment [10], respectively. The experiments in the boundary layers indicated that the entrainment is the multi-scale process [11]. The entrainment across the interface was studied in [12] with the propagation velocity of the enstrophy isosurface. These analyses on the isosurface movement showed that the propagation velocity is of the order of the Kolmogorov velocity $v_\eta = (\nu\varepsilon)^{1/4}$ [13,14], where ν is the kinematic viscosity and ε is the dissipation rate of turbulent kinetic energy, and the complex shape of the isosurface [15] relates the propagation velocity to the total entrainment rate, which can be written as a function of large-scale quantities [16]. The enstrophy isosurface is an infinitely thin surface located within the T/NT interface layer. Therefore, a more precise description of the entrainment process is the fluid movement across the entire T/NT interface layer than across the enstrophy isosurface. During the entrainment, the irrotational particles pass both the viscous superlayer and the turbulent sublayer. The Lagrangian analysis is useful for studying the entrainment, and both experiments and simulations have been used for tracking the fluid particles (tracers) being entrained from the non-turbulent regions [14,17,18]. These studies showed the evolution of turbulence characteristics during the entrainment. However, the relation between these Lagrangian statistics and the layer structures is not clear

because the particle tracking does not show the location within the T/NT interface layer because the T/NT interface also moves with the convective fluid motion.

In this study, we explore the connection between the T/NT interface structure and the Lagrangian statistics during the entrainment process based on our recent DNS results [19]. The DNS is performed for mixing layers and planar jets, and used for tracking the fluid particles being entrained. In addition to the fluid particles, the outer edge of the T/NT interface layer, defined by the enstrophy isosurface, is also tracked with the Lagrangian markers, enabling us to examine the location of the fluid particle within the T/NT interface layer and to relate the Lagrangian statistics to the Eulerian counterparts. The roles of small-scale eddy structures in the entrainment are considered from the Lagrangian and Eulerian statistics. This chapter is organized as follows: Section 2 presents the numerical methods and parameters as well as the conventional statistics for the validation of the DNS data. Section 3 discusses the analysis on the T/NT interface, such as the interface detection, and the conditional analysis based on the Eulerian and Lagrangian statistics. Finally, Section 4 closes the chapter with the conclusion.

2. Direct numerical simulations

Direct numerical simulations are performed for temporally evolving mixing layers and planar jets [19]. These flows develop from the initial state in the computational domain, which is periodic in the mean flow (x) and spanwise (z) directions. The flows spread in the cross-streamwise (y) direction. We consider the computational box with the size of ($L_x \times L_y \times L_z$) represented by ($N_x \times N_y \times N_z$) grid points. The boundaries in the y direction are treated as the slip wall [7]. The origin of the coordinate system is at the center of the computational domain. The DNS code is an incompressible Navier-Stokes solver based on the fractional step method [8]. In addition to the flow field, a passive scalar ϕ is simulated with the convection-diffusion equation. The governing equations are spatially discretized with a fully conservative finite-difference method [20]. The second-order and fourth-order schemes are used in the cross-streamwise and the periodic directions, respectively. The governing equations are integrated in time with a third-order Runge-Kutta method. The Poisson equation is solved with the fast Fourier transform along the periodic directions and the diagonal matrix algorithm along the x direction.

The initial velocity field is obtained by superimposing the statistically homogeneous and isotropic velocity fluctuations onto the mean velocity, which is given by

$$\langle U \rangle = 0.5U_M \tanh\left(\frac{2y}{\theta_M}\right) \text{ in mixing layers,} \quad (1)$$

$$\langle U \rangle = 0.5U_J + 0.5U_J \tanh\left(\frac{H-2|y|}{4\theta_J}\right) \text{ in planar jets.} \quad (2)$$

Here, U_M is the velocity difference in the mixing layers, U_j the jet velocity, H the width of the jet inlet and θ_M (θ_j) the initial shear layer thickness in the mixing layers (planar jets). The angular bracket denotes the averaged value in a $x - y$ plane. We set $\theta_j = 0.015H$. The initial velocity fluctuations are generated by a diffusion process [21], where the characteristics length scales are $0.07H$ in the planar jets and $0.25\delta_M$ in the mixing layers. The initial rms velocity is $0.04U_j$ for $|y|/H \leq 0.5$ in the planar jets and is $0.025U_M$ for $|y|/\delta_M \leq 3$ in the mixing layer. Except these regions, the fluctuations are not imposed on the mean velocity. The initial scalar profiles are given by

$$\phi = 0.5 \tanh\left(\frac{2y}{\theta_M}\right) \text{ in mixing layers,} \quad (3)$$

$$\phi = 0.5 + 0.5 \tanh\left(\frac{H - 2|y|}{4\theta_j}\right) \text{ in planar jets.} \quad (4)$$

Run	ML04	ML08	PJ50	PJ90
Flow type	Mixing layer	Mixing layer	Planar jet	Planar jet
Re	400	800	5000	9000
L_x	$16\pi\theta_M$	$16\pi\theta_M$	$2.4\pi H$	$2.6\pi H$
L_y	$16\pi\theta_M$	$16\pi\theta_M$	$4.8\pi H$	$3.8\pi H$
L_z	$8\pi\theta_M$	$8\pi\theta_M$	$2.4\pi H$	$1.3\pi H$
N_x	512	1 024	512	1 024
N_y	500	700	850	1 150
N_z	256	512	512	512
Time step dt	$0.08\theta_M/U_M$	$0.04\theta_M/U_M$	$0.012H/U_j$	$0.006H/U_j$
$\Delta_x = \Delta_z$	1.5η	1.2η	1.5η	1.4η
Δ_y ($y=0$)	1.0η	1.1η	1.2η	1.2η
Re_λ	105	151	94	158
η	$0.064\theta_M$	$0.041\theta_M$	$0.0096H$	$0.0059H$
λ	20.8η	23.3η	14.8η	20.3η

Table 1. Physical and computational parameters of the DNS. The displayed turbulence characteristics are from the turbulent core regions.

The Reynolds numbers Re are defined by $U_M\theta_M/\nu$ and U_jH/ν . We perform the DNS for the planar jets with Re = 5 000 and 9 000 and for the mixing layers with Re = 400 and 800. The Schmidt number of ϕ is $Sc = \nu/D = 1$, where D is the molecular diffusivity. **Table 1** shows the physical and computational parameters, such as the Kolmogorov scale η , Taylor microscale λ_{ν} and the turbulent Reynolds number Re_λ , where the Taylor microscale and turbulent

Reynolds number are calculated from the streamwise velocity statistics. The computational grid size, Δ_i , is comparable to η , and is able to capture turbulent motions in very small scales.

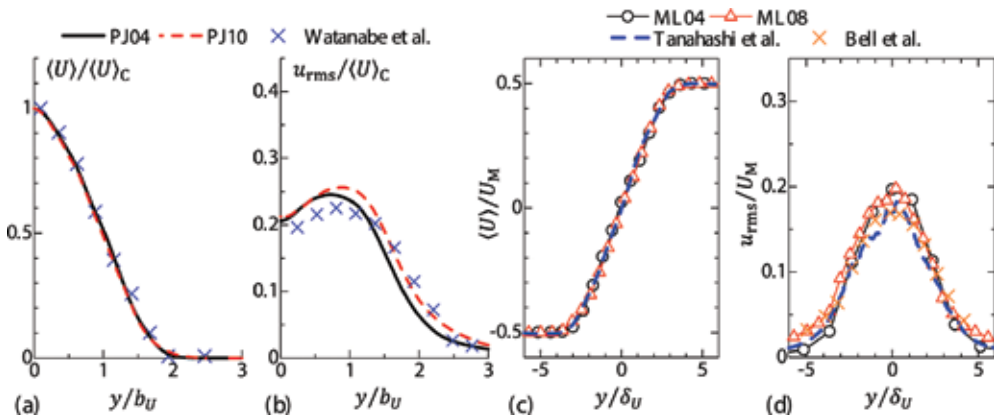


Figure 1. Self-similar profiles of mean streamwise velocity $\langle U \rangle$ and rms streamwise velocity u_{rms} in (a and b) planar jets and (c and d) mixing layers. $\langle U \rangle_c$ and b_U denote the mean streamwise velocity on the centerline and the jet half-width obtained from $\langle U \rangle$, respectively. The mixing layer thickness δ_U is defined as $\delta_U = \int (0.5U_M - \langle U \rangle) (\langle U \rangle - 0.5U_M) / (U_M)^2 dy$. The present DNS results are compared with the experiments and DNS on the planar jets [22] and mixing layers [23,24].

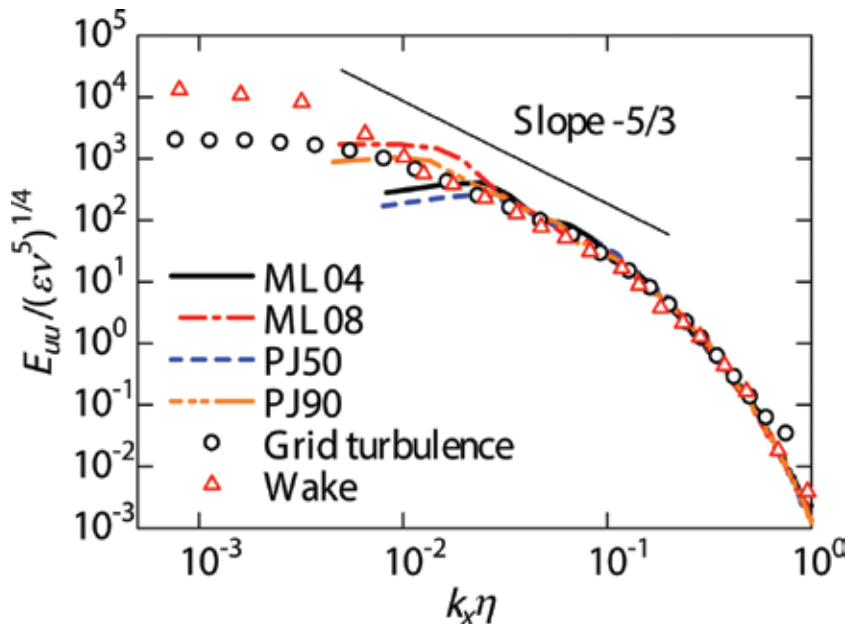


Figure 2. One-dimensional longitudinal spectrum E_{uu} on the centerline of the planar jets and mixing layers compared with the experimental plots in grid turbulence [25] and axisymmetric wake [26].

The fundamental characteristics of the planar jets and mixing layers are compared with other DNS and experiments for validation of the DNS. **Figure 1** compares the self-similar profiles of mean velocity and rms velocity fluctuations. The present DNS reproduces well the self-similar profiles of these statistics in previous studies. **Figure 2** shows the one-dimensional longitudinal spectrum on the centerline with the experimental plots. We can see the overlap of the spectrum in small scales, and the small-scale turbulent fluctuations are well resolved in the DNS.

3. Analysis on turbulent and non-turbulent interface

3.1. Detection of the T/NT interface

The turbulent regions are characterized by high vorticity [3]. Therefore, following [5], we define the turbulent region as where the vorticity magnitude $|\omega|$ exceeds the threshold ω_{th} . Then, with an appropriate value of ω_{th} , the isosurface of $|\omega| = \omega_{th}$ can be detected so that it is located near the outer edge of the T/NT interface layer. The specific value of ω_{th} is obtained from a well-known dependence of turbulent volume on ω_{th} [18]. **Figure 3(a)** shows the volume fraction of turbulent regions as a function of ω_{th} . We can see a plateau in the turbulent volume, and the isosurface location hardly changes with ω_{th} for the plateau. We choose $\omega_{th} = 0.04\langle|\omega|\rangle_C$, which is from the plateau shown in **Figure 3(a)**. This value is chosen so that the isosurface is located at the outer edge of the T/NT interface layer. We call this isosurface as the *irrotational boundary* hereafter. **Figure 3(b)** and **(c)** show the enstrophy profile and the irrotational boundary. The irrotational boundary surrounds the high enstrophy region and is located at the outer edge of the turbulent fluids. Thus, the outer edge of the T/NT interface layer is well defined by thresholding the vorticity magnitude.

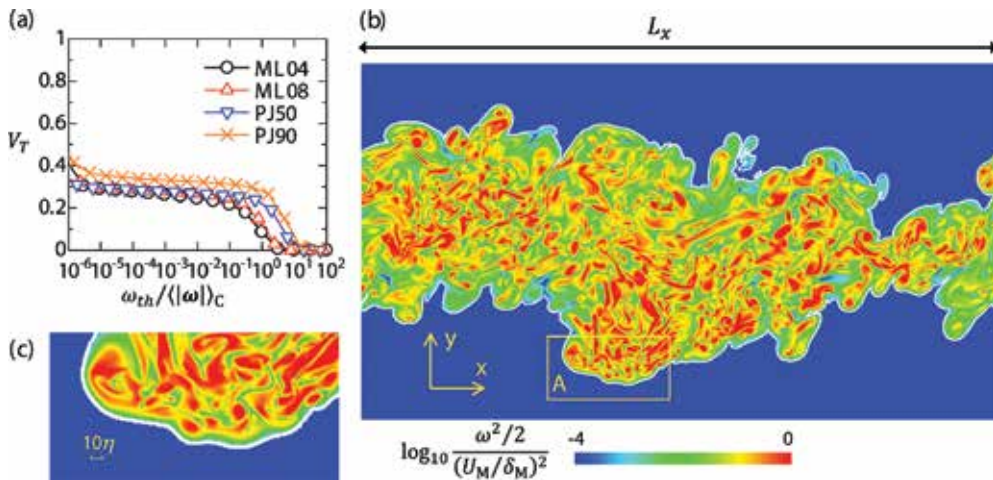


Figure 3. Detection of the T/NT interface. (a) Dependence of the turbulent volume fraction on the normalized threshold $\omega_{th}/\langle|\omega|\rangle_C$. (b) Visualization of the irrotational boundary in ML08 (white line). The color contours show enstrophy levels in $\log_{10}(\omega^2/2)$. (c) The close-up of the T/NT interface (the region A in (b)).

The irrotational boundary is visualized in **Figure 4**. The T/NT interface has a very complex shape. The Re dependence is also clear; the higher Re mixing layer has smaller-scale structures because of the small length scales of turbulence.

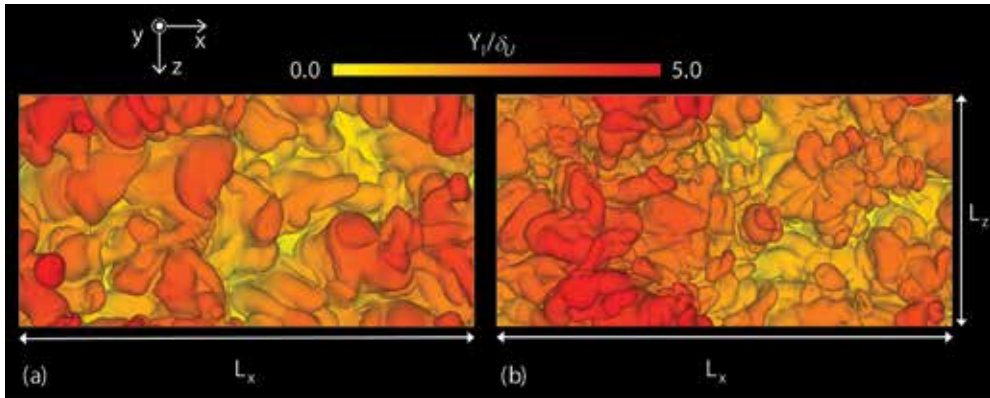


Figure 4. Visualization of the irrotational boundary (the vorticity magnitude isosurface) in the mixing layers with (a) Re = 400 and (b) Re = 800. The color shows the interface height Y_1 from the centerline normalized by the mixing layer thickness $\delta_U = \int (0.5U_M - \langle U \rangle)(U - 0.5U_M)/(U_M)^2 dy$.

3.2. Statistics conditioned on the location of the T/NT interface

The vorticity dynamics is studied with the statistics conditioned on the location from the irrotational boundary. This interface coordinate, ζ_i , is taken in the normal direction of the irrotational boundary $\mathbf{n} = -\nabla \omega^2 / |\nabla \omega^2|$, where $\zeta_i = 0$ is the location of the irrotational boundary.

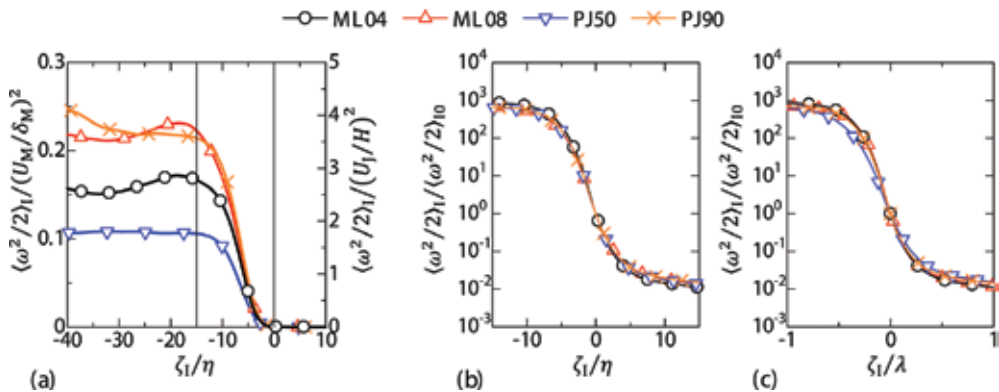


Figure 5. (a) Conditional mean enstrophy $\langle \omega^2/2 \rangle_i$. The vertical lines, from right to left, denote $\zeta_i = 0$ and $\zeta_i = -15\eta$, where $\langle \omega^2/2 \rangle_i$ reaches the value close to the turbulent core region. Conditional mean enstrophy divided by the value at the irrotational boundary $\langle \omega^2/2 \rangle_{i0}$ against the interface coordinate normalized by (b) Kolmogorov scale η and (c) Taylor microscale $\lambda = (\lambda_x + \lambda_y + \lambda_z)$.

The non-turbulent region is indicated by $\zeta_1 > 0$. Because of the complicated shape of the T/NT interface, a turbulent (non-turbulent) fluid and an associated irrotational boundary can appear for $\zeta_1 > 0$ ($\zeta_1 < 0$). For separating the statistics into the turbulent and non-turbulent parts, the statistics are calculated solely from turbulent and non-turbulent regions in $\zeta_1 < 0$ and $\zeta_1 > 0$, respectively. When another irrotational boundary is found at $\zeta_1 \neq 0$, the region within the distance of λ from this boundary is excluded from the statistics for preventing the T/NT interface layer from affecting the statistics for $\zeta_1 \gg 0$ or $\ll 0$. Note that previous studies have shown that the T/NT interface layer thickness is about 0.5λ [27]. Hereafter, $\langle \cdot \rangle_1$ denotes the conditional mean value.

Figure 5 shows the conditional mean enstrophy profiles. The mean enstrophy is matched in the layer with the thickness of $\approx 15\eta$. The scaling of the thickness of the interface layer is examined in the plots of $\langle \omega^2/2 \rangle_1$ normalized by the value at $\zeta_1 = 0$, $\langle \omega^2/2 \rangle_{10}$ in **Figure 5(b)** and **(c)**, where ζ_1 is normalized by the Kolmogorov scale η and Taylor microscale λ , respectively. The plots tend to better collapse onto a single curve for ζ_1/η than ζ_1/λ , and thus the thickness of the T/NT interface layer, across which the enstrophy changes, is scaled with the Kolmogorov scales. It should be noted that the Taylor microscale can be the characteristics length scale of the T/NT interface when the large-scale coherent structures exist near the T/NT interface [28].

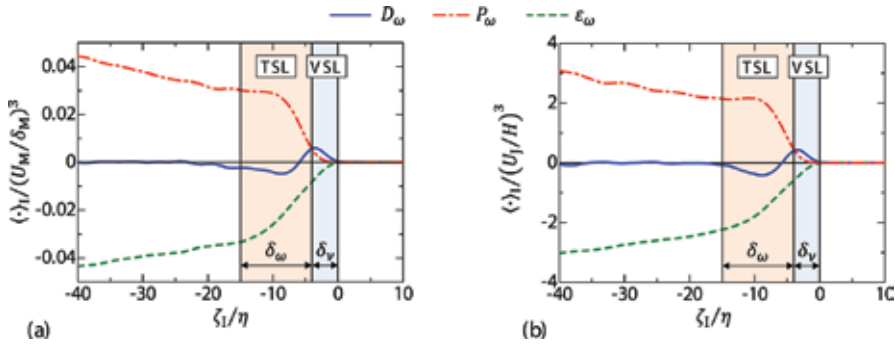


Figure 6. Conditional enstrophy budget in (a) ML08 and (b) PJ90, where $D_\omega = \nu \nabla^2 \omega^2/2$ is the viscous diffusion term, $P_\omega = \omega_i S_{ij} \omega_j$ is the production term, $\epsilon_\omega = -\nu \nabla \omega_i \cdot \nabla \omega_i$ is the viscous dissipation term. The vertical lines, from right to left, denote $\zeta_1 = 0$, $\zeta_1 = -4\eta$, where $\langle D_\omega \rangle_1 = \langle P_\omega \rangle_1$, and $\zeta_1 = -15\eta$. The viscous superlayer (VSL) with the thickness δ_v and the turbulent sublayer (TSL) with the thickness δ_ω are highlighted.

The vorticity evolution near the interface is studied by the enstrophy transport equation:

$$\frac{D\omega^2/2}{Dt} = \omega_i S_{ij} \omega_j + \nu \nabla^2 (\omega^2/2) - \nu \nabla \omega_i \cdot \nabla \omega_i, \quad (5)$$

where the first term on the right-hand side is the enstrophy production P_ω (S_{ij} : strain-tensor), the second is the viscous diffusion D_ω , and the third is the viscous dissipation ϵ_ω . The conditional average of each term is plotted in **Figure 6** for ML08 and PJ90. The plots are very similar for these flows in the T/NT interface layer; the enstrophy grows by the viscous diffusion near

the outer edge of the T/NT interface, whereas the inviscid vortex stretching becomes important slightly inside the outer edge. The profile of $\langle D_\omega \rangle_I$ exhibits negative and positive values in the T/NT interface layer, indicating the vorticity transport toward the non-turbulent region. Near the outer edge of the T/NT interface layer, $\langle D_\omega \rangle_I$ is larger than $\langle P_\omega \rangle_I$ in the region of $-4\eta \leq \zeta \leq 0$. This thickness, $\delta_v = 4\eta$, agrees with the direct observation of the viscous superlayer thickness [4]. Thus, from the conditional mean profiles of enstrophy and its budget, we can identify the viscous superlayer in $-4\eta \leq \zeta \leq 0$ and the adjutant layer, turbulent sublayer, with the thickness of $\delta_\omega = 11\eta$ in $-15\eta \leq \zeta \leq -4\eta$. This structure of the T/NT interfaces is observed in all DNS dataset. In the turbulent core region, the mean enstrophy production $\langle P_\omega \rangle_I$ almost balances with the mean viscous dissipation $\langle \varepsilon_\omega \rangle_I$. This balance is absent in the T/NT interface layer; from $\zeta_1 = -15\eta$, $\langle \varepsilon_\omega \rangle_I$ becomes small toward the irrotational boundary, whereas $\langle P_\omega \rangle_I$ hardly changes with the location for $-15\eta \leq \zeta \leq -9\eta$.

Figure 7 gives the conditional plots of passive scalar ϕ and scalar dissipation rate $\chi = D\nabla\phi \cdot \nabla\phi$. In the mixing layer, the conditional statistics are calculated from the upper interface, for which the non-turbulent fluid has $\phi = 0.5$, where the upper interface is detected as the irrotational boundary with $\nabla\omega^2 \cdot \nabla\phi < 0$. The conditional mean scalar, $\langle \phi \rangle_I$, also changes in the T/NT interface layer, and is adjusted between the turbulent and non-turbulent regions. The jump in $\langle \phi \rangle_I$ is very similar in all DNS, and the thickness of this jump scales with the Kolmogorov scale at $Sc = 1$ and in the Re range studied here. Because of the difference in $\langle \phi \rangle$ between the turbulent and non-turbulent regions, the scalar gradient becomes large in the T/NT interface layer. Therefore, as shown in **Figure 7(b)**, the scalar dissipation has a large peak at $\zeta_1 = -4.9\eta$ in the T/NT interface layer. This location is shown in **Figure 7(a)** by the vertical line, and is close to the inflection point of $\langle \phi \rangle_I$ and to the boundary between the viscous superlayer and the turbulent sublayer.

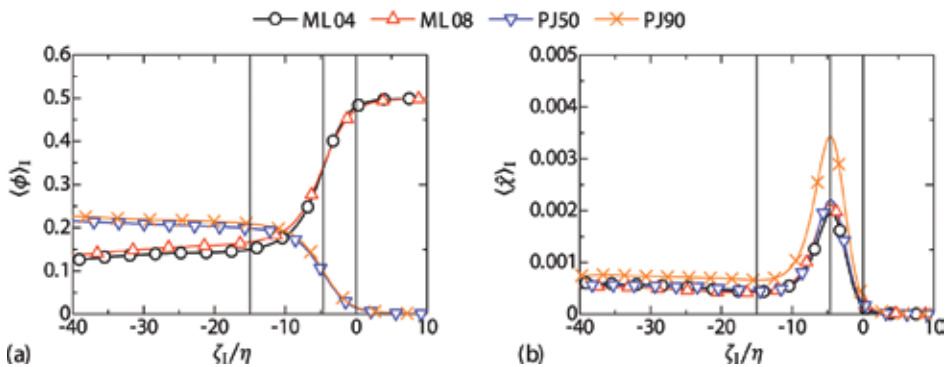


Figure 7. Conditional mean scalar $\langle \phi \rangle$ and normalized scalar dissipation rate $\langle \hat{\chi} \rangle$, where $\hat{\chi} = (\delta_m^2 / ReSc) \nabla\phi \cdot \nabla\phi$ in the mixing layers and $\hat{\chi} = (H^2 / ReSc) \nabla\phi \cdot \nabla\phi$ in the planar jets. The vertical lines, from right to left, denote $\zeta_1 = 0$, $\zeta_1 = -4.9\eta$, where $\langle \hat{\chi} \rangle_I$ reaches a peak, and $\zeta_1 = -15\eta$.

The strain-rate tensor S_{ij} plays an important role in small-scale dynamics of turbulence. The interaction between strain and vorticity leads to the vortex stretching $\omega_i S_{ij}$ and in turn to

enstrophy production $\omega_i S_{ij} \omega_j$. The gradient of passive scalar, $G_i = \partial\phi/\partial x_i$, is also affected by the strain field via the straining term $-G_i S_{ij}$, which appears as the production term of χ . The effective strains acting on the vorticity and the scalar gradient are written as follows [29]:

$$\alpha_\omega = \frac{\omega_i S_{ij} \omega_j}{\omega_k \omega_k}, \quad (6)$$

$$\gamma_\chi = -\frac{G_i S_{ij} G_j}{G_k G_k}, \quad (7)$$

where α_ω and γ_χ are the production rates of enstrophy and of scalar dissipation rate, respectively [30]. Note that the vortex stretching and the compression of the scalar gradient are denoted by positive α_ω and γ_χ , respectively, and positive values of the effective strains contribute to the amplification of enstrophy and of scalar dissipation rate. **Figure 8** shows the conditional average of α_ω and γ_χ normalized by the strain product on the centerline $\langle S_{ij} S_{ij} \rangle_C$. The profiles are almost independent of the flows. $\langle \alpha_\omega \rangle_1$ and $\langle \gamma_\chi \rangle_1$ decrease toward the interface in the turbulent core region, but peaks can be found in the turbulent sublayer, where the amplification of enstrophy and scalar dissipation rate becomes more efficient. This results in a predominance of the enstrophy production over the viscous dissipation in the T/NT interface layer ($\langle P_\omega \rangle_1 > |\langle \varepsilon_\omega \rangle_1$) in **Figure 6**.

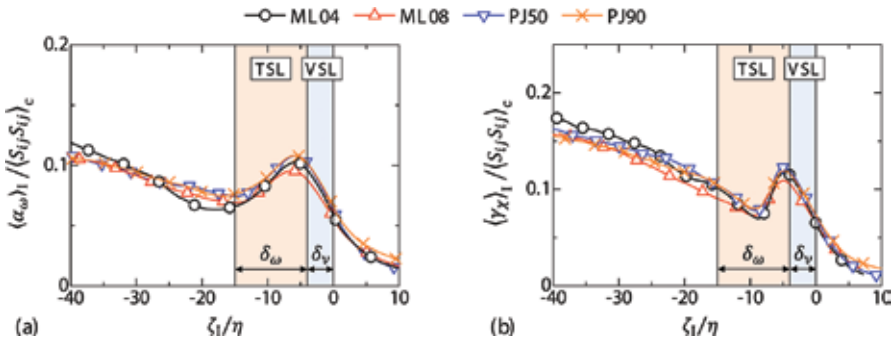


Figure 8. Conditional mean profiles of (a) effective extensive strain acting on vorticity $\alpha_\omega = \omega_i S_{ij} \omega_j / (\omega_k \omega_k)$ and (b) effective compressive strain acting on scalar gradient $\gamma_\chi = -G_i S_{ij} G_j / (G_k G_k)$, where the mean strain product on the centerline $\langle S_{ij} S_{ij} \rangle_C$ is used for normalization. The viscous superlayer and turbulent sublayer are also indicated.

3.3. Lagrangian statistics of entrained fluid particles

The Lagrangian particle tracking is used for investigating the vorticity growth during the entrainment of non-turbulent fluids. Once the flows have reached the self-similar regime, 140,000 particles are seeded in the non-turbulent regions near the irrotational boundary. The particles are tracked with a third-order Runge-Kutta method and a trilinear interpolation

scheme [31]. The flow characteristics are changed depending on the location in the T/NT interface layer. Therefore, it is important to know the entrained fluid particle location within the T/NT interface layer for better understanding of the Lagrangian properties of the entrainment. Because of the T/NT interface movement, the entrained particle tracking does not show the location in the T/NT interface layer. Here, in addition to the fluid particles, the irrotational boundary is also tracked with a marker, which moves with the velocity of the enstrophy isosurface movement u_i . As in **Figure 9(a)**, the marker is placed on the irrotational boundary where the fluid particle has crossed. u_i is the sum of the fluid velocity at the irrotational boundary u_0 and the propagation velocity of the enstrophy isosurface $u_p = v_E n$, where $v_E = (D\omega^2/Dt)/|\nabla\omega^2|$. It was shown that only a negligible fraction of entrained fluid particles is trapped inside a non-turbulent region completely surrounded by turbulent fluids [18]. Because the irrotational boundary of this region disappears after it becomes turbulent, the markers of this irrotational boundary are no longer located on the enstrophy isosurface. Therefore, $|\omega|$ on the markers is monitored at every time step, and markers with $|\omega| > 2\omega_{th}$ are excluded from the subsequent analysis.

The Lagrangian statistics are calculated for the fluid particles, conditioned on the time τ elapsed after a fluid particle has crossed the irrotational boundary, and the Lagrangian conditional average is denoted by $\langle \cdot \rangle_\tau$. A separation vector δx is introduced as in **Figure 9(a)**, and is used for examining the particle location in the T/NT interface layer.

Figure 9(b) shows the Lagrangian conditional average of $\delta x = |\delta x|$, where δx and τ are normalized by the Kolmogorov length scale η and time scale τ_η at the time when the fluid particles are seeded. The plots are quite similar for small τ in all DNS. It takes about $7\tau_\eta$ for the entrained particles to reach the turbulent sublayer by moving across the viscous superlayer. A difference in δx becomes clear in the turbulent sublayer; the time needed for the particles to move across the turbulent sublayer changes depending on the flow configuration and Reynolds number. The relation between $\langle \delta x \rangle_\tau$ and τ is used for relating the Lagrangian statistics

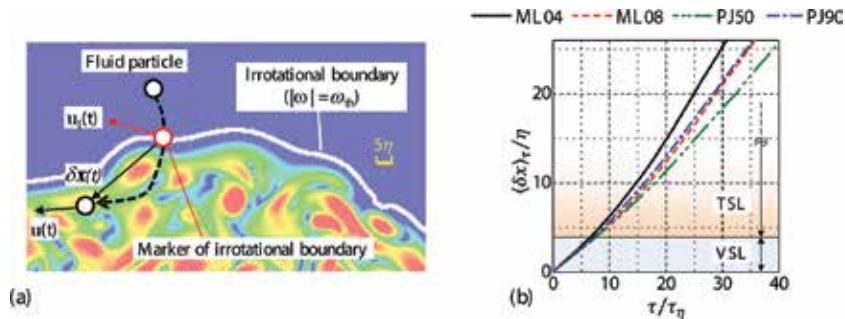


Figure 9. (a) The fluid particle movement is analyzed in relation to the irrotational boundary, which is tracked with a marker moving with the velocity of the enstrophy isosurface movement. A marker is introduced at the boundary where the fluid particle crosses. The irrotational boundary is indicated by a white line while enstrophy levels are shown with the color contours. (b) Conditional mean distance between the entrained fluid and the irrotational boundary marker $\langle |\delta x| \rangle_\tau$ against τ/τ_η where the Kolmogorov time scale $\tau_\eta = (\nu/\varepsilon)^{1/2}$ and length scale η are taken on the centerline at the time when the fluid particles are seeded. The viscous superlayer (VSL) and the turbulent sublayer (TSL) estimated from the Eulerian statistics are indicated in the figure.

with the interface structure by plotting the Lagrangian statistics, which is a function of τ , against $\langle \delta x \rangle_\tau$.

The separation vector $\delta \mathbf{x}(\tau)$, a fluid particle location relative to a marker of the irrotational boundary, changes as

$$\frac{d\delta \mathbf{x}(\tau)}{d\tau} = \delta \mathbf{u}(\tau) \equiv \mathbf{u}(\tau) - \mathbf{u}_1(\tau), \quad (8)$$

where $\delta \mathbf{u}$ is the fluid particle velocity in relation to the velocity of the marker of the irrotational boundary, and is simply referred to as the relative velocity. The dot product of Eq. (8) with $\delta \mathbf{x}$ yields the following equation [32]:

$$\frac{d\delta x^2}{d\tau} = 2 \int_0^\tau \delta \mathbf{u}(\tau) \cdot \delta \mathbf{u}(\tau') d\tau'. \quad (9)$$

The relative velocity can be decomposed into the two components: the irrotational boundary propagation velocity (\mathbf{u}_p) and the fluid velocity difference ($\mathbf{u} - \mathbf{u}_0$) between the fluid particle and the location of the marker of the irrotational boundary:

$$\delta \mathbf{u}(\tau) = -\mathbf{u}_p(\tau) + (\mathbf{u}(\tau) - \mathbf{u}_0(\tau)). \quad (10)$$

For small τ , we can assume that the fluid particles are located in the proximity of the irrotational boundary [14], and the fluid velocity is almost the same between the locations of the fluid particle and the marker of the irrotational boundary. Then, $|\mathbf{u}_p| \gg |\mathbf{u} - \mathbf{u}_0| \approx 0$, and the relative velocity can be approximated by $\delta \mathbf{u}(\tau) \approx -\mathbf{u}_p(0)$ [33]. Thus, Eq. (9) is simply,

$$\frac{d\delta x^2}{d\tau} = 2 \int_0^\tau (\mathbf{u}_p(0) \cdot \mathbf{u}_p(0)) dt' = 2v_E^2 \tau. \quad (11)$$

Integration of Eq. (11) yields $\delta x^2 = v_E^2 \tau^2$, where v_E is taken at $\tau = 0$. Thus, the Lagrangian conditional root-mean-squared distance changes with

$$\langle \delta x^2 \rangle_\tau^{1/2} = \langle v_E^2 \rangle_{\tau=0}^{1/2} \tau \quad (\text{for small } \tau). \quad (12)$$

It was shown that the propagation velocity scales with the Kolmogorov velocity [14]. By contrast, the fluid velocity difference between two points can be much larger in turbulent flows. Therefore, once the fluid particle has reached far away from the irrotational boundary, the fluid velocity difference can be large compared with the propagation velocity. Then, in the

case of $\delta u \approx u - u_0$, the fluid particle movement in relation to the irrotational boundary is described as the two-particles dispersion problem [34]. Similar to Richardson’s law for the relative diffusion, under the assumption that δx changes by eddies of size $\delta x(\tau)$ [35], we can obtain the following relationship in the self-similar regime:

$$\left\langle \delta x^2 / \varepsilon \right\rangle_{\tau}^{1/2} = C \tau^{3/2} \quad (\text{for large } \tau), \quad (13)$$

where C is a constant, and the mean kinetic energy dissipation rate ε is time dependent. Here, we use ε obtained in the turbulent core region. This expression can be obtained with the modified Richardson’s law for decaying turbulence [36,37] in the self-similar regime, where $\varepsilon(t)$ decays as $\varepsilon(t) \sim t^{-n}$.

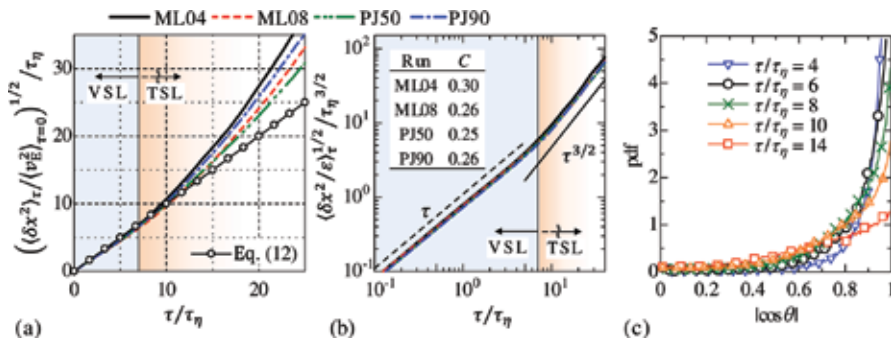


Figure 10. The scalings for the mean-squared distance between entrained fluid particle and irrotational boundary. (a) The ballistic evolution in the initial stage of the entrainment. (b) The modified Richardson-like scaling for the mean-squared distance. The viscous superlayer (VSL) and the turbulent sublayer (TSL) estimated from the Eulerian statistics are indicated in (a) and (b). (c) Pdf of the cosine of the angle between δx and the irrotational boundary normal n .

Figure 10(a) shows $\langle \delta x^2 \rangle_{\tau}^{1/2}$ for comparison between the DNS results and Eq. (12). For $\tau/\tau_{\eta} \lesssim 10$, Eq. (12) well predicts $\langle \delta x^2 \rangle_{\tau}^{1/2}$. Thus, within the viscous superlayer ($\tau/\tau_{\eta} \lesssim 7$), δx is changed by the irrotational boundary propagation with only a negligible influence of the fluid velocity. Since the irrotational boundary is located at the outer edge of the T/NT interface, where the enstrophy grows by the viscous diffusion with only a negligible influence of vortex stretching, the outward enstrophy diffusion causes the fluid particles to reach the turbulent sublayer. **Figure 10(b)** shows $\langle \delta x^2 / \varepsilon \rangle_{\tau}^{1/2}$ against τ . The plots of $\langle \delta x^2 / \varepsilon \rangle_{\tau}^{1/2}$ are similar in all DNS presented in this study. For $\tau \approx 0$, Eq. (12) yields $\langle \delta x^2 / \varepsilon \rangle_{\tau}^{1/2} \propto \tau$. Both scaling laws, Eqs. (12) and (13), are recovered in all simulations. The relationship for larger τ , Eq. (13), is satisfied from $\tau/\tau_{\eta} \approx 9$, which is the time slightly after the particles reach the turbulent sublayer (see **Figure 9(b)**). Eq. (13) is valid for larger τ/τ_{η} , including the entire turbulent sublayer. The values of the constant C , obtained with the least-squares methods, are between 0.25 and 0.30 as displayed in **Figure 10(b)**. The important assumption behind the relationship, Eq. (13), is that the fluid particle movement in relation to the irrotational boundary is caused solely by eddies of size

δx without viscous effects nor eddies with different sizes. The entrained particles within the turbulent sublayer, $\delta_v \lesssim \delta x \lesssim \delta_v + \delta_\omega$, obey Eq. (13), indicating that the particle movement is caused by the small-scale eddy motions whose size is from δ_v to $\delta_v + \delta_\omega$. These small-scale eddies with core radius of about 5η ($\approx \delta_v$) were found within the turbulent sublayer as intense vorticity structures [38].

Figure 10(c) shows the pdf of the cosine of the angle between the separation vector δx and the irrotational boundary normal \mathbf{n} . Because the particle location within the viscous superlayer changes with the irrotational boundary propagation, whose direction is given by \mathbf{n} , the particle in the viscous superlayer stays in the normal direction of the irrotational boundary. This is confirmed by a large peak in the pdf associated with a parallel alignment of δx and \mathbf{n} .

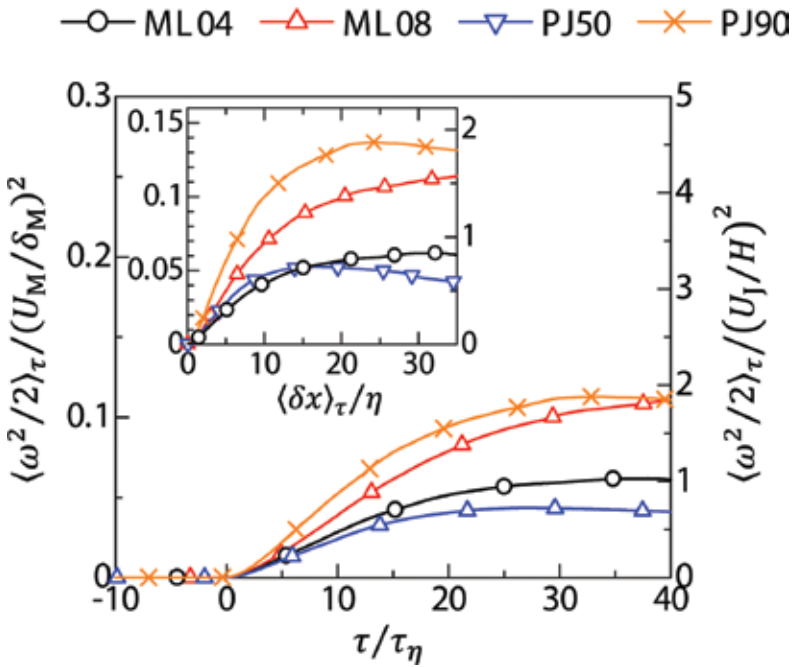


Figure 11. Lagrangian conditional mean enstrophy $\langle \omega^2/2 \rangle_\tau$. The inset plots $\langle \omega^2/2 \rangle_\tau$ against the mean distance between the particle and the irrotational boundary.

Figure 11 shows the Lagrangian conditional mean enstrophy $\langle \omega^2/2 \rangle_\tau$, where the inset plots $\langle \omega^2/2 \rangle_\tau$ against $\langle \delta x \rangle_\tau$ for comparison with the Eulerian statistics in **Figure 5**. Once the particle moves into the T/NT interface layer, the enstrophy begins to grow. The inset shows that even after the particle reaches deep inside the turbulent region, the mean enstrophy on the particle path is much smaller than the Eulerian conditional mean enstrophy in **Figure 5(a)**. It should be noted that the Lagrangian statistics are obtained only from the fluid being entrained, whereas the Eulerian statistics contain the contributions from the entrained fluid and the fluid from the turbulent core region. This makes differences between the Lagran-

gian and Eulerian statistics, and the Eulerian statistics are not enough for studying the entrainment process across the T/NT interface layer.

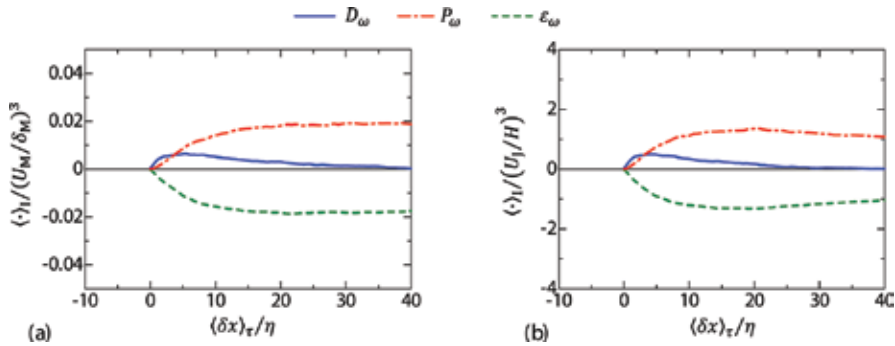


Figure 12. Lagrangian conditional mean enstrophy budget of the entrained particles plotted against the mean distance $\langle \delta x \rangle_\tau$ between the particle and the irrotational boundary. (a) ML08 and (b) PJ90.

Figure 12 shows the Lagrangian conditional statistics of the enstrophy budget, where again the Lagrangian statistics are plotted against $\langle \delta x \rangle_\tau$ for comparison with the Eulerian statistics in **Figure 6**. Qualitative differences can be found between the Eulerian and Lagrangian conditional means of D_ω . The Eulerian $\langle D_\omega \rangle_1$ displays both positive and negative values indicating an outward mean enstrophy transport, whereas the Lagrangian $\langle D_\omega \rangle_\tau$ is positive even for large $\langle \delta x \rangle_\tau$. Thus, although the fluid being entrained possesses an important level of enstrophy in the T/NT interface layer, the enstrophy transport toward the non-turbulent region is hardly associated with this entrained fluid. The Lagrangian enstrophy production and dissipation terms are smaller than their corresponding Eulerian counterparts. Note that these terms are proportional to the enstrophy, and this difference between Lagrangian and Eulerian statistics seems to be due to a smaller enstrophy level on the entrained particle path.

Figure 13(a) compares the Eulerian and Lagrangian conditional averages of the second invariant of velocity gradient tensor $Q = (\omega_i \omega_i - 2S_{ij}S_{ij})/4$. A large positive value of Q implies the predominance of vorticity over the strain while its negative value is related to where dissipation is dominant. The vortex core region of an eddy often has positive Q while negative Q appears around the core region [35]. The Eulerian $\langle Q \rangle_1$ has a negative peak near the irrotational boundary and a large positive peak inside the turbulent region. However, the Lagrangian $\langle Q \rangle_\tau$ is negative even for large $\langle \delta x \rangle_\tau$ in the turbulent core region. The third invariant of the velocity gradient tensor is defined by $R = -(S_{ij}S_{jk}S_{ki}/3 - \omega_i S_{ij} \omega_j / 4)$, and the joint pdf of Q and R has been used for investigating the local flow topology in various turbulent flows [39–41]. **Figure 13(b) and (c)** compares the joint pdf of Q and R obtained as the Eulerian and Lagrangian statistics in the turbulent sublayer. Both Eulerian and Lagrangian pdfs show a “teardrop” shape similar to various turbulent flows, but a difference is found for large positive Q ; the probability of finding intense values of $Q \gg 0$ is smaller in the Lagrangian pdf than in the Eulerian counterpart. These statistics of Q show that although there are regions with $Q \gg 0$ within the T/NT interface layer, the fluid particles being entrained tend to circumvent these

regions. The regions with $Q \gg 0$ can be related to the core of the intense eddies. Thus, a circular motion induced by these eddies may explain this entrained particle path.

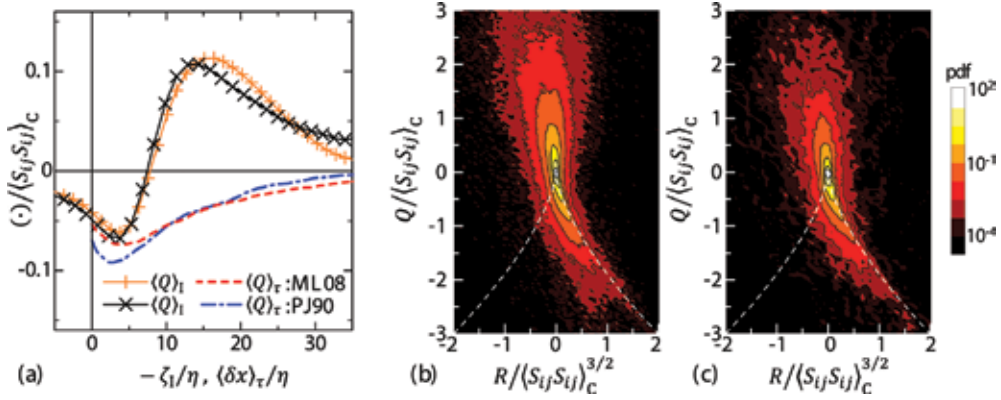


Figure 13. (a) Comparison between the Eulerian and Lagrangian conditional averages of the second invariant of the velocity gradient tensor ($\langle Q \rangle_l$ and $\langle Q \rangle_r$, respectively). The Lagrangian conditional average is plotted against $\langle \delta x \rangle_\tau$. Joint pdf of the second and third invariants of the velocity gradient tensors in (b) Eulerian and (c) Lagrangian statistics. Invariants are normalized by the mean strain product on the centerline $\langle S_{ij}S_{ij} \rangle_c$ at the time when the particles are seeded.

4. Conclusion

The DNS of planar jets and mixing layers was performed for investigating the vorticity dynamics near the T/NT interface. The outer edge of the T/NT interface layer, irrotational boundary, is detected as an isosurface of the vorticity magnitude. The Eulerian and Lagrangian statistics were investigated in this study. The former was calculated conditioned on the distance from the irrotational boundary. For investigating the Lagrangian properties of the entrainment, a large number of fluid particles are seeded in the non-turbulent region of the self-similar regime. The Lagrangian statistics were calculated as a function of time elapsed after the particle crosses the irrotational boundary. Furthermore, a marker of the irrotational boundary is also tracked with the velocity of the enstrophy isosurface movement, and is used for examining the fluid particle location within the T/NT interface layer.

The Eulerian conditional mean enstrophy and its budget showed that the T/NT interface is a layer with the thickness of about 15η , and consists of the viscous superlayer and the turbulent sublayer with the thickness of $\delta_v \approx 4\eta$ and $\delta_\omega \approx 11\eta$, respectively. It was also found that the amplification of the vorticity and scalar gradient is efficient in the turbulent sublayer. The passive scalar exhibits a jump in the T/NT interface layer, where the large scalar dissipation rate appears near the boundary between the viscous superlayer and the turbulent sublayer in all simulations.

The Lagrangian statistics of the entrained particle and the marker of the irrotational boundary showed that it takes about $7\tau_\eta$ for the entrained particle to pass across the viscous superlayer.

The mean-squared distance exhibited two different scalings depending on the location: a ballistic evolution in the viscous superlayer and the Richardson-like scaling for the relative dispersion in the turbulent sublayer. These scalings indicate that the different mechanisms govern the entrained fluid movement between the two layers. A ballistic evolution was explained reasonably based on the irrotational boundary propagation, which arises from the viscous diffusion of vorticity. The Richardson-like scaling implies the importance of inviscid motions of small-scale eddies in the entrainment. The Lagrangian statistics also showed that although the fluid being entrained possesses an important level of enstrophy, it does not contribute, in a mean sense, to the viscous diffusion of vorticity to the irrotational region. Thus, the fluid existing in the turbulent core region plays an important role in the vorticity diffusion near the T/NT interface. The $Q - R$ analysis indicates that the entrained fluid path appears around the core of the small-scale eddy structures related to very large Q .

Acknowledgements

This work was supported by JSPS KAKENHI Grant numbers 25289030 and 16K18013. C.B. da Silva acknowledges IDMEC, under LAETA projects PTDC/EME-MFE/122849/2010 and UID/EMS/50022/2013. The authors acknowledge Prof. Yasuhiko Sakai (Nagoya University) for a number of insightful comments. A part of the results presented in this chapter was published in *Physics of Fluids* (<http://scitation.aip.org/content/aip/journal/pof2/28/3/10.1063/1.4942959>).

Author details

Tomoaki Watanabe^{1*}, Koji Nagata¹ and Carlos B. da Silva²

*Address all correspondence to: watanabe@nuae.nagoya-u.ac.jp

¹ Nagoya University, Nagoya, Japan

² Instituto Superior Técnico, Universidade de Lisboa, Lisboa, Portugal

References

- [1] Thorpe SA. The near-surface ocean mixing layer in stable heating conditions. *J. Geophys. Res.* 1978; 83:2875–2885. DOI: 10.1029/JC083iC06p02875
- [2] Mahrt L. Stratified atmospheric boundary layers. *Boundary-Layer Meteorol.* 1999; 90:375–396. DOI: 10.1023/A:1001765727956

- [3] Corrsin S, Kistler AL. Free-stream boundaries of turbulent flows. NACA Technical Report No. TN-1244; 1955. DOI: 19930092246
- [4] Taveira RR, da Silva CB. Characteristics of the viscous superlayer in shear free turbulence and in planar turbulent jets. *Phys. Fluids* 2014;26:021702. DOI: 10.1063/1.4866456
- [5] Bisset DK, Hunt JCR, Rogers MM. The turbulent/non-turbulent interface bounding a far wake. *J. Fluid Mech.* 2002;451:383–410. DOI: 10.1017/S0022112001006759.
- [6] da Silva CB, Hunt JCR, Eames I, Westerweel J. Interfacial layers between regions of different turbulence intensity. *Annu. Rev. Fluid Mech.* 2014;46:567–590. DOI: 10.1146/annurev-fluid-010313-141357
- [7] van Reeuwijk M, Holzner M. The turbulence boundary of a temporal jet. *J. Fluid Mech.* 2014;739:254–275. DOI: 10.1017/jfm.2013.613
- [8] Watanabe T, Sakai Y, Nagata K, Ito Y, Hayase T. Turbulent mixing of passive scalar near turbulent and non-turbulent interface in mixing layers. *Phys. Fluids* 2015;27:085109. DOI: 10.1063/1.4928199
- [9] Westerweel J, Fukushima C, Pedersen JM, Hunt JCR. Mechanics of the turbulent-nonturbulent interface of a jet. *Phys. Rev. Lett.* 2005;95:174501. DOI: 10.1103/PhysRevLett.95.174501
- [10] Townsend AA. *The Structure of Turbulent Shear Flow*. Cambridge University Press; Cambridge 1976.
- [11] Philip J, Meneveau C, de Silva CM, Marusic I. Multiscale analysis of fluxes at the turbulent/non-turbulent interface in high Reynolds number boundary layers. *Phys. Fluids* 2014;26:015105. DOI: 10.1063/1.4861066
- [12] Holzner M, Lüthi B. Laminar superlayer at the turbulence boundary. *Phys. Rev. Lett.* 2011;106:134503. DOI: 10.1103/PhysRevLett.106.134503
- [13] Wolf M, Lüthi B, Holzner M, Krug D, Kinzelbach W, Tsinober A. Investigations on the local entrainment velocity in a turbulent jet. *Phys. Fluids* 2012;24:105110. DOI: 10.1063/1.4761837
- [14] Wolf M, Holzner M, Lüthi B, Krug D, Kinzelbach W, Tsinober A. Effects of mean shear on the local turbulent entrainment process. *J. Fluid Mech.* 2013;731:95–116. DOI: 10.1017/jfm.2013.365
- [15] de Silva CM, Philip J, Chauhan K, Meneveau C, Marusic I. Multiscale geometry and scaling of the turbulent-nonturbulent interface in high Reynolds number boundary layers. *Phys. Rev. Lett.* 2013;111:044501. DOI: 10.1103/PhysRevLett.111.044501
- [16] Deo RC, Nathan GJ, Mi J. Similarity analysis of the momentum field of a subsonic, plane air jet with varying jet-exit and local Reynolds numbers. *Phys. Fluids* 2013;25:015115. DOI: 10.1063/1.4776782

- [17] Holzner M, Liberzon A, Nikitin N, Lüthi B, Kinzelbach W, Tsinober A. A Lagrangian investigation of the small-scale features of turbulent entrainment through particle tracking and direct numerical simulation. *J. Fluid Mech.* 2008;598:465–475. DOI: 10.1017/S0022112008000141
- [18] Taveira RR, Diogo JS, Lopes DC, da Silva CB. Lagrangian statistics across the turbulent-nonturbulent interface in a turbulent plane jet. *Phys. Rev. E* 2013;88:043001. DOI: 10.1103/PhysRevE.88.043001
- [19] Watanabe T, da Silva CB, Sakai Y, Nagata K, Hayase T. Lagrangian properties of the entrainment across turbulent/non-turbulent interface layers. *Phys. Fluids* 2016;28:031701. DOI: 10.1063/1.4942959
- [20] Morinishi Y, Lund TS, Vasilyev OV, Moin P. Fully conservative higher order finite difference schemes for incompressible flow. *J. Comput. Phys.* 1998;143:90–124. DOI: 10.1006/jcph.1998.5962
- [21] Kempf A, Klein M, Janicka J. Efficient generation of initial-and inflow-conditions for transient turbulent flows in arbitrary geometries. *Flow Turbul. Combust.* 2005;74:67–84. DOI: 10.1007/s10494-005-3140-8
- [22] Watanabe T, Sakai Y, Nagata K, Terashima O. Experimental study on the reaction rate of a second-order chemical reaction in a planar liquid jet. *AIChE J.* 2014;60:3969–3988. DOI: 10.1002/aic.14610
- [23] Bell JH, Mehta RD. Development of a two-stream mixing layer from tripped and untripped boundary layers. *AIAA J.* 1990;28:2034–2042. DOI: 10.2514/3.10519
- [24] Tanahashi M, Iwase S, Miyauchi T. Appearance and alignment with strain rate of coherent fine scale eddies in turbulent mixing layer. *J. Turbulence* 2001;2:1–18. DOI: 10.1088/1468-5248/2/1/006
- [25] Kitamura T, Nagata K, Sakai Y, Sasoh A, Terashima O, Saito H, Harasaki T. On invariants in grid turbulence at moderate Reynolds numbers. *J. Fluid Mech.* 2014;738:378–406. DOI: 10.1017/jfm.2013.595
- [26] Uberoi MS, Freymuth P. Turbulent energy balance and spectra of the axisymmetric wake. *Phys. Fluids* 1970;13:2205–2210. DOI: 10.1063/1.1693225
- [27] Attili A, Cristancho JC, Bisetti F. Statistics of the turbulent/non-turbulent interface in a spatially developing mixing layer. *J. Turbulence* 2014;15:555–568. DOI: 10.1080/14685248.2014.919394
- [28] da Silva CB, Taveira RR. The thickness of the turbulent/nonturbulent interface is equal to the radius of the large vorticity structures near the edge of the shear layer. *Phys. Fluids* 2010;22:121702. DOI: 10.1063/1.3527548
- [29] Smyth WD. Dissipation-range geometry and scalar spectra in sheared stratified turbulence. *J. Fluid Mech.* 1999;401:209–242. DOI: 10.1017/S0022112099006734

- [30] Tsinober A. An informal conceptual introduction to turbulence. ***Springer; Berlin 2009. DOI: 10.1007/978-90-481-3174-7
- [31] Yang Y, Wang J, Shi Y, Xiao Z, He XT, and Chen S. Acceleration of passive tracers in compressible turbulent flow. *Phys. Rev. Lett.* 2013;110:064503. DOI: 10.1103/PhysRevLett.110.064503
- [32] Batchelor GK. The application of the similarity theory of turbulence to atmospheric diffusion. *Q. J. R. Meteorol. Soc.* 1950;76:133–146. DOI: 10.1002/qj.49707632804
- [33] Watanabe T, Sakai Y, Nagata K, Ito Y, Hayase T. Vortex stretching and compression near the turbulent/nonturbulent interface in a planar jet. *J. Fluid Mech.* 2014;758:754–785. DOI: 10.1017/jfm.2014.559
- [34] Salazar JPLC, Collins LR. Two-particle dispersion in isotropic turbulent flows. *Annu. Rev. Fluid Mech.* 2009;41:405–432. DOI: 10.1146/annurev.fluid.40.111406.102224
- [35] Davidson PA. *Turbulence: An Introduction for Scientists and Engineers.* Oxford ***University Press; Oxford 2004.
- [36] Larcheveque M, Lesieur M. The application of eddy-damped Markovian closures to the problem of dispersion of particle pairs. *J. Méc.* 1981;20:113–134. DOI: 10.1007/978-3-540-32603-8_44
- [37] Nelkin M, Kerr RM. Decay of scalar variance in terms of a modified Richardson law for pair dispersion. *Phys. Fluids* 1981;24:1754–1756. DOI: 10.1063/1.863597
- [38] da Silva CB, dos Reis RJN, Pereira JCF. The intense vorticity structures near the turbulent/non-turbulent interface in a jet. *J. Fluid Mech.* 2011;685:165–190. DOI: 10.1017/jfm.2011.296
- [39] Soria J, Sondergaard R, Cantwell BJ, Chong MS, Perry AE. A study of the fine-scale motions of incompressible time-developing mixing layers. *Phys. Fluids* 1994;6:871–884. DOI: 10.1063/1.868323
- [40] Blackburn HM, Mansour NN, Cantwell BJ. Topology of fine-scale motions in turbulent channel flow. *J. Fluid Mech.* 1996;310:269–292. DOI: 10.1017/S0022112096001802
- [41] Zhou Y, Nagata K, Sakai Y, Suzuki H, Ito Y, Terashima O, Hayase T. Development of turbulence behind the single square grid. *Phys. Fluids* 2014;26:045102. DOI: 10.1063/1.4870167

Simulation of Axisymmetric Flows with Swirl in Vorticity-Stream Function Variables Using the Lattice Boltzmann Method

Omar D. Lopez, Sergio Pedraza and Jose R. Toro

Additional information is available at the end of the chapter

<http://dx.doi.org/10.5772/65650>

Abstract

In the present work, a Lattice Boltzmann formulation in vorticity-stream function variables is proposed for axisymmetric flows with swirl. For this purpose, several source terms are proposed and implemented. Although containing velocity gradients, these sources are in the Lattice Boltzmann framework and fulfill the Euler and Navier-Stokes equations in their conservative form. The main characteristics of the proposed method are: First, the momentum equation is solved using a unified Lattice Boltzmann solver; second, the proposed sources are consistent with the nonviscous and viscous momentum equations; and third, the implemented method is second-order accurate in space. Numerical tests on the Taylor-Couette flow with finite aspect ratio of 3.8 and the lid-driven cylindrical cavity flow were carried out showing good agreement with numerical and experimental results found in the literature, evidencing the ability of the implemented method to solve axisymmetric flows with swirl. In the case of the lid-driven cylindrical cavity flow, the implemented method is able to correctly reproduce some qualitative characteristics of this flow such as the vortex breakdown close to the cavity axis at different Reynolds numbers and cavity aspect ratio.

Keywords: Lattice Boltzmann method, vorticity-stream function, axisymmetric flow with swirl, lid-driven cylindrical cavity, source terms

1. Introduction

The Lattice Boltzmann method (LBM) was created in the late 1980s as a derivation of the Lattice Gas Automata (LGA). This method has shown to be an efficient solver not only for the Navier-

Stokes (NS) equations but also for some other nonlinear partial differential equations [1]. In several cases, LBM has been used for the solution of axisymmetric flows, modeling the problem in two dimension (2D) [2–7] and three dimension (3D) [8–10].

Although it is well known that axisymmetric flows can be mathematically described as a 2D problem, considering the governing equations in a cylindrical coordinate form, there is an inherent discrepancy between the cylindrical behavior of the flow and the two dimensional spatial discretization (i.e., the type of lattice used). In order to overcome these discrepancies, Halliday et al. [11] included position and time-dependent sources in the Lattice Boltzmann evolution equation to achieve the proper evolution equations through the Chapman-Enskog methodology. Subsequent studies have successfully used this idea to improve the Lattice Boltzmann method in order to solve different axisymmetric flows with or without swirl. Huang et al. [12] proposed a hybrid Lattice Boltzmann finite-difference axisymmetric formulation where the planar velocities were solved through a pressure-velocity ($p-v$) LBM. The azimuthal component through a finite-difference scheme was solved by inserting source terms into the two-dimensional Lattice Boltzmann equation. In order to avoid the use of different frameworks and solving every momentum equation within the LBM approach, Guo et al. [13] proposed a simple and straightforward incorporation of source terms in a LB $p-v$ formulation. This way, they were able to predict steady and unsteady axisymmetric flows starting from the general Lattice Boltzmann equation. Li et al. [4] proposed an improved axisymmetric Lattice Boltzmann scheme where a multiple relaxation time (MRT) collision model was used to insert source terms that contained no velocity gradients. The same approach was also explained and implemented by Zhou [5]. Regarding LBM formulations in vorticity-stream function, Chen et al. [14] developed an axisymmetric Lattice Boltzmann formulation without swirl considering vorticity and the stream-function as its primitive variables. Improvements were made coupling a thermal LBM [15] and finally proposing an axisymmetric formulation [16, 17].

In the present work, different source terms are proposed for the Lattice Boltzmann implementation of axisymmetric flows with swirl. Although containing velocity gradients, these sources are in the Lattice Boltzmann framework and fulfill the Euler and NS equations in their conservative form. This implementation is tested with some flows such as the lid-driven cylindrical cavity flow: a benchmark case for axisymmetric flow solvers, deeply studied both numerically [18–20] and experimentally [21]. The main characteristic of the lid-driven cylindrical cavity flow is that for certain Reynolds number (Re) and cavity aspect ratio (Ar), it can undergo structural changes such as vortex breakdowns that are triggered by azimuthal vorticity stretching and its interaction with the azimuthal velocity [20, 22].

2. Axisymmetric Lattice Boltzmann implementation

2.1. Governing equations

Let $\vec{v}(r, z, t) = u_r \hat{e}_r + u_\theta \hat{e}_\theta + u_z \hat{e}_z$ be the velocity field of an axisymmetric, viscous flow with swirl with the corresponding vorticity ($\vec{\omega}$) defined as shown in Eq. (1)

$$\vec{\omega} = -\frac{\partial u_\theta}{\partial z} \hat{e}_r + \omega_\theta(r, z, t) \hat{e}_\theta + \frac{1}{r} \frac{\partial(r u_\theta)}{\partial r} \hat{e}_z \quad (1)$$

For such flows, the 3D Navier-Stokes equations are equivalent to the following simplified vorticity-stream function formulation

$$\frac{\partial u_\theta}{\partial t} + \nabla \cdot (\vec{u} u_\theta) = -2u_r \frac{u_\theta}{r} + \nu \left[\frac{\partial^2 u_\theta}{\partial r^2} + \frac{\partial^2 u_\theta}{\partial z^2} + \frac{1}{r} \frac{\partial u_\theta}{\partial r} - \frac{u_\theta}{r^2} \right] \quad (2)$$

$$\frac{\partial \omega_\theta}{\partial t} + \nabla \cdot (\vec{u} \omega_\theta) = 2 \frac{u_\theta}{r} \frac{\partial u_\theta}{\partial z} + \nu \left[\frac{\partial^2 \omega_\theta}{\partial r^2} + \frac{\partial^2 \omega_\theta}{\partial z^2} + \frac{1}{r} \frac{\partial \omega_\theta}{\partial r} - \frac{\omega_\theta}{r^2} \right] \quad (3)$$

$$\omega_\theta = -\frac{1}{r} \frac{\partial^2 \psi}{\partial z^2} - \frac{\partial}{\partial r} \left(\frac{1}{r} \frac{\partial \psi}{\partial r} \right) \quad (4)$$

$$u_r = -\frac{1}{r} \frac{\partial \psi}{\partial z} \quad u_z = \frac{1}{r} \frac{\partial \psi}{\partial r} \quad (5)$$

where $\vec{u} = (u_r, u_z)$. The definition of the velocity in terms of the stream function ψ fulfills the continuity equation $\nabla \cdot \vec{u} = 0$. Note that the convective terms of these governing equations are written in a conservative form in order to match the operators achieved by the numerical discretization based on LBM.

2.2. Numerical method

The discrete Lattice Boltzmann equation (LBE) is given by

$$f_i(\mathbf{x} + \mathbf{e}_i \Delta t, t + \Delta t) - f_i(\mathbf{x}, t) = \Omega_i(f_i(\mathbf{x}, t)) \quad (6)$$

where f_i is the particle distribution function along the i th direction, \mathbf{e}_i is a vector in the direction of the microscopic velocities and $\Omega_i(f_i(x, t))$ is the collision operator. Δx and Δt are space and time increments, and $\Delta x / \Delta t = |\mathbf{e}_i| = c$ is the magnitude of the microscopic velocity. Employing a second-order Taylor expansion on the convective part (LHS of Eq. (6)) and using the BGK approximation of the collision operator $\Omega_i(f_i(x, t))$, Eq. (7) is achieved.

$$(\partial_t + \nabla \cdot \mathbf{e}_i) f_i + \frac{1}{2} (\partial_t^2 + 2\partial_t \nabla \cdot \mathbf{e}_i + \nabla \nabla : \mathbf{e}_i \mathbf{e}_i) f_i = -\frac{1}{\tau} [f_i - f_i^{eq}] \quad (7)$$

where τ is the dimensionless relaxation time of the distribution function f_i and f_i^{eq} is the equilibrium function distribution. Using the Chapman-Enskog expansion, the distribution function f_i is expanded as

$$f_i = f_i^{(0)} + \varepsilon f_i^{(1)} + \varepsilon^2 f_i^{(2)} + \dots \quad (8)$$

where ε is a formal parameter in the expansion that allows to keep track of different orders of magnitude. It will be considered only as a *label* and will be dropped out of the final results setting $\varepsilon = 1$ [23]. The time and space derivatives are also expanded in terms of ε as shown in Eqs. (9) and (10).

$$\partial_t = \varepsilon \partial_t^{(1)} + \varepsilon^2 \partial_t^{(2)} \quad (9)$$

$$\partial_x = \varepsilon \partial_x^{(1)} \quad (10)$$

According to Wolf-Gladrow [23], the reasons behind the different expansions in time and space lie in the fact that different macroscopic processes such as convection and diffusion can be distinguished by their time scales but act on similar spatial scales. Replacing Eq. (8) through Eq. (10) in Eq. (7), Eq. (11) is obtained

$$D_i(f_i^{(0)} + \varepsilon f_i^{(1)}) + \frac{1}{2} D_i^2(f_i^{(0)} + \varepsilon f_i^{(1)}) = -\frac{1}{\tau} [f_i^{(0)} + \varepsilon f_i^{(1)} - f_i^{eq}] \quad (11)$$

where $D_i = \varepsilon \partial_t^{(1)} + \varepsilon^2 \partial_t^{(2)} + \varepsilon \partial_x^{(1)} \cdot \mathbf{e}_i$ is the total derivative operator expanded through ε . Finally, source terms (h_i) are included in the RHS of Eq. (11) in order to fulfill the momentum equations constraints where $h_i^{(0)}$ and $h_i^{(2)}$ are the expansion of h_i in terms of ε .

$$D_i(f_i^{(0)} + \varepsilon f_i^{(1)}) + \frac{1}{2} D_i^2(f_i^{(0)} + \varepsilon f_i^{(1)}) = -\frac{1}{\tau} [f_i^{(0)} + \varepsilon f_i^{(1)} - f_i^{eq}] + \varepsilon h_i^{(1)} + \varepsilon^2 h_i^{(2)} \quad (12)$$

According to the expansion in Eq. (12), every time scale is grouped starting with the terms of order $O(1)$

$$f_i^{(0)} = f_i^{eq} \quad (13)$$

followed by terms of order $O(\varepsilon)$

$$\partial_t^{(1)} f_i^{(0)} + (\partial_x^{(1)} \cdot \mathbf{e}_i) f_i^{(0)} = -\frac{1}{\tau} f_i^{(1)} + h_i^{(1)} \quad (14)$$

and finally the terms of order $O(\varepsilon^2)$

$$\begin{aligned} \partial_t^{(2)} f_i^{(0)} + \frac{1}{2} (\partial_t^{(1)})^2 f_i^{(0)} + \partial_t^{(1)} (\partial_x^{(1)} \cdot \mathbf{e}_i) f_i^{(0)} + \frac{1}{2} (\partial_x^{(1)} \partial_x^{(1)} : (\mathbf{e}_i)_\alpha (\mathbf{e}_i)_\beta) f_i^{(0)} \\ + \partial_t^{(1)} f_i^{(1)} + (\partial_x^{(1)} \cdot \mathbf{e}_i) f_i^{(1)} = \frac{1}{\tau} f_i^{(2)} + h_i^{(2)}. \end{aligned} \quad (15)$$

where $(\mathbf{e}_i)_\alpha$ is the component of the velocity vector \mathbf{e}_i on the α -coordinate direction.

2.3. Lattice

The D2Q5 lattice model (two dimensions and five directions) has shown to be adequate for advection-diffusion problems based on its easy implementation and its inherent orthogonality ($\mathbf{e}_i \mathbf{e}_j = \delta_j^i$) [14–17, 24]. The D2Q5 model has discrete velocity directions given by Eq. (16)

$$\mathbf{e}_i = c \times \begin{cases} \vec{0} & i = 0, \\ [\cos(i-1)\pi/2, \sin(i-1)\pi/2] & i \neq 0. \end{cases} \quad (16)$$

Considering the evolution equations as the main purpose of our discretization, the equilibrium functions are defined for u_θ and ω_θ as

$$f_i^{eq} = \frac{u_\theta}{5} \left[1 + \frac{\vec{u} \cdot \mathbf{e}_i}{c_s^2} \right] \quad (17)$$

$$g_i^{eq} = \frac{\omega_\theta}{5} \left[1 + \frac{\vec{u} \cdot \mathbf{e}_i}{c_s^2} \right] \quad (18)$$

where $c_s = |c| \sqrt{2/5}$ is the speed of sound in the lattice. These equilibrium functions fulfill the lattice constraints: $\sum_{i=0}^4 f_i = u_\theta$, $\sum_{i=0}^4 f_i \mathbf{e}_i = u_\theta \vec{u}$ and $\sum_{i=0}^4 \mathbf{e}_i \mathbf{e}_i f_i = c_s^2 u_\theta$ for u_θ . The same holds for ω_θ replacing f_i by g_i .

2.4. Recovery of the governing equations

In order to recover the governing equations, zeroth and first moments are taken to Eqs. (14) and (15). Defining $H^{(l)} = \sum_{i=0}^4 h_i^{(l)}$ for $l = 1, 2$ and the fact that $\sum_{i=0}^4 f_i^{(k)} = 0$ for $k \geq 1$ (see reference [24]) the zeroth moment of Eq. (14) produces Eq. (19), while the zeroth moment of Eq. (15) produces Eq. (20).

$$\partial_t^{(1)} u_\theta + \partial_x^{(1)} \cdot (\bar{u} u_\theta) = H^{(1)} \quad (19)$$

$$\begin{aligned} \partial_x^{(1)} \cdot \left(\sum_{i=0}^4 f_i^{(1)} \mathbf{e}_i \right) + \frac{1}{2} \left(2\partial_t^{(2)} u_\theta + \partial_t^{(1)} \partial_t^{(1)} u_\theta \right. \\ \left. + 2\partial_t^{(1)} \partial_x^{(1)} \cdot (\bar{u} u_\theta) + c_s^2 \partial_x^{(1)} \partial_x^{(1)} u_\theta \right) = H^{(2)} \end{aligned} \quad (20)$$

The first term on the LHS of Eq. (20) is rewritten with the first moment of Eq. (14)

$$\sum_{i=0}^4 f_i^{(1)} \mathbf{e}_i = \tau \left(\sum_{i=0}^4 h_i^{(1)} \mathbf{e}_i - \partial_t^{(1)} (\bar{u} u_\theta) - c_s^2 \partial_x^{(1)} u_\theta \right) \quad (21)$$

which is replaced into Eq. (20) and produces

$$\begin{aligned} \tau \partial_x^{(1)} \cdot \left(\sum_{i=0}^4 h_i^{(1)} \mathbf{e}_i - \partial_t^{(1)} (\bar{u} u_\theta) - c_s^2 \partial_x^{(1)} u_\theta \right) + \frac{1}{2} \left(2\partial_t^{(2)} u_\theta \right. \\ \left. + \partial_t^{(1)} \partial_t^{(1)} u_\theta + 2\partial_t^{(1)} \partial_x^{(1)} (\bar{u} u_\theta) + c_s^2 \partial_x^{(1)} \partial_x^{(1)} u_\theta \right) = H^{(2)} \end{aligned} \quad (22)$$

The second time derivative over u_θ on the LHS of Eq. (22), i.e., $\partial_t^{(1)} \partial_t^{(1)} u_\theta$, is rewritten by taking ∂_t on Eq. (19) as follows:

$$\partial_t^{(1)} (\partial_t^{(1)} u_\theta) = \sum_{i=0}^4 \partial_t^{(1)} h_i^{(1)} - \partial_x^{(1)} \cdot (\bar{u} u_\theta) \quad (23)$$

Replacing Eq. (23) into Eq. (22) leads to

$$\begin{aligned} \tau \partial_x^{(1)} \cdot \left(\sum_{i=0}^4 h_i^{(1)} \mathbf{e}_i - \partial_t^{(1)} (\bar{u} u_\theta) - c_s^2 \partial_x^{(1)} u_\theta \right) + \frac{1}{2} \left(2\partial_t^{(2)} u_\theta + \sum_{i=0}^4 \partial_t^{(1)} h_i^{(1)} \right. \\ \left. - \partial_t^{(1)} \partial_x^{(1)} (\bar{u} u_\theta) + 2\partial_t^{(1)} \partial_x^{(1)} (v u_\theta) + c_s^2 \partial_x^{(1)} \partial_x^{(1)} u_\theta \right) = H^{(2)} \end{aligned} \quad (24)$$

Finally, the source terms are redefined in order to eliminate the time derivative of the source within the evolution equation [25].

$$h_i = \varepsilon h_i^{(1)} + \varepsilon^2 (h_i^{(2)} + \frac{1}{2} \partial_{t_i} h_i^{(1)}) \tag{25}$$

Equation (25) combined with Eqs. (19) and (24) produces the momentum equation for u_θ

$$\begin{aligned} \partial_t u_\theta + \varepsilon \partial_x^{(1)} \cdot (\bar{u} u_\theta) + \varepsilon^2 \left(\tau \partial_x^{(1)} \cdot \sum_{i=0}^4 h_i^{(1)} \mathbf{e}_i + \right. \\ \left. \left(\frac{1}{2} - \tau \right) \left(\partial_t^{(1)} \partial_x^{(1)} \cdot (\bar{u} u_\theta) + c_s^2 \partial_x^{(1)} \partial_x^{(1)} u_\theta \right) \right) = \varepsilon H^{(1)} + \varepsilon^2 H^{(2)} \end{aligned} \tag{26}$$

The same procedure is applied to ω_θ replacing f_i by g_i obtaining an equation similar to Eq. (26) but in terms of ω_θ .

$$\begin{aligned} \partial_t \omega_\theta + \varepsilon \partial_x^{(1)} \cdot (\bar{u} \omega_\theta) + \varepsilon^2 \left(\tau \partial_x^{(1)} \cdot \sum_{i=0}^4 h_i^{(1)} \mathbf{e}_i + \right. \\ \left. \left(\frac{1}{2} - \tau \right) \left(\partial_t^{(1)} \partial_x^{(1)} \cdot (\bar{u} \omega_\theta) + c_s^2 \partial_x^{(1)} \partial_x^{(1)} \omega_\theta \right) \right) = \varepsilon H^{(1)} + \varepsilon^2 H^{(2)} \end{aligned} \tag{27}$$

Comparing Eqs. (26) and (27) with Eqs. (2) and (3) it is observed that the terms $\partial_t^{(1)} \partial_x^{(1)} \cdot (\bar{u} u_\theta)$ and $\partial_t^{(1)} \partial_x^{(1)} \cdot (\bar{u} \omega_\theta)$ have to be neglected in order to match both momentum equations. An order analysis is done for these terms assuming U_c , L_c and t_c as the characteristic velocity, length, and time scales, respectively. Considering Eq. (27) for azimuthal vorticity, the term $\partial_t^{(1)} \partial_x^{(1)} \cdot (\bar{u} \omega_\theta)$ is the same order of $U_c / t_c^2 L_c$ and the term $c_s^2 \partial_x^{(1)} \partial_x^{(1)} \omega_\theta$ is the same order of $c_s^2 / L_c t_c$. Taking the ratio of the order of the latter terms, we obtain

$$O\left(\frac{\partial_t^{(1)} \partial_x^{(1)} \cdot (\bar{u} \omega_\theta)}{c_s^2 \partial_x^{(1)} \partial_x^{(1)} \omega_\theta}\right) = O\left(\frac{U_c / t_c^2 L_c}{c_s^2 / L_c t_c}\right) = O\left(\frac{U_c^2}{c_s^2}\right) = O(M^2) \tag{28}$$

where $M = U_c / c_s$ is the Mach number of the lattice. Eq. (28) shows that the term $\partial_t^{(1)} \partial_x^{(1)} \cdot (\bar{u} \omega_\theta)$ is very small compared with $c_s^2 \partial_x^{(1)} \partial_x^{(1)} \omega_\theta$ and it can be neglected if $M \ll 1$, according to the LBM dynamics. This procedure is also valid for the azimuthal velocity leading to neglect the term $\partial_t^{(1)} \partial_x^{(1)} \cdot (\bar{u} u_\theta)$.

After the order analysis is performed, Eqs. (26) and (27) are rewritten as

$$\begin{aligned} \partial_t u_\theta + \varepsilon \partial_x^{(1)} \cdot (\bar{u} u_\theta) + \varepsilon^2 \left(\bar{w} \partial_x^{(1)} \cdot \sum_{i=0}^4 h_i^{(1)} \mathbf{e}_i + \right. \\ \left. \left(\frac{1}{2} - \tau \right) c_s^2 \partial_x^{(1)} \partial_x^{(1)} u_\theta \right) = \varepsilon H^{(1)} + \varepsilon^2 H^{(2)} \end{aligned} \quad (29)$$

$$\begin{aligned} \partial_t \omega_\theta + \varepsilon \partial_x^{(1)} \cdot (\bar{u} \omega_\theta) + \varepsilon^2 \left(\bar{w} \partial_x^{(1)} \cdot \sum_{i=0}^4 h_i^{(1)} \mathbf{e}_i + \right. \\ \left. \left(\frac{1}{2} - \tau \right) c_s^2 \partial_x^{(1)} \partial_x^{(1)} \omega_\theta \right) = \varepsilon H^{(1)} + \varepsilon^2 H^{(2)} \end{aligned} \quad (30)$$

2.5. Source definition

As it was stated in the introduction, there exists a discrepancy between the lattice dimension and the dimensional nature of the flow. The discrepancy arises in the operators achieved through the multiscale analysis (Cartesian) and those that are natural to the momentum equations (cylindrical). As shown in the RHS of Eq. (31), there is an additional derivative that contains the swirl of the flow which is not captured by the operators achieved through the multiscale analysis.

$$\frac{D}{Dt_{car}} = \frac{\partial}{\partial t} + u_r \frac{\partial}{\partial r} + u_z \frac{\partial}{\partial z} \neq \frac{\partial}{\partial t} + u_r \frac{\partial}{\partial r} + u_z \frac{\partial}{\partial z} + u_\theta \frac{\partial}{\partial \theta} = \frac{D}{Dt_{cyl}} \quad (31)$$

In order to overcome this problem, the inclusion of a source terms is needed and therefore defined to match the governing equations, Eqs. (2, 3) with Eqs. (29, 30).

Consequently, the source terms for u_θ are defined as

$$h_i^{(1)} \equiv -t_i 2u_r \frac{u_\theta}{r} \quad \text{and} \quad h_i^{(2)} \equiv t_i \left(\tau - \frac{1}{2} \right) c_s^2 \left[\frac{1}{r} \frac{\partial u_\theta}{\partial r} - \frac{u_\theta}{r^2} \right] \quad (32)$$

and for ω_θ as

$$h_i^{(1)} \equiv t_i 2 \frac{u_\theta}{r} \frac{\partial u_\theta}{\partial z} \quad \text{and} \quad h_i^{(2)} \equiv t_i \left(\tau - \frac{1}{2} \right) c_s^2 \left[\frac{1}{r} \frac{\partial \omega_\theta}{\partial r} - \frac{\omega_\theta}{r^2} \right] \quad (33)$$

where $\sum_{i=0}^4 t_i = 1$ and $\tau = \nu / c_s^2 + 1/2$.

The source terms of $O(\varepsilon)$ were defined, both for u_θ and ω_θ , in order to reproduce the Euler equations in their conservative form. Then, the terms of $O(\varepsilon^2)$ were defined in order to reproduce the cylindrical terms of the Laplacian operator that appears in Eqs. (2) and (3).

Finally, due to the symmetries of the lattice, the term $\partial_x^{(1)} \cdot \sum_{i=0}^4 h_i^{(1)} \mathbf{e}_i$ is eliminated in Eqs. (29) and (30) since $\sum_{i=0}^4 h_i^{(1)} \mathbf{e}_i = 0$.

3. LBM algorithm

This section describes the algorithm used to solve every Lattice Boltzmann evolution equation within the same framework producing a LBM solver able to solve axisymmetric flows. The implementation of the algorithm is based on the key steps in LBM: streaming and collision that are given by Eq (6).

3.1. Poisson equation solver

In order to solve Eq. (4), which is a Poisson equation for ψ , the model proposed by Chai et al. [26] is employed. The evolution equation is given by

$$L_i(t + \Delta t, x + \Delta x) - L_i(t, x) = -\frac{1}{\tau_\psi} [L_i(t, x) - L_i^{eq}(t, x)] + S \Delta t \bar{\psi}_i c^2 (0.5 - \tau_\psi) / 2 \quad (34)$$

where L is the distribution function associated with ψ and S accounts for the source terms. τ_ψ is the dimensionless relaxation time that is set with accurate results to 1 [26]. $\bar{\psi}_i$ is the weight coefficient for the source terms, and they must satisfy the constrain $\sum_{i=1}^4 \bar{\psi}_i = 1$. In the present study, the source term S is defined in Eq. (35)

$$S \equiv -r\omega_\theta + uz \quad (35)$$

and the equilibrium distribution is defined as in Eq. (36)

$$L_i^{eq}(x, t) = \begin{cases} -\psi(x, t), & i = 0 \\ \frac{1}{4}\psi(x, t), & i = 1, 2, 3, 4 \end{cases} \quad (36)$$

where $\psi(x, t) = \sum_{i=1}^4 L_i(x, t)$. u_r and u_z are calculated with Eq. (5), employing a central difference scheme in the lattice domain.

3.2. Algorithm

With every evolution equation discretized in the LBM framework, an algorithm of the method is finally proposed:

1. **Numerical parameters definition:** $Re, \Omega, R, Ar, N = (\text{Grid size})$.
2. **Initial and boundary conditions definition**
3. **Time loop until steady state is reached:**
 - a. $u_\theta^t \rightarrow \text{LBM solver} \rightarrow u_\theta^{t+\Delta t}$
 - b. $u_\theta^{t+\Delta t} \rightarrow \text{LBM solver} \rightarrow \omega_\theta^{t+\Delta t}$
 - c. $\omega_\theta^{t+\Delta t} \rightarrow \text{LBM solver} \rightarrow \psi^{t+\Delta t}$ until:

$$\frac{D\psi}{Dt} = \nabla^2 \psi + \omega_\theta \text{ tends to } \frac{D\psi}{Dt} = 0 \rightarrow \nabla^2 \psi = -\omega_\theta$$

- d. Computation of u_r and u_z .

3.2.1. LBM solver

As shown in the algorithm the time loop uses a unified Lattice-Boltzmann solver in which five steps are performed:

1. Equilibrium function calculation through Eqs. (17, 18, and 36).
2. Source term calculations through Eqs. (32, 33, and 35) using the information obtained at time t
3. Collision step for every particle function distribution.

$$\Omega_i(f_i(\mathbf{x}, t)) = -\frac{1}{\tau} [f_i - f_i^{eq}]$$

4. Streaming step for every particle function distribution.

$$f_i(\mathbf{x} + \mathbf{e}_i \Delta t, t + \Delta t) = \Omega_i(f_i(\mathbf{x}, t)) + f_i(\mathbf{x}, t)$$

5. Variable recover through the summation of the distribution functions, i.e., $\sum_{i=0}^4 f_i = u_\theta$
 $\sum_{i=0}^4 g_i = \omega_\theta$ and $\sum_{i=1}^4 L_i = \psi$.

As stated in the algorithm, the time loop is performed until the steady state is reached which numerically is considered when

$$\frac{\|u(t) - u(t - 1000\delta t)\|}{\|u(t)\|} < 10^{-7} \tag{37}$$

where the relative error of the velocity field is calculated between 1000 consecutive time steps.

4. Numerical results

In the present section, the proposed source terms are validated using some well-known benchmarks flows, including the circular Couette flow, the Taylor-Couette flow, and the swirling flow within the lid-driven cylindrical cavity. All cases were validated for a laminar regime. For each case, the boundary and initial conditions will be discussed.

4.1. Circular Couette flow

In this case, the flow between two infinitely long concentric cylinders is simulated. The inner cylinder rotates at constant speed Ω , while the outer is stationary (see **Figure 1**). The analytic solution of this flow is used to prove that the proposed method is second order. The boundary conditions for the fluid variables are as follows:

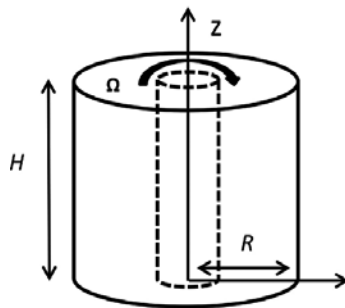


Figure 1. Configuration of the Circular Couette and Taylor-Couette Flow.

$$\begin{aligned} r = R_{in} : (u_r, u_\theta, u_z) &= (0, \Omega R_{in}, 0), \quad \omega_\theta = \nabla^2 \psi, \quad \psi = 0, \\ r = R_{out} : u_r = u_\theta = u_z &= 0, \quad \omega_\theta = \nabla^2 \psi, \quad \psi = 0. \end{aligned} \tag{38}$$

where the Laplacian of ψ on the boundaries is calculated using a second-order Taylor approximation employing the inner nodes values. Symmetry is imposed on the top and bottom boundaries.

Figure 2 compares the analytic solution with the numerical results for a laminar flow with $Re < 10$, inner cylinder's radius $R_{in} = 0.5m$ and angular velocity $\Omega_{in} = 0.2rad/s$, and outer cylinder's radius $R_{out} = 1m$ and angular velocity $\Omega_{out} = 0$. With these parameters, the analytic solution for this flow is given by Eq. (39)

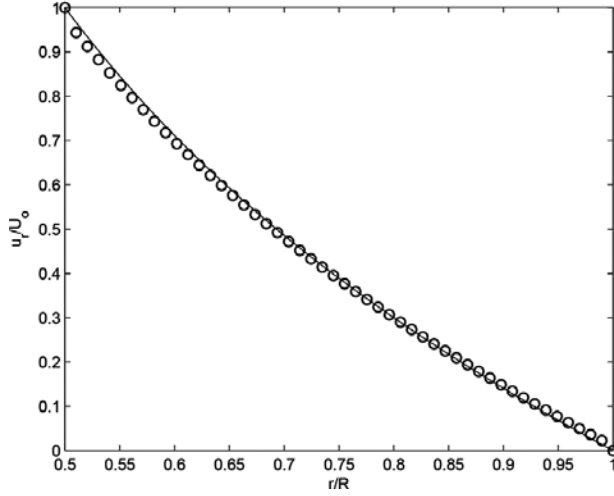


Figure 2. Azimuthal velocity comparison of the Circular Couette flow. (-): Analytical solution, (o): present LBM solution.

$$u_{\theta} = Ar + \frac{B}{r} \tag{39}$$

where

$$A = \frac{\Omega_{in} R_{in}^2 - \Omega_{out} R_{out}^2}{R_{in}^2 - R_{out}^2} = -0.0667 \quad \text{and} \quad B = R_{in}^2 R_{out}^2 \frac{\Omega_{in} - \Omega_{out}}{R_{out}^2 - R_{in}^2} = 0.0667.$$

Results were obtained with a lattice resolution of $\Delta x = (R_{out} - R_{in})/(N - 1)$, i.e., $N = 50$. It is clear that the numerical results are in good agreement with the analytical solution. The relative global error, defined by Eq. (40), is presented in **Figure 3** for different mesh sizes.

$$E = \|u_a - u_{LBM}\|_2 \tag{40}$$

In Eq. (40) u_{LBM} is the azimuthal velocity predicted by the present method. The slope of the fitting in **Figure 3** is 2.04, which shows that the proposed method is second-order accurate in space.

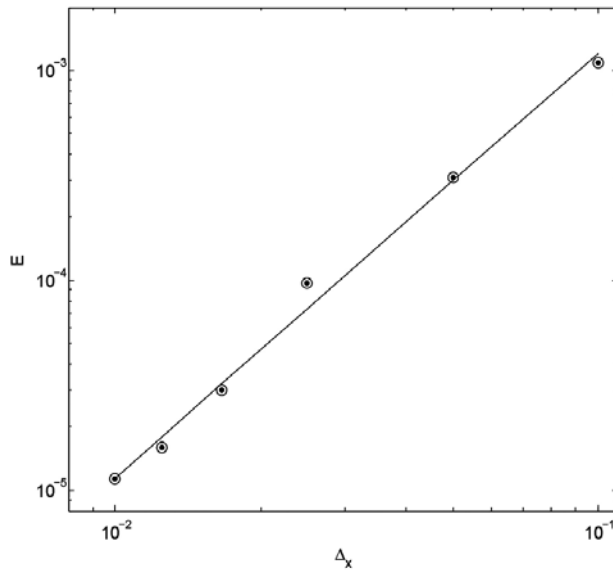


Figure 3. Convergence analysis. (–): least-square fitting with slope 2.04.

4.2. Taylor-Couette flow with finite aspect ratio

A Taylor-Couette flow consists of a viscous fluid confined between two concentric rotating cylinders of length $H = Ar(R_{out} - R_{in})$ with aspect ratio $Ar = 3.8$. The Reynolds number is defined as $Re = R_{in}\Omega_{in}A/\nu$, where Ω_{in} is the angular velocity of the inner cylinder and A is the gap of the annulus. In this case, the boundary conditions for z , due to the finite length, have to be specified, besides the boundary conditions for r used in the Circular Couette flow, as

$$\begin{aligned} z = 0: \quad \psi = u_z = 0, \quad \omega_\theta = \nabla^2\psi, \\ z = H: \quad \psi = u_z = 0, \quad \omega_\theta = \nabla^2\psi. \end{aligned} \tag{41}$$

Three different Re were simulated and analyzed; $Re = 85, 100$ and 150 . The maximum stream-function values in the $r - z$ plane are listed in **Table 1** and compared to those presented by Huang et al. [12]. There is a good agreement between the present formulation and the hybrid scheme demonstrating the versatility of the proposed numerical method.

Re	ψ_{max}	ψ_{max} [12]
85	4.32×10^{-2}	4.810×10^{-2}
	5.252×10^{-2}	5.501×10^{-2}
	6.38×10^{-2}	6.427×10^{-2}

Table 1. Maximum stream-function comparison for the (r, z) with the proposed results in [12].

In order to validate the qualitative characteristic of the flow in terms of axisymmetric toroidal vortices, **Figure 4** shows the contours of stream-function and vorticity for $Re = 150$ and $Ar = 3.8$. Similar flow patterns consistent with those reported by Huang et al. [12] are observed.

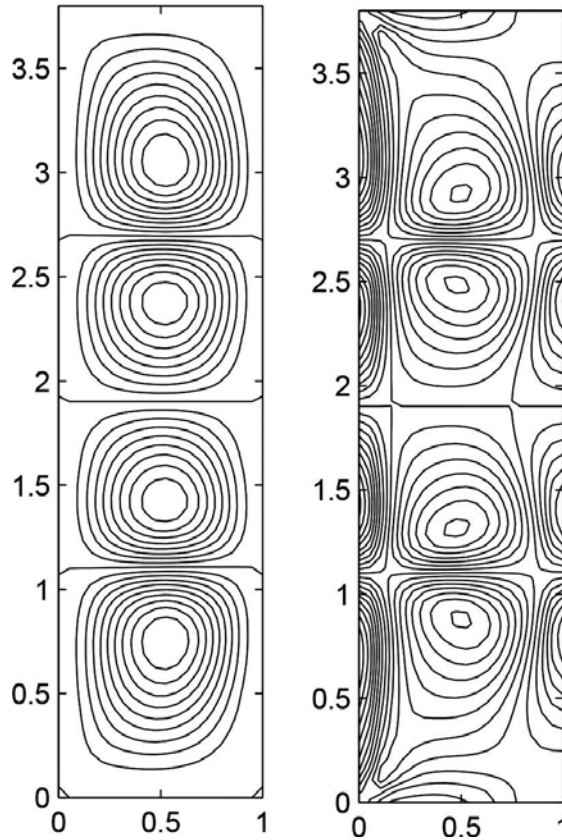


Figure 4. Contours of stream-function (left) and vorticity (right).

4.3. Lid-driven cylindrical cavity flow

Cylindrical cavity steady flow have been studied both numerically [9, 18] and experimentally [21]. One of the interesting features of this flow is that vortex breakdowns takes place within the cavity producing recirculating zones located in the cavity axis. In 1984, Escudier [21] was able to summarize the flow regimes in the *Escudier diagram* varying the Reynolds number $Re = R^2\Omega/\nu$ and the aspect ratio $Ar = H/R$ of the cavity. The flow problem consists of a cylinder with top and bottom walls, where the top wall rotates at a constant angular velocity (see **Figure 5**). Four cases were chosen from the Escudier diagram: Case 1 ($Ar = 1.5$, $Re = 990$), Case 2 ($Ar = 1.5$, $Re = 1290$), Case 3 ($Ar = 2.5$, $Re = 1010$), and Case 4 ($Ar = 2.5$, $Re = 2200$) in order to demonstrate the quantitative and qualitative accuracy of the present formulation.

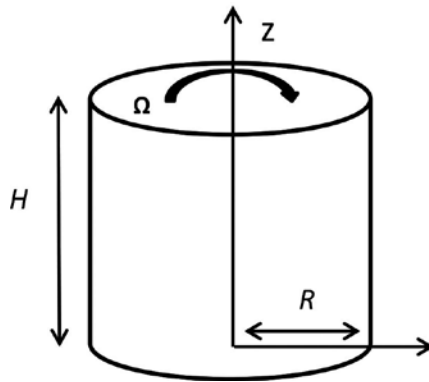


Figure 5. Configuration of the cylindrical cavity flow.

The parameters in the simulation were set to $R = 1$ and $\Omega = 0.1$, which makes the characteristic velocity $U_c = \Omega R = 0.1$ ensuring that $M = U_c / c_s^2 = 0.25 \ll 1$. The boundary conditions for the primitive variables are defined as

$$\begin{aligned}
 r = 0: & \quad u_r = u_\theta = 0 \quad \text{and} \quad \frac{\partial u_z}{\partial r} = 0, \quad \omega_\theta = 0, \quad \psi = 0 \\
 r = R: & \quad u_r = u_\theta = u_z = 0, \quad \omega_\theta = \nabla^2 \psi, \quad \psi = 0 \\
 z = 0: & \quad u_r = u_\theta = u_z = 0, \quad \omega_\theta = \nabla^2 \psi, \quad \psi = 0 \\
 z = H: & \quad u_r = u_z = 0, u_\theta = \Omega r, \quad \omega_\theta = \nabla^2 \psi, \quad \psi = 0
 \end{aligned}
 \tag{42}$$

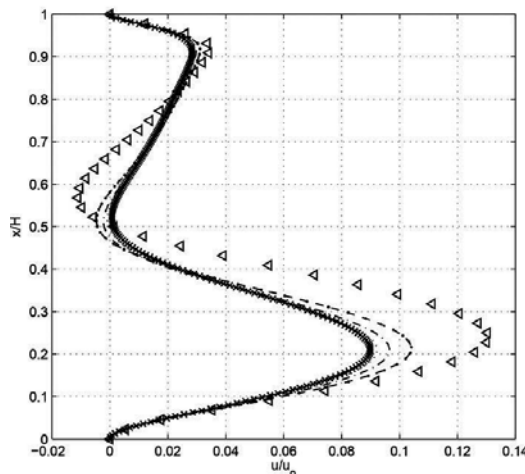


Figure 6. Normalized axial velocity u_z of Case 1 depending on mesh size: (x): 200×300 , (-): 150×225 , (): 100×150 , (- -): 70×105 , (- - -): 50×75 , (>): 30×45 .

In order to establish mesh independence in the solution, different grid sizes were used on the $r - z$ domain. Case 1 was simulated using the following meshes: 30×45 , 50×75 , 70×105 , 100×150 , 150×225 , 200×300 , and the results are shown in **Figure 6**. It is observed that the solution is independent if the grid size used is larger or equal to 150×225 . Based on this fact, it is believed that a lattice size of $\Delta x = R/150 = 0.0067$ will produce accurate solutions and will be used to simulate the other cases.

	$Re = 990$		$Re = 1290$		$Re = 1010$	
Reference	$u_{z,max}/u_0$	x_{max}/H	$u_{z,max}/u_0$	x_{max}/H	$u_{z,max}/u_0$	x_{max}/H
Present	0.0901	0.2098	0.0727	0.1696	0.1109	0.498
Expt.[27]	0.097	0.21	0.068	0.14	0.103	0.46
Zhou [5]	0.0992	0.207	0.0706	0.147	0.105	0.448
DLBM [9]	0.093	0.22	0.072	0.16	0.102	0.52
DNS [9]	0.099	0.19	0.0665	0.125	0.106	0.44
Li [4]	0.0987	0.213	0.0716	0.147		

Table 2. Comparisons of maximum axial velocities.

In order to verify the precision of the present method, the maximum axial velocity is compared with experimental data [27] and to numerical results proposed previously [3–5, 9] in steady state. Three of these numerical results were taken under consideration: Zhou [5] in which a LBM in p-v is employed, Bhaumik et al. [9] results in which a 3DLBM using MRT is employed, and the improved model results proposed by Li et al. [4]. Also a DNS solution is considered [9].

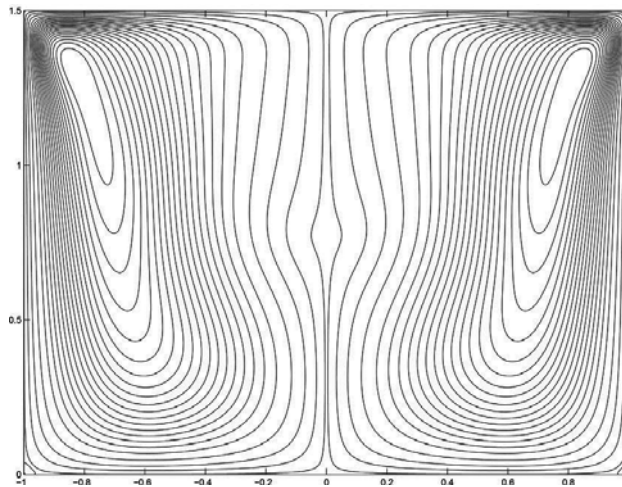


Figure 7. Stream function contours for Case 1: $Re = 990$ and $Ar = 1.5$ (y -coordinate corresponds to Z and x -coordinate to R).

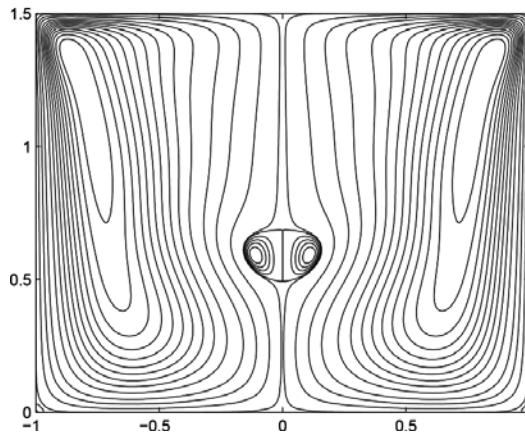


Figure 8. Stream function contours for Case 2: $Re = 1290$ and $Ar = 1.5$ (y -coordinate corresponds to Z and x -coordinate to R).

The maximum axial velocities for Cases 1, 2, and 3 are shown in **Table 2**, comparing the solution of the present model with previous reported results. The relative error is calculated as $(u_{present} - u_{exp})/u_{exp}$. Case 1 presents a relative error of 7.1%, Case 2 of 6.9%, and Case 3 of 7.6%. Finally, in order to establish the present formulation proficiency of solving complex flows we present in **Figures 7–9** stream function contours for three different cases. **Figures 8 and 9** clearly show the formation of recirculating bubbles close to the axis of symmetry, known as vortex breakdowns.

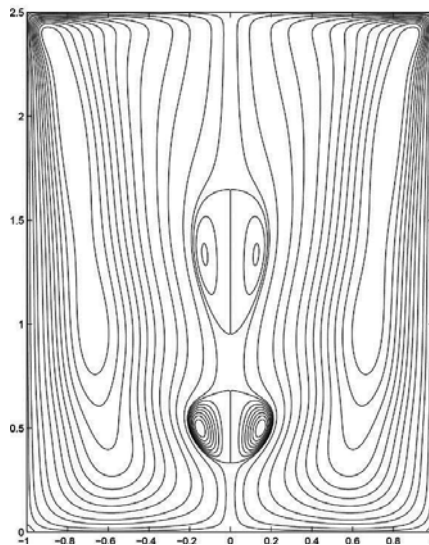


Figure 9. Stream function contours for Case 3: $Re = 2200$ and $Ar = 2.5$ (y -coordinate corresponds to Z and x -coordinate to R).

The streamlines shown in previous figures are in agreements with those presented in mentioned references.

5. Conclusion

In the present work, a LBM in vorticity-stream function variables for axisymmetric flow with swirl is presented and implemented. By considering the convective term of the evolution equations in their conservative form, proper sources are carefully proposed being able to reproduce both nonviscous and viscous momentum equations. Through a multiscale analysis, performed in Cartesian coordinates, it was found that a discrepancy between the operators and the governing equations was achieved. This difference is overcome by the definition and inclusion of source terms in the proposed LB formulation. The Chapman-Enskog analysis was used to achieve conservative operators that arise naturally in the implemented LBM. As a result a unified LBM algorithm was built in which every evolution equations is solved with the same algorithm. The numerical method proved to be second-order accurate in space. Finally, the method was able to reproduce complex flows, such as the Taylor-Couette flow where toroidal vortices were observed and good agreement was found with qualitative results proposed in the literature. Furthermore, the proficiency of the method to solve the lid-driven cylindrical cavity flow quantitatively showed an error below 8% when compared with experimental data. Qualitatively, the method solved the flow through many flow regimes observing one and two vortex breakdown located in the cavity axis.

Author details

Omar D. Lopez^{1*}, Sergio Pedraza² and Jose R. Toro¹

*Address all correspondence to: od.lopez20@uniandes.edu.co

1 The University of Los Andes, Bogota, Colombia

2 ISMO Consulting SAS, Bogota, Colombia

References

- [1] Z. Chai, B. Shi, and L. Zheng. A unified Lattice Boltzmann model for some nonlinear partial differential equations. *Chaos Soliton Fract.*, 36:874–882, 2008.
- [2] H. Huang and X. Lu. Theoretical and numerical study of axisymmetric Lattice Boltzmann models. *Phys. Rev. E*, 80, 016701:51–50, 2009.

- [3] Z. Guo, B. Han, H. Shi, and C. Zheng. Theory of the Lattice Boltzmann equation: Lattice Boltzmann model for axisymmetric flows. *Phys. Rev. E*, 79, 046708:51–50, 2009.
- [4] Q. Li, Y.L. He, G.H. Tang, and W.Q. Tao. Improved axisymmetric Lattice Boltzmann scheme. *Phys. Rev. E*, 81, 056707:51–50, 2010.
- [5] J.G. Zhou. Axisymmetric Boltzmann method revised. *Phys. Rev. E*, 84, 036704:51–50, 2011.
- [6] Y. Peng, C. Shu, T.Y. Chew, and J. Qiu. Numerical investigations of flows in czochralski crystal growth by an axisymmetric Lattice Boltzmann. *J. Comput. Phys.*, 186:295–307, 2003.
- [7] R.G.M. van der Sman. Galilean invariant Lattice Boltzmann scheme for natural convection on square and rectangular lattices. *Phys. Rev. E*, 74, 026705:295–307, 2006.
- [8] R.W. Mei, W. Shyy, D. Yu, and L. Luo. Lattice Boltzmann method for 3-d flows with curved boundary. NASA/CR-2002-211657, ICASE Report No. 2002–17:51–50, 2002.
- [9] S.K. Bhaumik and K.N. Lakshmisha. Lattice Boltzmann simulation of lid-driven swirling flow in confined cylindrical cavity. *Comput. Fluids*, 36:1163–1173, 2007.
- [10] A.M. Artoli, A.G. Hoekstra, and P.M.A. Sloot. 3d pulsatile flow in the Lattice Boltzmann bgk method. *Int. J. Mod. Phys. C*, 13:1119–1134, 2002.
- [11] I. Halliday, L.A. Hammond, C.M. Care, K. Good, and A. Stevens. Lattice Boltzmann equation hydrodynamics. *Phys. Rev. E*, 64, 011208:874–882, 2000.
- [12] H. Huang, T.S. Lee, and C. Shu. Hybrid Lattice Boltzmann finite-difference simulation of axisymmetric swirling and rotating flows. *Int. J. Numer. Meth. Fl.*, 53:1707–1726, 2007.
- [13] Z. Guo, C. Zheng, and B. Shi. Discrete lattice effects on the forcing term in the Lattice Boltzmann method. *Phys. Rev. E*, 65, 046308:990–996, 2002.
- [14] S. Chen, J. Toelke, and M. Krafczyk. Lattice Boltzmann model for incompressible axisymmetric flow. *Phys. Rev. E*, 78, 046703:2093–2107, 2008.
- [15] S. Chen, J. Toelke, and M. Krafczyk. Numerical simulation of fluid flow and heat transfer inside a rotating disk-cylinder conjugation by a Lattice Boltzmann model. *Phys. Rev. E*, 80, 016702:2093–2107, 2009.
- [16] S. Chen, J. Toelke, and M. Krafczyk. Simulation of buoyancy-driven flows in a vertical cylinder using a simple Lattice Boltzmann model. *Phys. Rev. E*, 79, 016704:2093–2107, 2009.
- [17] S. Chen. Simulating compositional convection in the presence of rotation by Lattice Boltzmann model. *Int. J. Therm. Sci.*, 49:2093–2107, 2010.
- [18] G.L. Brown and J.M. Lopez. Axisymmetric vortex breakdown Part 2. Physical mechanisms. *J. Fluid Mech.*, 221:533–552, 1990.

- [19] J.M. Lopez. Axisymmetric vortex breakdown Part 1. Confined swirling flow. *J. Fluid Mech.*, 221:533–552, 1990.
- [20] J.M. Lopez and A.D. Perry. Axisymmetric vortex breakdown Part 3. Onset of periodic flow and caothic advection. *J. Fluid Mech.*, 234:449–471, 1992.
- [21] M.P. Escudier. Observations of the flow produced in a cylindrical container by a rotating endwall. *Exp. Fluids*, 2:189–196, 1984.
- [22] S. Leibovich. The structure of vortex breakdown. *Annu. Rev. Fluid Mech.*, 10:221–246, 1978.
- [23] D.A. Wolf-Gladrow. *Lattice-Gas Cellular Automata and Lattice Boltzmann Models – An Introduction*. Springer, Berlin, Heidelberg, 2000.
- [24] S. Chen and G. Doolen. Lattice Boltzmann method for fluid flows. *Annu. Rev. Fluid Mech.*, 30:329–364, 1998.
- [25] B. Deng, B. Shi, and G. Wang. A new lattice bhatnagar-gross-krook model for the convection-diffusion equation with a source term. *Chinese Phys. Lett.*, 22:267–270, 2005.
- [26] Z. Chai and B. Shi. A novel Lattice Boltzmann model for the Poisson equation. *Appl. Math. Model.*, 32:2050–2058, 2008.
- [27] K. Fujimura, H.S. Koyama, and J.M. Hyun. Time dependent vortex breakdown in a cylinder with a rotating lid. *J. Fluid Eng-T. Asme*, 119:450–453, 1997.

Thickness and Thermal Conductivities of the Walls and Fluid Layer Effects on the Onset of Thermal Convection in a Horizontal Fluid Layer Heated from Below

Ildebrando Pérez-Reyes,
René Osvaldo Vargas-Aguilar,
Eduardo Valente Gómez-Benítez and
Iván Salmerón-Ochoa

Additional information is available at the end of the chapter

<http://dx.doi.org/10.5772/66325>

Abstract

The thermal boundary conditions have important effects on the hydrodynamics of a thermo-convective fluid layer. These effects are introduced through the Biot number under the Robin type boundary conditions. The thermal conductivity and thicknesses of the walls are key properties to bridge two known ideal situations widely studied: the fluid layer bounded by two insulating walls and the fluid layer bounded by two perfect thermal conducting walls. This chapter is devoted to the physical mechanisms involved in the thermal boundary conditions, its influence on the linear stability of the fluid layer and its implications with the pattern formation. A review of very important investigations on the subject is also given. The role of the thermal conductivities and thicknesses of the walls is explained with help of curves of criticality for the thermoconvection in a horizontal Newtonian fluid layer.

Keywords: thermal convection, boundary condition, hydrodynamic stability, Biot number, patterns

1. Introduction

The present work is devoted to the study of some important physical properties and geometrical configurations that may modify the pattern formation in Newtonian fluid layers. The theory presented here may be of interest for a number of applications such as for the control of convective motions [1, 2], for the study of movements in the mantle of the earth [3], in the

study of convective cell formation in the surface of the sun [3] and in biotechnological appliances involving the Rayleigh convection phenomena [4].

The formation of patterns is a very interesting subject in fluid mechanics. This topic involves complex physics and mathematics [5]. From the physical point of view, various parameters influence the onset of convection and later the evolution of the formed patterns. Some variables affecting the patterns are,

- type of fluid: Newtonian or non-Newtonian
- the properties of the fluid (like density and viscosity) and properties of the bounding surfaces (like thickness and thermal conductivity), among others

This chapter focuses on the points given in the above-mentioned list. The bounding surfaces have become an interesting topic of study since the boundary conditions are mathematically written according to their nature [6, 7]. The thickness and thermal conductivity of the walls and the fluid layer are strongly related to the familiar eigenvalue Rayleigh number and to the wavenumber. They are also related to two classical approximations commonly found in hydrodynamic stability. These two classical approximations are:

- insulating walls and
- perfect thermal conducting walls.

For short, the insulating wall approximation correspond to constant heat flux boundary conditions while the perfect thermal conducting walls approximation correspond to the constant temperature boundary conditions. The critical Rayleigh and wavenumber are ($R_c = 720$, $k_c = 0$) and ($R_c = 1707.96$, $k_c = 3.12$), respectively. Then the purpose of considering the thickness and thermal conductivity of the walls are to bridge ideal approximations to the problem of thermal convection and to provide critical conditions that better simulate the lab experiments.

The boundary conditions are of paramount importance for proper understanding of the physical phenomenon of thermal convection [1, 6, 7], for comparison between theoretical and experimental data and for its control [1]. As new technologies and appliances develop, more sophisticated mathematical models are needed. A good example for the previous statement is that of the manufacturing of corrugated surfaces [8, 9] in which the formed convective pattern is deposited on the lower boundary after evaporation of the solvent. This may occur for convection in polymer solutions which are composed of polymeric chains and solvents.

This chapter is organized as follows. In Section 2, a general formulation for the natural convection in a horizontal fluid layer heated from below is given along with some data on the basic state of the temperature. Section 3 presents a brief explanation on how the thermal boundary conditions are related to the linear hydrodynamic stability. In Section 4, a discussion on the basic state of the temperature is presented. Some points about the effect of the thermal conductivities and thicknesses of the walls on the pattern formation are discussed in Section 5. Section 6 is devoted to list some challenges in hydrodynamic stability that are

connected to the thermal boundary conditions. Finally, in Section 7 a general discussion on the subject is given.

2. The problem of convection in a fluid layer

The importance of the thermal boundary conditions can be seen from the point of view of the familiar problem of Rayleigh thermal convection in a horizontal infinite fluid layer vertically bounded by two solid and rigid walls [10, 11]. Consider the scheme presented in **Figure 1** which shows the thermal and geometrical properties of the bounding walls. This extension to the problem of convection has been presented in Ref. [2], and studied by Cerisier et al. [7] and Howle [1], among others.

The two problems of thermal convection that have been widely studied are that of bounding insulating walls (see Refs. [11, 12] for more details) and that of bounding perfect thermal conducting walls (see Refs. [10, 13] for more details). These two cases can be mathematically expressed as,

- $dT/dz = 0$ at the boundaries. For insulating walls (according to Chapman et al. [11]).
- $T = 0$ at the boundaries. For perfect thermal conducting walls (according to Chandrasekhar [10]).

On the other hand, it is well known that lab experiments and technological developments are not restricted to these ideal cases. In other words, more general boundary conditions are needed to satisfy the requirements of intermediate cases, as represented in **Figure 2**. Mathematically speaking, the proper thermal boundary conditions for non-ideal situations are those of the Robin type. This is a boundary condition encompassing both cases mentioned above.

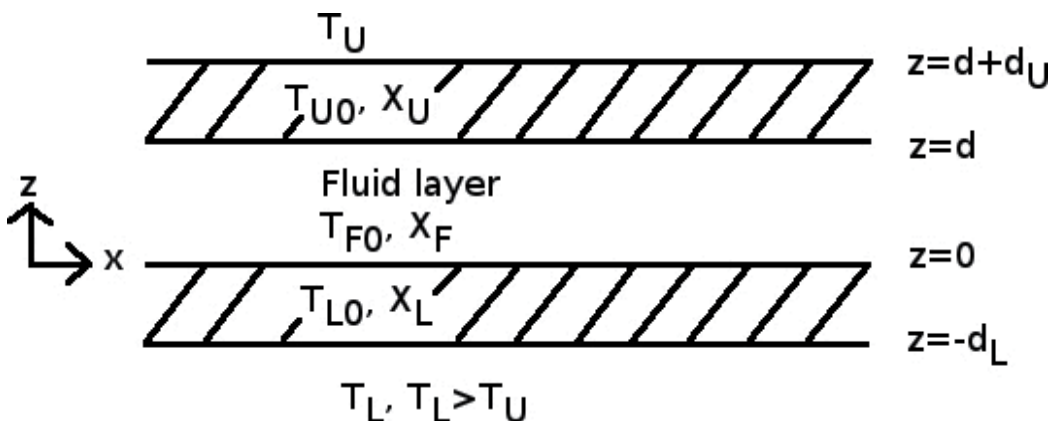


Figure 1. Scheme for the problem of Rayleigh convection including the thickness and thermal conductivities of the walls. $T_{L,U}$ stand for the constant temperature at the lower and upper walls, $T_{L0,U0,F0}$ stand for the basic state temperature profile at the lower wall, upper wall and fluid layer; while $X_{L,U,F}$ represent the thermal conductivities of the lower wall, upper wall and fluid layer, respectively. Dimensional variables are used.

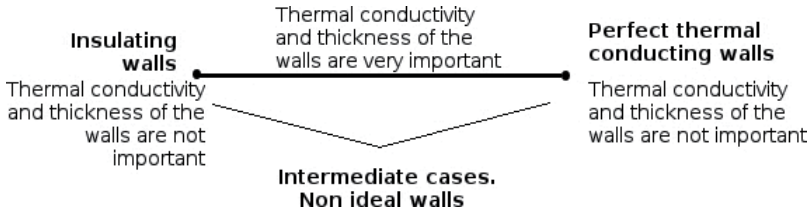


Figure 2. A heuristic explanation about the connection of the thermal and geometrical properties of the walls with the boundary conditions from one ideal case to the other.

When considering bounding walls of non-ideal properties the Biot number appears in the boundary conditions. The Biot number actually is derived from the geometrical and thermal properties of the walls and the working fluid allowing mapping the critical conditions (mainly, critical Rayleigh number, R_c and critical wavenumber, k_c) for the onset of convection from the insulating to perfect conducting walls, as shown in **Figure 2**. Some of investigations have been carried out to fill this gap in the theory of hydrodynamic stability in Newtonian [7, 14, 15] and non-Newtonian fluids [6], as well. Another implication of the thermal conductivities and thicknesses of the bounding walls and that of the fluid layer is the more general temperature profile in the basic state. Even, two more temperature profiles in the basic state appear, one for the lower wall and another one for the upper wall (see **Figure 1**).

The temperature profiles are then defined as:

$$T_{F0} = -z + T_U + 1 + \overline{X_U} \overline{d_U} \tag{1}$$

$$T_{L0} = -\overline{X_L} z + T_L + 1 - \overline{X_L} \overline{d_L} \tag{2}$$

$$T_{U0} = \overline{X_U} (1 + \overline{d_U} - z) + T_U \tag{3}$$

where the variables in Eqs. (1)–(3) are in non-dimensional form (the reader may see Refs. [6, 7] for more details). Here, $X_U = X_F / X_U$, $X_L = X_F / X_L$, $d_U = d_U / d_F$ and $d_L = d_L / d_F$. Notice that Eqs. (2) and (3) are not considered in studies related to the limiting cases of insulating and perfect conducting walls.

Eq. (1) represents the temperature profile of the fluid layer, Eq. (2) represents the temperature profile of the lower bounding wall and Eq. (3) represents the temperature profile of the upper wall. These temperature profiles may be easily obtained by considering the set of boundary conditions for the temperature below. These conditions assure the continuity and smoothness of the temperature across the whole system including the two walls and the fluid layer (as seen in **Figure 1**):

$$T_{L0} = T_L \text{ at } z = -d_L \tag{4}$$

$$T_{U0} = T_U \text{ at } z = d + d_U \tag{5}$$

$$T_{F0} = T_{L0} \text{ at } z = 0 \tag{6}$$

$$\overline{X}_L \frac{dT_{F0}}{dz} = \frac{dT_{L0}}{dz} \text{ at } z = 0 \tag{7}$$

$$T_{F0} = T_{U0} \text{ at } z = d \tag{8}$$

$$\overline{X}_U \frac{dT_{F0}}{dz} = \frac{dT_{U0}}{dz} \text{ at } z = d \tag{9}$$

where Eqs. (4)–(9) are given in non-dimensional form. As the differential equations to be solved to calculate T_{F0} , T_{L0} and T_{U0} are homogeneous of a single second order term, the solutions are linear polynomials. This means that the three temperature profiles in the basic state lie over a straight line going from $z = -d_L$ to $z = d + d_U$, if continuity and smoothness are expected.

3. Importance in the linear stability

In the linear stability of a fluid layer, its basic state is subjected to small perturbations. This is made to determine whether the fluid layer is stable or not. The linear stability is featured by two parameters, for steady situations: the critical Rayleigh and wavenumbers. **Figures 3 and 4** show the critical points for the two ideal cases mentioned above.

The basic state for the fluid temperature as given in Eq. (1) conveys information not only of the fluid properties but also of the walls through the parameters X_U , d_U and T_U . Unfortunately, the information of the thermal and geometrical properties pass only to the boundary conditions and leaving the governing differential unchanged. This is valid for cases in which the structure of the equations allows only the derivative of the basic state temperature profile in the equation for the perturbation of the temperature.

An example case is that of the convection of Rayleigh. The differential equations for this problem are:

$$Pr^{-1} \sigma \left(\frac{d}{dz^2} - k^2 \right) W(z) - \left(\frac{d}{dz^2} - k^2 \right)^2 W(z) = Rk^2 \theta(z) \tag{10}$$

$$\left[\sigma - \left(\frac{d}{dz^2} - k^2 \right) \right] \theta(z) = \frac{dT_{F0}}{dz} W(z) \tag{11}$$

where W and θ are the perturbations for the velocity and the temperature of the fluid, and Pr is the Prandtl number. $\sigma = \sigma_{R+i\sigma_i}$, with σ_R being the growth rate of the perturbations and σ_i , the frequency of oscillation. It is well known that there is no frequency of oscillation in the case of Rayleigh convection, so that if $\sigma_R = 0$ is set, then $R_c = 720, 1707.96$, for the insulating and perfect thermal conducting walls are obtained.

At this point, no information of the basic state is given to Eqs. (4) and (5) since only dT_{F0}/dz is required. This may represent a limitation to the model since the linear stability of the system

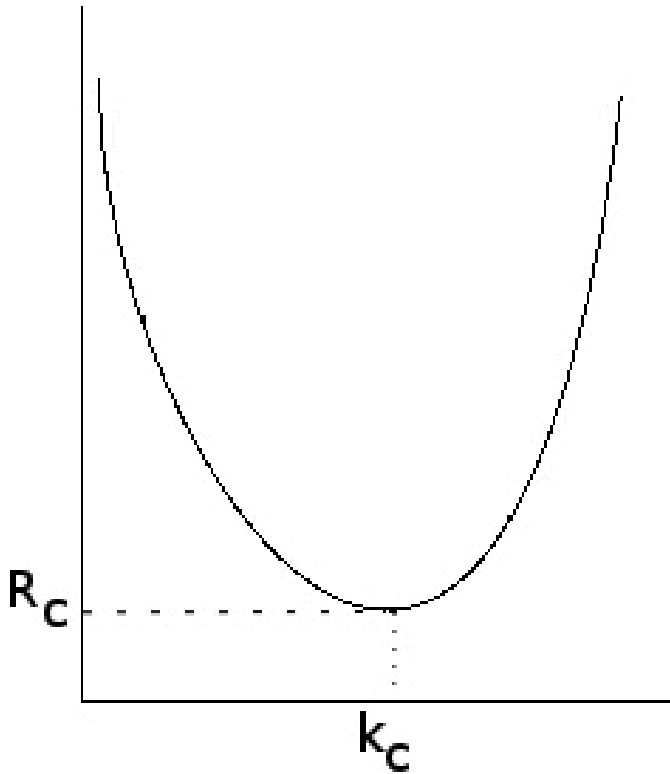


Figure 3. A curve showing the critical point (k_c, R_c) for steady convection of a fluid layer bounded by two insulating walls.

comes from the basic state. The only way to introduce the effect of the thermal conductivities and thickness of the walls and the fluid layer is through the Biot number in the Robin type boundary conditions. These can be expressed as:

$$\left(\left[\frac{d\theta}{dz} - \frac{\sqrt{k^2 + \overline{\kappa}_L} \sigma \theta}{\overline{X}_L \tanh[\sqrt{k^2 + \overline{\kappa}_L} d_L]} \right] \right)_{z=0} = 0 \tag{12}$$

$$\left(\left[\frac{d\theta}{dz} - \frac{\sqrt{k^2 + \overline{\kappa}_U} \sigma \theta}{\overline{X}_U \tanh[\sqrt{k^2 + \overline{\kappa}_U} d_U]} \right] \right)_{z=1} = 0 \tag{13}$$

where $\overline{\kappa}_L = \kappa_L/\kappa_F$ and $\overline{\kappa}_U = \kappa_U/\kappa_F$ are ratios of the thermal diffusivities of the walls to that of the fluid layer. The Biot number is a key component of the Robin type thermal boundary conditions and according to Eqs. (12) and (13), the Biot number for the lower wall is:

$$B_L = \frac{\sqrt{k^2 + \overline{\kappa}_U} \sigma}{\overline{X}_U \tanh[\sqrt{k^2 + \overline{\kappa}_U} d_U]} \tag{14}$$

while for the upper bounding wall, its corresponding Biot number is

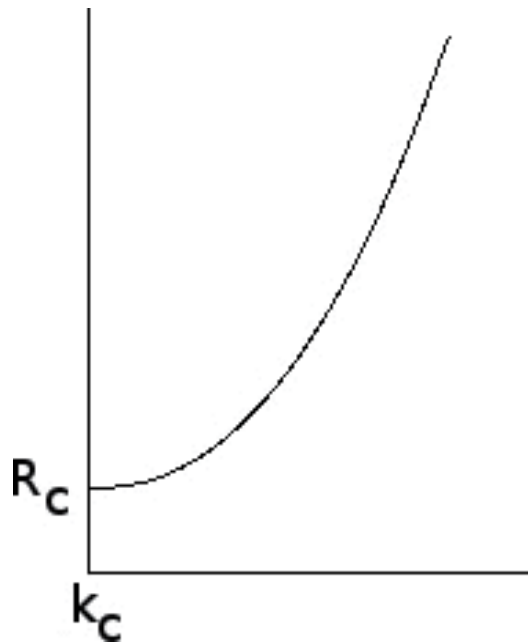


Figure 4. A curve showing the critical point (k_c, R_c) for steady convection of a fluid layer bounded by two perfect thermal conducting walls.

$$B_U = \frac{\sqrt{k^2 + \overline{\kappa_U} \sigma}}{\overline{X_U} \tanh[\sqrt{k^2 + \overline{\kappa_U} \sigma} d_U]} \quad (15)$$

The set of Eqs. (4)–(7) represent the complete eigenvalue problem for the Rayleigh number R . Then, by mapping with the thermal conductivity ratios $\overline{X_L}$ and $\overline{X_U}$ from limiting values of zero to infinity it is possible to bridge the two ideal case mentioned above. The importance of the thermal and geometrical properties are shown in the following set of curves of criticality, given in **Figures 5** and **6**.

The middle region of the curves in **Figures 5** and **6** show two graphs that collapse in the extremes. This middle region clearly shows the effect of the walls thicknesses which disappears as the thermal conductivities ratio approaches zero or a very large magnitude. This behaviour can be easily explained by recalling the two occurring ideal situations when the thermal conductivity ratios $\overline{X_L}$ and $\overline{X_U}$ are zero or infinity, for an insulator or a perfect thermal conductor. No matter how large the thicknesses of the perfect thermal conducting or perfect insulating walls are, the heat shall be transferred instantaneously. This can be also mathematically seen from Eqs. (12) and (13) since in the limit of insulating walls, the boundary conditions reduce to $\frac{d\theta}{dz} = 0$ and in the limit of perfect thermal conducting walls, these conditions give $\theta = 0$. In this last sentence, it should be remarked that the thicknesses of the bounding walls, and that of the fluid, vanish.

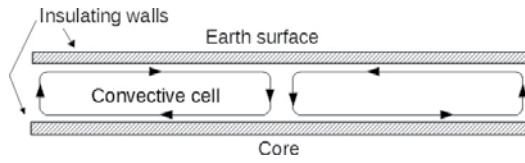


Figure 5. Curves of criticality for the Rayleigh number showing the effect of the thermal conductivities and thickness of the walls on the Rayleigh convection in a Newtonian fluid. For these curves of criticality $\overline{X}_L = \overline{X}_U$ and $\overline{d}_L = \overline{d}_U$ was set.

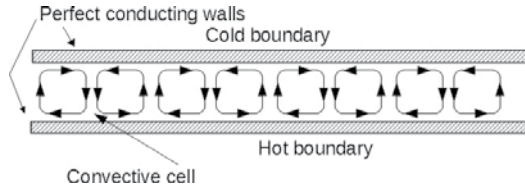


Figure 6. Curves of criticality for the wavenumber number showing the effect of the thermal conductivities and thickness of the walls on the Rayleigh convection in a Newtonian fluid. For these curves of criticality $\overline{X}_L = \overline{X}_U$ and $\overline{d}_L = \overline{d}_U$ was set.

As it can be seen, from **Figure 5**, in the extremes of the horizontal axis, $R_c = 720$ and 1707.96 . Correspondingly, from **Figure 6**, in the extremes of the horizontal axis $k_c = 0$ and $R_c = 3.12$. The data presented in the set of curves of criticality were first reported by Riahi [14, 15] and later by Cerisier et al. [7].

Pérez-Reyes and Dávalos [6] presented a study of the influence of the thermal and geometrical properties on the convection of viscoelastic Maxwell fluids. They found a behaviour similar to that shown in **Figures 5** and **6** and reported the appearance of a codimensional-two point. This is due to the competition between stationary and oscillatory convection to destabilize the system. Besides, if the linear stability is changed, then the nonlinear stability results are to be changed too.

4. About the basic state for the temperature

At this point, some qualitative information may be given about the basic state for the temperature given in Eqs. (1)–(3). The obvious question is: are the parameters \overline{X}_L and \overline{X}_U , and the Eqs. (1)–(3) useless? It should be mentioned that these are not used in the computation of the data shown in **Figures 5** and **6**. This is a direct consequence of the symmetry of the equations and of the adimensionalization of the problem. In fact, the Rayleigh number in **Figures 5** and **6** is modified by a factor $1/(1 + \overline{X}_L \overline{d}_L + \overline{X}_U \overline{d}_U)$. This is a shortcut in the solution to the problem. Furthermore, the proper basic state should be one including the three basic states, Eqs. (1)–(3) which would have the same form as that of Eq. (3).

This last equation may become important for problems represented by differential equations with additional terms to the base model as shown in Eqs. (10) and (11). For example, a

comparison of the basic state for the temperature in any of the ideal cases would show that at the boundaries $T_{F0} = T_L$ and $T_{F0} = T_U$, respectively. Eq. (3) does not match these results at the boundaries due to the effect of the thickness of the walls. However T_{F0} may satisfy the same requirements through T_{L0} and T_{U0} .

The additional terms to the base, shown in Eqs. (10) and (11), model equations for the hydrodynamics in the fluid layer could come from variations in the viscosity of the fluid, for example. In situations where the viscosity varies with temperature, its effect appears in the viscous term of the momentum balance equation. This type of problems has been studied by Palm et al. [16], by Wall and Nagata [17] and by Wall and Wilson [18], among others. The working equations of these studies show that a temperature dependent viscosity may introduce terms requiring T_{F0} and dT_{F0}/dz . This can be seen in the following set of equations corresponding to the problem of thermal convection in a fluid layer with temperature dependent viscosity being heated from below:

$$C_1 \frac{d^4 W}{dz^4} + \bar{\gamma} \frac{d^3 W}{dz^3} + C_2 \frac{d^2 W}{dz^2} - k^2 \bar{\gamma} \frac{dW}{dz} + C_3 W + Rk^2 \theta = 0 \tag{16}$$

$$W + \frac{d^2 \theta}{dz^2} + C_4 \theta = 0 \tag{17}$$

where the coefficients are defined as:

$$C_1 = \bar{\gamma}(T_{F0} - T_L) - 1 \tag{18}$$

$$C_2 = Pr^{-1} \sigma + k^4 [\bar{\gamma}(T_{F0} - T_L) - 1] \tag{19}$$

$$C_3 = -Pr^{-1} \sigma k^2 - 2k^2 [\bar{\gamma}(T_{F0} - T_L) - 1] \tag{20}$$

$$C_4 = -(\sigma + k^2) \tag{21}$$

So that the second and third terms in right-hand side of Eq. (1) should appear in the final eigenvalue problem explicitly. These additional terms may be of interest for a proper understanding of the convective phenomena.

5. Influence on the pattern formation

The pattern formation in convective systems is a subject widely studied. One common approach to the study of convective patterns is the problem of pattern selection in a given geometry [5]. The formation of convective cells is highly dependent on the boundary conditions. This is true not only because of the mathematical structure of the boundary conditions but also because of the nature of the bounding surfaces. In the limiting case of insulating walls are very large convection cells of slow motion. A good example of this system is the mantle convection occurring between the earth core and its surface. **Figure 7** shows a simple scheme of a convection cell driven by the difference of temperature between the core and the

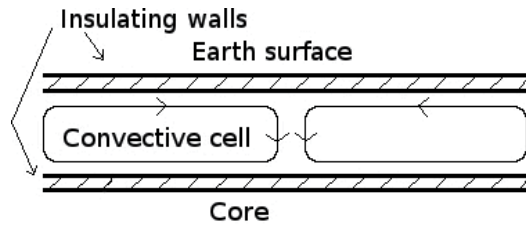


Figure 7. A simple representation of the mantle convection.

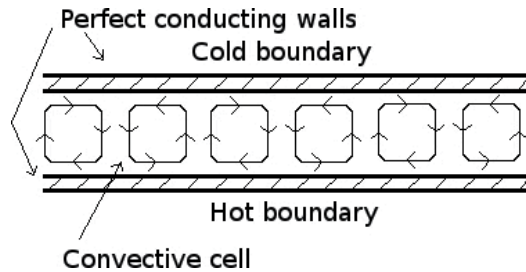


Figure 8. A simple representation of the thermal convection in a fluid layer bounded by two perfect conducting walls.

surface. It has been demonstrated that these convection cells are very large and that the liquid rock material moves slowly [3, 12, 19]. Thus, a feature of this type configuration is the presence of large convection cells of slow moving fluid, since the critical wave number is zero ($k_c = 0$).

The case of perfect conducting walls is quite different. In this configuration, more than one convection cell appear since the critical wavenumber is finite ($k_c = 3.12$). A representation of this case is given in **Figure 8**. Another consequence of the idealized perfect thermal conducting walls is a faster re-circulating fluid motion in comparison with the previous described situation. The study of these ideal cases includes a variation in which one of the walls is a perfect thermal conductor while the other is considered an insulating wall.

The study of the effect of the boundaries on the pattern formation has called the attention of a number of researchers and diverse cases have been studied. Chapman and Proctor [20] were interested in the behaviour of the system when non-ideal walls were considered so that they applied an analytical approximation for poorly thermal conducting boundaries. Chapman and Proctor [20] were able to calculate critical wavenumbers different from zero which made more sense for experimentalists. Additionally, Proctor [21] studied the selection of patterns in finite domains for rolls, square, rectangles and hexagonal patterns. The approximation of poorly thermal conducting walls becomes so interesting and tractable that these ideas were extended to problems of double diffusion by Proctor [22] and by Cox [23] for example. Other areas of the fluid mechanics have used similar ideas like in magnetohydrodynamics by Dávalos-Orozco [24] and in convection of second order fluids by Dávalos-Orozco [25], for example.

The pattern formation is studied as a nonlinear problem which is linked to the results of the linear hydrodynamic stability of the system. Therefore, introducing more general thermal boundary conditions shall convey more information to the study of the behaviour of the moving fluid. Some efforts have been made including the thermal and geometrical properties of the walls by Riahi [14], for example. The thermal conductivities and thicknesses of the walls shall clearly modify the convective cells. One clear effect would be on the size of the patterns. It is possible that the selected structure remains at least not for set domains like squares, rectangles, etc.

6. Some problems to engage

Most of the problems with analytical solutions and interesting physical mechanisms in it have already been studied. In fact, fluid mechanics is called a mature area of physical sciences. The remaining problems are complex, mostly without analytical solutions and with many variables involved.

Some interesting problems to study in hydrodynamic stability, linked to the thermal boundary conditions, are mentioned here.

- There is lack of information about the role of the thermal diffusivities of the walls and the fluid layer for intermediate values of the ratio of thermal conductivities. In the literature, it has been assumed that the fluid layer and the bounding walls have the same thermal diffusivities.
- The Robin type thermal boundary conditions are assumed to convey pore physical information to the eigenvalue problem. To the best knowledge of the author, there are no reports about experiments to corroborate this.
- Nonlinear problems about pattern selection shall become more difficult to handle. Perhaps, more efficient numerical computations would be needed.

7. Discussion

A number of problems have been discussed here. The physical implications of the thermal boundary conditions were highlighted in terms of the thermal conductivities and thicknesses of the bounding walls. Although only the classical horizontal infinite two-plate configuration was considered, the main ideas can be used to understand more complex geometries.

The ratio of thermal conductivities allow the mapping of the critical conditions for the onset of convection from insulating walls ($\bar{X} \rightarrow \infty$) to perfect thermal conducting walls ($\bar{X} \rightarrow 0$). On the other hand, small thicknesses ratio destabilize the system while large thicknesses ratio help to stabilize the fluid layer. The physical mechanisms behind this behaviour is explained through thermal diffusion times across the bounding walls and the fluid layer. These observations are valid for fixed values of the thermal diffusivities.

It is shown from the qualitative point of view, that additional terms in the base model equations of the problem of Rayleigh convection may carry more information from the temperature basic states of the bounding walls and fluid layer to the eigenvalue problem. The temperature basic states of the walls may help to understand the physical mechanisms involved in diverse thermal convection problems.

Acknowledgements

Professor Pérez-Reyes would like to thank the financial support of the Mexican Consejo Nacional de Ciencia y Tecnología (CONACyT) through the basic science project number 255839 for young researchers.

Author details

Ildebrando Pérez-Reyes^{1*}, René Osvaldo Vargas-Aguilar², Eduardo Valente Gómez-Benítez¹ and Iván Salmerón-Ochoa¹

*Address all correspondence to: ildebrando3@gmail.com

1 Chemical Sciences Faculty, Autonomous University of Chihuahua, New University Campus, Chihuahua, Mexico

2 SEPI ESIME Azcapotzalco, National Polytechnic Institute, Santa Catarina, Azcapotzalco, Mexico City, Mexico

References

- [1] L. E. Howle. The effect of boundary properties on controlled Rayleigh-Bénard convection. *J. Fluid Mech.*, 411:39–58, 2000.
- [2] L. E. Howle. Active control of Rayleigh-Bénard convection. *Phys. Fluid*, 9(7):1861–1863, 1997.
- [3] M. Lapa. *Thermal Convection: Patterns, Evolution and Stability*. John Wiley and Sons, Singapore, 2010.
- [4] R. Muddu, Y. A. Hassan, and V. M. Ugaz. Rapid PCR thermocycling using microscale thermal convection. *J. Vis. Exp.*, 49:e2366, 2011.
- [5] R. Hoyle. *Pattern Formation: An Introduction to Methods*. Cambridge University Press, Cambridge, 2006.

- [6] I. Pérez-Reyes and L. A. Dávalos-Orozco. Effect of thermal conductivity and thickness of the walls in the convection of a viscoelastic Maxwell fluid layer. *Int. J. Heat Mass Transfer*, 54:5020–5029, 2011.
- [7] P. Cerisier, S. Rahal, J. Cordonnier, and G. Lebon. Thermal influence of boundaries on the onset of Rayleigh-Bénard convection. *Int. J. Heat Mass Transfer*, 41:3309–3320, 1998.
- [8] Z. Nie, A. Petukhova, and E. Kumacheva. Properties and emerging applications of self-assembled structures made from inorganic nanoparticles. *Nat. Nanotech.*, 5:15–25, 2010.
- [9] S. Sakurai, C. Furukawa, A. Okutsu, A. Miyoshi, and S. Nomura. Control of mesh pattern of surface corrugation via rate of solvent evaporation in solution casting of polymer film in the presence of convection. *Polymer*, 43:3359–3364, 2002.
- [10] S. Chandrasekhar. *Hydrodynamic and Hydromagnetic Stability*. Dover Publications, Inc., New York, USA, 1981.
- [11] S. Chapman, C. J. Childress and M. R. E. Proctor. Long wavelength thermal convection between non-conducting boundaries. *Earth Plane. Sci. Let.*, 51(2):362–369, 1980.
- [12] J. M. Hewitt, D. P. McKenzie, and N. O. Weiss. Large aspect ratio cells in two-dimensional thermal convection. *Earth Planet. Sci. Lett.*, 51:370–380, 1980.
- [13] A. Pellew and R. V. Southwell. On maintained convective motion in a fluid heated from below. *Proc. R. Soc. London A*, 176(966):313–343, 1940.
- [14] N. Riahi. Nonlinear thermal convection with finite conducting boundaries. *J. Fluid Mech.*, 152:113–123, 1985.
- [15] N. Riahi. Nonlinear convection in a porous layer with finite conducting boundaries. *J. Fluid Mech.*, 129:153–171, 1981.
- [16] E. Palm, T. Ellingsen, and B. Gjevik. On the occurrence of cellular motion in Bénard convection. *J. Fluid Mech.*, 30(04):651–661, 1967.
- [17] D. P. Wall and M. Nagata. Nonlinear equilibrium solutions for the channel flow of fluid with temperature-dependent viscosity. *J. Fluid Mech.*, 406:1–26, 2000.
- [18] D. P. Wall and S. K. Wilson. The linear stability of channel flow of fluid with temperature-dependent viscosity. *J. Fluid Mech.*, 323:107–132, 1996.
- [19] G. Schubert, D. L. Turcotte, and P. Olson. *Mantle Convection in the Earth and Planets*. Cambridge University Press, New York, 2001.
- [20] C. J. Chapman and M. R. E. Proctor. Nonlinear Rayleigh-Bénard convection between poorly conducting boundaries. *J. Fluid Mech.*, 101(4):759–782, 1980.
- [21] M. R. E. Proctor. Planform selection by finite-amplitude thermal convection between poorly conducting slabs. *J. Fluid Mech.*, 113:469–485, 1981.
- [22] M. R. E. Proctor. Steady subcritical thermohaline convection. *J. Fluid Mech.*, 105:507–521, 1981.

- [23] S. M. Cox. Thermosolutal convection between poorly conducting plates. *J. Eng. Math.*, 28:463–482, 1994.
- [24] L. A. Dávalos-Orozco. Magnetoconvection in a rotating fluid between walls of very low thermal conductivity. *J. Phys. Soc. Jpn.*, 53(7):2173–2176, 1984.
- [25] L. A. Dávalos-Orozco and Octavio Manero. Thermoconvective instability of a second-order fluid. *J. Phys. Soc. Jpn.*, 55(2):442–445, 1986.

Role of Vortex Dynamics in Relativistic Fluids

Gunraj Prasad

Additional information is available at the end of the chapter

<http://dx.doi.org/10.5772/65372>

Abstract

Relativistic versions of Helmholtz's three theorems on vorticity flux conservation are derived by invoking an alternative approach based on Greenberg's theory of spacelike congruence generated by vortex lines and $(1 + 1) + 2$ decomposition of the gradient of fluid's 4-velocity. It is shown that the meridional circulation causes vorticity winding due to the breakdown of gravitational isorotation via differential rotation. A new streamline invariant describing energy conservation associated with vorticity flux is shown to exist.

Keywords: vorticity flux, vorticity winding, fluid helicity, vortex motion

1. Introduction

Vortices are found in classical, relativistic and quantum fluids [1–7]. It is well known from classical theory of vortices that the dynamics of vortices is described by Kelvin-Helmholtz's flux conservation theorem. There are three theorems of Helmholtz on vortex tubes in the classical theory of fluids [2]. The product of the magnitude of fluid's vorticity vector and of vortex tube's cross-sectional area is called the strength of a vortex tube. Helmholtz's first theorem states that the strength of vortex tube remains constant along the vortex tube. This result is purely kinematical in nature in the sense that its derivation does not require Euler's equations which govern the motion of a fluid. The second theorem tells us that the vortex lines are material lines in the case of perfect fluid flows. The third theorem says that the vortex tube's strength multiplied by the fluid's chemical potential remains constant along the flow lines (or streamlines) for perfect fluid flows. Since a two-dimensional surface across which fluid's vorticity flux passes is usually bounded by a closed circuit, Kelvin's circulation theorem is intimately connected with that of Helmholtz's flux conservation theorem for perfect fluid flows. The circulation of a fluid motion

around any closed curve on a vortex tube wall is equal to the flux of vorticity along a vortex tube. Kelvin's circulation theorem asserts that the circulation of a perfect fluid motion around a closed material curve is conserved in time as the fluid evolves. This assertion in turn implies that the vortex tube is a material tube and moves with the fluid (i.e., vortex lines are material lines) [1, 2].

Since relativistic fluid dynamics differs from that of Newtonian fluid dynamics in many ways, Greenberg [8] developed a theory of a family of spacelike curves in order to study the kinematical behavior of vortex lines (i.e., spacelike curves) appearing in an isentropic perfect fluid motion. Greenberg [8] formulated a relativistic analogue of Helmholtz's first theorem on the basis of Ehlers' divergence identity of fluid's vorticity vector [9] in the Newtonian limit (i.e., ignoring the fluid's acceleration term). The relativistic divergence identity of fluid's vorticity vector involves fluid's acceleration vector which embodies the curvature of space-time, and thereby, it differs from classical divergence identity of vorticity vector. This is the reason that the exact relativistic version of Helmholtz's first theorem is not obtainable kinematically. Greenberg [8] further extended his analysis to obtain a relativistic version of Helmholtz's third theorem using Euler's equations of motion for an isentropic perfect fluid. In this derivation, the concept of vortex lines to be material lines is automatically implemented because of his transport law (i.e., it is presently known as Greenberg's transport law).

The necessary and sufficient conditions for the existence of conservation of flux associated with a vector field have been given firstly by Bekenstein and Oron [10] and then secondly by Carter [11]. Of two conditions, the first condition is satisfied if a vorticity 2-form is expressed as a curl of momentum covector associated with a fluid and the second condition when imposed on vorticity 2-form gives Euler's equations that govern fluid's motion. Vorticity 2-form satisfying these two conditions led to the formulation of a relativistic version of Kelvin's circulation conservation theorem and Helmholtz's flux conservation theorem [10, 11].

There is a link between Greenberg's transport law [8] and Carter's formulation [11] of vorticity flux conservation. Carter's vorticity flux conservation is based on vorticity 2-form of rank 2 (i.e., simple vorticity bivector field). The matrix of vorticity 2-form admits eigen vectors with zero eigen values. Such eigen vectors are referred to as flux vectors. The flux vectors span two-dimensional tangent subspaces at each point of a four-dimensional space-time. These tangent subspaces mesh together to form a family of timelike 2-surfaces because simple vorticity bivector field satisfies Frobenius condition [12] of 2-surface forming. Such timelike 2-surfaces are called flux surfaces. It is to be noted that Greenberg's transport law is an alternative version of Frobenius condition [12] due to which congruences of fluid flow lines and vortex lines form a family of timelike two-dimensional surfaces in the case of an isentropic perfect fluid flows. Furthermore, vortex lines are material lines. Flux surfaces are also material surfaces.

An intimate connection between Kelvin's circulation theorem and the fluid helicity (i.e., helicity of vorticity vector field) conservation was long ago demonstrated by Moffat [13]. The geometric structure of streamlines and vortex lines (forming a vortex tube) inherent in the helicity conservation was discovered by expressing the conservation of the sum of writhe and twist of vortex tubes undergoing continuous deformation in a fluid flow [14, 15]. The fluid helicity is conserved when vortex lines are frozen lines (i.e., material lines) in a fluid flow [14]. Such

topological consequences have been extensively investigated by several authors [16, 17] in classical fluid dynamics.

Although relativistic version of fluid helicity conservation has been formulated by Carter [11] and Bekenstein [18], yet its topological consequences remained unknown. In a relativistic frame work, frozen-in property of spacelike vortex lines is describable by Greenberg's transport law [8], which in turn leads to the fact that an isolated vortex is a timelike two-dimensional connected manifold called vortex world sheet. The deformation of timelike fluid flow lines and spacelike vortex lines caused by gravitation forbids the application of Biot-Savart-like law and Frenet-like transport frame along a spacelike vortex line. Furthermore, the kinematic deformation of a vortex tube is not independent of the kinematic deformation of fluid flow lines forming a stream tube. The deformation of a vortex tube is determined in terms of the expansion, shear and acceleration associated with fluid flow lines and the magnetic part of Weyl curvature tensor representing the free gravitational field [19]. In particular, the variation in cross-sectional area of a vortex tube along the tube is controlled by free gravitational field even if the acceleration vector of the fluid motion and the shear are ignored [19].

An inherent connection between helicity conservation and streamline invariant has already been pointed out by Bekenstein [18] in order to extract relevant information of astrophysical significance from nonlinear equations of relativistic fluid (or magnetofluid) dynamics. But such relationship between fluid helicity conservation and inherently connected streamline invariant is still to be investigated. This is the idea which motivates to work further in order to understand the role of vorticity in the rotational evolution of relativistic fluid, since most, if not all, compact stars composed of fluids rotate. It may be conceived that the gravitational effect on vorticity can be significant in the understanding of the internal structures of compact stars. It is known that differential rotation of fluid elements of which stars are composed arises from the gravitational collapse of massive stellar cores [20, 21]. Differential rotation produces vorticity which twists streamlines in fluid's motion. It is expected that the winding up of vortex lines caused by differential rotation will change the angular velocity profile in a similar way as has been found in magnetized stars due to the presence of magnetic fields [22].

In the present work, we confine our attention to the derivation of streamline invariants which adhere to the fluid helicity conservation and a formulation of vorticity winding due to meridional circulation via differential rotation along poloidal components of vorticity. Furthermore, we derive new conservation law for vorticity flux.

The present paper is organized as follows. In Section 2, relativistic versions of Helmholtz's three theorems on vorticity flux conservation are derived using an alternative approach based on Greenberg's theory of spacelike congruence generated by vortex lines and $(1 + 1) + 2$ decomposition of gradient of fluid's 4-velocity. Section 3 is devoted to the derivation of streamline invariants and the formulation of vorticity winding. In Section 4, we obtain new conservation law for the vorticity flux.

Convention: Space-time metric is of signature +2. Semi-colon (;) and comma (,) are, respectively, used to denote covariant derivative and partial derivative. Speed of light c is assumed to be unity.

2. Helmholtz's theorems

In this section, we obtain an alternative derivation of exact relativistic version of Helmholtz's theorems. We demonstrate that a relativistic version of Helmholtz's first theorem describes vorticity flux conservation inside a vortex tube when the variation of flux is measured by a comoving observer with the fluid along a vortex tube. Such conservation of flux is independent of proper time. We will also show that a relativistic version of Helmholtz's third theorem describes vorticity flux conservation in a streamline tube whose cross-sectional area lies in a spacelike two-dimensional subspace orthogonal to both stream and vortex lines. Such flux conservation is in proper time as the perfect fluid evolves and vortex lines are material lines. In order to prove these two results, we begin with Euler's equation that governs the motion of a perfect fluid. Euler's equation is as follows [23]:

$$(\rho + p)u'_a = -p_{,a} - p_{,b}u^b u_a \quad (2.1)$$

where $u'_a = u_{a;b} u^b$ denotes the 4-acceleration vector field of the fluid. u_a is the 4-velocity of the fluid and normalized according to $u^a u_a = -1$. The proper mass density and pressure are, respectively, represented by ρ and p . It is assumed that the fluid is composed of baryons whose proper number density n is conserved

$$(nu^a)_{;a} = 0. \quad (2.2)$$

The first law of thermodynamics is [23]:

$$d\left(\frac{\rho}{n}\right) = Tds - pd\left(\frac{1}{n}\right), \quad (2.3)$$

where T and s denote, respectively, the local temperature and the entropy per baryon. The relativistic enthalpy per baryon called chemical potential is expressed as:

$$\mu = \frac{\rho + p}{n} \quad (2.4)$$

If we assume that the entropy per baryon s is constant, then it follows from Eqs. (2.3) and (2.4) that

$$dp = nd\mu \tag{2.5}$$

Substituting Eqs. (2.4) and (2.5) in Eq. (2.1), we can reduce Euler’s equation in the following form:

$$\mu u'_a + \mu_{,a} + \mu_{,b} u^b u_a = 0. \tag{2.6}$$

It is known from relativistic version of Kelvin’s circulation theorem for a perfect fluid that the vorticity flux equals the closed contour line integral $\oint \mu u_a dx^a$. This integral is equivalent to a surface integral $\oint W_{ab} dS^{ab}$ where W_{ab} is the fluid particle vorticity 2-form [24] and dS^{ab} is an element of area on a two-dimensional surface bounded by the contour C . The conservation of vorticity flux means that the value of this integral is the same for all times when each point in the contour C is dragged along the fluid flow (mathematically, it is Lie transported along u^a) [11, 18]. The conditions required for flux conservation are as follows: (i) W_{ab} satisfies the closure property (i.e., $W_{[ab;c]} = 0$, where the square bracket indicates skew-symmetrization), and (ii) the matrix of W_{ab} admits eigen vectors with zero eigen values [11]. The closure property of W_{ab} is automatically satisfied in the case of a perfect fluid if W_{ab} is expressed as a curl of particle energy-momentum convector μu_a [24]. Its explicit expression is given by

$$W_{ab} = (\mu u_b)_{;a} - (\mu u_a)_{;b}. \tag{2.7}$$

Contraction of Eq. (2.7) with u^a yields Euler’s equation in the form given as below:

$$u^a W_{ab} = 0. \tag{2.8}$$

Dualizing Eq. (2.7) and contracting the resulting equation with u_b , we get

$$W^*{}^{ab} u_b = -V^a, \tag{2.9}$$

where an overhead star (*) is used for Hodge dualization. $V^a = \mu \omega^a$ and $\omega^a = \eta^{abcd} u_{b;c} u_d$ represents the kinematic vorticity vector of the fluid. It is to be noted that the factor $\frac{1}{2}$ which

appears in the usual definition of vorticity vector [9] is ignored only for calculational purpose, and due to this omission, there is no loss of generality. η^{abcd} denotes the Levi-Civita skew-symmetric tensor.

Inverting Eq. (2.9), we get

$$W^{ab} = -\eta^{abcd} V_c u_d \quad (2.10)$$

which satisfies

$$W_{ab} V^b = 0. \quad (2.11)$$

It is evident from Eqs. (2.8) and (2.11) that u^a and V^a are eigen vectors of vorticity 2-form W_{ab} with zero eigen value. Inverting Eq. (2.10), we get

$${}^*W^{ab} = V^a u^b - V^b u^a, \quad (2.12)$$

Since $V^a = \mu \omega^a$ is an eigen vector of W_{ab} with zero eigen value, it represents a flux vector of W_{ab} [11]. Hereafter, V^a will be referred to as a ‘‘vorticity flux’’ vector.

Because W_{ab} is a curl, we have

$${}^*W_{;b}^{ab} = 0. \quad (2.13)$$

Substituting Eq. (2.12) in Eq. (2.13) and contracting the resulting equation with u^a and m^a , respectively, we get

$$V_{;a} m^a + V \left(m_{;a}^a - u_a' m^a \right) = 0 \quad (2.14)$$

and

$$V_{;a} u^a + V \left(u_{;a}^a - u_{a,b} m^a m^b \right) = 0, \quad (2.15)$$

where m^a is unit spacelike vector field along vortex lines.

A spacelike congruence of vortex lines is generated by unit spacelike vector field m^a with properties $m^a m_a = 1$, $m_{a;b} m^a = 0$, and $m_a u^a = 0$. In the derivation of Eqs. (2.14) and (2.15), we have used $V^a = V m^a$, where V denotes the magnitude of the vorticity flux vector V^a and is equal to $\mu\omega$.

Since the vorticity flux vector V^a is orthogonal to the 4-velocity of the fluid at all points along a vortex line, a comoving observer with the fluid to observe deformation of a vortex tube erects a screen lying in a spacelike two-dimensional tangent subspace orthogonal to both stream and vortex lines generated by u^a and m^a , respectively. Greenberg's expansion parameter $\hat{\theta}$ of a vortex tube is expressed as:

$$\hat{\theta} = u'_a m^a \tag{2.16}$$

and

$$\hat{\theta} = \frac{1}{\hat{A}} \frac{d\hat{A}}{d\sigma}, \tag{2.17}$$

where $p_b^a = \delta_b^a + u^a u_b - m^a m_b$ is the projection tensor and \hat{A} is the cross-sectional area of a vortex tube that lies in a spacelike two-dimensional tangent subspace orthogonal to both u^a and m^a . The arc-length is denoted by σ and $\frac{d}{d\sigma}$ is the directional derivative along a vortex line. Substituting Eqs. (2.16) and (2.17) in Eq. (2.14), we get

$$\frac{d}{d\sigma} (\mu\omega\hat{A}) = 0, \tag{2.18}$$

which is an exact relativistic version of Helmholtz's first theorem. It is evident from Eq. (2.18) that the variation in vorticity flux of a vortex tube is measured along the tube and the flux remains constant inside a tube. The proper time τ plays no role in such variation of flux. Since an observer employed to measure flux is comoving along vortex line, a vortex tube is a material tube. In relativistic framework, a vortex tube to be a material tube is automatically associated with Helmholtz's first theorem because its derivation originates from Euler's equation. An exact relativistic analogue of Helmholtz's first theorem is not obtainable kinematically.

In order to obtain Helmholtz's third theorem, we use (1 + 1) + 2 decomposition of the gradient of 4-velocity u_a of the fluid. In this formulation [25], the expansion parameter $\tilde{\theta}$ of a stream tube is expressed as:

$$\tilde{\theta} = u_{a,b} m^a m^b \quad (2.19)$$

and

$$\tilde{\theta} = \frac{1}{\tilde{A}} \frac{d\tilde{A}}{d\tau}, \quad (2.20)$$

where \tilde{A} denotes cross-sectional area of a stream tube lying in a spacelike two-dimensional tangent subspace orthogonal to both u^a and m^a . The arc-length measured along a streamline (or worldline) is denoted by τ and $\frac{d}{d\tau}$ represents the directional derivative along a streamline. On account of Eqs. (2.19) and (2.20), Eq. (2.15) takes the form

$$\frac{d}{d\tau} (\mu \omega \tilde{A}) = 0, \quad (2.21)$$

which is a relativistic version of Helmholtz's third theorem. It is observed from Eq. (2.21) that the variation in vorticity flux is measured along a streamline and the flux inside a stream tube remains constant in proper time τ as the fluid evolves according to Euler's equation of motion. This result can be understood in a sense that the volume occupied by a stream tube is the product of cross-sectional area of a stream tube and its length measured along a vortex line (being a material line). The vorticity flux passing through such cross-sectional area remains constant in proper time τ .

On account of Eq. (2.12), Eq. (2.13) can be put in two different forms which are given as below:

$$L_u V^a = V^b_{;b} u^a - u^b_{;b} V^a \quad (2.22)$$

where L_u denotes the Lie derivative with respect to u^a .

$$\left(\frac{V^a}{n} \right)_{;b} u^b = u^a_{;b} \left(\frac{V^b}{n} \right) + u^a \left(u^b_{;b} \frac{V^b}{n} \right), \quad (2.23)$$

In the derivation of Eq. (2.23), baryon conservation law Eq. (2.2) is used.

Projecting Eq. (2.22) orthogonal to both u^a and V^a , we get

$$p_b^a L_u V^b = 0, \tag{2.24}$$

which is Greenberg’s transport law [8]. Eq. (2.24) tells us that the timelike congruence generated by u^a and the spacelike congruence generated by V^a span a family of timelike 2-surfaces. Such 2-surfaces are referred to as vortex flux surfaces (or vorticity flux surfaces) [11]. Furthermore, Eq. (2.24) implies that vortex lines are material lines.

Eq. (2.23) is in a form as has been derived by Bekenstein and Oron [10] in the case of the magnetic field vector in order to show the frozen-in property of the magnetic field in a perfectly conducting magnetofluid dynamics. Similar conclusion holds for the vorticity flux vector V^a . Eq. (2.23) shows that the orthogonal connecting vector of any two fluid particles lying on a vortex line is proportional to $\left(\frac{V^a}{n}\right)$. This in turn leads to the fact that the fluid particles lying once on a vortex line will continue to remain on the same vortex line for all times as the fluid evolves.

3. Vorticity winding in axisymmetric stationary fluid configuration

This section is devoted to the study of vorticity winding caused by meridional circulation via differential rotation of a perfect fluid which is assumed to be axisymmetric and stationary. In this case, a space time admits two linearly independent commuting Killing vectors: $\xi_{(t)}^a$ generating a translational symmetry with open timelike lines as orbits and the other is a spacelike Killing vector $\xi_{(\varnothing)}^a$ generating rotations with closed orbits about a symmetry axis. There exists a family of invariant timelike 2-surfaces (which are identified with vorticity flux surfaces) generated by these two Killing vectors that correspond to ignorable coordinates $x^4 = t$ and $x^3 = \varnothing$ (so that $\xi_{(t)}^a = \delta_t^a$ and $\xi_{(\varnothing)}^a = \delta_{\varnothing}^a$). The ignorable coordinates t and \varnothing are usually called toroidal coordinates. We choose poloidal coordinates $x^1 = r$ and $x^2 = \theta$. All physical quantities including the metric tensor g_{ab} are independent of t and \varnothing .

From Eq. (2.8), we get

$$W_{t\theta} = -W_{tr} \frac{u^r}{u^\theta} \tag{3.1a}$$

$$W_{\varnothing\theta} = -W_{\varnothing r} \frac{u^r}{u^\theta} \tag{3.1b}$$

$$W_{rt}u^t + W_{r\varnothing}u^\varnothing + W_{r\theta}u^\theta = 0. \quad (3.1c)$$

Since W_{ab} is a curl, we have

$$W_{[ab;c]} = 0, \quad (3.2)$$

where the square bracket around indices indicates skew-symmetrization. From Eq. (3.2), we get

$$W_{tr,\theta} + W_{\theta t,r} = 0, \quad (3.3a)$$

$$W_{\theta\varnothing,r} + W_{\varnothing r,\theta} = 0. \quad (3.3b)$$

It follows from Eqs. (3.1a) and (3.3a) that

$$\frac{d}{d\tau}(\ln W_{tr}) = -u^\theta \left(\frac{u^r}{u^\theta} \right)_{,r}. \quad (3.4a)$$

Similarly, substitution of Eq. (3.1b) in Eq. (3.3b) gives

$$\frac{d}{d\tau}(\ln W_{\varnothing r}) = -u^\theta \left(\frac{u^r}{u^\theta} \right)_{,r}. \quad (3.4b)$$

From Eqs. (3.4a) and (3.4b), we get

$$\frac{d}{d\tau} \left(\ln \frac{W_{tr}}{W_{\varnothing r}} \right) = 0 \quad (3.5)$$

which on integration along the streamline generated by u^a gives

$$\frac{W_{tr}}{W_{\varnothing r}} = A = \frac{W_{t\theta}}{W_{\varnothing\theta}}, \quad (3.6)$$

where A is constant along the streamline. Eq. (3.4b) can be rewritten as:

$$\frac{d}{d\tau}(\ln W_{\varnothing r}) = -(u_{,r}^r + u_{,\theta}^\theta) + \frac{d}{d\tau}(\ln u^\theta) \quad (3.7)$$

From Eq. (2.2), we get

$$u_{,r}^r + u_{,\theta}^\theta + \frac{d}{d\tau}(\ln \sqrt{-gn}) = 0 \quad (3.8)$$

Substitution of Eq. (3.8) in Eq. (3.7) gives

$$\frac{d}{d\tau} \left(\ln \frac{W_{\varnothing r}}{n\sqrt{-gu}^\theta} \right) = 0 \quad (3.9)$$

which on integration along the streamline gives

$$W_{\varnothing r} = Bn\sqrt{-gu}^\theta, \quad (3.10)$$

where B is constant along the streamline.

Substituting Eq. (3.10) in Eq. (3.1b), we get

$$W_{\varnothing \theta} = -Bn\sqrt{-gu}^r. \quad (3.11)$$

Substituting Eqs. (3.6) and (3.10) in Eq. (3.1c), we get

$$W_{r\theta} = Bn\sqrt{-gu}^t (A + \Omega), \quad (3.12)$$

where $\Omega = \frac{u^\theta}{u^t}$ is the local velocity of rotation of the fluid.

It follows from Eqs. (3.6), (3.10) and (3.11) that

$$W_{tr} = ABn\sqrt{-gu}^\theta, \quad W_{t\theta} = -ABn\sqrt{-gu}^r. \quad (3.13)$$

Eq. (2.9) gives

$$V^a = \frac{-1}{2} \eta^{abcd} u_b W_{cd}. \quad (3.14)$$

Substitution of Eqs. (3.10)–(3.13) in the coordinate expansion of Eq. (3.14) gives

$$V^a = -Bn \left[\left(\delta_t^a - A \delta_{\varnothing}^a \right) + (u_t - Au_{\varnothing}) u^a \right] \quad (3.15)$$

which is the required expression for the vorticity flux vector. We now use Eq. (3.15) to find conserved quantity along a streamline from the conservation of the fluid helicity. The fluid helicity vector is given by Carter [11, 24] and Bekenstein [18] as follows

$$H^a = .^{ab} (\mu u_b) = -\mu V^a \quad (3.16)$$

whose divergence vanishes,

$$\left(\mu V^a \right)_{;a} = 0. \quad (3.17)$$

This is fluid helicity conservation. Eq. (3.17) can be cast in form

$$\left(\mu \sqrt{-g} V^a \right)_{,a} = 0 \quad (3.18)$$

or equivalently

$$\left(\ln \mu \right)_{,a} V^a \sqrt{-g} + \left(\sqrt{-g} V^r \right)_{,r} + \left(\sqrt{-g} V^\theta \right)_{,\theta} = 0. \quad (3.19)$$

Substituting Eq. (3.15) in Eq. (3.19), we get

$$\frac{d}{d\tau} \left[\ln \mu B (u_t - Au_{\varnothing}) \right] = 0 \quad (3.20)$$

which on integration along a streamline gives

$$\mu(u_t - Au_\varnothing) = -C(\text{say}), \tag{3.21}$$

where the constant B is absorbed in a constant C along a streamline. The energy and angular momentum scalars in axisymmetric stationary fluid configuration are of the forms [11]

$$E = -\mu u_t, L = \mu u_\varnothing. \tag{3.22}$$

From Eqs. (3.21) and (3.22), it can be seen that

$$C = E + AL \tag{3.23}$$

which shows that the linear combination of energy and angular momentum is constant along a streamline but varies from streamline to streamline. Thus, C is a streamline invariant.

We now consider in view of Eq. (3.15) as follows

$$\Omega_{,a} V^a = -Bn\Omega_{,a} \left[(\delta_t^a - A\delta_\varnothing^a) + (u_t - Au_\varnothing)u^a \right] - B(u_t - Au_\varnothing)n\Omega_{,a}u^a. \tag{3.24}$$

Setting $V^a = \mu\omega^a$ and multiplying Eq. (3.24) by μ

and using Eq. (3.21) in the resulting equation, we get

$$\mu^2 \Omega_{,a} \omega^a = nBC \frac{d\Omega}{d\tau}. \tag{3.25}$$

In order to provide a meaningful interpretation of Eq. (3.25), we proceed as follows. In the absence of meridional circulation (i.e., $u^r = 0 = u^\theta$), it can be seen from Eqs. (3.1c) and (3.6) that $\frac{W_{tr}}{W_{\varnothing r}} = A = -\Omega$. This shows that the streamline invariant A is the angular velocity of vorticity flux surfaces commoving with the fluid in the absence of meridional circulation. But in the presence of meridional circulation (i.e., $u^r \neq 0, u^\theta \neq 0$, on account of Eqs. (3.1c) and (3.12), we observe that $A \neq -\Omega$. This means that the streamline invariant A which is seen to represent the angular velocity of vorticity flux surfaces will no longer be equal to fluid's angular velocity Ω in the presence of meridional circulation and hence we set $A = -\Omega_V$, where Ω_V represents the angular velocity of vorticity flux surfaces. Thus, meridional circulation causes mismatch between the angular velocities of vorticity flux surfaces and of the fluid. A short calculation from Eqs. (2.12) and (3.12) gives

$$\Omega - \Omega_V = \frac{\mu(u_\phi \omega_t - u_t \omega_\phi)}{nBK(u^t)^2} \quad (3.26)$$

where

$$K = (g_{t\phi}^2 - g_{tt}g_{\phi\phi}) > 0. \quad (3.27)$$

It is evident from Eq. (3.26) that the toroidal components ω_t and ω_ϕ of the fluid's vorticity vector vanish in the absence of meridional circulation. Notice that $A = -\Omega_V$ is streamline invariant, i.e., $\frac{d\Omega_V}{d\tau} = 0$. Thus, it follows from Eqs. (3.25) and (3.26) that

$$\mu^2 \Omega_{,a} \omega^a = nC \frac{d}{d\tau} \left[\frac{\mu(u_\phi \omega_t - u_t \omega_\phi)}{nK(u^t)^2} \right]. \quad (3.28)$$

The left-hand side of Eq. (3.28) represents the differential rotation along the poloidal components of the vorticity vector, whereas the right-hand side gives the proper time rate of change of a combination of toroidal components of the vorticity vector. This implies that the differential rotation along the poloidal vorticity cannot vanish until the vanishing of toroidal vorticity. Since the presence of meridional circulation ensures the existence of toroidal vorticity, meridional circulation causes the kind of effect that mimics like vorticity winding by stretching frozen-in vortex lines via differential rotation.

Because $\omega_t = 0 = \omega_\phi$ in the absence of meridional circulation, Eq. (3.28) reduces to

$$\Omega_{,a} \omega^a = 0 \quad (3.29)$$

which is the law of gravitational isorotation as is pointed out by Glass [26]. Thus, it seems that the meridional circulation causes vorticity winding due to the breakdown of the gravitational isorotation.

Further investigation is needed on the lines of recent work by Birkl et al. [27] in order to understand the role of meridional circulation in relation to vorticity winding via differential rotation.

4. Vorticity energy conservation in axisymmetric stationary case

This section is devoted to the derivation of vorticity energy conservation assuming that the perfect fluid configuration is axisymmetric and stationary. Substituting Eq. (2.12) in Eq. (2.13) and contracting the resulting equation with $V_{,a}$ we get

$$\frac{d}{d\tau} \left(\frac{1}{2} V^2 \right) = u_{;b}^a V_a V^b - V^2 u_{;b}^b. \quad (4.1)$$

Eliminating $u_{;b}^b$ with the aid of baryon conservation law Eq. (2.2), we obtain from Eq. (4.1) that

$$\frac{d}{d\tau} \left(\frac{1}{2} V^2 \right) = \frac{V^2}{n} \frac{dn}{d\tau} + V_{b;a} V^b u^a \quad (4.2)$$

which can be converted to the form

$$\frac{d}{d\tau} (V^2) = \frac{V^2}{n} \frac{dn}{d\tau} + (V_{b;a} - V_{a;b}) V^b u^a. \quad (4.3)$$

The last term on the right-hand side of Eq. (4.3) with the help of Eq. (3.15) can be simplified in the following form

$$(V_{b;a} - V_{a;b}) V^b u^a = nB \left(\frac{dV_t}{d\tau} - \frac{dV_\emptyset}{d\tau} \right). \quad (4.4)$$

Substitution of Eq. (4.4) in Eq. (4.3) gives

$$\frac{d}{d\tau} \left(\frac{V^2}{n} \right) + B \frac{d}{d\tau} (V_t - AV_\emptyset) = 0. \quad (4.5)$$

Since B and A are streamline invariant, we obtain from Eq. (4.5) that

$$\frac{d}{d\tau} \left[\frac{V^2}{n} + B(V_t - AV_\emptyset) \right] = 0 \quad (4.6)$$

which on integration along a streamline gives that

$$\frac{V^2}{n} + B(V_t - AV_\varnothing) = D \text{ (say)}. \quad (4.7)$$

Since $V^a = \mu\omega^a$, $V^2 = \mu^2\omega^2$, $V_t = \mu\omega_t$, and $V_\varnothing = \mu\omega_\varnothing$. Thus, Eq. (4.7) takes the form

$$\frac{\mu^2\omega^2}{n} + B\mu(\omega_t - A\omega_\varnothing) = D. \quad (4.8)$$

The first term of Eq. (4.8) represents the energy of the vorticity flux vector per baryon. The second term indicates the presence of covariant toroidal components of the vorticity vector ω^a . The quantity D is streamline invariant of the motion of frozen-in vortex lines and can be thought of as a vorticity energy conservation arising from fluid helicity conservation.

Acknowledgements

The author wishes to thank the Board of Editors for valuable suggestion regarding the revision of the manuscript.

Author details

Gunraj Prasad

Address all correspondence to: gunrajpr@gmail.com

Kamla Nehru Institute of Physical and Social Sciences, Sultanpur, UP, India

References

- [1] P. G. Saffman, *Vortex Dynamics*, Cambridge University Press, Cambridge 1992.
- [2] J. Serrin, *Mathematical Principle of Classical Fluid Dynamics* in, *Encyclopedia of Physics/Handbook der Physik* vol8/1 edited by S. Flugge (Springer Verlag Berlin 1959) p. 162–163.
- [3] W. Schröder and H. J. Treder, *Found. Phys.* 26, 417 (1996).
- [4] H. Eshraghi, *Phys. Plasma.* 10, 3577 (2003).

- [5] U. R. Fischer, *Ann. Phys.* 278, 62 (1999).
- [6] U. Ben-Yacov, *J. Phys. A: Math. Gen.* 27, 7165 (1994).
- [7] I. B. Birula, Z. B. Birula, and C. Sliwa, *Phys. Rev. A* 61, 032110 (2000).
- [8] P. J. Greenberg, *J. Math. Anal. Appl.* 30, 128 (1970).
- [9] J. Ehlers, *Gen. Rel. Grav.* 25, 1225 (1993).
- [10] J. D. Bekenstein and E. Oron, *Phys. Rev. D* 18, 1809 (1978).
- [11] B. Carter, in *Active Galactic Nuclei*, edited by C. Hazard and S. Mitton, p. 273–279, Cambridge University Press, Cambridge, 1979.
- [12] W. Kundt and M. Trümper, *Z. Phys.* 192, 41 (1966).
- [13] H. K. Moffat, *J. Fluid Mech.* 35, 117 (1969).
- [14] H. K. Moffat and R. L. Ricca, *Proc. Roy. Soc. Lond.* A439, 411 (1992).
- [15] H. K. Moffat, *Proc. Nat. Acad. Sci.* 111, 3663 (2014).
- [16] V. I. Arnold and B. A. Khesin, *Topological Methods in Hydrodynamics*, Springer-Verlag, NY, USA, 1998.
- [17] J. Cantarella, D. De Truck, H. Gluc, and M. Twytel, *J. Math. Phys.* 41, 5615 (2000).
- [18] J. D. Bekenstein, *Astroph. J.* 319, 207 (1987).
- [19] M. Tsamparlis and D. P. Mason, *J. Math. Phys.* 24, 1577 (1983).
- [20] T. Zwerger and E. Müller *Astron. Astroph.* 320, 209 (1997).
- [21] C. D. Ott, A. Burrows, E. Livine, and R. Walder, *Astroph. J.* 600, 834 (2004).
- [22] M. D. Duez, Y. T. Liu, S. L. Shapiro, M. Shibata, and B. C. Stephens, *Phys. Rev. D* 73, 104015 (2006).
- [23] C. W. Misner, K. S. Thorne, and J. A. Wheeler, *Gravitation*, Freeman, San Francisco 1973.
- [24] B. Carter and I. M. Khalatnikov, *Ann. Phys.* 219, 243 (1992).
- [25] G. Prasad, Rigidly Connected Magnetic lines: Twisting and Winding of magnetic lines, to be submitted for publication in *Gen. Rel. Grav.* (2016).
- [26] E. N. Glass, *J. Math. Phys.* 18, 708 (1977).
- [27] R. Birkel, N. Stergioulas, and E. Müller, *Phys. Rev. D* 84, 023003 (2011)

Statistics of Gyrotropic Vortex Dynamics in Submicron Magnetic Disks

Gary Matthew Wysin

Additional information is available at the end of the chapter

<http://dx.doi.org/10.5772/64849>

Abstract

Topological vortex excitations in thin magnetic nanodisks have attracted a lot of attention because of their dynamic stability and various charge-like properties, which make them suitable objects for data storage. They also have a natural gyrotropic orbital motion that can be described rather well by an approximate Thiele gyrotropic equation for the magnetization dynamics. The gyrotropic oscillation makes them available as a basis for natural oscillators at close to gigahertz frequencies. This gyrotropic motion is excited naturally even by thermal fluctuations. In addition, the gyrotropic oscillation frequency can be affected by external perturbations, which allows possibilities for the design of nanoscale detectors. The vortex moves in an effective potential, strongly determined by the shape anisotropy of the magnetic disk, which then determines the force appearing in the Thiele equation of motion. The motion of an individual vortex within a disk of circular or elliptical shape is considered theoretically, including stochastic thermal effects together with the deterministic gyrotropic effects. From simulations of the motion at different parameter values, a picture of the typical vortex position and velocity distribution within the disk is developed and compared with what is expected from the Thiele equation.

Keywords: magnetic vortex, topological charge, vortex potential, magnetic resonance, magnetic dots

1. Introduction: vortices in thin submicron magnetic disks

A cylindrically shaped thin disk of soft ferromagnetic material with a radius a on the order of 100 nm to a few microns and a thickness $L \ll a$ on the order of 10–50 nm provides an interesting system for the study of vortices [1, 2]. A magnetic configuration is described by its

local magnetization $\vec{M}(\mathbf{r})$, which is the magnetic dipole moment per unit volume, at position \mathbf{r} . A material is considered with saturation magnetization M_s , which is the magnitude when the medium is completely magnetized along some axis. Due to the demagnetization effect, which is responsible for *shape anisotropy*, any such magnetic system tends to avoid the formation of magnetic poles on the surfaces, if possible, which would raise the total energy. For a thin circular disk, the local magnetization $\vec{M}(\mathbf{r})$ as a function of position \mathbf{r} may tend to do two things: (1) $\vec{M}(\mathbf{r})$ will have a strong tendency to point within the plane of the disk [3], if possible; (2) $\vec{M}(\mathbf{r})$ may then follow the curved circular boundary at the disk edge, thereby completely avoiding the generation of any poles on the edge. This prevents any strong magnetic field lines from passing through the space surrounding the disk edge.

Within the disk, the forces of ferromagnetic exchange cause $\vec{M}(\mathbf{r})$ also to have a circular structure and remain close to the disk plane. At the disk center, which is a singular point, remaining in the disk plane is impossible, and $\vec{M}(\mathbf{r})$ then points perpendicular to the plane of the disk, forming tiny north/south poles on opposite faces at the disk center. The resulting circular form of $\vec{M}(\mathbf{r})$, together with its central poles in a core region, is a magnetic vortex. It is a type of magnetic excitation that is topologically stable and acts in many ways like a particle, when exposed to forces.

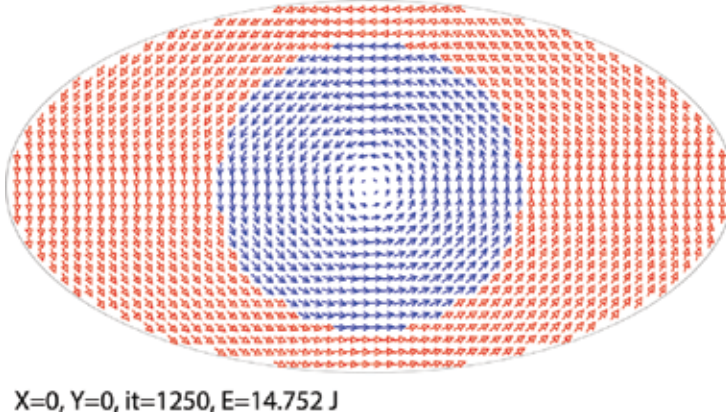


Figure 1. The magnetization field $\vec{M}(\mathbf{r}) = M_s \hat{m}(\mathbf{r})$ of a vortex centered in a nanodisk with principal axes $a = 60$ nm, $b = 30$ nm, thickness $L = 10$ nm, from the spin alignment relaxation scheme for the micromagnetics model, Section 2.4. The cell size is $a_{\text{cell}} = 2$ nm. Arrows show only the in-plane projection, (m_i^x, m_i^y) . Blue line (red open) arrows indicate positive (negative) values of out-of-plane component m_i^z . The core, where m_i^z is larger, appears as a hole in this projection. Even though the system is elliptical, note that the core region remains close to circular.

One can also consider deviations from circular symmetry, such as in elliptic nanodisks, where magnetic vortex dynamics has been studied by measuring their radio frequency oscillations [4] and even by direct electrical contact [5] to a nanodisk. An example of a magnetic vortex

centered in a thin elliptical nanodisk is shown in **Figure 1**. It has been obtained from a numerical relaxation algorithm [6], see Section 2.4 below. Although there is a tendency for $\vec{M}(r)$ to follow the boundary, one sees that the exchange forces are more dominating, and especially the core structure of the vortex retains a circular shape. The locus where the perpendicular component M^z changes sign is obvious as a circle in **Figure 1**.

1.1. Vortex charges

The magnetization profile $\vec{M}(\mathbf{r})$ of a vortex may point either in a counterclockwise (CCW) or clockwise (CW) direction around the disk. This twofold degeneracy is associated with its *circulation charge* $c = \pm 1$, which is also referred to as *chirality*. It provides one topologically stable geometric property that could be used for data storage in a vortex, if it can be reliably controlled and detected.

In principle, a vortex profile $\vec{M}(\mathbf{r})$ also has a *vorticity charge* $q = \pm 1$, which corresponds to the *direction of rotation* of $\vec{M}(\mathbf{r})$ as one moves along a closed path encircling the core. The value $q = +1$ holds for the vortices described here, which are controlled by demagnetization effects (\vec{M} being forced to follow the boundary). The value $q = -1$, known as an *antivortex*, would only be energetically stable if demagnetization effects were not present. The limit of zero thickness would eliminate the relevant demagnetization and make antivortices energetically possible.

The magnetization at the vortex core can take one of two values, $\vec{M}(0) = \pm M_s \hat{z} = p M_s \hat{z}$, where $p = \pm 1$ is the *polarization charge*. Because there is an energy barrier to flip the core polarization from $p = +1$ to $p = -1$, it offers yet another charge that could be useful for data storage and manipulation.

1.2. Vortex potential and forces

The above-described magnetic vortex will have its minimum energy when it is centered in the disk. The location of the poles (where \vec{M} points perpendicular to the disk) defines the location of the *vortex core*, which we denote by position vector $\mathbf{R} = (X, Y)$, measured along the x, y Cartesian axes within the disk plane. Because the system is assumed to be thin, only two coordinates X, Y are needed to locate the core. Further, the magnetization itself has little dependence on the coordinate (z) perpendicular to the disk. We take $\mathbf{R} = (0, 0)$ for the vortex at the center of the disk. It is possible to imagine that the vortex core becomes slightly displaced from the disk center. In that case, a slight deformation of the vortex structure $\vec{M}(r)$ takes place, while the demagnetization effects at the disk edge still try to maintain $\vec{M}(r)$ parallel to the edge. The net result of the displacement is a slight increase in total energy. The vortex, as a quasi-particle, lives in some effective potential $U(\mathbf{R})$, which has something approximating a parabolic form [6], with the minimum at the disk center,

$$U(\mathbf{R}) \approx \frac{1}{2} k_F \mathbf{R}^2, \quad (1)$$

where k_F is a force constant. This further implies an *effective force* \mathbf{F} back towards the disk center, according to the gradient of the potential,

$$\mathbf{F} = -\vec{\nabla}U(\mathbf{R}) \approx -k_F \mathbf{R}. \quad (2)$$

For a circular disk, the potential is circularly symmetric, and then small displacements lead to a circularly symmetric Hooke's law type of force. It is also possible to consider magnetic vortices in a cylindrical disk of *elliptical* shape [7], defined by principal axes a and $b < a$:

$$\frac{x^2}{a^2} + \frac{y^2}{b^2} = 1. \quad (3)$$

This situation leads correspondingly to a modification of the potential also to an approximately elliptic form [8],

$$U(\mathbf{R}) \approx \frac{1}{2} (k_x X^2 + k_y Y^2). \quad (4)$$

The parabolic functional form now has separate force constants k_x, k_y along the two principal axes. It gives a force,

$$\mathbf{F} = (-k_x X, -k_y Y). \quad (5)$$

While a vortex in a nanodisk experiences a force directed roughly towards the disk center, its motion tends to be in an orbital sense, which is the gyrotropic oscillation mode [9, 10]. This is discussed further in Section 3 on dynamics. Before coming to that, we begin by a quantitative description of the calculation of vortex structures.

2. Analysis of quasi-stationary vortices in a nanodisk

The theoretical analysis is based on the statics and dynamics of the magnetization field, which is now assumed to keep a uniform magnitude M_s , but a spatially varying direction, by writing $\vec{M}(\mathbf{r}) = M_s \hat{m}(\mathbf{r})$, where $\hat{m}(\mathbf{r})$ is a unit vector. From the energetics expressed in terms of $\hat{m}(\mathbf{r})$,

equations for the vortex structure and motion can be developed. See Ref. [11] for a general discussion of the calculation of magnetic vortex structures and properties.

2.1. Energetics of a continuum nanomagnet

The system is governed by ferromagnetic exchange energy and interactions of \vec{M} generally with the demagnetization field \vec{H}^M (self-generated by \vec{M}) and any possible externally applied field \vec{H}^{ext} . A continuum Hamiltonian for the system is

$$\mathcal{H} = \int dV \left\{ A \nabla \vec{m} \cdot \nabla \vec{m} - \mu_0 \left(\vec{H}^{ext} + \frac{1}{2} \vec{H}^M \right) \cdot \vec{M} \right\}, \quad (6)$$

where μ_0 is the permeability of free space, and A is the exchange stiffness. One commonly used material is Permalloy-79 (Py, 79% nickel, 21% iron), with exchange stiffness about 13 pJ/m and saturation magnetization $M_s = 860$ kA/m [12]. The magnetization changes its direction over a length scale λ_{ex} called the exchange length. Exchange energy of the order A/λ_{ex}^2 competes with demagnetization energy of the order $\frac{1}{2}\mu_0 M_s^2$. Equating these terms gives the definition of the length scale,

$$\lambda_{ex} = \sqrt{\frac{2A}{\mu_0 M_s^2}}. \quad (7)$$

For Py, $\lambda_{ex} \approx 5.3$ nm. Exchange forces dominate over lengths less than λ_{ex} , but demagnetization dominates over larger lengths, allowing the $\vec{M}(\mathbf{r})$ field to change its direction. At a boundary, the exchange effects are much less present, and demagnetization helps $\vec{M}(\mathbf{r})$ to point parallel to the boundary, if possible.

2.2. The demagnetization field \vec{H}^M in a thin magnetic film

The demagnetization field is determined by the global configuration of the magnetization of the system; it is derived from considerations of magnetostatics (see Ref. [13] for the details of the approach used here). In the absence of an external applied magnetic field, one has magnetic induction $\vec{B} = \mu_0(\vec{H}^M + \vec{M})$. Gauss' law, $\vec{\nabla} \cdot \vec{B} = 0$, then becomes

$$\vec{\nabla} \cdot \vec{H}^M = -\vec{\nabla} \cdot \vec{M}. \quad (8)$$

By assuming the demagnetization field comes from a scalar potential via $\vec{H}^M = -\vec{\nabla} \Phi_M$, a Poisson equation for the magnetostatics is obtained:

$$-\nabla^2 \Phi_M = \rho_M, \quad \rho_M \equiv -\vec{\nabla} \cdot \vec{M}. \quad (9)$$

Therefore, the magnetization $\vec{M}(\mathbf{r})$ produces an effective magnetic charge density ρ_M , which is the source in this Poisson equation. The solution for scalar potential Φ_M can be obtained by various numerical methods. Generally, we have used a scheme based on discretization of the system (introduction of a spatial grid), together with appropriate Green's functions for the Poisson equation. In addition, it is extremely helpful to use the approximation that the disk is very thin, $L \ll a$, where a is the radius (or the semi-major axis for an elliptical disk). In this case, both \vec{M} and \vec{H}^M do not depend on the vertical coordinate z along the disk axis. Then, the problem can be solved by effective two-dimensional (2D) Green's functions [14]. The components $\alpha = x, y, z$ of the demagnetization field can be expressed as 2D convolution integrals,

$$H_\alpha^M(\mathbf{r}) = \int d^2 \mathbf{r}' \sum_{\beta=x,y,z} G_{\alpha\beta}(\mathbf{r}-\mathbf{r}') M_\beta(\mathbf{r}') \quad (10)$$

where $G_{\alpha\beta}(\mathbf{r}-\mathbf{r}')$ represents a tensor Green's function, and the integration is over 2D positions, for example now $\mathbf{r} = (x, y)$. The evaluation of these integrals can be accelerated through the use of fast Fourier transforms [15].

2.3. Discretization and micromagnetics for simulations

For numerical solutions of the magnetization field $\vec{M}(\mathbf{r}) = M_s \hat{m}(\mathbf{r})$, it is necessary to partition the system into cells labeled by index i for positions \mathbf{r}_i . We use a square grid of cells of individual size $a_{\text{cell}} \times a_{\text{cell}} \times L$, with $a_{\text{cell}} = 2.0$ nm, and disk thickness $L = 5$ nm and $L = 10$ nm. At the center of each cell is a unit direction vector \hat{m}_i , whose motion is to be followed. Each cell contains a magnetic dipole moment $\vec{\mu}_i$ of magnitude $\mu = La_{\text{cell}}^2 M_s$ and direction \hat{m}_i . This *micromagnetics* approach [16, 17] then represents the original continuum system, but with a discretized 2D micromagnetics Hamiltonian,

$$\mathcal{H} = -J \left[\sum_{(i,j)} \hat{m}_i \cdot \hat{m}_j + \frac{a_{\text{cell}}^2}{\lambda_{\text{ex}}^2} \sum_i \left(\tilde{H}_i^{\text{ext}} + \frac{1}{2} \tilde{H}_i^M \right) \cdot \hat{m}_i \right], \quad (11)$$

where the effective exchange constant and energy scale between nearest-neighbor cells is $J = 2AL$, and magnetic fields have been brought to dimensionless forms,

$$\tilde{H}_i^{\text{ext}} = \tilde{H}_i^{\text{ext}} / M_s, \quad \tilde{H}_i^M = \tilde{H}_i^M / M_s. \quad (12)$$

The presence of the factor $a_{\text{cell}}^2 / \lambda_{\text{ex}}^2$ gives the relative strength of demagnetization effects compared with exchange effects. For the micromagnetics approach to be valid, this factor should be much less than 1. The transverse cell size a_{cell} should then be less than the exchange length. The micromagnetics approach, with the assumption that only the direction of \vec{M} is changing, makes the implicit assumption that demagnetization effects are a perturbation on exchange effects. Obviously, the Green's functions $G_{\alpha\beta}(\mathbf{r} - \mathbf{r}')$ must also be brought to a discrete form to carry out the calculation of \tilde{H}_i^M .

The Hamiltonian can be used to define the net magnetic inductions that act on each cell's magnetic dipole $\vec{\mu}_i$ according to

$$\vec{B}_i = -\frac{\delta \mathcal{H}}{\delta \vec{\mu}_i} = \frac{J}{\mu} \vec{b}_i, \quad (13)$$

where the dimensionless magnetic inductions are

$$\vec{b}_i = \sum_{j \in z(i)} \hat{m}_j + \frac{a_{\text{cell}}^2}{\lambda_{\text{ex}}^2} (\tilde{H}_i^{\text{ext}} + \tilde{H}_i^M). \quad (14)$$

The first term involves a sum over the nearest neighbors $z(i)$ of cell i ; it is the exchange field. The second term represents the combination of external and demagnetization fields. The effective strength of magnetic inductions is indicated by the unit we use for simulations,

$$B_0 \equiv J / \mu = \mu_0 M_s \lambda_{\text{ex}}^2 / a_{\text{cell}}^2. \quad (15)$$

In the results presented here with $a_{\text{cell}} = 2.0$ nm, and Py parameters, one has $\mu_0 M_s^2 \approx 1.08$ T and $B_0 \approx 7.59$ T. B_0 gives the order of magnitude of the exchange fields; the demagnetization fields are considerably weaker.

2.4. Static vortex configurations from a relaxation scheme

Static vortex configurations are derived as the stationary solutions of the dynamic equations of motion. At zero temperature, the undamped dynamic equation of motion is a simple torque equation for each magnetic dipole, which interacts with its local net field:

$$\frac{d\vec{\mu}_i}{dt} = \gamma \vec{\mu}_i \times \vec{B}_i. \quad (16)$$

Note that this holds because $\vec{\mu}_i/\gamma = \vec{S}_i$ is the spin angular momentum of the cell, whose time derivative is the torque, $\vec{\mu}_i \times \vec{B}_i$. The equation can be written in terms of the dimensionless quantities, also defining a dimensionless time τ ,

$$\frac{d\hat{m}_i}{d\tau} = \hat{m}_i \times \vec{b}_i, \quad \tau \equiv \gamma B_0 t. \quad (17)$$

The unit of time used for simulations is $t_0 \equiv (\gamma B_0)^{-1}$. For Py parameters, it takes the value $t_0 \approx 0.75$ ps. Its reciprocal also defines a simulation frequency unit, $f_0 \equiv \gamma B_0 \approx 1.336$ THz.

For static configurations, however, the time derivatives in Eq. (17) are zero. This implies that each dipole $\vec{\mu}_i$ or its unit vector \hat{m}_i must align with the local field in that cell, \vec{b}_i .

Thus, an algorithm that iteratively points each \hat{m}_i along its current value of \vec{b}_i will tend to move the system towards a static configuration. We call this approach a *spin alignment* relaxation scheme [18]. To carry it out, some initial state must be chosen from which to begin the iteration. Assume that the direction vectors are defined in terms of *spherical planar angles* (ϕ_i, θ_i) , according to

$$\hat{m}_i = (\cos \theta_i \cos \phi_i, \cos \theta_i \sin \phi_i, \sin \theta_i). \quad (18)$$

In this notation, ϕ_i is referred to as the *in-plane angle* and θ_i is the *out-of-plane angle*, which can be positive or negative. The approximate in-plane structure of a vortex located at position $\mathbf{R} = (X, Y)$ in a disk can be expressed using the vorticity $q = +1$ as

$$\phi_i = q \tan^{-1} \left(\frac{y_i - Y}{x_i - X} \right) + \phi_0 \quad (19)$$

where (x_i, y_i) is the 2D location of micromagnetics cell i , and $\phi_0 = c \frac{\pi}{2}$ depends on the vortex circulation charge. There is not a corresponding analytic form for the out-of-plane component. Instead, one can start with all $\theta_i = 0$, that is, a planar vortex. However, the iteration will be such that all θ_i will remain zero, unless some small nonzero deviation is included. Therefore, small random values of θ_i can be used for the initial state. A nonzero out-of-plane component

will then grow naturally as the system relaxes into a vortex state. The process is repeated until the changes in the \hat{m}_i become insignificant (less than about one part in 10^8).

For a circular or elliptic disk, if the vortex is initiated away from the center, as the spin alignment relaxation proceeds, the vortex will be found to both develop an out-of-plane component and also move to the disk center. Spin relaxation is an energy minimization algorithm; the system moves to its nearest minimum energy state, which is that configuration centered in the disk. A profile of a vortex obtained this way in an elliptic disk is shown in **Figure 2**. The projection of the dipoles onto the disk plane is shown. Note that there is a core region with a radius of the order of λ_{ex} (region where \vec{M} has significant out-of-plane components, appearing as a hole in the diagram). Interestingly, the core tends to keep a reasonably circular form, as seen by the locus of points where the sign of M^Z reverses.

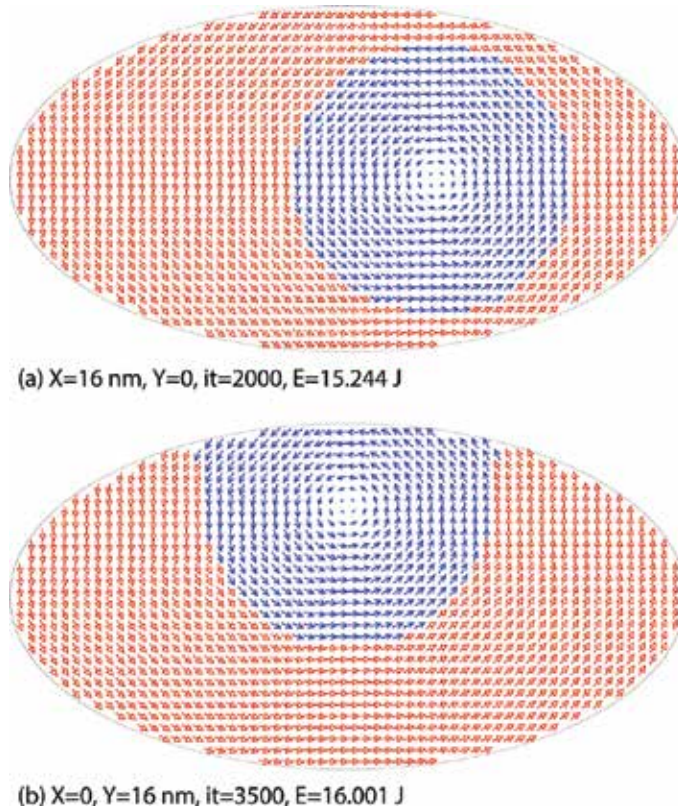


Figure 2. Vortex structures for an elliptical nanodisk with $a=60 \text{ nm}$, $b=30 \text{ nm}$, $L=10 \text{ nm}$, using cell size $a_{cell}=2.0 \text{ nm}$ in the spin alignment relaxation scheme, including a Lagrange constraint on position. (a) Vortex is held at $X=16 \text{ nm}$, $Y=0$, resulting in total energy $E=15.244 \text{ J}$ after 2000 iterations. (b) Vortex is held at $X=0$, $Y=16 \text{ nm}$, resulting in total energy $E=16.001 \text{ J}$ after 3500 iterations. Compare Figure 1, where $X=Y=0$ and the energy is lower.

2.5. Effective potentials of a vortex in a nanodisk

Spin alignment relaxation can also be used to estimate the effective potential $U(\mathbf{R})$ for the vortex, by including a constraint on the vortex position $\mathbf{R} = (X, Y)$. The effective potential is the system energy \mathcal{H} less any constraint energy, for a chosen vortex position. A constraint on vortex position can be enforced with the use of Lagrange's undetermined multipliers [6]. Physically, a vortex can be shifted away from the disk center, by the application of a magnetic field within the disk plane. A uniform field \vec{H}^{ext} along $\pm x$ will displace the vortex along $\pm y$, and vice versa, with the sign determined by the vortex chirality. Buchanan et al. [8] were able to map out the vortex potential energy numerically using the field to move the vortex to different equilibrium positions. This gives one way to obtain the effective force constants k_x and k_y .

Rather than using a uniform applied field, it is possible to imagine the application of a spatially varying field, which primarily acts on the core region of the vortex. These fictitious extra fields are the undetermined Lagrange multipliers; they are determined through course of the calculation. Simultaneously, another constraint is applied that ensures unit length for the direction vectors \hat{m}_i . The fictitious fields exert torques on the cells in the core region, which hold the vortex in the desired location, without significantly changing the overall vortex structure. Thus, a quasi-static vortex structure can be obtained numerically, for whatever position is desired, within reason. The approach works best for a vortex near the disk center. For the same elliptical disk of **Figure 1**, the vortex has been relaxed by this scheme to positions 16 nm from the center, in **Figure 2**. Note that the energy is higher for a displacement along the shorter axis of the ellipse [8].

The work here considers stable vortex states. It should be kept in mind that for some parameters or disk sizes, the vortex could become unstable towards the formation of a lower energy quasi-single-domain state (nearly uniform $\vec{M}(\mathbf{r})$), or some other multi-domain state without a vortex. This is especially likely in the case of elliptic disks with a high aspect ratio ($b \ll a$), where demagnetization will strongly favor \vec{M} aligning with the longer axis [7]. The vortex state will also become unstable in a circular disk if it is too thin, which minimizes the demagnetization forces from the circular edge, which usually stabilize a vortex. Also, if the disk is too thick ($L \gg a$), again, demagnetization will cause \vec{M} to approximately align with the long axis and a vortex will not be stable.

Typical vortex potentials obtained from Lagrange-constrained spin alignment for circular nanodisks are shown in **Figure 3**, for various radii with fixed thickness $L = 4.0$ nm. The minimum energy region is close to parabolic form; however, as the vortex is placed closer to the edge, a lack of stability (downward curvature) appears. Using the interior region of the potential, the effective force constants k_F for circular disks or even k_x and k_y for elliptical disks can be estimated quite accurately. In the example of **Figure 3**, one can observe that k_F becomes smaller for the larger radii disks. See Refs. [6, 7] for further details.

In elliptical disks [4, 7, 8], the force constant for displacement along the longer disk axis is found to be weaker than that along the shorter disk axis; see **Figures 1** and **2**. Thus, the potential

acquires an elliptical shape that is determined by the original geometrical shape of the disk. For a disk with semi-major axes a and b with $b < a$, we have found that for adequately large nanodisks and b of sufficient size to stabilize the vortex, the ratio of force constants asymptotically approaches the relation,

$$\sqrt{k_x/k_y} \approx b/a. \tag{20}$$

This has the correct limit for a circular disk, $k_x = k_y$. The relation is summarized by saying that the *geometric ellipticity*, b/a , directly determines an *energetic ellipticity*, $\sqrt{k_x/k_y}$. The energetic ellipticity can be seen to determine the shape of the elliptical vortex orbits at constant energy in the phase space.

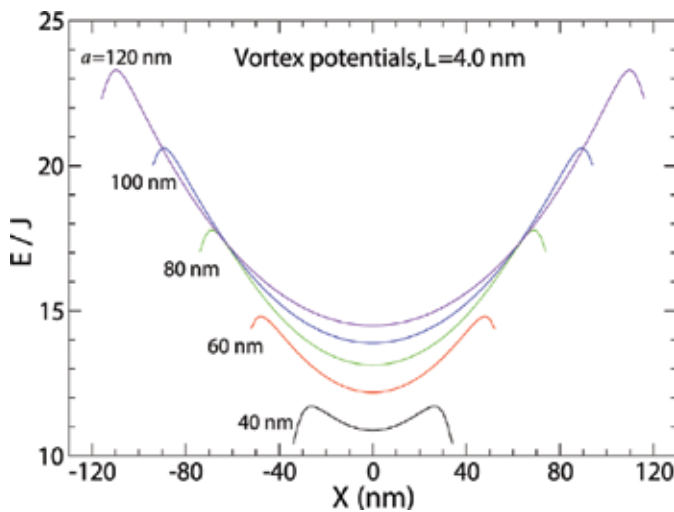


Figure 3. Numerically determined vortex potentials, in units of the effective cell exchange constant $J = 2AL$, for circular Py nanodisks of thickness $L = 4.0$ nm and indicated radii, as found from the Lagrange-constrained spin alignment relaxation. The vortex becomes unstable towards escaping from the disk in the regions of downward curvature.

3. Magnetic dynamics and the Landau-Lifshitz-Gilbert-Langevin equations

The dynamics described by Eq. (16) or its dimensionless form in Eq. (17) is not completely realistic, because it does not include the effects of damping nor of temperature and its statistical fluctuations. Both the damping and thermal effects could be quite large on a vortex. When only damping with a dimensionless parameter α is included, the well-known Landau-Lifshitz-Gilbert (LLG) dynamic equation [19, 20] is obtained [Eq. (21) but with all $\vec{b}_{s,i} = 0$]. Here, we

take that one step further and also include stochastic magnetic fields $\vec{b}_{s,i}(t)$ that represent the effects of temperature. This leads to a Langevin equation derived from the LLG equation [21], for an individual micromagnetics cell,

$$\frac{d\hat{m}_i}{d\tau} = \hat{m}_i \times (\vec{b}_i + \vec{b}_{s,i}) - \alpha \hat{m}_i \times [\hat{m}_i \times (\vec{b}_i + \vec{b}_{s,i})]. \quad (21)$$

The changes in \hat{m}_i are a superposition of deterministic effects (from \vec{b}_i) and stochastic effects (from $\vec{b}_{s,i}$). The stochastic fields act to bring the system to thermal equilibrium. That takes place provided their correlations follow the fluctuation–dissipation (FD) theorem, which can be written for this problem in the dimensionless quantities as (site index i is suppressed)

$$\langle b_s^\lambda(\tau) b_s^{\lambda'}(\tau') \rangle = 2\alpha \mathcal{T} \delta_{\lambda\lambda'} \delta(\tau - \tau'). \quad (22)$$

Here, $\delta_{\lambda\lambda'}$ is a Kronecker delta and the indices λ, λ' refer to any of the Cartesian coordinates; $\delta(\tau - \tau')$ is a Dirac delta function. The dimensionless temperature \mathcal{T} is thermal energy scaled by J ,

$$\mathcal{T} \equiv \frac{kT}{J} = \frac{kT}{2AL}, \quad (23)$$

where k is Boltzmann's constant and T is the absolute temperature. The FD relation indicates how the stochastic magnetic fields move energy into and out of the system, in random processes that nevertheless can be quantitatively measured. The stochastic fields are included only when a study of temperature effects in real time is desired. They can be set to zero if the zero-temperature dynamics is of interest, producing the LLG equation. Below we use solutions of Eq. (21) obtained appropriately for the type of system under study, be it $T = 0$ or $T > 0$.

3.1. The Thiele equation for vortex core motion

Magnetic excitations such as domain walls and vortices do not obey Newtonian dynamics. Instead, it can be shown from magnetic torque considerations (i.e., analysis of the $T = 0$ LLG equations) that the steady-state dynamics of the core velocity $V = \dot{R}$ is described by a *Thiele equation* [22],

$$\mathbf{F} + \mathbf{G} \times \mathbf{V} = 0. \quad (24)$$

The motion is governed by the *gyrovector* \mathbf{G} , which for vortices is a vector that points perpendicular to the disk plane, in a direction determined by the magnetization at the vortex core.

Consider a material with saturation magnetization M_s . In terms of the magnetization per unit area, $m_0 \equiv M_s L$, and the gyromagnetic ratio $\gamma = -1.76 \times 10^{11} \text{ T}^{-1} \text{ s}^{-1}$ of an electron (its magnetic moment divided by its angular momentum), the gyrovector of a vortex is

$$\mathbf{G} = G\hat{z} = 2\pi pqm_0\hat{z} / \gamma. \quad (25)$$

For the vortices in a disk, $q = +1$, while there are two core polarizations $p = \pm 1$ possible. The gyrovector points perpendicular to the disk in two possible directions. A solution of the Thiele equation then gives a description of the motion of a vortex, provided it remains as a particle-like stable object under the dynamic environment it is found in. A general review of vortex motion obeying a Thiele equation, even including an intrinsic mass, is given in [11].

Here, we suppose that a vortex is moving within a nanodisk of elliptical shape, at position $\mathbf{R} = (X, Y)$, with the force in Eq. (5) acting on it. One finds that it makes an elliptical orbital motion, whose gyrotropic frequency can be estimated from the Thiele equation [7]. A solution for the vortex velocity is obtained quickly by taking the cross product of $\mathbf{G} = G\hat{z}$ with the Thiele equation,

$$\mathbf{G} \times \mathbf{F} + \mathbf{G} \times (\mathbf{G} \times \mathbf{V}) = 0. \quad (26)$$

A vector identity is useful,

$$\mathbf{G} \times (\mathbf{G} \times \mathbf{V}) = (\mathbf{G} \cdot \mathbf{V})\mathbf{G} - (\mathbf{G} \cdot \mathbf{G})\mathbf{V}. \quad (27)$$

The vortex velocity points in the plane of the disk, but \mathbf{G} is perpendicular to that plane, so $\mathbf{G} \cdot \mathbf{V} = 0$. This gives the velocity as

$$\mathbf{V} = \frac{\mathbf{G} \times \mathbf{F}}{G^2} = \frac{1}{G} (k_y Y, -k_x X). \quad (28)$$

With $\mathbf{V} = (\dot{X}, \dot{Y})$, this is a pair of first-order differential equations, which can be directly integrated, starting from some initial vortex position $\mathbf{R}(0) = (X_0, Y_0)$. An elementary calculation gives elliptical motion, with instantaneous coordinates

$$\begin{aligned} X(t) &= X_0 \cos \omega_G t + Y_0 \frac{k_y}{G\omega_G} \sin \omega_G t \\ Y(t) &= Y_0 \cos \omega_G t - X_0 \frac{k_x}{G\omega_G} \sin \omega_G t \end{aligned} \quad (29)$$

where the gyrotropic frequency is determined by the geometric mean of the force constants, $\bar{k} \equiv \sqrt{k_x k_y}$:

$$\omega_G = -\frac{\sqrt{k_x k_y}}{G} = -\frac{\bar{k}}{G}. \quad (30)$$

The negative square root is used, because a vortex with \mathbf{G} along $+\hat{z}$ and a centrally directed force will move in the clockwise (or negative) direction in the xy plane. This result applies even when the vortex equilibrium position is displaced from the disk center by an applied magnetic field, using the effective force constants at that displaced location [8]. Buchanan et al. [8] found that the experimentally measured vortex oscillation frequency can be controlled by the application of an in-plane field, \vec{H}^{ext} ; especially, \vec{H}^{ext} along the short (or hard) axis of the ellipse displaces the vortex on the long axis, where its frequency increases substantially due to position-dependent increases in both force constants with X .

With $\vec{H}^{ext} = 0$, one can find the shape of the elliptical orbit and compare with the shape of the nanodisk. The vortex in undamped motion must move along an equipotential centered in the disk. The orbital energy U is found to be

$$U = \frac{1}{2}(k_x X^2 + k_y Y^2) = \frac{1}{2}(\sqrt{k_x} X_0 + \sqrt{k_y} Y_0)^2. \quad (31)$$

Dividing through by the constant, U , this is the standard equation of an ellipse, with the semi-major and minor axes X_{\max}, Y_{\max} given by

$$X_{\max} = \sqrt{\frac{2U}{k_x}}, \quad Y_{\max} = \sqrt{\frac{2U}{k_y}}. \quad (32)$$

Their ratio is then

$$\frac{Y_{\max}}{X_{\max}} = \sqrt{\frac{k_x}{k_y}} \approx \frac{b}{a}. \quad (33)$$

The last approximate result in terms of the disk axes a, b was obtained by using relation (20), valid only in the limit of larger ellipses. Thus, the shape of the vortex orbit is nearly the same as the shape of the nanodisk. The *energetic ellipticity* (not to be confused with the eccentricity),

$$e \equiv \sqrt{\frac{k_x}{k_y}}, \quad (34)$$

determines the ratio of the orbital axes. Indeed, the potential can be brought to a circular form, with a new coordinate $\vec{\rho}$:

$$U(\vec{\rho}) = \frac{1}{2} \bar{k} \vec{\rho}^2, \quad \vec{\rho} \equiv \left(\sqrt{e} X, \frac{1}{\sqrt{e}} Y \right). \quad (35)$$

Then, it is possible to show that the velocity follows a typical expression for circular motion,

$$\dot{\vec{\rho}} = (\dot{\rho}_x, \dot{\rho}_y) = \vec{\omega}_G \times \vec{\rho}. \quad (36)$$

where $\vec{\omega}_G = \omega_G \hat{z}$. This equivalent circular coordinate $\vec{\rho}$ is useful for the analysis of vortex position statistics in elliptical disks.

3.2. Numerical methods for magnetization dynamics

The analysis of vortex motion via the Thiele equation is expected to be approximate. Numerical simulations can be used to give a more complete and reliable description of the dynamics. We require the time evolution from Eq. (21) solved either for zero temperature or finite temperature. These results are generated for Py parameters, based on the exchange length of $\lambda_{ex} = 5.3$ nm, together with a micromagnetics cell size of $a_{cell} = 2.0$ nm.

3.2.1. Zero temperature: fourth-order Runge-Kutta

At zero temperature, a stable integration scheme is the well-known fourth-order Runge-Kutta (RK4) scheme, which we have used. A time step in dimensionless simulation units of $\Delta\tau = 0.04$ is sufficient to insure good energy conserving dynamics (at zero damping), resulting in energy conservation to one part in 10^{12} over as many as 5.0×10^5 time steps, in systems with up to 4000 cells. To insure this high precision control of the energy, it is essential to evaluate the demagnetization field continuously during every substep of the RK4 algorithm. In the zero temperature simulations used to estimate gyrotropic frequencies, the initial state of the dynamics is a vortex obtained by spin alignment relaxation to a desired position. It is also helpful to run the time evolution initially with some weak damping ($\alpha \approx 0.02$) for a limited time, followed by energy conserving dynamics ($\alpha = 0$). The inclusion of damping for a short interval helps to remove any spin wave oscillations that may be generated by a less than perfect initial vortex state. The subsequent energy conserving dynamics then gives precise estimates of the frequencies ω_G .

3.2.2. Finite temperature: Langevin dynamics via second-order Heun method

For finite temperatures, the Eq. (21) has been solved effectively by a second-order Heun method (H2) [21, 23]. This scheme is equivalent to a two-stage predictor-corrector algorithm, where the predictor stage is an Euler step and the corrector stage is the trapezoid rule. Both stages use the same random fields $\vec{b}_{s,i}$ which are produced by a random number generator. Any of the Cartesian components of these fields are to be random deviates with a zero mean value and a variance that must depend on both the dimensionless time step and temperature according to

$$\sigma_s = \sqrt{2\alpha\mathcal{T}\Delta\tau}. \quad (37)$$

This is a result of the FD theorem Eq. (22), and it is used to replace the stochastic fields integrated over a time step, by the relation

$$\int_{\tau_n}^{\tau_n+\Delta\tau} d\tau \vec{b}_{s,i}(\tau) \rightarrow \sigma_s \vec{w}_i. \quad (38)$$

The vectors \vec{w}_i are triplets of random deviates with zero mean and unit variance, for each site i . In usual programming, there are standard random number generators, which return a uniform deviate from 0 to 1, with a variance found to be $1/\sqrt{12}$. These can be shifted into the range from -0.5 to $+0.5$ and then rescaled by $\sqrt{12}\sigma_s$ to get stochastic field components of the correct mean and variance (it does not need to be a Gaussian distribution) [13, 7].

4. Vortex gyrotropic motion at zero temperature

In a circular nanodisk at zero temperature, with a radial force \mathbf{F} as in Eq. (2), the analysis from the Thiele equation (24) shows that the vortex velocity always points along the azimuthal direction:

$$\mathbf{V} = \frac{G\hat{z} \times \mathbf{F}}{G^2} = -\frac{\gamma k_f R}{2\pi p q L M_s} \hat{\phi}. \quad (39)$$

The minus sign indicates that a vortex with positive gyrovector (along \hat{z}) will move in the clockwise or negative sense, in uniform circular motion, and oppositely for those with negative gyrovector. More generally, for elliptic nanodisks, the predicted gyrotropic frequency obtained from the Thiele equation is

$$\omega_G = -\frac{\bar{k}}{G} = -\frac{\gamma\bar{k}}{2\pi pqLM_s}, \quad (40)$$

where \bar{k} is the geometric mean of the force constants along the principal axes. For a circular system, $\bar{k} \rightarrow k_F$. These results depend strongly on the force constants, which can be estimated from the static vortex configurations. It has been found [9, 24, 13] that for sufficiently large circular disks far from any stability limits of the vortex, the force constants are very roughly proportional to L^2/R , that is,

$$k_F \approx \frac{1}{4} \frac{L^2}{R} \frac{A}{a_{cell}^2} \approx 0.878 \mu_0 M_s^2 \frac{L^2}{R}. \quad (41)$$

The frequency unit $f_0 = t_0^{-1} = \gamma B_0$ used in the simulations depends on the cell size, which is inconvenient for comparison with experiment. Thus, it is important to convert the results to a commonly used frequency unit,

$$\omega_0 \equiv \frac{\mu_0}{4\pi} \gamma M_s. \quad (42)$$

This is $\omega_0 = \gamma M_s$ in the centimeter-gram-second (CGS) system of units. With the help of definition (7) for the exchange length, expression (40) for gyrotropic frequency can be written,

$$p\omega_G = -\left(\frac{\mu_0}{4\pi} \gamma M_s\right) \left(\bar{k} \frac{\lambda_{ex}}{A}\right) \left(\frac{\lambda_{ex}}{L}\right). \quad (43)$$

With vorticity $q = +1$ assumed, the sign of ω_G is determined by the core polarization p . This expression suggests using $k_0 \equiv A/\lambda_{ex}$ as the unit of force constant and λ_{ex} as the unit of length.

Simulations can verify the frequency predictions from the Thiele equation. As shown below in some examples, the dimensionless periods τ_G of gyrotropic motion can be estimated precisely, in simulation time units ($\tau = t/t_0$). Dimensionless angular frequencies are then $2\pi/\tau_G$, which are given physical values by multiplying by $f_0 = \gamma B_0$. Using Eq. (15), these can then be converted into units of ω_0 as follows:

$$\omega_G = \frac{2\pi}{\tau_G} f_0 = \frac{2\pi}{\tau_G} \gamma \mu_0 M_s \frac{\lambda_{ex}^2}{a_{cell}^2} = \frac{2\pi}{\tau_G} \frac{\lambda_{ex}^2}{a_{cell}^2} 4\pi \omega_0. \quad (44)$$

We use this below to convert the raw numerical data (τ_G) into frequencies in ω_0 units.

Of course, to get precise estimates of the frequency, the vortex must be instantaneously located to high precision. That is a two step process. The first step is to use the singularity in the in-plane magnetization angle ϕ , to locate the four cells nearest to the vorticity center, $\mathbf{R}_{\nu'}$, defined implicitly according to the relation

$$\vec{\nabla} \times \vec{\nabla} \phi(r) = 2\pi \hat{z} \delta(\mathbf{r} - \mathbf{R}_{\nu'}). \quad (45)$$

For the micromagnetics square grid, the vorticity center falls between the four cells that have a net 2π circulation in ϕ . This gives the location $\mathbf{R} \approx \mathbf{R}_{\nu'}$ only to a precision equal to the cell size. It can be greatly improved by making a weighted average of the cell locations \mathbf{r}_i , using their squared out-of-plane components, which are largest in the vortex core, as the weighting function:

$$\mathbf{R} = \frac{\sum_{|\mathbf{r}_i - \mathbf{R}_{\nu'}| < 4\lambda_{ex}} (m_i^z)^2 \mathbf{r}_i}{\sum_{|\mathbf{r}_i - \mathbf{R}_{\nu'}| < 4\lambda_{ex}} (m_i^z)^2}. \quad (46)$$

For better efficiency, the sum is restricted to cells within four exchange lengths of the vorticity center. This avoids using useless data from the core of interest (e.g., spin wave oscillations near the edge of the disk should be ignored). As the vortex moves, the resulting estimate for \mathbf{R} changes smoothly. This algorithm even works very well for vortices moving in response to thermal fluctuations.

4.1. Circular nanodisks simulations

Some typical vortex motions in circular nanodisks of radius $a = 120$ nm are presented in **Figure 4**, as obtained from integration of the LLG equations by the RK4 scheme. The initial states came from Lagrange-constrained spin alignment to the initial position $\mathbf{R} = (4.0, 0)$ nm. A weak damping with parameter $\alpha = 0.02$ was included but turned off at dimensionless time $\tau = 1000$. The remaining evolution was used to estimate the periods, τ_G , which are then converted using Eq. (44).

For the motions displayed in **Figure 4**, the dimensionless periods for $L = 5$ nm, 10 nm, and 20 nm are $\tau_G \approx 5800, 3270$, and 1872, respectively. From statics calculations of the effective potentials as described earlier, the corresponding raw force constants are $k_f a_{cell}/A \approx 0.033863, 0.120192$ and 0.419143, respectively, using $a_{cell} = 2.0$ nm. Rescaling by a factor $\lambda_{ex}/a_{cell} = 5.3/2.0$ converts them into $k_F \lambda_{ex}/A$, which appears in the Thiele theory expression (43). For these and other similar vortex motion simulations with L ranging from 2.0 to 20 nm, one can compare to the Thiele prediction by plotting the frequency ω_G versus k_F/L with units as

suggested from Eq. (43) (see **Figure 5**). Note that for a given radius a , the disk with the smallest L has the largest frequency. The result is that ω_G , obtained from *dynamics* simulations, is very close to linearly related to k_F/L , obtained from *static* simulations, with a unit slope for these units. This gives a strong verification of the Thiele equation being applicable to vortex motion in nanodisks where the vortex is stable. Note that all simulations here used a reasonably small vortex orbital radius of about 4.0 nm, avoiding having the vortex core approach the disk edge, which would tend to destabilize the vortex.

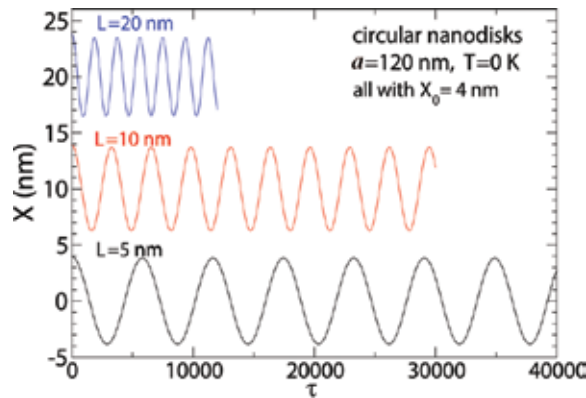


Figure 4. Motions for one component of vortex position in circular nanodisks from RK4 integration of the LLG equations (shifted for clarity). The damping $\alpha = 0.02$ was turned off after dimensionless time $\tau = 1000$. The periods can be calculated accurately from the undamped motion. Graphs of $Y(\tau)$ are of the same amplitudes and frequencies but shifted a quarter of a period.

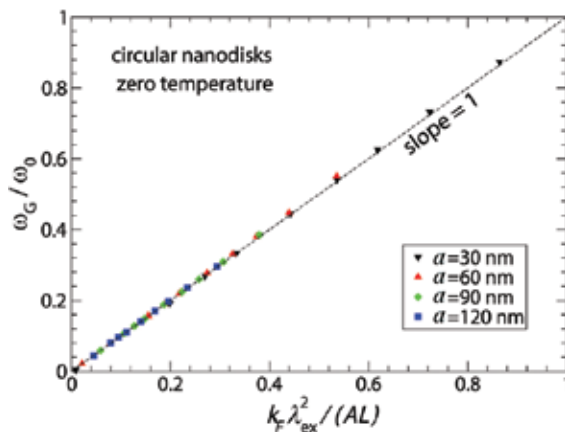


Figure 5. Vortex gyrotropic frequency magnitudes from RK4 (dynamics) simulations for circular nanodisks, with thicknesses ranging from $L = 2.0$ – 20 nm, and indicated disk radii, versus force constants scaled by disk thickness, obtained from Lagrange-constrained spin alignment (static) simulations. The dashed line is the theoretical result (43) from the Thiele equation.

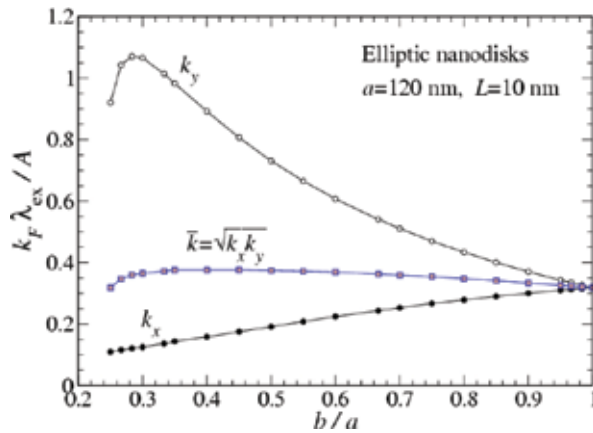


Figure 6. Effective potential force constants versus geometric ellipticity b/a , for elliptic nanodisks of semi-major axis $a = 120$ nm, and thickness $L = 10$ nm. Results were found by Lagrange-constrained spin alignment relaxation.

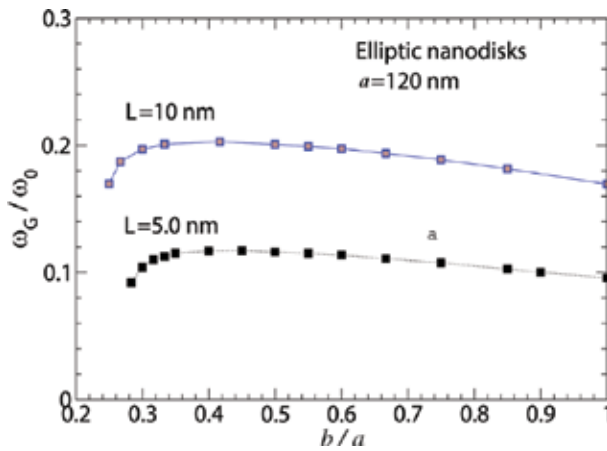


Figure 7. Gyrotropic frequency magnitudes versus geometric ellipticity b/a , for elliptic nanodisks of semi-major axis $a = 120$ nm, and thicknesses $L = 5.0$ and 10 nm. Results were found by simulations of the LLG equations using RK4 integration. For $L = 10$ nm, compare the similar shape of the curve of \bar{k} in **Figure 6**, as expected from $\omega_G \propto \bar{k}$ in Eq. (43).

4.2. Elliptical nanodisk simulations

Simulations for elliptic nanodisks [7] offer an even wider range of possibilities, because the variations with geometric ellipticity b/a can be studied. For instance, the variation of the effective potential force constants has a behavior like that in **Figure 6**, for the particular case $a = 120$ nm and $L = 10$ nm. Both k_x and k_y were determined from the potentials derived by spin alignment with a position constraint. Their geometric mean \bar{k} , which determines gyrotropic

frequencies, is also shown. The curves for these force constants do not go below a minimum value of b/a , where the vortex becomes unstable.

The corresponding gyrotropic frequencies ω_G for $L = 10$ nm and also for $L = 5.0$ nm are shown in **Figure 7**, versus b/a . These were obtained from simulations the same as those described for circular nanodisks. Note that the shapes of these curves are very similar to the curves of \bar{k} in **Figure 6**, which is to be expected if the Thiele theory (43) is valid. The additional results for $L = 5.0$ nm are included to demonstrate the dependence on disk thickness. With thicker disks having a greater restoring force and $\bar{k} \propto L^2$, due to the extra area on the disk edges, the dependence of $G \propto L$ results is gyrotropic frequencies increasing roughly linearly in L . The results can be presented in another view in **Figure 8**, showing ω_G/\bar{k} versus ellipticity for different L . One again gets a clear and quantitative verification of the Thiele theory result (43), seeing that $\omega_G/\bar{k} \propto \lambda_{ex}/L$ with the correct constant of proportionality.

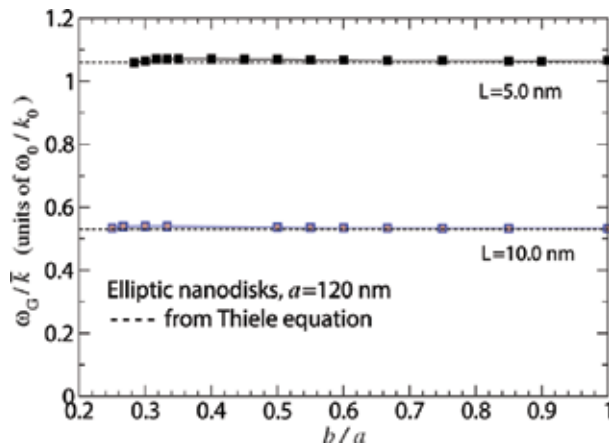


Figure 8. Gyrotropic frequency magnitudes (from dynamics) scaled by mean force constants (from statics), versus geometric ellipticity b/a , for elliptic nanodisks with $a = 120$ nm and two different thicknesses. The results confirm the predictions from the Thiele theory, dashed lines from Eq. (43), using exchange length $\lambda_{ex} = 5.3$ nm, with no adjustable parameters.

5. Spontaneous gyrotropic motion from thermal fluctuations

Now we consider the effects of temperature on a vortex. Specifically, the temperature effectively acts as a bath of random magnetic fields that exchange torques and energy with the vortex. Even though that exchange is somewhat random, one sees that it is able to spontaneously initiate the organized gyrotropic motion of the vortex. That motion proceeds over a noisy background of spin waves. Even so, it is readily apparent and persistent. Here, we show typical time evolutions, and then later discuss statistical properties.

5.1. Simulation of a vortex initially at disk center

A vortex that has been relaxed to its minimum energy configuration (e.g., by the spin alignment scheme) is situated in the disk center, whether it be circular or elliptical. This assumes that a quasi-single-domain state is not lower in energy. Then, in the absence of any external forces or forces due to a thermal environment, it would statically remain centered in the disk and exhibit no dynamics. However, Machado et al. [25] noticed that finite temperature micromagnetics simulations demonstrate the spontaneous motion of the vortex, even if it starts in its minimum energy location. This is rather surprising, although it is really not much different than any spin wave mode from being excited thermally in an equilibrium system with temperature. From the point of view of statistical mechanics, any excitable modes (i.e., independent degrees of freedom) should share equally in available thermal energy, and because the energy present in the vortex gyrotropic motion is quite small, rather large orbital motions can develop solely due to the effects of temperature.

In the numerical solution [13] of the magnetic Langevin equation (21), the dimensionless temperature is required. For the simulation units being used, $J = 2AL$ determines the energy scale and depends on the disk thickness. As an example, we consider a disk with $a = 60$ nm, $b = 30$ nm, and thickness $L = 5.0$ nm, at temperature $T = 300$ K. For Py parameters ($A = 13$ pJ/m), the energy unit is $J = 130$ zJ, while the thermal energy scale is $kT = 4.14$ zJ, which gives the dimensionless temperature,

$$\mathcal{T} = \frac{kT}{2AL} = 0.032, \quad \text{for } T = 300\text{K}, L = 5.0 \text{ nm}. \quad (47)$$

This was used to determine the variance of the random magnetic fields, Eq. (37), together with a damping parameter $\alpha = 0.02$. A dimensionless time step $\Delta\tau = 0.01$ for the second-order Heun method was used. The resulting vortex core coordinates $(X(\tau), Y(\tau))$ are displayed in **Figure 9**, out to a time of $\tau = 50,000$. From **Figure 9**, a clockwise orbital motion takes place, together with a noisy background, and there are about 15 complete orbits for $\tau < 50,000$ (period $\tau_G \approx 3300$). The period is somewhat longer than that found at zero temperature, $\tau_G \approx 2970$. This softening of the mode with temperature is to be expected. In addition, the amplitudes of X and Y motions are not equal, as expected from the elliptical disk shape. The gyrotropic orbital motion continues indefinitely; it was followed out to $\tau = 2.5 \times 10^5$ to get vortex statistics.

For comparison, an identical simulation but with the disk thickness increased by a factor of 2 to $L = 10$ nm is shown in **Figure 10**, again starting the vortex from the disk center. The greater thickness approximately quadruples \bar{k} , but also doubles the gyrovector, thereby resulting in the frequency being double that for $L = 5.0$ nm. It is also clearly apparent that the amplitude of the thermally induced motion is reduced in the thicker nanodisk (the graphs have different vertical scales). These differences then are primarily driven by the modifications to the force constants and to G .

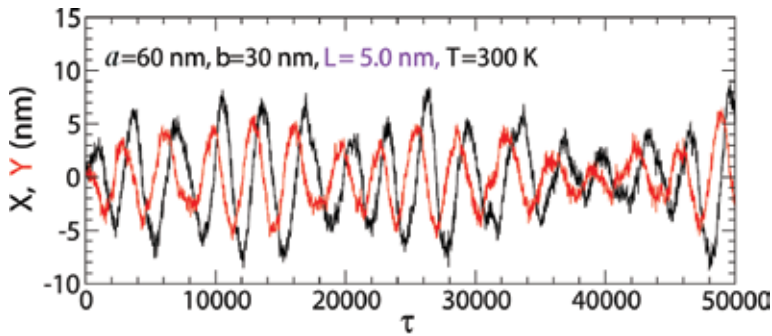


Figure 9. Spontaneous vortex core motion caused by thermal fluctuations, as found by H2 integration of the LLG-Langevin equations (21) for a nanodisk with thickness $L = 5.0$ nm. The vortex was initiated at the disk center, $X = Y = 0$. This graph shows only 1/5 of the total data generated and used subsequently for analysis of vortex statistics, corresponding to hundreds of gyrotropic periods.

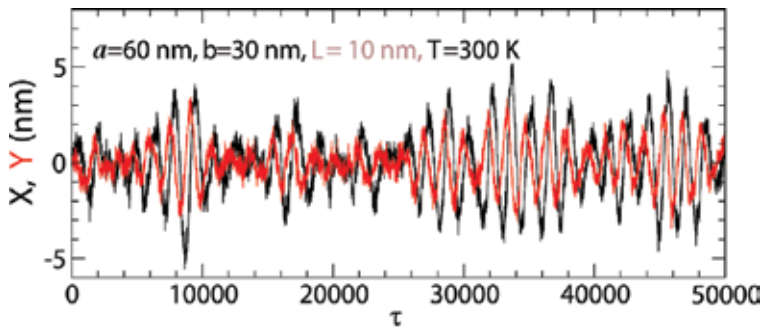


Figure 10. Spontaneous vortex core motion caused by thermal fluctuations, for a nanodisk simulation identical to that in Figure 9, but with double the thickness, $L = 10$ nm. Note the considerably smaller amplitude of gyrotropic oscillations, and the much higher frequency.

5.2. Thermal vortex motion as described by the Thiele equation

Next, we consider the statistical mechanics of the vortex core position $\mathbf{R} = (X, Y)$, based on an effective Lagrangian and Hamiltonian that give back the Thiele equation. The analysis [7] makes use of the general elliptic potential $U(\mathbf{R})$ in Eq. (4). It is straightforward to check that a Lagrangian whose Euler-Lagrange variations gives back the Thiele equation is [13]

$$L = -\frac{1}{2}G(X\dot{Y} - Y\dot{X}) - \frac{1}{2}(k_x X^2 + k_y Y^2) \quad (48)$$

This is a particular choice of gauge and this Lagrangian is not unique (see Ref. [26] for a different choice). To transform to the associated Hamiltonian, one finds the canonical momentum for this symmetric gauge,

$$\mathbf{P} = \frac{\partial L}{\partial \mathbf{V}} = \frac{1}{2}(GY, -GX). \quad (49)$$

This shows that the Lagrangian can be expressed as $L = \mathbf{P} \cdot \mathbf{V} - U$. As \mathbf{P} is determined by X and Y , without any time derivatives, one can interpret this as a pair of constraint relations between components of \mathbf{P} and \mathbf{R} . It means that of four original coordinates plus momenta, only two are independent.

The Hamiltonian is obtained in the usual way,

$$H = \mathbf{P} \cdot \mathbf{V} - L = U = \frac{1}{2}(k_x X^2 + k_y Y^2) = \frac{1}{2} \bar{k} \rho^2. \quad (50)$$

Curiously, this has no momenta present. This strange situation seems to imply that there is no dynamics, because the Hamilton equations of motion are

$$\dot{\mathbf{P}} = -\frac{\partial H}{\partial \mathbf{R}}, \quad \dot{\mathbf{R}} = \frac{\partial H}{\partial \mathbf{P}}. \quad (51)$$

That would give $\mathbf{V} = \dot{\mathbf{R}} = 0$, which is clearly wrong. This singular situation comes about because of the constraint (49) between momentum and position components. In order to get a true dynamics, one needs to rewrite the Hamiltonian half as a potential part and half as a kinetic part, that is,

$$H = \frac{1}{4}(k_x X^2 + k_y Y^2) + \frac{1}{4} \left(\frac{2}{G} \right)^2 (k_x P_y^2 + k_y P_x^2). \quad (52)$$

This is exactly equal to H in Eq. (50), but now it does give back the Thiele equation when its time dynamics is found from Eq. (51). Because of the constraint, the vortex motion depends on only two independent coordinates, or degrees of freedom, rather than four. For the purposes of statistical mechanics, then, the thermalized vortex motion contains an average energy, $\langle H \rangle = 2 \times \frac{1}{2} kT$.

5.3. Thermalized vortex probability distributions from the Thiele equation

One can assume that any of the coordinates, X, Y, P_X, P_Y , as well as effective circular coordinate $\vec{\rho} = (\rho_x, \rho_y)$, obey a Boltzmann distribution, whose parameters are determined by the average energy,

$$\langle H \rangle = kT. \tag{53}$$

This directly gives the mean squared effective circular radius for an elliptic disk,

$$\langle \rho^2 \rangle = \langle 2H / \bar{k} \rangle = 2kT / \bar{k}. \tag{54}$$

This becomes the usual mean squared radius, $\langle \rho^2 \rangle \rightarrow \langle R^2 \rangle$, in the limit of a circular disk. Using expression (50) for H , with the energy shared equally between X and Y motions (equipartition theorem for quadratic degrees of freedom) implies that each coordinate has a mean square value,

$$\langle X^2 \rangle = kT / k_x, \quad \langle Y^2 \rangle = kT / k_y. \tag{55}$$

For the systems we study, with $b < a$ and $k_x < k_y$, this implies a wider range of motion for the X coordinate, as could obviously be expected. These relations for the mean square values indicate the importance of the force constants for describing the statistical distribution of vortex position.

Now consider determining the probability distributions for the vortex core location. The Hamiltonian is circularly symmetric when expressed in terms of the square of the effective circular coordinate $\vec{\rho}$. We can suppose that each possible location has a probability determined from a Boltzmann factor, $e^{-\beta H}$, where $\beta = (kT)^{-1}$. Employing the circular symmetry for this coordinate, the probability $p(\rho)d\rho$ of finding the vortex core within some range $d\rho$ centered at radius ρ is proportional to the area $2\pi\rho d\rho$ in a ring of radius ρ , and the Boltzmann factor $e^{-\beta H}$.

$$p(\rho)d\rho \propto 2\pi\rho d\rho e^{-\beta H} = 2\pi\rho d\rho e^{-\frac{1}{2}\beta\bar{k}\rho^2}. \tag{56}$$

By including a normalization constant, the unit normalized probability distribution function is easily found to be

$$p(\rho) = \beta\bar{k}\rho e^{-\frac{1}{2}\beta\bar{k}\rho^2}. \tag{57}$$

The root-mean-square radius $\rho_{\text{rms}} = \sqrt{2kT / \bar{k}}$ implied from relation (54) can be verified with this probability function. One can also get the mean radius and the most probable radius:

$$\langle \rho \rangle = \sqrt{\frac{1}{2} \pi k T / \bar{k}}, \quad \rho_{\max} = \sqrt{k T / \bar{k}}. \quad (58)$$

For the simulations shown in **Figures 9** and **10**, with $a = 60$ nm, $b = 30$ nm, $T = 300$ K, position data out to $\tau = 2.5 \times 10^5$ was used to find histograms of vortex core position, and thereby get the radial probability distribution to compare with Eq. (57). The results are shown in **Figure 11**. To compare with theory, the force constants from spin alignment relaxations were used (see the **Figure 11** caption). Note also that as the gyrotropic frequency is considerably larger for $L = 10$ nm, those data correspond to many more orbits of the vortex, equivalent to a more complete averaging. Even so, the distributions for both thicknesses follow very closely to the expected form that depends on the validity of the Thiele equation, with no adjustable parameters (see **Figure 12**).

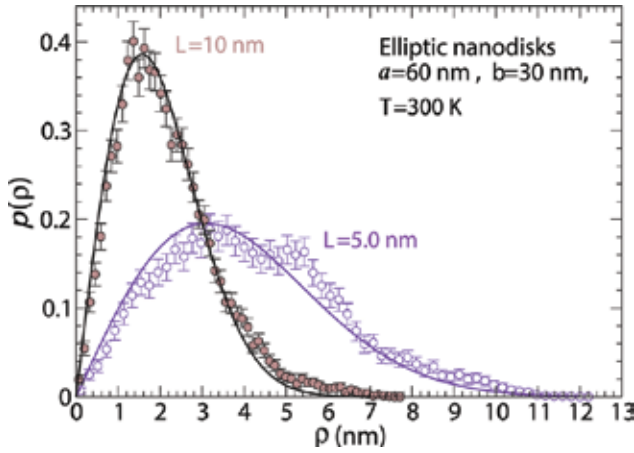


Figure 11. The radial distribution of vortex core positions for the simulations in Figures 9 and 10, with $a = 60$ nm, $b = 30$, and thicknesses $L = 5.0, 10$ nm. Data out to final time $\tau = 2.5 \times 10^5$ was used. The solid curves are the theory expression (57), using force constants $\bar{k} = 0.1753 k_0$ for $L = 5.0$ nm and $\bar{k} = 0.6832 k_0$ for $L = 10$ nm, as obtained from spin alignment calculations, with force constant unit $k_0 = A/\lambda_{\text{ex}}$.

Using H expressed in terms of both X and Y , the probability to find the vortex core within some range dX and dY of the location (X, Y) is $p(X, Y) dX dY \propto e^{-\beta H} dX dY$, where the normalized probability function is found to be

$$p(X, Y) = \sqrt{\frac{\beta k_x}{2\pi}} e^{-\frac{1}{2} \beta k_x X^2} \sqrt{\frac{\beta k_y}{2\pi}} e^{-\frac{1}{2} \beta k_y Y^2}. \quad (59)$$

This is a product of Gaussian distributions in each coordinate, $p(X, Y) = p(X)p(Y)$, with zero mean values, but variances given by

$$\sigma_x = \sqrt{kT/k_x}, \quad \sigma_y = \sqrt{kT/k_y}. \quad (60)$$

The distributions $p(X)$ and $p(Y)$ found from the simulation data of **Fig. 9** are shown in **Fig. 12**, and compare closely to the theoretical expression (59).

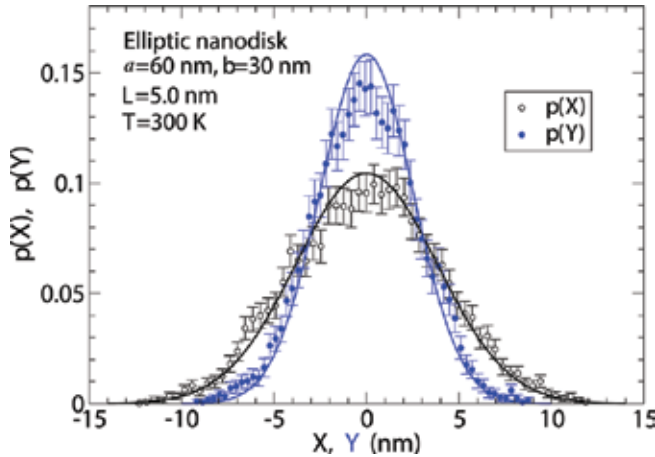


Figure 12. Distributions of vortex core coordinates for the LLG-Langevin simulation in Figure 9 with $a = 60$ nm, $b = 30$, and thickness $L = 5.0$ nm. The solid curves are the theory expressions from Eq. (59) based on the Thiele theory for vortex motion, using force constants $k_x = 0.1156k_0$ and $k_y = 0.2657k_0$ from spin alignment relaxation, where $k_0 = A/\lambda_{ex}$.

Clearly one could also find the corresponding distributions of the momentum components by similar reasoning.

Instead of looking at the momentum components, we can equivalently calculate a theoretical speed distribution for the vortex core [13]. This is simplest if we use the effective circular coordinate $\vec{\rho}$, and consider that fact that its velocity in Eq. (36) implies a speed $u \equiv |\dot{\rho}|$ given by

$$u = |\omega_G| \rho. \quad (61)$$

As u is proportional to ρ , so are their probability distributions. If $g(u)$ is the desired speed probability distribution, then conservation of probability states that

$$g(u)du = p(\rho)d\rho = p(u/|\omega_G|)du/|\omega_G|. \quad (62)$$

Thus, the speed distribution is derived from the effective circular coordinate distribution by

$$g(u) = |\omega_G|^{-1} p(u / |\omega_G|). \quad (63)$$

With $|\omega_G| = \bar{k}/G$, one obtains

$$g(u) = \frac{\beta G^2}{\bar{k}} u e^{-\frac{1}{2}\beta G^2 u^2 / \bar{k}} = \frac{2u}{u_{rms}^2} e^{-u^2 / u_{rms}^2}. \quad (64)$$

This depends on the root-mean-square speed, determined from ρ_{rms}

$$u_{rms} = |\omega_G| \rho_{rms} = \sqrt{2kT\bar{k}} / G. \quad (65)$$

The function $g(u)$ is a Maxwellian speed distribution similar to that for an ideal gas. One could consider the factor in the exponent as depending on a kinetic energy term $\frac{1}{2}m_G u^2$ for a particle, where m_G is some mass associated with that particle in gyrotropic motion. From Eq. (64), one can read off the value needed for this mass,

$$m_G = G^2 / \bar{k}. \quad (66)$$

This curious result gives a kind of effective mass that depends on the potential experienced by the vortex. Thus, it should not be considered an intrinsic vortex mass. Generally, G is linearly proportional to thickness L [see expression (25)], whereas \bar{k} tends to increase approximately with L^2 [see expression (41) and also Section 4.2], making this mass nearly independent of L . Probably, m_G is more strongly determined by the disk area, πab . In the case of circular disks, using the approximate expression (41) for $\bar{k} = k_F$ and the definition (25) of G gives a quantitative result,

$$m_G \approx \frac{(2\pi)^2 a}{0.878 \mu_0 \gamma^2}. \quad (67)$$

Thus, the mass is determined primarily by the disk radius a , and it does not depend on the material parameters such as the exchange stiffness or saturation magnetization. For a radius

$a = 100$ nm, the mass is 1.2×10^{-22} kg, an extremely small value. Even so, the mass can be taken to represent how a vortex responds dynamically to the potential. With the gyrotropic frequency given by $|\omega_G| = \bar{k}/G$, the mass is written equivalently as

$$m_G = G/|\omega_G| \propto L/|\omega_G|. \quad (68)$$

With m_G depending only on disk radius or possibly area in the xy plane, and the gyrovectore proportional to L , this re-expresses that $|\omega_G|$ is also proportional to L , as shown implicitly in **Figures 5** and **7**.

6. Summary and interpretation of results

This chapter has provided an overview of some methods for finding the static, dynamic, and statistical properties of vortex excitations in thin nanodisks of soft magnetic material. By assuming the thickness is much less than the principal radius, $L \ll a$, the magnetization points primarily within the plane of the disk, except within the vortex core, and it has only weak dependence on the coordinate z perpendicular to the plane. This allowed for the transformation to an equivalent 2D problem, which has been studied here using a form of micromagnetics, converting the continuum problem to one on a square grid.

The Lagrange-constrained spin alignment scheme was used to find static vortex energies while securing the vortex in a desired location \mathbf{R} , thereby allowing for the calculation of vortex potential $U(\mathbf{R})$ within the disk. For a vortex near the center of an elliptic disk, the force constants k_x and k_y for displacements along the principal axes a, b are found, with $k_x \leq k_y$ when $b \leq a$. However, the disk ellipticity b/a must be above a lower limiting value for a vortex to stable; a very narrow disk will prefer the formation of a quasi-single-domain state, or even a multi-domain state, but not a vortex. A vortex energetically prefers a displacement along the longer axis of the disk; that is consistent with the shape of its elliptic orbits, which have the same ellipticity as the disk itself [see Eq. (33)].

The vortex gyrotropic orbits can be described very well through the use of the Thiele equation (24), which replaces the dynamics of the many degrees of freedom in the magnetization field $M(\mathbf{r}, t)$ by the dynamics of only two Cartesian components in the vortex core location, $\mathbf{R} = (X(t), Y(t))$. This works best for a vortex near the disk center, where it is unlikely to be destabilized by deformations caused by the boundaries. For zero temperature, the dynamics from RK4 integration of the LLG equations is completely consistent with that from the Thiele equation. The Thiele equation predicts the vortex gyrotropic frequencies to be $\omega_G = -\bar{k}/G$, which is confirmed in the *dynamics* simulations while using force constants from the Lagrange-constrained *static* vortex structures. Generally, the zero-temperature gyrotropic frequencies are roughly proportional to L/a with only a weak dependence on disk ellipticity, as can be

concluded from the results in **Figure 7**. The frequencies are determined by the geometric mean force constant, $\bar{k} = \sqrt{k_x k_y}$, which shows why knowledge of the vortex potential is important for this problem.

Thermal effects for nonzero temperature have been included by introducing a Langevin equation (21) that results from including stochastic magnetic fields into the LLG equation. This Langevin equation gives the time evolution in the presence of thermal fluctuations. Solved numerically using a second-order Heun algorithm, a vortex initially at the disk center (the minimum energy point) will *spontaneously* undergo gyrotropic orbital motion, on top of a noisy spin wave background. The orbital motion takes place at a slightly lower frequency compared with its motion for $T = 0$, because the presence of spin waves weakens the exchange stiffness of the system. The resulting distribution of vortex position can be predicted using an effective Lagrangian and Hamiltonian that result from the Thiele equation. That Hamiltonian can be expressed in a form in Eq. (50) containing only a potential energy. This then shows that the distributions (and variances) of effective radial coordinate ρ and Cartesian coordinates X and Y depend on $\sqrt{kT/k_F}$, where k_F is either \bar{k} or k_x or k_y , respectively [see Eqs. (57) and (60)]. Surprisingly, large vortex rms displacements on the order of 1–10 nm can result, with the larger values taking place in the weaker potentials of thinner disks (**Figure 11**) and in disks with larger radii a . However, these noisy elliptical motions simply reflect the equipartition of energy into the two collective degrees of freedom available to the vortex (X, Y), with each receiving an average thermal energy of $\frac{1}{2}kT$. The radial coordinate, in contrast, receives a full kT of energy on average. The theoretical probability distributions are confirmed in simulations provided the time evolution averages over a large number of gyrotropic orbits.

A vortex speed distribution can also be derived from the position distribution, essentially because the momentum and position coordinates of a vortex are not independent. The speed distribution $g(u)$ can be characterized by a mass m_G proportional to the disk radius a , but independent of material properties. The mass has the sense that as the vortex position fluctuates, it has some Maxwellian speed distribution, with a kinetic energy $\frac{1}{2}m_G u^2$ that enters in the Boltzmann factor. This is in contrast to the Thiele equation, which has been used here with no intrinsic mass term. Indeed, the vortex gyrotropic frequency is the same as that for a corresponding 2D harmonic oscillator of mass m_G and spring constant \bar{k} , that is,

$$\omega_G = \sqrt{\bar{k}/m_G}$$

Acknowledgements

Portions of this work benefited substantially from discussions with Afranio Pereira and Winder Moura-Melo at the Universidade Federal de Viçosa, Minas Gerais, Brazil, and Wagner Figueiredo at the Universidade Federal de Santa Catarina, Florianópolis, Brazil, and from use of computation facilities at both universities.

Author details

Gary Matthew Wysin

Address all correspondence to: wysin@phys.ksu.edu

Department of Physics, Kansas State University, Manhattan, KS, USA

References

- [1] N.A. Usov and S.E. Peschany, Magnetization curling in a fine cylindrical particle. *J. Magn. Magn. Mater.* 118, 290 (1993).
- [2] J. Raabe, R. Pulwey, S. Sattler, T. Schweinbock, J. Zweck and D. Weiss, Magnetization pattern of ferromagnetic nanodisks. *J. Appl. Phys.* 88, 4437 (2000).
- [3] G. Gioia and R.D. James, Micromagnetics of very thin films. *Proc. R. Soc. London Ser. A* 453, 213 (1997).
- [4] K.S. Buchanan, P.E. Roy, F.Y. Fradkin, K. Yu Guslienko, M. Grimsditch, S.D. Bader and V. Novosad, Vortex dynamics in patterned ferromagnetic ellipses. *J. Appl. Phys.* 99, 08C707 (2006).
- [5] D. Ruzmetov and V. Chandrasekhar, The Dynamics of magnetic vortex states in a single permalloy nanoparticle. *J. Magn. Magn. Mater.* 320, 47 (2008).
- [6] G.M. Wysin, Vortex-in-nanodot potentials in thin circular magnetic dots. *J. Phys.: Condens. Matter* 22, 376002 (2010).
- [7] G.M. Wysin, Vortex dynamics in thin elliptic ferromagnetic nanodisks. *Low Temp. Phys. (Fizika Nizkih Temperatur)*, 41(10), 1009–1023 (2015).
- [8] K.S. Buchanan, P.E. Roy, M. Grimsditch, F.Y. Fradkin, K.Yu Guslienko, S.D. Bader and V. Novosad, Magnetic-field tunability of the vortex translational mode in micron-sized permalloy ellipses: Experiment and micro-magnetic modeling. *Phys. Rev. B* 74, 064404 (2006).
- [9] K.Yu Guslienko, B.A. Ivanov, V. Novosad, Y. Otani, H. Shima and K. Fukamichi, Eigenfrequencies of vortex state excitations in magnetic submicron-size disks. *J. Appl. Phys.* 91, 8037 (2002).
- [10] K.Yu Guslienko, X.F. Han, D.J. Keavney, R. Divan and S.D. Bader, Magnetic vortex core dynamics in cylindrical ferromagnetic dots. *Phys. Rev. Lett.* 96, 067205 (2006).
- [11] G.M. Wysin, *Magnetic Excitations & Geometric Confinement: Theory and Simulations*, ISBN: 978-0-7503-1074-1 (Institute of Physics Expanding Physics ebook, 2015).

- [12] R.P. Cowburn, D.K. Koltsov, A.O. Adeyeye, M.E. Welland and D.M. Tricker, Single-domain circular nanomagnets. *Phys. Rev. Lett.* 83, 1042 (1999).
- [13] G.M. Wysin and W. Figueiredo, Thermal vortex dynamics in thin circular ferromagnetic nanodisks. *Phys. Rev. B* 86, 104421 (2012).
- [14] Z. Huang, High accuracy numerical method of thin-film problems in micromagnetics. *J. Comp. Math.* 21(1), 33 (2003).
- [15] J. Sasaki and F. Matsubara, Circular phase of a two-dimensional ferromagnet with dipolar interactions. *J. Phys. Soc. Jpn.* 66, 2138 (1997).
- [16] C.J. García-Cervera, "Magnetic Domains and Magnetic Domain Walls," Ph.D. thesis, New York University, New York (1999).
- [17] C.J. García-Cervera, Z. Gimbutas and E. Weinan, Accurate numerical methods for micromagnetics simulations with general geometries. *J. Comp. Phys.* 184, 37 (2003).
- [18] G.M. Wysin, Magnetic vortex mass in two-dimensional easy-plane magnets. *Phys. Rev. B* 54, 15156 (1996).
- [19] L.D. Landau and E.M. Lifshitz, On the theory of the dispersion of magnetic permeability in ferromagnetic bodies. *Phys. Z. Sowjet.* 8, 153 (1935).
- [20] F.H. de Leeuw, R. van den Doel and U. Enz, Dynamic properties of magnetic domain walls and magnetic bubbles. *Rep. Prog. Phys.* 43, 44 (1980).
- [21] J.L. García-Palacios and F.J. Lázaro, Langevin-dynamics study of the dynamical properties of small magnetic particles. *Phys. Rev. B* 58, 14937 (1998).
- [22] A.A. Thiele, Steady-state motion of magnetic domains. *Phys. Rev. Lett.* 30, 230 (1973).
- [23] U. Nowak, in *Annual Reviews of Computational Physics IX*, p. 105, edited by D. Stauffer (World Scientific, Singapore, 2000).
- [24] B.A. Ivanov and C.E. Zaspel, Gyrotropic mode frequency of vortex-state permalloy disks. *J. Appl. Phys.* 95, 7444 (2004).
- [25] T.S. Machado, T.G. Rappoport and L.C. Sampaio, Vortex core magnetization dynamics induced by thermal excitation. *Appl. Phys. Lett.* 100, 112404 (2012).
- [26] B.A. Ivanov, E.G. Galkina and A.Yu Galkin, Quantum dynamics of vortices in small magnetic particles. *Low Temp. Phys.* 36, 747 (2010).

Two-Dimensional Solitons and Vortices in Linear and Nonlinear Lattice Potentials

Jianhua Zeng and Boris A. Malomed

Additional information is available at the end of the chapter

<http://dx.doi.org/10.5772/106163>

Abstract

Periodic potentials, such as photonic crystals and optical lattices, have shown great ability to manipulate the dynamics of photonic and atomic waves. The interplay of the periodic potentials and material nonlinearity (self-focusing or defocusing) can create and stabilize several types of solitons, including ordinary and gap solitons, which populate, respectively, in the semi-infinite gap and finite bandgaps of the corresponding linear spectrum. Besides, lattice defects have also been used to construct solitons. This review reports the generation of two-dimensional (2D) solitons in lattice potentials with local defects, under the self-focusing nonlinearity. The numerical analysis demonstrates a novel kind of embedded solitons (or intraband solitons), which are continuous families of 2D localized modes (different from isolated solutions reported before in usual embedded-soliton models) embedded into the first and second Bloch bands of the underlying linear spectrum, and pinned to the defect, which determines the spatial position of the modes. We call these modes *embedded defect solitons*. Further, double, triple, and quadruple lattice defects can also support stable dipole-mode solitons and vortices. In addition to that, combined linear and nonlinear lattice potentials are also used to construct stable fundamental solitons, gap ones, and solitary vortices.

Keywords: Bose-Einstein condensates, periodic potentials, solitons, vortices, optical lattices, photonic crystals, nonlinear guided waves

1. Introduction

In their many realizations in various areas of mathematics and physics, solitons are localized “waves of translation” resulting from the balance between linear (dispersive) and nonlinear effects in the medium. For the first time, what is nowadays called as soliton was reported by John Scott Russell as a solitary water wave as early as in 1834. In his experiments, Russel

observed that when propagating along a narrow channel, a rounded, smooth, and well-defined heap of water kept its shape over a long distance. This remarkable phenomenon is now called as Russell's solitary wave in fluid dynamics. The soliton phenomenology had started to develop after the advent of modern computers in 1960s. Solitons are, by definition, solitary waves that behave like a "particles," keeping their amplitude, shape, and velocity in the course of propagation and even after colliding with other solitons. Nowadays, soliton phenomena have been identified in various physical systems. For instance, in astrophysics, a robust long soliton behavior appears as a vortex in the rotating atmosphere, which can effectively explain the Great Red Spot in the Jupiter's atmosphere. Rigorously speaking, solitons refer to integrable partial differential equations [1]. In reality, most governing equations concerning soliton phenomena are not integrable [2]. In the latter case, stable pulses are named "solitary waves," rather than "solitons," in mathematical literature, while in physics, the name of solitons is applied to robust pulses in nonintegrable models equally well. In fact, they can readily demonstrate dynamics similar to that in integrable systems over experimentally relevant timescales [3]. In this brief review, we adopt the term soliton to refer to localized waves supported by the balance of linear dispersion and nonlinearity.

Theoretical and experimental studies of the solitons dynamics have drawn a great deal of interest in the course of several past decades. It is now known that solitons are universal collective excitations in very diverse areas, ranging from mathematics to physics and chemistry, and even to biology. In physics, the studies of solitons chiefly refer to self-trapped light pulses and beams in nonlinear optics, strain waves in elastic media, matter waves in superfluids (especially, solitons in Bose-Einstein condensates—BECs), various species of magnetic solitons, and other nonlinear waves in magnetic media, etc. The studies in these areas are focused on the existence, stability, mobility, and interactions of solitons. They are most often found in one-dimensional (1D) physical systems, although they exist in multidimensional settings too. In the two-dimensional (2D) case, the ubiquitous cubic self-focusing readily gives rise to formal solutions for solitons. However, the same setting brings about the critical collapse [4]; therefore, fundamental solitons in the free 2D space (*Townes solitons* [5]) are unstable, as a separatrix between collapsing and decaying modes. Vortex solitons exist too in the 2D free space [6], while being vulnerable to a stronger splitting instability against azimuthal perturbations [7, 8]. Vortex solitons are a special type of solitons containing screw phase dislocations. To stabilize solitons in such physical systems, researchers have turned to adding different types of periodic potentials, alias linear lattices (LLs) to the systems under the consideration [9].

Suggested by the ability of crystals to mold the flow of electrons in solids, different periodic potentials, such as ones induced by photonic crystals and lattices in optics [10], gratings built into plasmonic waveguides [11], optical lattices in BECs [12–14] or degenerate Fermi gases [15], etc., were used to gain control of the dynamics of photonic, plasmonic, and atomic waves, respectively. Periodic potentials, when combined with the self-focusing or defocusing material nonlinearity, have been shown as excellent candidates for stabilizing various types of solitons [8, 9, 13, 14, 16], including ordinary ones, lying in the semi-infinite gap (SIG) of the corresponding linear spectrum, and *gap solitons* (GSs) populating finite bandgaps.

Periodic potentials have recently been extended to make them nonlinear (sometimes called pseudopotentials in that context), in the form of nonlinear lattices (NLs). The NLs, as the names suggest, induced pseudopotentials with periodically modulated local strength and/or sign of the nonlinearity. In optics, NLs may be built as material structures with spatially periodic modulations of the local Kerr nonlinearity or other nonlinear coefficients. In terms of BEC, NLs may be engineered via the Feshbach resonance mechanism by using spatially periodic external fields to induce the local nonlinearity [17]. The studies of the soliton dynamics in NLs, and in NL-LL combinations, have been comprehensively summarized in recent review [18].

This review aims to provide a brief survey of our results reported in the context of theoretical studies of 2D solitons and vortices in linear and nonlinear lattice potentials [19, 20]. In Section 2, we introduce a dynamical model of lattice potentials with defects and self-focusing nonlinearity and report the existence and stability of a new type of 2D *embedded* (alias intraband) solitons, which we call as embedded defect solitons (EDSs), as they are embedded, as localized modes, into the first and second Bloch bands of the underlying linear spectrum, being pinned to local lattice defects. Stable dipole-mode solitons and vortices supported by multiple defects are also reported in this section. The variational approximation (VA) based on the Gaussian ansatz, along with numerical methods, is presented to study 2D ordinary solitons in the setting combining the LL and NL with incommensurate periodicities of the two lattices in Section 3. GSs and vortex solitons in the same setting are studied too by means of numerical simulations. Finally, we formulate conclusion in Section 4.

2. 2D intraband solitons and vortices in lattice potentials with local defects

2.1. Introduction

As mentioned above, the model with the integration of periodic potentials and material nonlinearity (self-focusing or defocusing) can give rise to various types of solitons, such as ordinary solitons and GSs, existing, respectively, inside the SIG and the finite bandgaps of the corresponding linear spectrum.

Furthermore, it was also demonstrated that, counter-intuitively, specific species of solitary waves, known as embedded solitons, may exist inside spectral Bloch bands populated by radiation modes [21–35]. Generally, embedded solitons cannot exist in continuous families because of the resonance with radiation waves. However, isolated embedded modes are possible, as the rate of the decay into radiation may vanish at particular spectral points. Under some specific conditions, continuous families of embedded solitons were constructed too [30–33]. Recently, the formation of such solitons was demonstrated in a model combining the quadratic ($\chi^{(2)}$) nonlinearity and a complex lattice potential, whose real and imaginary parts are subject to the condition of parity-time (PT) symmetry, representing symmetrically placed and mutually balanced local gain and loss [34]. While embedded solitons have been widely

investigated in general 1D models, it remains an open issue to discover them inside 2D Bloch bands. Previously, stable intraband solitons have been found in a 2D potential which consists of a periodic lattice in one direction and a harmonic-oscillator trap applied in the orthogonal direction [35].

Besides the perfect lattices, lattice defects have also been introduced to help constructing solitons. In particular, solitons supported by local defects in the form of the localized $\chi^{(2)}$ nonlinearity have been studied in [36–38]. Recently, solitons pinned to local PT -symmetric defects, inserted into the 1D medium with the uniform $\chi^{(2)}$ nonlinearity, were considered too [39]. Along these lines, the current section aims to report the numerical analysis of 2D solitons in lattice potentials with local defects, under the action of self-focusing nonlinearity. Numerical results demonstrate a novel kind of embedded solitons (or intraband solitons), which form continuous families of 2D localized modes (different from isolated solutions reported before in general embedded-soliton models), existing inside the first and second Bloch bands of the underlying linear spectrum, in terms of the propagation constant, and pinned to the defect. We call them as embedded defect solitons (EDSs) accordingly. It is necessary to point out that, for localized modes pinned to local lattice defects, one can define the location of their propagation constant relative to the underlying bandgap spectrum of the infinite uniform LL, as the latter is defined as the spectrum of radiation waves into which the localized mode may decay.

Since the EDSs exist with the norm exceeding a finite minimum value (and the propagation constant of linear defect modes cannot be located inside a Bloch band), they do not emerge from a continuation of linear localized defect modes. Systematic direct simulations verify that the EDSs are totally stable in the first Bloch band, and partially stable in the second. Along with the regular defect solitons indwelling the SIG, and gap defect solitons (GDSs) localized inside the first finite bandgap (the spectral interval between the first and second bands) and pinned to the same defect, the intraband EDSs constitute a continuous “superfamily” throughout the overall bandgap structure. It is important to identify the stability of the GDSs under the self-attractive nonlinearity, since previous results for stable gap solitons supported by perfect 2D lattices were limited to the case of self-repulsion, while the case of self-attraction was assumed to be always unstable [8, 40, 41]. Although GSs bifurcating under the self-attractive nonlinearity from edges of adjacent Bloch bands into the first finite bandgap have been constructed in [42], their stability has not been considered there. In addition, 2D fundamental GSs under the self-attractive nonlinearity were found to be completely unstable in the first finite bandgap, while a family of dipole-mode gap solitons is stable in a part of the first bandgap as long as the depth of the lattice potential takes values above a certain threshold [43].

2.2. Model

The model is the 2D mean-field Gross-Pitaevskii (GP) equation for the BEC wave function (or the nonlinear Schrödinger equation for the amplitude of the electromagnetic wave), $\psi(x, y, z)$,

$$i \psi_z = \frac{-1}{2} \nabla^2 \psi - [1 - \delta(x, y)] V_{ol} \psi - \psi^2 \psi \quad (1)$$

(in BEC, propagation distance z is replaced by time t), with the self-focusing cubic nonlinearity, and $\nabla^2 \equiv \partial_x^2 + \partial_y^2$. The perfect lattice potential with depth 2ε and period π is taken in the general form, $V_{OL} = \varepsilon[\cos(2x) + \cos(2y)]$. The defect is defined by $\delta(x, y) = 1$ at $x^2 + y^2 < r_0^2$ and $\delta(x, y) = 0$ at $x^2 + y^2 \geq r_0^2$ in Eq. (1), with a "hole" of radius $r_0 = 1.2$ in the potential. Numerous simulations demonstrate that, for this shape of the defect with fixed $\varepsilon = 2$, fully stable solitons can only be found in the interval of $1.1 \leq r_0 \leq 1.3$, for different shapes of the "hole." The contour plots of the LL potential with the single or compound defects are shown in **Figure 1**.

Stationary solutions to Eq. (1) with propagation constant $-\mu$ (or chemical potential μ , in terms of BEC) are sought for as $\psi = \varphi(x, y)\exp(-i\mu z)$, with amplitude $\varphi(x, y)$ obeying the stationary equation,

$$\mu\varphi = \frac{-1}{2}\nabla^2\varphi - [1 - \delta(x, y)]V_{OL}\varphi - |\varphi|^2\varphi. \tag{2}$$

It should be noted that the fundamental and dipole-like solitons are represented by real solutions for $\varphi(x, y)$, while the vortical counterparts (vortices that can be supported by quadruple defects, as shown below) correspond to complex solution.

The linear spectrum of Eq. (1), obtained by a numerical solution of the linearized version of Eq. (2), is displayed in **Figure 2**. It can be seen that, for the given parameters, a growing number of defect-induced isolated eigenvalues emerge in the second finite bandgap with the increase in the number of the defects (single \rightarrow double \rightarrow triple), although the first bandgap remains unchanged. In the following Sections 2.3 and 2.4, rather than discussing apparent

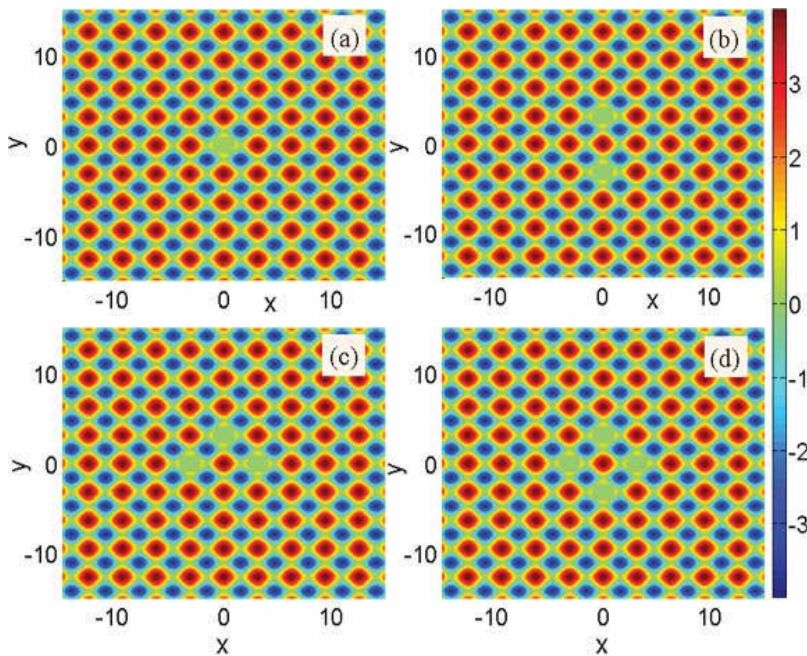


Figure 1. Contour plots of the lattice potential with (a) single, (b) double, (c) triple, and (d) quadruple defects, at $\varepsilon = 2$.

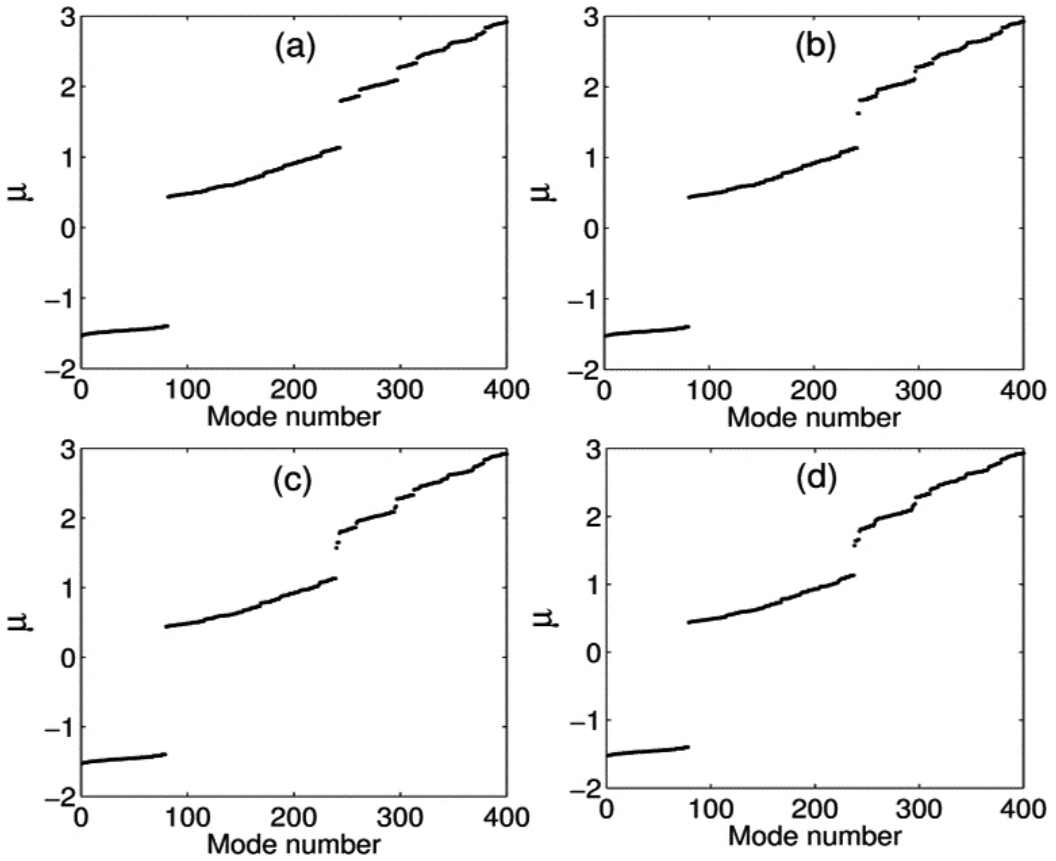


Figure 2. (a) Linear spectra of the perfect lattice potential and in the cases of (b) single, (c) double, and (d) triple defects showed in Figure 1. Isolated points rising in the second finite bandgap represent the corresponding linear defect modes that are irrelevant to solitons described in this review.

quasi-linear defect modes generated from these isolated eigenvalues, we will analyze localized states that have no linear limit but are supported by the defects, in the first finite bandgap and in the two Bloch bands adjacent to it. Numerically, such states were constructed as solutions of Eq. (2), using the Newton's method in the domain of size 30×30 , with a spatial grid of 192×192 points. The initial wave was the usual Gaussian, $\varphi(x, y) = A \exp[-(x^2 + y^2)/(2W^2)]$, with amplitude A , width W , and total power (or number of atoms, in the BEC) $N = \iint \varphi^2(x, y) dx dy = \pi (AW)^2$. Stability of the solutions was then checked in direct simulations of the perturbed evolution in the framework of Eq. (1).

2.3. Numerical results for the single defect

The existence of continuous families of localized modes (fundamental EDSs), pinned to the single defect (the one shown in **Figure 1a**), is illustrated in **Figure 3**. The numerical solution proves that the stability region of EDSs lies inside the first and second Bloch bands and is connected to the family of GDSs that are pinned to the same defect, but with the propagation

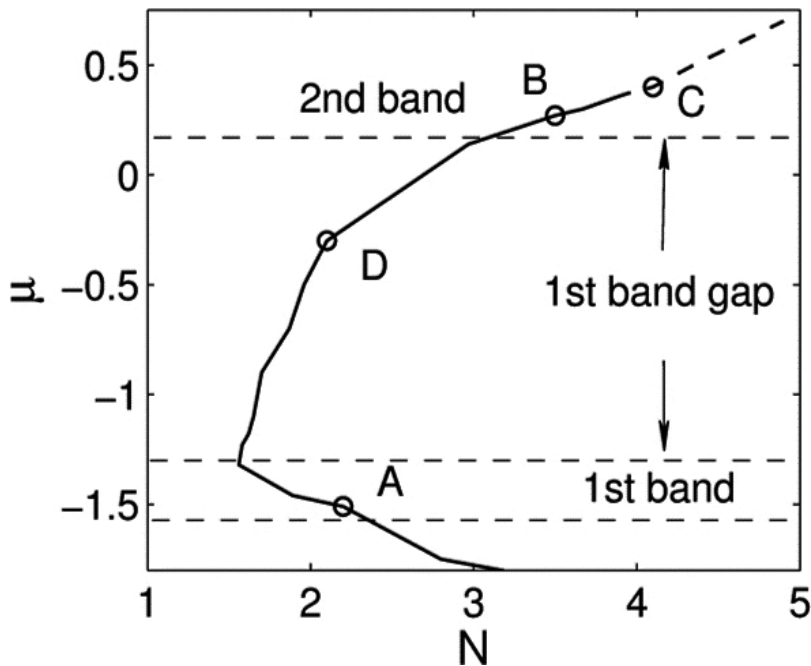


Figure 3. Propagation constant ($-\mu$) versus the total power (norm) for various solitons pinned to the single defect (as shown in Figure 1a)). The solid and dashed curves indicate, respectively, stable and unstable solutions. The stability region of solitons is located inside the first and second Bloch bands, as well as in the first finite bandgap between them. Typical examples of the pinned solitons, marked by the points A, B, C, and D, are shown below in Figures 4 and 5. The curves have some irregularity since they were plotted with interval $\Delta\mu = 0.1$.

constant belonging to the first finite bandgap. The EDS solutions in the first Bloch band begin at its boundary with the SIG, which makes them linked to the stable regular solitons pinned to the defect. Solitons of the latter type are not displayed here, as their existence and properties are evident.

It can be seen from **Figure 3** that the combined family of the pinned solitons exists above a finite minimum value of the total power, $N_{\min} = 1.56$, which exactly corresponds to the junction point between the first Bloch band and the first finite bandgap. This implies, as mentioned above, that the family of localized modes (the regular solitons, EDSs and GDSs) supported by the single defect does not appear as a nonlinear evolution of any linear defect mode because the latter would lead to $N \rightarrow 0$.

Numerical calculations prove that the EDS is totally stable within the first Bloch band, while being only partially stable in the second band. A noteworthy feature is that, in the first Bloch band, the stability of the intraband solitons pinned to the defect satisfies the Vakhitov-Kolokolov (VK) criterion, which is relevant for all kinds of localized modes supported by a self-focusing nonlinearity [44], $\partial\mu/\partial N < 0$. On the other hand, the EDS branch features $\partial\mu/\partial N > 0$ in the second Bloch band, where the stability region is very narrow (actually, it may be a region of weak instability, which is, however, equivalent to stability in a possible experiment). Of course, there is no rigorous proof of the applicability of the VK criterion to the current model.

Shapes of stable EDSs inside the first and second Bloch bands (at points marked A and B in **Figure 3**), and an unstable EDS at point C, are depicted in **Figure 4**. In the whole first band, the form of the EDSs is similar to that shown in **Figure 4a**. Furthermore, in the second band (as shown in **Figure 4b and**), the localized modes feature a more complex structure, with pronounced side peaks, in line with the principle that the shape of the Bloch modes is more complex too in the same band. As a matter of fact, the expanding tail of the soliton displayed in **Figure 4c** initiates the onset of the instability of this soliton. Direct simulations demonstrated that the unstable modes decay into radiation (not shown here in detail).

The current model can support a new type of nonlinear localized states found inside Bloch bands of the spectrum induced by the 2D lattice (2D solitons of the embedded type were found in Ref. [35], but the lattice was one-dimensional in that case). Actually, the EDS family traversing the first Bloch band serves as a missing link between the two famous kinds of solitons created by the lattice potential, which are regular solitons nested in the SIG, and gap solitons populating the first finite bandgap (in the current case, both of them are pinned to the single defect).

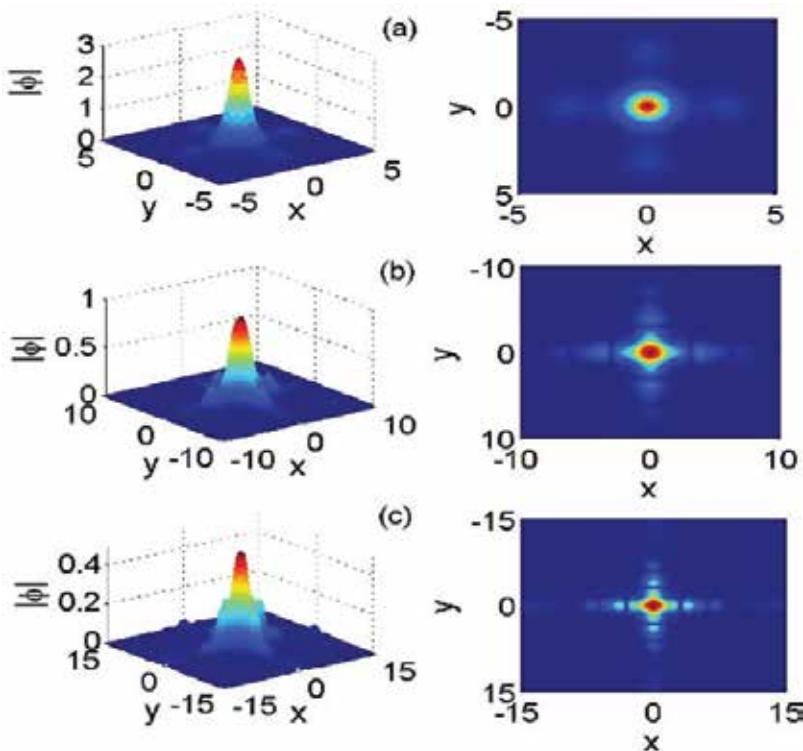


Figure 4. Examples of the intraband (embedded) defect solitons, EDSs, found in the first (a, b) and second (c) Bloch bands, which correspond to points A, B, and C, respectively, in Figure 3. The 3D images and contour plots of the modes are shown in the left and right plots, respectively. The modes in panels (a) and (b) are stable, while the one in (c) is unstable.

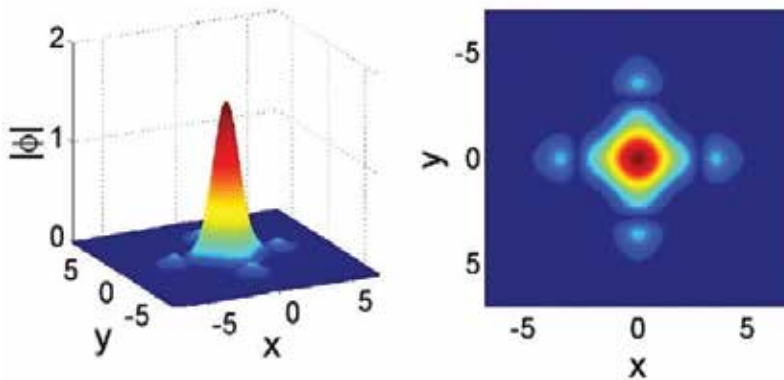


Figure 5. Example of a stable gap defect soliton, GDS, pinned to the single defect, found in the first finite bandgap (at point D marked in Figure 3) under the self-focusing nonlinearity. Left and right panels show 3D image and contour plot of the stationary solution.

The GDS family was also found in the first finite bandgap, being linked to the intraband EDS solutions between the two nearby Bloch bands (as in **Figure 3**). Our simulations have confirmed that these gap solitons, also pinned to the defect, are stable under the self-focusing nonlinearity [defined as in Eq. (1)], in contrast to their counterparts in ideal lattices, where gap solitons are generally considered to be stable only under the self-defocusing nonlinearity [8, 40].

Furthermore, the GDSs were also explored under the self-defocusing nonlinearity, and it was concluded that they are always unstable (not displayed here in detail). The reason is that the effective mass is negative for the gap soliton under the self-defocusing nonlinearity, therefore inverting the feature of the soliton-defect interaction, and rendering unstable the localized state of the gap soliton in the case of the attractive defect. Additional analysis strengthens this argument: if the local defect was replaced by one with the opposite sign, the pinned states of gap solitons were demonstrated to be stable under the self-defocusing nonlinearity and unstable in the case of self-focusing. The negative mass of gap solitons explains a number of other counterintuitive dynamical effects featured by these modes [45–48].

Figure 5 presents a typical example of the stable pinned GDS, corresponding to the point D in **Figure 3**, found in the first finite bandgap and supported by the self-focusing nonlinearity. Our simulations further suggest that stable GDSs pinned to the defect cannot be created in the relatively narrow second finite bandgap (see **Figure 2**), in agreement with the general trend of gap solitons to be unstable in the second bandgap [13, 14, 49].

2.4. Numerical results for multiple defects: stable dipoles and vortices

The above analysis was also extended to the cases of double, triple, and quadruple lattice defects, such as those displayed in **Figure 1b–d**. As shown above, the solitary defect can only support the family of the fundamental solitons of both the EDS and GDS types, while the double defects can support the stable dipole-mode bound states of two solitons with opposite signs. Two examples of such modes of the EDS and GDS types, found in the first Bloch band and in the first finite bandgap, respectively, are shown in **Figure 6**.

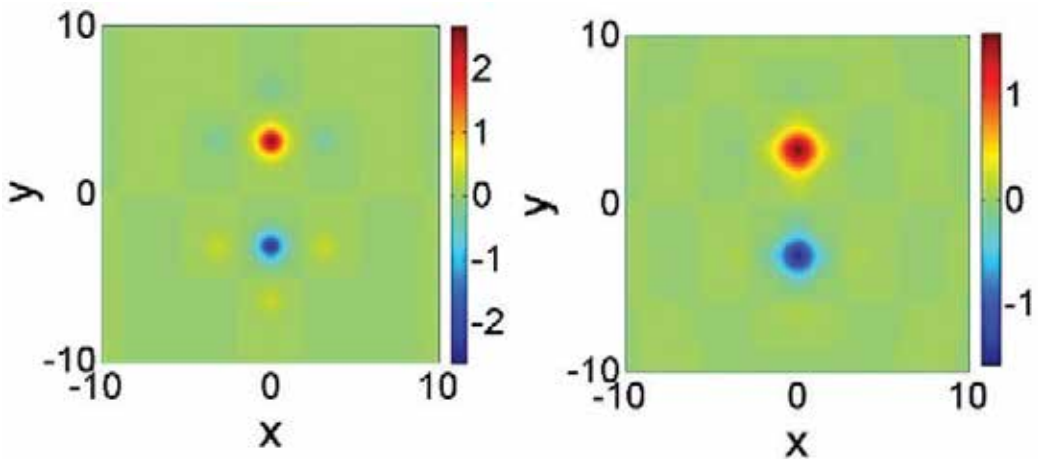


Figure 6. Examples of stable dipole-mode solitons of both the EDS and GDS types supported by the double defect (shown in Figure 1b), in the first Bloch band (left, with $\mu = -1.4$, $N = 3.9$) and in the first finite bandgap (right, with $\mu = -0.3$, $N = 5.4$).

The triangular defects (see **Figure 1c**) are able to support stable triangularly shaped dipole modes too, see examples displayed in **Figure 7**. Typical vortices supported by lattice potentials can be constructed as orthogonal forms of four intensity peaks [8, 9] and an almost hollow site at the pivot (vortices of this kind are usually called onsite-centered ones), featuring the phase differences of $\pi/2$ between adjacent peaks, which amounts to the total phase circulation of 2π (i.e., topological charge 1). The quadruple defects (see **Figure 1d**) can create such stable solitary vortices, characteristic examples of which are shown in **Figure 8**, while the entire “superfamily” is presented in **Figure 9**. As indicated in **Figure 9**, direct simulations demonstrate that the pinned vortices are unstable in the second Bloch band, being stable elsewhere.

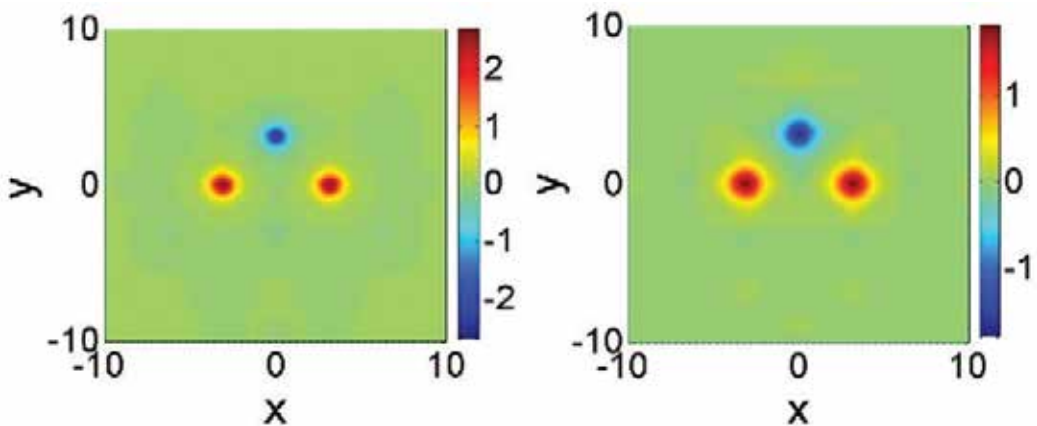


Figure 7. Examples of stable dipole-mode solitons of the EDS and GDS types supported by the triple triangular defect (shown in Figure 1c), in the first Bloch band (left, with $\mu = -1.45$, $N = 6.3$) and in the first finite bandgap (right, with $\mu = -0.5$, $N = 6.9$).

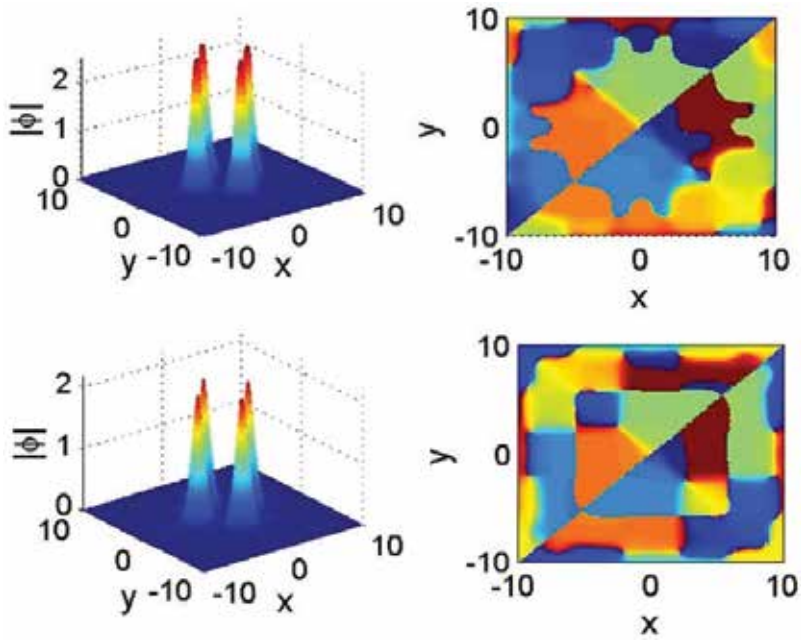


Figure 8. Examples of stable vortices with topological charge 1 supported by the quadruple defect inside the first Bloch band (top, $\mu = -1.5$, $N = 8.8$), and in the first bandgap (bottom, $\mu = -0.8$, $N = 7.2$). Phase distributions of the vortices are shown in the right panels.

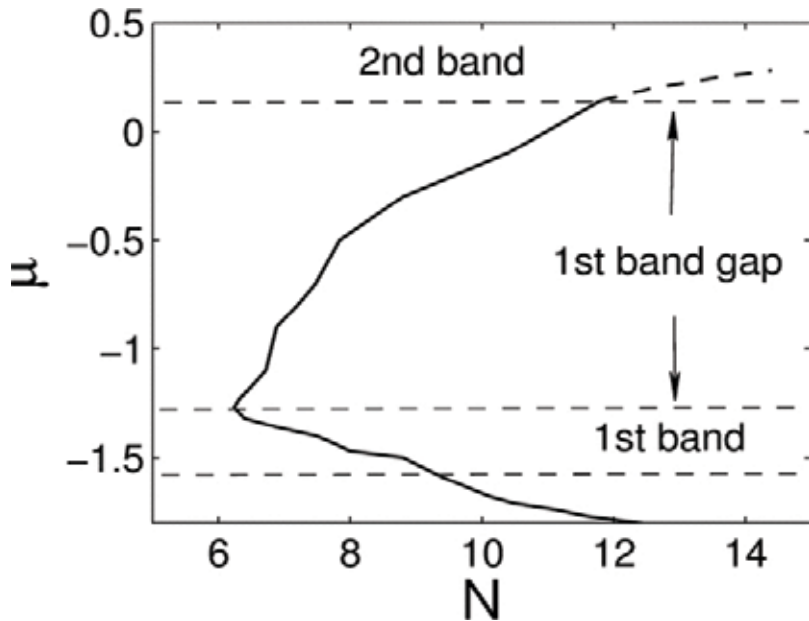


Figure 9. Curve $\mu(N)$ for the vortices with topological charge 1, pinned to the quadrupole lattice defect. The solid and dashed curves show stable and unstable solutions, respectively.

3. 2D solitons and vortices in incommensurate linear and nonlinear lattice potentials

3.1. Introduction

Besides the LL potentials, NLs have also been proposed to support localized modes in recent years. In optics, the photonic-crystal structures can induce an effective combined LL-NL potential, formed by congruent periodic spatial modulations of the linear refractive index and local nonlinear Kerr coefficient. In terms of BEC, the NLs can be introduced using external magnetic fields that affect the nonlinearity coefficient via the Feshbach resonance. Results produced by studies of localized modes (solitons and vortical ones) in NLs and LL-NL combinations have been reviewed in [18]. Experimentally, NL-supported optical solitons have been created at an interface of two lattices [50].

A natural consideration of the combined LL-NL system is the one with different or incommensurate periodicities between the two lattices. In the 1D model, both numerical simulations and analytical approximations have demonstrated that such a combination of competing linear and nonlinear potentials can support various localized modes, both ordinary solitons and GSs [51]. In particular, intriguing results were obtained for existence borders of the solitons as functions of the LL-NL incommensurability and for the empirical “anti-Vakhitov-Kolokolov” (anti-VK) stability criterion for GSs, which is expressed as the dependence of the chemical potential, μ , on the norm, N , of the soliton: $d\mu/dN > 0$ (ordinary solitons supported by the self-focusing nonlinearity in the SIG obey the VK criterion, $d\mu/dN < 0$ [44]). Here, we focus on the case of 2D solitons supported by the incommensurate LL-NL combinations. A VA approach and numerical methods are applied to ordinary solitons, while GSs in the first finite bandgap are studied only numerically, as the analytical consideration would be too cumbersome. Vortex solitons, in the semi-infinite and finite gaps alike, are constructed in a numerical form too.

We study the physical settings including both full 2D and quasi-1D (Q1D) lattice potentials, the latter depending on the single coordinate (the Q1D LL potential is sufficient to stabilize 2D ordinary solitons in diverse 2D self-focusing media [52–54]). Actually, the combination of the incommensurate LL and NLs (with different periods) makes the medium an effective *quasi-crystal* for nonlinear excitations. Theoretical work on fundamental solitons and solitary vortices has been done for linear quasi-periodic potentials [55], and experiments with 2D photonic quasi-crystals counterpart have been reported recently [56, 57]. Another relevant work [58] dealt with 2D solitons supported by combined crossed Q1D linear and nonlinear periodic potentials.

3.2. The model

The 2D theoretical model combining the periodic LL potential and NL pseudopotential is based on the scaled Gross-Pitaevskii (or nonlinear Schrödinger) equation for the BEC wave function, or the local amplitude of the electromagnetic wave in optics, $\psi(x, y, z)$:

$$i \psi_z = -\frac{1}{2} \nabla^2 \psi - \varepsilon [\cos(2\pi x) + \cos(2\pi y)] \psi - g [\cos(q\pi x) + \cos(q\pi y)] |\psi|^2 \psi, \quad (3)$$

where z is propagation distance (or time t in BEC), $\nabla^2 = \partial_x^2 + \partial_y^2$, the LL period is set to be 1, the period of the NL is $2/q$ (q is the *incommensurability index*), and the NL strength is normalized to $g = \pm 1$. The center of the soliton will be fixed at point $x = y = 0$, thus $g = +1$ and -1 pertain, severally, to the self-attraction and self-repulsion nonlinearity, which support ordinary solitons in the SIG or GSs in finite bandgap(s), respectively.

The remaining parameter in Eq. (3) is the LL strength, ε . The relevant band structure, for a fixed strength, $\varepsilon = 7.4$, in the reduced Brillouin zone [1], produced by linearizing Eq. (3), is shown in **Figure 10**.

Eq. (3) corresponds to the general model with the LL potential and spatially constant nonlinearity at $q = 0$. The model is commensurate, with respect to the LL and NL, at $q = 2$, and subharmonically commensurate once the ratio between the LL and NL periods is 1:2 at $q = 1$. The model features the full incommensurability (the system is totally quasi-periodic) when q becomes an irrational number, while, actually, the incommensurability is emulated by setting $q = 1.5$, which yields the period ratio 3:4. The Q1D model corresponds to discarding the linear potentials $\cos(2\pi y)$ and/or nonlinear terms $\cos(q\pi y)$.

Stationary solutions of Eq. (3) with chemical potential μ (or, in terms of optics, propagation constant $-\mu$) can be looked for as $\psi = \varphi(x, y)\exp(-i\mu z)$, with wave function $\varphi(x, y)$ obeying the stationary equation,

$$\mu\varphi = \frac{-1}{2}\nabla^2\varphi - \varepsilon[\cos(2\pi x) + \cos(2\pi y)]\varphi - g[\cos(q\pi x) + \cos(q\pi y)]|\varphi|^2\varphi. \quad (4)$$

The VA is based on the Lagrangian of Eq. (4), which is

$$L = \iint \left\{ \mu|\varphi|^2 - \frac{1}{2}|\nabla\varphi|^2 + \varepsilon[\cos(2\pi x) + \cos(2\pi y)]|\varphi|^2 + \frac{g}{2}[\cos(q\pi x) + \cos(q\pi y)]|\varphi|^4 \right\} dx dy.$$

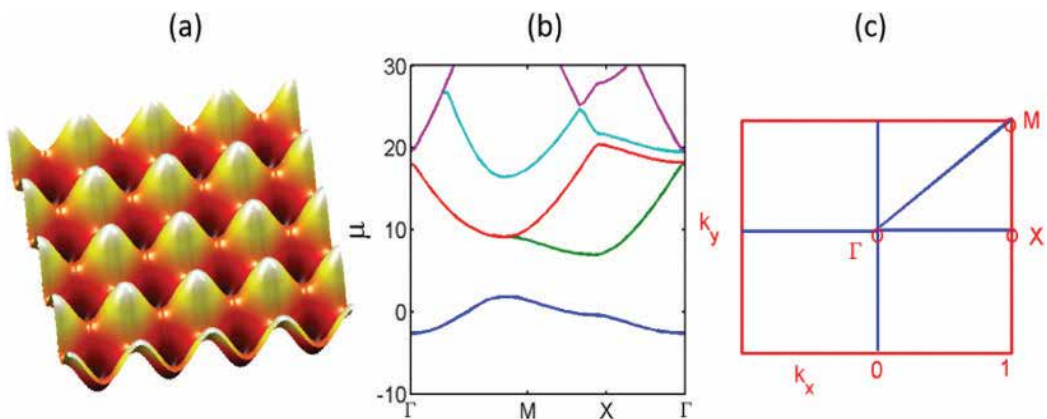


Figure 10. The band structure (b) of the linearized Eq. (3) in the first Brillouin zone (ΓXM , shown in (c)) for depth $\varepsilon = 7.4$ of the LL; μ is the chemical potential of the Bloch waves. The 3D image in (a) shows the profile of LL.

3.3. Localized modes in the semi-infinite gap

3.3.1. Fundamental solitons

The ordinary solitons, which are expected to form in the SIG under the action of the self-focusing nonlinearity ($g = +1$) in Eq. (3), are first sought by means of the VA based on the Gaussian ansatz, $\varphi(x, y) = A \exp[-(x^2 + y^2)/(2W^2)]$, with the corresponding norm $N = \iint |\varphi(x, y)|^2 dx dy \pi A^2 W^2$. Substituting this ansatz into the Lagrangian produces the following result, expressed in terms of N and width W :

$$L_{eff} = \frac{N}{2} \left[\mu - \frac{1}{2W^2} + 2\varepsilon e^{-(\pi W)^2} + \frac{gN}{2\pi W^2} e^{-(\pi q W)^2/8} \right], \tag{5}$$

and the respective variational equations, $\partial L_{eff}/\partial W = \partial L_{eff}/\partial N = 0$:

$$\begin{aligned} (2\pi W^2)^2 \varepsilon e^{-(\pi W)^2} + \pi^{-1} gN e^{-\frac{(\pi q W)^2}{8}} [1 + (\pi q W)^2] &= 1, \\ (2W^2)^{-1} - 2\varepsilon e^{-(\pi W)^2} - gN (\pi W^2)^{-1} e^{-(\pi q W)^2/8} &= \mu. \end{aligned} \tag{6}$$

Figure 11 shows the $\mu(N)$ relation for the soliton families at various values of incommensurability parameter q , as produced by solving Eqs. (6) and by their numerical counterparts for solutions of stationary Eq. (4). The stationary solutions were checked by using them as initial conditions in direct simulations of the dynamical Eq. (3).

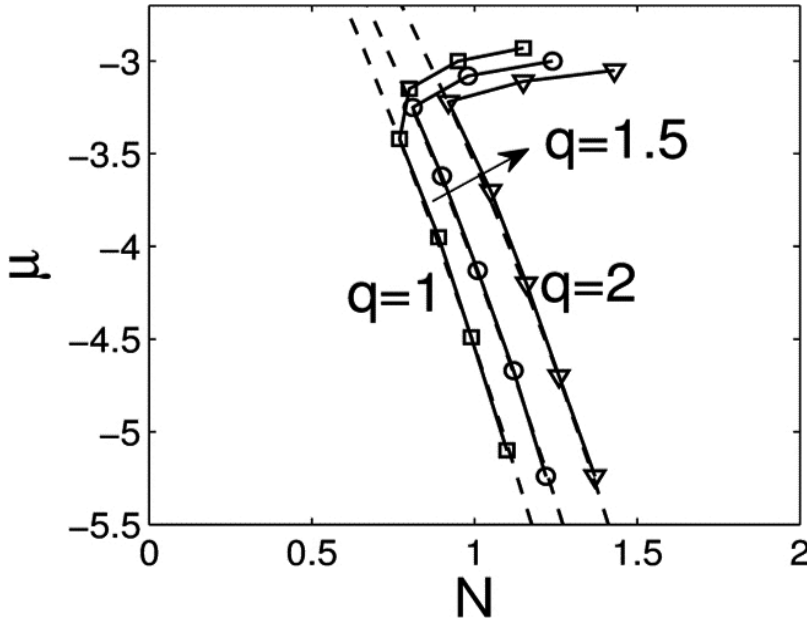


Figure 11. Curve $\mu(N)$ for soliton families in the semi-infinite gap of the model with the full 2D linear and nonlinear potentials produced by the VA (dashed curves) and the numerical solutions of Eq. (4) (chain of symbols).

Typical shapes of stable solitons created inside the SIG by the full 2D model, as well as by its version with the Q1D linear potential, are shown in **Figures 12** and **13**. Obviously, these shapes correspond, respectively, to quasi-isotropic and strongly elongated localized modes, resembling those found previously in other 2D models stabilized by LL potentials [8, 9, 18, 58].

It can be seen from **Figure 11** that the VA predicts the ordinary solitons with a reasonable accuracy, except near the edge of the SIG, where the Gaussian ansatz is irrelevant, due to the complex shape of the soliton. Furthermore, direct simulations of the dynamics of disturbed solitons prove that the solitons' stability correctly follows the VK criterion, $d\mu/dN < 0$ (the dependence $\mu(N)$ is obtained numerically). These properties for the family of ordinary solitons resemble those reported previously in the 1D combined LL-NL model [51].

Figure 14 summarizes the stability of the 2D ordinary solitons in the SIG for all four realizations of the model (2D or Q1D linear and/or nonlinear potentials). The unstable solitons suffer decay into radiation waves (rather than transforming into stable solitons). A notable feature is that replacing full 2D NL by its Q1D version results in expansion of the stability areas, which can be explained by the fact that, in the Q1D NL, ordinary solitons attempt to "elude" the destabilizing locally self-repulsive nonlinearity only in one direction, rather than in two.

In addition, we tried to test the mobility of the solitons by studying their evolution initiated by a sudden "kick," that is, multiplication of the wave function of a stable quiescent soliton by the phase-tilt factor, $\exp[i(k_x x + k_y y)]$, with the vectorial kick parameter \mathbf{k} . The solitons were found to be immobile under the action of the Q1D LL or NL potential, except for an obvious case when both the LL and NL have a collinear Q1D structure, while the kick is applied in the unconfined direction. A sufficiently strong kick would destroy the soliton, instead of setting it in motion.

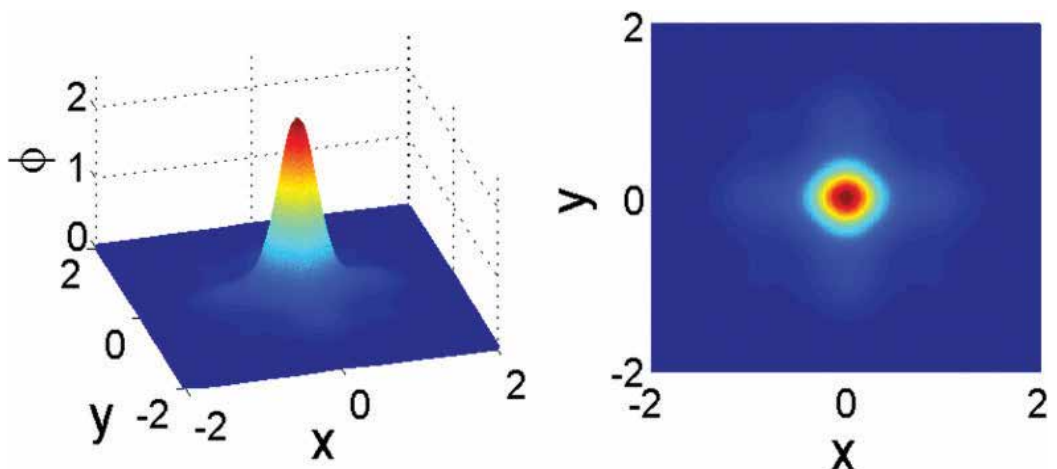


Figure 12. The shape of a stable fundamental soliton in the semi-infinite gap supported by the full 2D linear and nonlinear potentials, for $g = +1$, $q = 1.5$, $\mu = -5.24$, and $N = 1.22$. The contour plot of the stationary real wave function $\varphi(x, y)$ for the soliton is shown in the right panel.

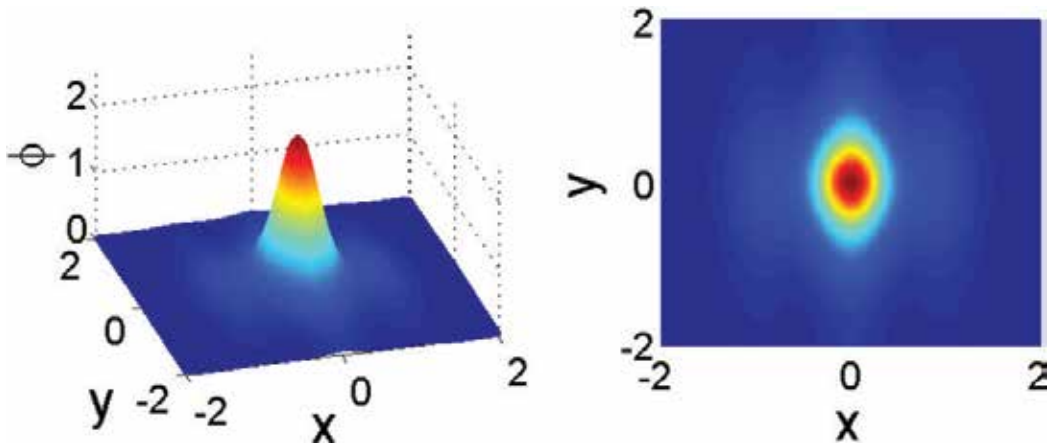


Figure 13. The same as in Figure 12, but in the case of the Q1D linear potential (combined with the 2D nonlinear potential), for $g = +1$, $q = 1$, $\mu = -2.91$, and $N = 1.68$. The shape of the solitons in the model with the quasi-1D nonlinear potential is similar to the present one.

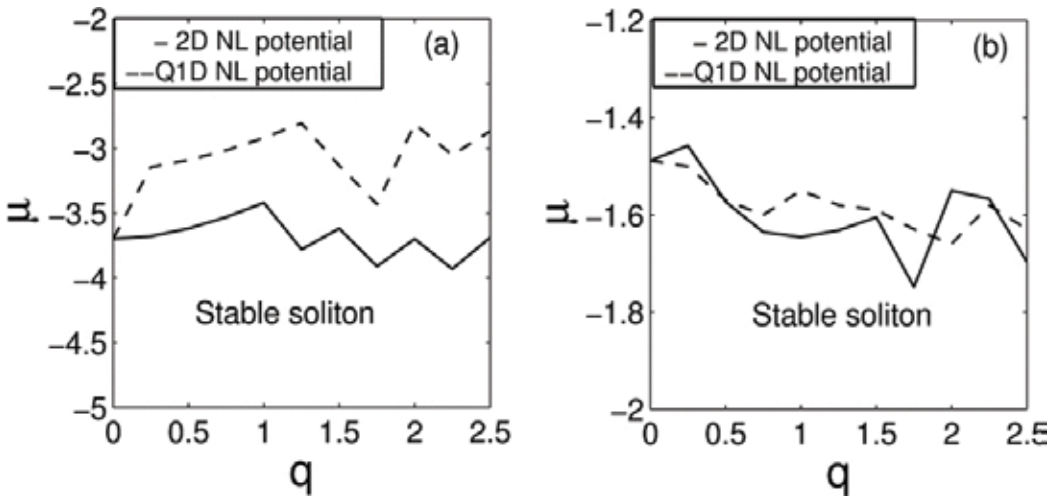


Figure 14. (a) Stability borders of the ordinary soliton family (inside the semi-infinite gap) supported by the 2D linear potential and 2D or Q1D nonlinear potential (shown, respectively, by solid and dashed lines). (b) The same as (a) but for the Q1D linear potential. Areas of stable solitons are located under the corresponding borders.

3.3.2. Solitary vortices

Figure 15 displays a typical example of stable solitary vortices with topological charge 1, which can be built as four-peak patterns, with the distance between peaks amounting to double period of the LL potential ($\Delta x = \Delta y = 2$), and an almost hollow cell at the pivot. This type of solitary vortices is generally stable, owing to the weak interaction between the peaks. More densely packed vortex patterns can be constructed too, but they were found to

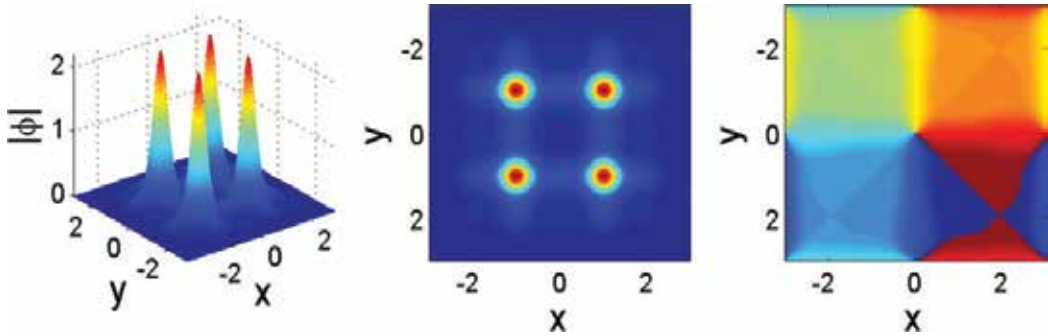


Figure 15. Shape of a stable vortex with topological charge 1 inside the semi-infinite gap supported by the full 2D linear and nonlinear potentials, for $q = 1$ and $g = +1$. The left, middle to right panels show, respectively, the absolute value of the field, $|\varphi(x, y)|$, in cylindrical coordinates and its contour plot, as well as the phase distribution that carries the vorticity. Parameters of the vortex are $\mu = -5.1$ and $N = 4.4$.

be unstable. Studies of other models have also proved that the vortices with inner “voids” are more likely to be stable [8, 18].

Numerical simulations have verified that stable vortices may only be created for values of incommensurability index close to $q = 0, 1$, and 2 , namely, within intervals of the half-width $\Delta q \approx 0.1$ around these values. The latter observation makes sense, as both the linear and nonlinear potentials have minima at or close to sites where the power (density) peaks are located, at such values of q . The stable vortices of the type shown in **Figure 15** can only be observed (in the SIG) under the fully 2D LL potential, and the NL, however, can be taken in 2D or Q1D form. **Figure 16** shows $\mu(N)$ curves for the families of the vortex modes. The analysis proves that the stability of such solutions totally obeys the VK criterion, that is, the families with $d\mu/dN < 0$ are stable.

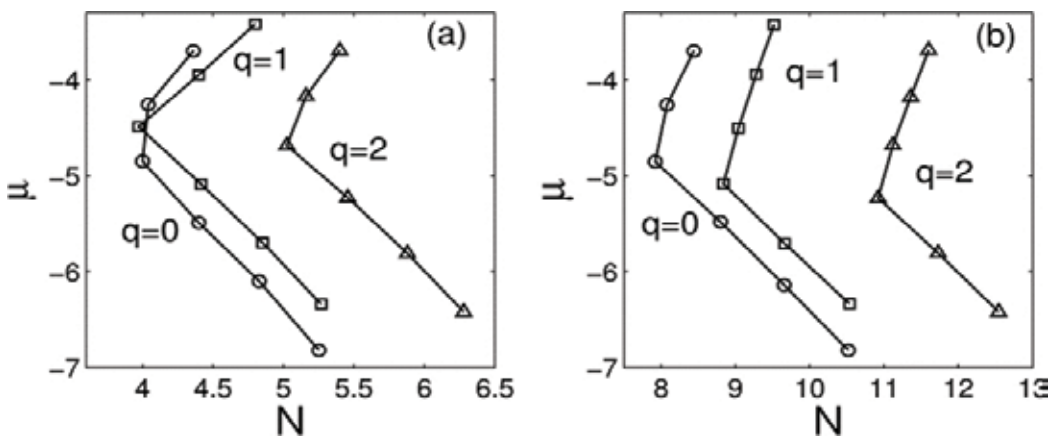


Figure 16. The same as in Figure 11, but for solitary vortices in the semi-infinite gap, and in the case of the full 2D linear potential combined with the 2D (a) or Q1D (b) NL potential.

3.4. Localized modes in finite bandgaps

3.4.1. Fundamental solitons

Figure 17 shows an example of stable GS generated sufficiently far from edges of the finite bandgap (the shapes of the GSs are quite similar in the model combining the 2D LL and Q1D NL). It is seen that the numerically found fundamental GSs feature, as usual, is in more complex shapes than that in the ordinary solitons. The $\mu(N)$ curves for the GS families are shown in **Figure 18a**. Unlike the ordinary solitons (cf. **Figure 12**), GSs always feature $d\mu/dN > 0$, thus complying with the anti-VK criterion [51].

Direct simulations demonstrate that the GSs become stable sufficiently deep inside the finite bandgap and unstable near its edges (unstable GSs suffer decay into radiation). The numerically found stability borders for the GSs in the full 2D NL and Q1D versions of the current model are displayed in **Figure 18(b)**. It is observed that, on the contrary to the ordinary solitons in the SIG, the stability region for GSs becomes extremely narrow for the Q1D NL, compared to the case of the full 2D NL. The latter feature seems obvious, since, in contrast to the ordinary solitons, and the NL may provide necessary support to the GSs.

The GS stability areas gradually shrink to zero with an increase in q , as can be seen in **Figure 18b** for the variant of the Q1D NL model (we envisage similar situation for the full 2D NL model, while numerical troubles stem from expanding the stability diagram at larger values of q). This tendency can be understood due to the fact that the fast oscillating NL field averages itself to zero at large q ; thus, the broad (see **Figure 17**) GS cannot feel the action of the nonlinearity. The ordinary solitons within the SIG do not follow this trend (cf. **Figure 14**) because, as q increases, these solitons can shrink in a single cell of the structure, remaining confined to a self-attractive nonlinearity region. Lastly, numerical simulations demonstrate that, similar to what was found above for the ordinary solitons, GSs are immobile objects too (not shown here in detail).

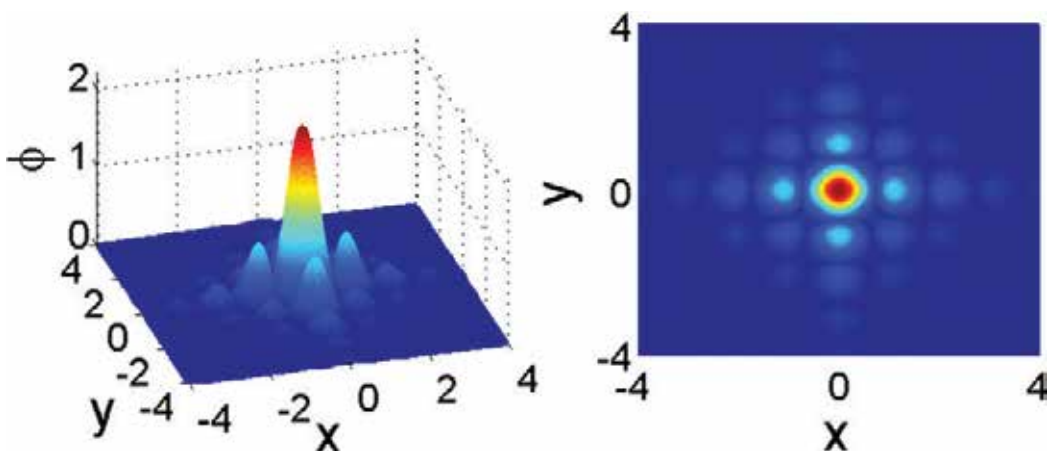


Figure 17. An example of a stable gap soliton in the model with the full 2D NL, for $g = -1$, $q = 1.5$, $\mu = 3.4$, and $N = 1.4$. Left and right panels show 3D image and contour plot of the stationary solution.

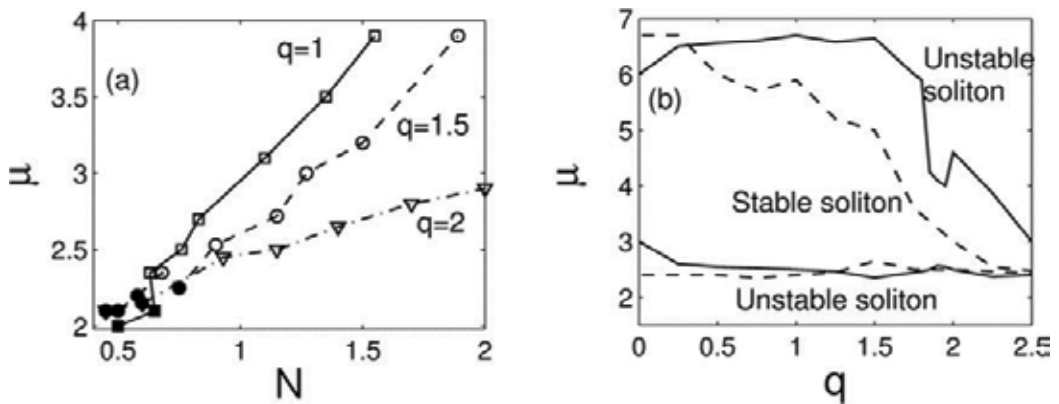


Figure 18. (a) Curves $\mu(N)$ for gap-soliton families in the model with the full 2D nonlinear potential. Unstable solitons near the bottom edge of the bandgap are denoted by black squares. (b) Stability borders for GS solutions supported by the 2D and Q1D nonlinear potentials (shown, respectively, by solid and dashed lines). Areas of stable solitons are delimited by the corresponding stability borders. The top border and the bottom one are situated close to the respective edges of the first finite bandgap.

3.4.2. Solitary vortices

Figure 19 displays an example of stable vortex solitons created in the first finite bandgap. Such vortex soliton features the form similar to its counterparts in the SIG, cf. **Figure 15**, namely, it is composed of four peaks which is separated by twice the LL period, while the phase distribution carries the vorticity. Opposite to the case in the SIG, the solitary vortices inside the finite bandgap may be stable only when *both* LL and NL are taken in the full 2D form (i.e., the vortices are unstable if the Q1D NL is used).

Like their counterparts in the SIG, stable solitary vortices in the finite bandgap are found as long as the incommensurability index is close to $q = 0, 1$, and 2 . Families of these vortices are displayed in **Figure 20** by means of the $\mu(N)$ curves. As in the case of the fundamental GSs, the stable vortices in the finite bandgap obey the anti-VK criterion, $d\mu/dN > 0$.

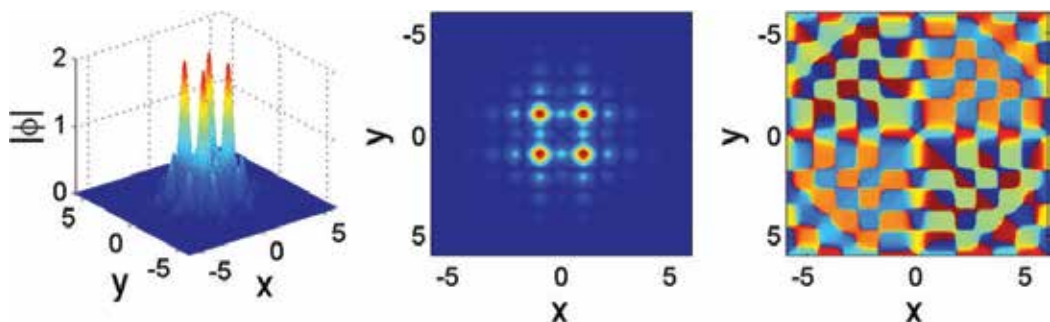


Figure 19. An example of a stable vortex soliton found in the finite bandgap, for $q = 1$, $g = -1$, $\mu = 3.5$, and $N = 5.36$. The meaning of the three panels is the same as in Figure 15.

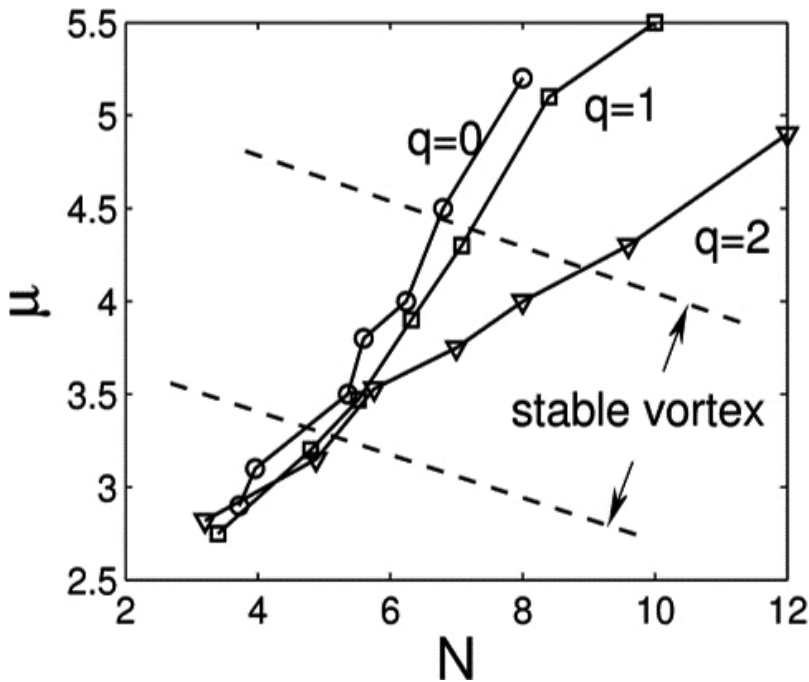


Figure 20. Curve $\mu(N)$ for families of solitary vortices in the finite bandgap. Stable portions of the vortex families are located in the marked stripe.

4. Conclusion

We have studied localized states in the framework of the nonlinear Schrödinger equation by introducing single, double, triple, and quadruple defects into the 2D lattice potentials in the self-focusing medium. The model can be realized as lattices in nonlinear photonic media, and BECs trapped in the OL. A new type of 2D embedded (alias intraband) solitons, which we call embedded defect solitons (EDSs), has been constructed. These modes are stable in the first Bloch band and partially stable in the second band. Contrary to the fact that 2D fundamental gap solitons may be stable only under the self-repulsion in uniform lattices, stable gap solitons pinned to the defect are found under the self-attractive nonlinearity. Stable dipole-mode solitons and vortices maintained by multiple defects have been identified too.

Localized states supported by the model of 2D nonlinear photonic crystals or BEC under the effect of linear and nonlinear lattices with different (generally incommensurate) periods have also been investigated. The combined incommensurate linear and nonlinear lattices may be considered as a “nonlinear quasi-crystal.” Both fully 2D periodic potentials and their Q1D reductions were considered, and the VA (variational approximation) was developed for ordinary (fundamental) solitons in the semi-infinite gap. The stability regions for the entire sets of ordinary solitons and gap ones as well as the vortex solitons (built as “hollow” four-peak complexes) of both types have been produced.

New directions can be naturally explored in the future. Introducing defects in complex lattices, whose real and imaginary parts obey the PT symmetry, one may consider the stabilization of localized modes and, in particular, of 2D gap solitons that were found to be unstable in uniform PT -symmetric lattices [59]. Search for stable vortex solitons with higher topological charges and, possibly, “supervortices” (vortex rings built of compact localized vortices) [60, 61] may be relevant too. On the other hand, it may be interesting to extend the analysis to higher-order bandgaps, aiming to construct solitons and solitary vortices in those gaps.

Acknowledgements

J. Z. acknowledges support from the NSFC (Project No. 11204151), the Initiative Scientific Research Program of the State Key Laboratory of Transient Optics and Photonics, and the Youth Innovation Promotion Association of Chinese Academy of Sciences (No. 2016357).

Author details

Jianhua Zeng^{1*} and Boris A. Malomed²

*Address all correspondence to: zengjh@opt.ac.cn

1 State Key Laboratory of Transient Optics and Photonics, Xi’an Institute of Optics and Precision Mechanics of CAS, Xi’an, China

2 Department of Physical Electronics, School of Electrical Engineering, Faculty of Engineering, Tel Aviv University, Tel Aviv, Israel

References

- [1] Y. S. Kivshar and B. A. Malomed. Dynamics of solitons in nearly integrable systems. *Rev. Mod. Phys.* 1989;**61**(4):763–915. doi:10.1103/RevModPhys.61.763
- [2] J. Yang. *Nonlinear Waves in Integrable and Non-Integrable Systems*. Philadelphia: SIAM; 2010.
- [3] J. H. V. Nguyen, P. Dyke, D. Luo, B. A. Malomed, and R. G. Hulet. Collisions of matter-wave solitons. *Nature Phys.* 2014;**10**:918–922. doi:10.1038/NPHYS3135
- [4] L. Bergé. Wave collapse in physics: principles and applications to light and plasma waves. *Phys. Rep.* 1998;**303**:259–370. doi:10.1016/S0370-1573(97)00092-6
- [5] R. Y. Chiao, E. Garmire, and C. H. Townes. Self-trapping of optical beams. *Phys. Rev. Lett.* 1964;**13**:479–482. doi:10.1103/PhysRevLett.13.479
- [6] V. I. Kruglov, Y. A. Logvin, and V. M. Volkov. The theory of spiral laser beams in nonlinear media. *J. Mod. Opt.* 1992;**39**:2277–2291. doi:10.1080/09500349214552301

- [7] A. I. Yakimenko, Y. A. Zaliznyak, and Y. S. Kivshar. Stable vortex solitons in nonlocal self-focusing nonlinear media. *Phys. Rev. E.* 2005;**71**:065603(R). doi:10.1103/PhysRevE.71.065603
- [8] B. A. Malomed, D. Mihalache, F. Wise, and L. Torner. Spatiotemporal optical solitons. *J. Opt. B.* 2005;**7**:R53–R72. doi:10.1088/1464-4266/7/5/R02
- [9] B. B. Baizakov, B. A. Malomed, and M. Salerno. Multidimensional solitons in periodic potentials. *Europhys. Lett.* 2003;**63**:642–648. doi:10.1209/epl/i2003-00579-4
- [10] J. D. Joannopoulos, S. G. Johnson, J. N. Winn, and R. D. Meade. *Photonic Crystals: Molding the Flow of Light.* New Jersey: Princeton University; 2008.
- [11] L. Dal Negro and S. V. Boriskina. Deterministic aperiodic nanostructures for photonics and plasmonics applications. *Laser Photon. Rev.* 2012;**6**:178–218. doi:10.1002/lpor.201000046
- [12] C. J. Pethick and H. Smith. *Bose-Einstein Condensate in Dilute Gas.* Cambridge, UK: Cambridge University; 2008.
- [13] V. A. Brazhnyi and V. V. Konotop. Theory of nonlinear matter waves in optical lattices. *Mod. Phys. Lett. B.* 2004;**18**:627–651. doi:10.1142/S0217984904007190
- [14] O. Morsch and M. Oberthaler. Dynamics of Bose-Einstein condensates in optical lattices. *Rev. Mod. Phys.* 2006;**78**:179–215. doi:10.1103/RevModPhys.78.179
- [15] H. T. C. Stoof, K. B. Gubbels, and D. B. M. Dickerscheid. *Ultracold Quantum Fields.* The Netherlands: Springer; 2009.
- [16] Y. V. Kartashov, V. A. Vysloukh, and L. Torner. Soliton shape and mobility control in optical lattices. *Progr. Optics.* 2009;**52**:63–148. doi:10.1016/S0079-6638(08)00004-8
- [17] B. A. Malomed. *Soliton Management in Periodic Systems.* New York: Springer; 2006.
- [18] Y. V. Kartashov, B. A. Malomed, and L. Torner. Solitons in nonlinear lattice. *Rev. Mod. Phys.* 2011;**83**:247–305. doi:10.1103/RevModPhys.83.247
- [19] J. Zeng and B. A. Malomed. Two-dimensional intraband solitons in lattice potentials with local defects and self-focusing nonlinearity. *J. Opt. Soc. Am. B.* 2013;**60**:1786–1793. doi:10.1364/JOSAB.30.001786
- [20] J. Zeng and B. A. Malomed. Two-dimensional solitons and vortices in media with incommensurate linear and nonlinear lattice potentials. *Phys. Scr.* 2012;**T149**:014035. doi:10.1088/0031-8949/2012/T149/014035
- [21] J. Fujioka and A. Espinosa. Soliton-like solution of an extended NLS equation existing in resonance with linear dispersive waves. *J. Phys. Soc. Jpn.* 1997;**66**:2601–2607. doi:10.1143/JPSJ.66.2601
- [22] J. Yang, B. A. Malomed, and D. J. Kaup. Embedded solitons in second-harmonic-generating systems. *Phys. Rev. Lett.* 1999;**83**:1958–1961. doi:10.1103/PhysRevLett.83.1958

- [23] A. R. Champneys and B. A. Malomed. Moving embedded solitons. *J. Phys. A.* 1999;**32**:L547–L553. doi:10.1088/0305-4470/32/50/103
- [24] A. R. Champneys, B. A. Malomed, J. Yang, and D. J. Kaup. Embedded solitons: solitary waves in resonance with the linear spectrum. *Physica D.* 2001;**152**:340–354. doi:10.1016/S0167-2789(01)00178-6
- [25] J. Atai and B. A. Malomed. Solitary waves in systems with separated Bragg grating and nonlinearity. *Phys. Rev. E.* 2001;**64**:066617. doi:10.1103/PhysRevE.64.066617
- [26] D. E. Pelinovsky and J. Yang. A normal form for nonlinear resonance of embedded solitons. *Proc. R. Soc. A.* 2002;**458**:1469–1497. doi:10.1098/rspa.2001.0916
- [27] A. Espinosa-Cerón, J. Fujioka, and A. Gómez-Rodríguez. Embedded solitons: four-frequency radiation, front propagation and radiation inhibition. *Phys. Scr.* 2003;**67**:314–324. doi:10.1088/0031-8949/67/4/008
- [28] R. F. Rodríguez, J. A. Reyes, A. Espinosa-Cerón, J. Fujioka, and B. A. Malomed. Standard and embedded solitons in nematic optical fibers. *Phys. Rev. E.* 2003;**68**:036606. doi:10.1103/PhysRevE.68.036606
- [29] A. Gubeskys and B. A. Malomed. Spontaneous soliton symmetry breaking in two-dimensional coupled Bose-Einstein condensates supported by optical lattices. *Phys. Rev. A.* 2007;**76**:043623. doi:10.1103/PhysRevA.76.043623
- [30] J. Yang. Dynamics of embedded solitons in the extended Korteweg-de Vries equations. *Stud. Appl. Math.* 2001;**106**:337–365. doi:10.1111/1467-9590.00169
- [31] J. Yang and T. R. Akylas. Continuous families of embedded solitons in the third-order nonlinear Schrödinger equation. *Stud. Appl. Math.* 2003;**111**:359. doi:10.1111/1467-9590.t01-1-00238
- [32] J. Yang. Stable embedded solitons. *Phys. Rev. Lett.* 2003;**91**:143903. doi:10.1103/PhysRevLett.91.143903
- [33] W. C. K. Mak, B. A. Malomed, and P. L. Chu. Symmetric and asymmetric solitons in linearly coupled Bragg gratings. *Phys. Rev. E.* 2004;**69**:066610. doi:10.1103/PhysRevE.69.066610
- [34] F. C. Moreira, V. V. Konotop, and B. A. Malomed. Solitons in PT–symmetric periodic systems with the quadratic nonlinearity. *Phys. Rev. A.* 2013;**87**:013832. doi:10.1103/PhysRevA.87.013832
- [35] J. Yang. Fully localized two-dimensional embedded solitons. *Phys. Rev. A.* 2010;**82**:053828. doi:10.1103/PhysRevA.82.053828
- [36] A. A. Sukhorukov and Y. S. Kivshar. Spatial optical solitons in nonlinear photonic crystals. *Phys. Rev. E.* 2002;**65**:036609. doi:10.1103/PhysRevE.65.036609
- [37] A. Shapira, N. Voloch-Bloch, B. A. Malomed, and A. Arie. Spatial quadratic solitons guided by narrow layers of a nonlinear material. *J. Opt. Soc. Am. B.* 2011;**28**:1481. doi:10.1364/JOSAB.28.1481

- [38] V. A. Brazhnyi and B. A. Malomed. Symmetric and asymmetric localized modes in linear lattices with an embedded pair of $\chi^{(2)}$ –nonlinear sites. *Phys. Rev. A.* 2012;**86**:013829. doi:10.1103/PhysRevA.86.013829
- [39] F. C. Moreira, F. K. Abdullaev, V. V. Konotop, and A. V. Yulin. Localized modes in $\chi^{(2)}$ media with PT–symmetric localized potential. *Phys. Rev. A.* 2012;**86**:053815. doi:10.1103/PhysRevA.86.053815
- [40] E. A. Ostrovskaya and Y. S. Kivshar. Matter-wave gap solitons in atomic band-gap structures. *Phys. Rev. Lett.* 2003;**90**:160407. doi:10.1103/PhysRevLett.90.160407
- [41] E. A. Ostrovskaya and Y. S. Kivshar. Photonic crystals for matter waves: Bose-Einstein condensates in optical lattices. *Opt. Express.* 2004;**12**:19. doi:10.1364/OPEX.12.000019
- [42] Z. Shi and J. Yang. Solitary waves bifurcated from Bloch-band edges in two-dimensional periodic media. *Phys. Rev. E.* 2007;**75**:056602. doi:10.1103/PhysRevE.75.056602
- [43] N. Dror and B. A. Malomed. Stability of dipole gap solitons in two-dimensional lattice potentials. In: *Spectral Analysis, Stability and Bifurcations in Nonlinear Physical Systems*. O. Kirillov and D. E. Pelinovsky, eds. London, Wiley; 2013. p. 111–138.
- [44] M. Vakhitov and A. Kolokolov. Stationary solutions of the wave equation in a medium with nonlinearity saturation. *Radiophys. Quantum Electron.* 1973;**16**:783–789. doi:10.1007/BF01031343
- [45] H. Sakaguchi and B. A. Malomed. Dynamics of positive- and negative-mass solitons in optical lattices and inverted traps. *J. Phys. B.* 2004;**37**:1443–1459. doi:10.1088/0953-4075/37/7/006
- [46] H. Sakaguchi and B. A. Malomed. Two-dimensional loosely and tightly bound solitons in optical lattices and inverted traps. *J. Phys. B.* 2004;**37**:2225–2239. doi:10.1088/0953-4075/37/11/001
- [47] M. Matuszewski, B. A. Malomed, and M. Trippenbach. Competition between attractive and repulsive interactions in two component Bose-Einstein condensates trapped in an optical lattice. *Phys. Rev. A.* 2007;**76**:043826. doi:10.1103/PhysRevA.76.043826
- [48] S. K. Adhikari and B. A. Malomed. Symbiotic gap and semigap solitons in Bose-Einstein condensates. *Phys. Rev. A.* 2008;**77**:023607. doi:10.1103/PhysRevA.77.023607
- [49] D. E. Pelinovsky. *Localization in Periodic Potential: From Schrödinger Operators to the Gross-Pitaevskii Equation*. Cambridge, UK: Cambridge University; 2011.
- [50] Y. V. Kartashov, V. A. Vysloukh, A. Szameit, F. Dreisow, M. Heinrich, S. Nolte, A. Tunnermann, T. Pertsch, and L. Torner. Surface solitons at interface of arrays with spatially modulated nonlinearity. *Opt. Lett.* 2005;**33**:1120–1122. doi:10.1364/OL.33.1120
- [51] H. Sakaguchi and B. A. Malomed. Solitons in combined linear and nonlinear lattice potentials. *Phys. Rev. A.* 2010;**81**:013624. doi:10.1103/PhysRevA.81.013624

- [52] B. Baizakov, B. A. Malomed, and M. Salerno. Multidimensional solitons in a low-dimensional periodic potential. *Phys. Rev. A.* 2004;**70**:053613. doi:10.1103/PhysRevA.70.053613
- [53] D. Mihalache, D. Mazilu, F. Lederer, Y. V. Kartashov, L. C. Crasovan, and L. Torner. Stable three-dimensional spatiotemporal solitons in a two-dimensional photonic lattice. *Phys. Rev. E.* 2004;**70**:055603. doi:10.1103/PhysRevE.70.055603
- [54] L. Gubeskys and B. A. Malomed. Symmetric and asymmetric solitons in two-dimensional dual-core waveguides with a one-dimensional lattice. *Phys. Rev. A.* 2009;**79**:045801. doi:10.1103/PhysRevA.79.045801
- [55] H. Sakaguchi and B. A. Malomed. Gap solitons in quasiperiodic optical lattices. *Phys. Rev. E.* 2006;**74**:026601. doi:10.1103/PhysRevE.74.026601
- [56] L. Levi, M. Rechtsman, B. Freedman, T. Schwartz, O. Manela, and M. Segev. Disorder-enhanced transport in photonic quasicrystals. *Science.* 2011;**332**:1541–1544. doi:10.1126/Science.332.1541
- [57] Z. V. Vardeny and A. Nahata. Photonic quasicrystals: disorder-enhanced light transport. *Nature Photon.* 2011;**5**:453. doi:10.1038/nphoton.2011.173
- [58] H. L. F. da Luz, F. K. Abdullaev, A. Gammal, M. Salerno, and L. Tomio. Matter-wave two-dimensional solitons in crossed linear and nonlinear optical lattices. *Phys. Rev. A.* 2010;**82**:043618. doi:10.1103/PhysRevA.82.043618
- [59] J. Zeng and Y. Lan. Two-dimensional solitons in PT linear lattice potentials. *Phys. Rev. E.* 2012;**85**:047601. doi:10.1103/PhysRevE.85.047601
- [60] H. Sakaguchi and B. A. Malomed. Higher-order vortex solitons, multipoles, and super-vortices on a square optical lattice. *Europhys. Lett.* 2005;**72**:698–704. doi:10.1209/epl/i2005-10295-7
- [61] R. Driben and B. A. Malomed. Stabilization of two-dimensional solitons and vortices against supercritical collapse by lattice potentials. *Eur. Phys. J. D.* 2008;**80**:317–323. doi:10.1140/epjd/e2008-00239-3

Relaxation Theory for Point Vortices

Ken Sawada and Takashi Suzuki

Additional information is available at the end of the chapter

<http://dx.doi.org/10.5772/67075>

Abstract

We study relaxation dynamics of the mean field of many point vortices from quasi-equilibrium to equilibrium. Maximum entropy production principle implies four consistent equations concerning relaxation-equilibrium states and patch-point vortex models. Point vortex relaxation equation coincides with Brownian point vortex equation in micro-canonical setting. Mathematical analysis to point vortex relaxation equation is done in accordance with the Smoluchowski-Poisson equation.

Keywords: point vortex, quasi-equilibrium, relaxation dynamics, maximum entropy production, global-in-time solution

1. Introduction

The physical object studied in this chapter is non-viscous, noncompressible fluid with high Reynolds number occupied in bounded, simply-connected domain. $\Omega \in \mathbb{R}^2$. Motion of this fluid is described by the Euler-Poisson equation

$$\omega_t + \nabla \cdot u\omega = 0, \quad \Delta\psi = -\omega, \quad u = \nabla^\perp\psi, \quad \psi|_{\partial\Omega} = 0 \quad (1)$$

where

$$\nabla^\perp = \begin{pmatrix} \frac{\partial}{\partial x_2} \\ -\frac{\partial}{\partial x_1} \end{pmatrix}, \quad x = (x_1, x_2),$$

and u , ω and ψ stand for the velocity, vorticity and stream function, respectively.

In the point vortex model

$$\omega(x, t) = \sum_{i=1}^N \alpha_i \delta_{x_i(t)}(dx) \tag{2}$$

system of Eq. (1) is reduced to

$$\alpha_i \frac{dx_i}{dt} = \nabla_{x_i}^\perp H_N, \quad i = 1, 2, \dots, N \tag{3}$$

associated with the Hamiltonian

$$H_N(x_1, \dots, x_N) = \frac{1}{2} \sum_i \alpha_i^2 R(x_i) + \sum_{i < j} \alpha_i \alpha_j G(x_i, x_j), \tag{4}$$

where $G = G(x, x')$ is the Green's function of $-\Delta$ provided with the Dirichlet boundary condition and

$$R(x) = \left[G(x, x') + \frac{1}{2\pi} \log|x-x'| \right]_{x'=x}.$$

Onsager [1] proposed to use statistical mechanics of Gibbs to Eq. (3). In the limit $N \rightarrow \infty$ with $\alpha N = 1$, local mean of vortex distribution is given by

$$\bar{\omega}(x) = \int_I \tilde{\alpha} \rho^{\tilde{\alpha}}(x) P(d\tilde{\alpha}), x \in \Omega \tag{5}$$

where $\alpha_i = \tilde{\alpha}^i \alpha$, $\tilde{\alpha}^i \in I = [-1, 1]$ is the intensity of the i -th vortex, $\rho^{\tilde{\alpha}}(x)$ is the existence probability of the vortex at x with relative intensity $\tilde{\alpha}$, which satisfies

$$\int_{\Omega} \rho^{\tilde{\alpha}}(x) dx = 1, \quad \forall \tilde{\alpha} \in I,$$

and $P(d\tilde{\alpha})$ is the numerical density of the vortices with the relative intensity $\tilde{\alpha}$. Under $H_N = E = \text{constant}$, $\alpha^2 N \beta_N = \beta = \text{constant}$ and $N \rightarrow \infty$, mean field equation is derived by several arguments [2-7], that is,

$$-\Delta \bar{\psi} = \int_I \tilde{\alpha} \frac{e^{-\beta \tilde{\alpha} \bar{\psi}}}{\int_{\Omega} e^{-\beta \tilde{\alpha} \bar{\psi}}} P(d\tilde{\alpha}), \quad \bar{\psi}|_{\partial\Omega} = 0 \tag{6}$$

with

$$\bar{\omega} = -\Delta \bar{\psi}, \quad \rho^{\tilde{\alpha}} = \frac{e^{-\beta \tilde{\alpha} \bar{\psi}}}{\int_{\Omega} e^{-\beta \tilde{\alpha} \bar{\psi}}}$$

where

$$\begin{aligned} \rho^{\tilde{\alpha}}(x) &= \lim_{N \rightarrow \infty} \int_{\Omega^{N-1}} \mu_N^{\beta_N}(dx, dx_2, \dots, dx_N) \\ \mu_N^{\beta_N}(dx_1, \dots, dx_N) &= \frac{1}{Z(N, \beta_N)} e^{-\beta_N H_N} dx_1 \dots dx_N \\ Z(N, \beta_N) &= \int_{\Omega^N} e^{-\beta_N H_N} dx_1 \dots dx_N. \end{aligned}$$

Since Ref. [8], structure of the set of solutions to Eq. (6) has been clarified in accordance with the Hamiltonian given by Eq. (4) (see [9] and the references therein).

Quasi-equilibria, on the other hand, are observed for several isolated systems with many components [10]. Thus, we have a relatively stationary state, different from the equilibrium, which eventually approaches the latter. Relaxation indicates this time interval, from quasi-equilibrium to equilibrium. To approach relaxation dynamics of many point vortices, patch model

$$\omega(x, t) = \sum_{i=1}^{N_p} \sigma_i 1_{\Omega_i(t)}(x) \tag{7}$$

is used. It describes detailed vortex distribution, where N_p , σ_i and $\Omega_i(t)$ denote the number of patches, the vorticity of the i -th patch and the domain of the i -th patch, respectively. Mean field equations for equilibrium and for relaxation time are derived by the principles of maximum entropy [11, 12] and maximum entropy production [13, 14], respectively. For the latter case, one obtains a system on $p = p(x, \sigma, t)$,

$$\begin{aligned} \frac{\partial p}{\partial t} + \nabla \cdot p \bar{u} &= \nabla \cdot D \left(\nabla p + \beta_p (\sigma - \bar{\omega}) p \nabla \bar{\psi} \right), \quad \beta_p = - \frac{\int_{\Omega} D \nabla \bar{\omega} \cdot \nabla \bar{\psi}}{\int_{\Omega} D (\int_I \sigma^2 p d\sigma - \bar{\omega}^2) |\nabla \bar{\psi}|^2} \\ \bar{\omega} &= \int_I \sigma p d\sigma = -\Delta \bar{\psi}, \quad \bar{\psi}|_{\partial\Omega} = 0, \quad \bar{u} = \nabla^{\perp} \bar{\psi} \end{aligned} \tag{8}$$

with the diffusion coefficient $D = D(x, t) > 0$.

In this chapter, we regard Eq. (2) as a limit of Eq. (7). First, point vortex model valid to the relaxation time is derived from Eq. (8), that is, a system on $\rho^{\tilde{\alpha}} = \rho^{\tilde{\alpha}}(x, t)$, $\tilde{\alpha} \in I$, in the form of

$$\begin{aligned} \frac{\partial \rho^{\tilde{\alpha}}}{\partial t} + \nabla \cdot \rho^{\tilde{\alpha}} \bar{u} &= \nabla \cdot D (\nabla \rho^{\tilde{\alpha}} + \beta \tilde{\alpha} \rho^{\tilde{\alpha}} \nabla \bar{\psi}), \\ \bar{\omega} &= \int_I \tilde{\alpha} \rho^{\tilde{\alpha}} P(d\tilde{\alpha}) = -\Delta \bar{\psi}, \quad \bar{\psi}|_{\partial\Omega} = 0, \quad \bar{u} = \nabla^{\perp} \bar{\psi} \\ \beta &= - \frac{\int_{\Omega} D \nabla \bar{\omega} \cdot \nabla \bar{\psi}}{\int_{\Omega} D \int_I \tilde{\alpha}^2 \rho^{\tilde{\alpha}} P(d\tilde{\alpha}) |\nabla \bar{\psi}|^2}. \end{aligned} \tag{9}$$

Second, the stationary state of Eq. (9) is given by Eq. (6). Third, Eq. (9) coincides with the Brownian point vortex model of Chavanis [15]. Finally, system of Eq. (9) provided with the boundary condition

$$\frac{\partial \rho^{\tilde{\alpha}}}{\partial v} + \beta \tilde{\alpha} \rho^{\tilde{\alpha}} \frac{\partial \bar{\psi}}{\partial v} \Big|_{\partial \Omega} = 0 \quad (10)$$

satisfies the requirements of isolated system in thermodynamics.

In fact, averaging Eq. (9) implies

$$\begin{aligned} \frac{\partial \bar{\omega}}{\partial t} + \nabla \cdot \bar{\omega} \bar{u} &= \nabla \cdot D(\nabla \bar{\omega} + \beta \bar{\omega}_2 \nabla \bar{\psi}), \quad \frac{\partial \bar{\omega}}{\partial v} + \beta \bar{\omega}_2 \frac{\partial \bar{\psi}}{\partial v} \Big|_{\partial \Omega} = 0 \\ \bar{\omega} &= -\Delta \bar{\psi}, \quad \bar{\psi}|_{\partial \Omega} = 0, \quad \bar{u} = \nabla^\perp \bar{\psi}, \quad \beta = -\frac{\int_{\Omega} D \nabla \bar{\omega} \cdot \nabla \bar{\psi}}{\int_{\Omega} D \bar{\omega}_2 |\nabla \bar{\psi}|^2} \end{aligned} \quad (11)$$

for

$$\bar{\omega} = \int_I \tilde{\alpha} \rho^{\tilde{\alpha}} P(d\tilde{\alpha}), \quad \bar{\omega}_2 = \int_I \tilde{\alpha}^2 \rho^{\tilde{\alpha}} P(d\tilde{\alpha}). \quad (12)$$

Then, we obtain mass and energy conservations

$$\frac{d}{dt} \int_{\Omega} \bar{\omega} = 0, \quad (\bar{\omega}_t, \bar{\psi}) = \frac{1}{2} \frac{d}{dt} (\bar{\omega}, (-\Delta)^{-1} \bar{\omega}) = 0 \quad (13)$$

where (\cdot) stands for the L^2 inner product. Assuming $\rho^{\tilde{\alpha}} > 0$, we write the first equation of (9) as

$$\frac{\partial \rho^{\tilde{\alpha}}}{\partial t} + \nabla \cdot \rho^{\tilde{\alpha}} \bar{u} = \nabla \cdot D \rho^{\tilde{\alpha}} \nabla (\log \rho^{\tilde{\alpha}} + \beta \tilde{\alpha} \bar{\psi}). \quad (14)$$

Then, it follows that

$$\frac{d}{dt} \int_{\Omega} \Phi(\rho^{\tilde{\alpha}}) dx + \beta \tilde{\alpha} (\rho_t^{\tilde{\alpha}}, \bar{\psi}) = - \int_{\Omega} D \rho^{\tilde{\alpha}} |\nabla (\log \rho^{\tilde{\alpha}} + \beta \tilde{\alpha} \bar{\psi})|^2 \quad (15)$$

from Eq. (10), where

$$\Phi(s) = s(\log s - 1) + 1 \geq 0, \quad s > 0.$$

Hence, it follows that

$$\frac{d}{dt} \int_{\Omega} \left(\int_I \Phi(\rho^{\tilde{\alpha}}) P(d\tilde{\alpha}) \right) = - \int_{\Omega} \left(\int_I D \rho^{\tilde{\alpha}} |\nabla (\log \rho^{\tilde{\alpha}} + \beta \tilde{\alpha} \bar{\psi})|^2 P(d\tilde{\alpha}) \right) \leq 0 \quad (16)$$

from Eq. (13), that is, entropy increasing.

2. Vorticity patch model

In Eq. (7), the vorticity σ_i is uniform in a region with constant area $\Omega_i(t)$, called vorticity patch. A patch takes a variety of forms as the time t varies. We collect all the vorticity patches in a small region, called cell. Cell area Δ thus takes the relation $|\Omega_i| \ll \Delta \ll |\Omega|$. The probability that the average vorticity at x is σ is denoted by $p(x, \sigma, t)dx$ which satisfies

$$\int p(x, \sigma, t) d\sigma = 1. \tag{17}$$

Let

$$\int_{\Omega} p(x, \sigma, t) dx = M(\sigma) \tag{18}$$

be independent of t . Since

$$|\Omega| = \iint p(x, \sigma, t) dx d\sigma = \int M(\sigma) d\sigma \tag{19}$$

equality (18) means conservation of total area of patches of the vorticity σ . Then, the macroscopic vorticity is defined by

$$\bar{\omega}(x, t) = \int \sigma p(x, \sigma, t) d\sigma, \tag{20}$$

which is associated with the stream function $\bar{\psi} = \bar{\psi}(x, t)$ and the velocity $\bar{u} = \bar{u}(x, t)$ through

$$\bar{\omega} = -\Delta \bar{\psi}, \quad \bar{\psi}|_{\partial\Omega} = 0, \quad \bar{u} = \nabla^{\perp} \bar{\psi}. \tag{21}$$

To formulate equilibrium, we apply the principle of maximum entropy [11, 12], seeking the maximal state of

$$S(p) = -\iint p(x, \sigma) \log p(x, \sigma) dx d\sigma \tag{22}$$

under the constraint Eqs. (17), (18) and

$$E = \frac{1}{2} \int_{\Omega} \bar{\omega} \bar{\psi}. \tag{23}$$

With the Lagrange multipliers $(\beta_p, c(\sigma), \zeta(x))$, it follows that

$$\delta S - \beta_p \delta E - \int c(\sigma) \delta M(\sigma) d\sigma - \int_{\Omega} \zeta(x) \left(\delta \int p d\sigma \right) dx = 0, \tag{24}$$

which is reduced to

$$p(x, \sigma) = e^{-c(\sigma) - (\zeta(x)+1) - \beta_p \sigma \bar{\psi}}. \quad (25)$$

Here, β_p and $c(\sigma)$ may be called inverse temperature and chemical potential, respectively. We put $c(0) = 0$ because of the degree of freedom of $c(\sigma)$ admitted by Eq. (19). Then, it follows that

$$p(x, \sigma) = p(x, 0) e^{-c(\sigma) - \beta_p \sigma \bar{\psi}} \quad (26)$$

and hence, Eq. (17) implies

$$p(x, \sigma) = \frac{e^{-c(\sigma) - \beta_p \sigma \bar{\psi}}}{\int e^{-c(\sigma') - \beta_p \sigma' \bar{\psi}} d\sigma'}. \quad (27)$$

From Eqs. (18) and (26), similarly, it follows that

$$c(\sigma) = \log \left(\frac{\int_{\Omega} p(x, 0) e^{-\beta_p \sigma \bar{\psi}} dx}{\int_{\Omega} p(x, \sigma) dx} \right). \quad (28)$$

The equilibrium mean field equation of vorticity patch model is thus given by Eqs. (20), (21), (27) and (28), which is reduced to

$$\begin{aligned} -\Delta \bar{\psi} &= \int \sigma M(\sigma) \frac{p(x, 0) e^{-\beta_p \sigma \bar{\psi}}}{\int_{\Omega} p(x, 0) e^{-\beta_p \sigma \bar{\psi}}} d\sigma, \quad \bar{\psi}|_{\partial\Omega} = 0 \\ \bar{\omega} &= \int_I \sigma p d\sigma = -\Delta \bar{\psi}, \quad \int_{\Omega} p(x, \sigma, t) dx = M(\sigma). \end{aligned} \quad (29)$$

One may use the principle of maximum entropy production to describe near from equilibrium dynamics [13, 14]. We apply the transport equation

$$\frac{\partial p}{\partial t} + \nabla \cdot (p \bar{u}) = -\nabla \cdot J, \quad J \cdot \nu|_{\partial\Omega} = 0 \quad (30)$$

with the diffusion flux $J = J(x, \sigma, t)$ of $p = p(x, \sigma, t)$, where ν denotes the outer unit normal vector. We obtain the total patch area conservation for each σ ,

$$\frac{\partial M}{\partial t} = \frac{\partial}{\partial t} \int_{\Omega} p(x, \sigma, t) = 0 \quad (31)$$

because $\bar{u} \cdot \nu|_{\partial\Omega} = 0$ follows from Eq. (21). Eq. (30) implies

$$\frac{\partial \bar{\omega}}{\partial t} + \nabla \cdot (\bar{\omega} \bar{u} + J_{\omega}) = 0, \quad (32)$$

where $J_{\omega} = \int \sigma J(x, \sigma, t) d\sigma$ stands for the local mean vorticity flux. Since $J_{\omega} \cdot \nu = 0$ on $\partial\Omega$,

Eq. (32) implies conservation of circulation $\Gamma = \int_{\Omega} \bar{\omega}$. Furthermore, J_{ω} is associated with the detailed fluctuation of (ω, u) from $(\bar{\omega}, \bar{u})$ by Eq. (1).

Here, we ignore the diffusion energy $E_d = \frac{1}{2} \iint \frac{J^2}{p} d\sigma dx$ to take

$$E = \frac{1}{2} \int_{\Omega} \bar{\omega} \bar{\psi} \tag{33}$$

as the total energy of this system. Using maximum entropy production principle, we chose the flux J to maximize entropy production rate \dot{S} under the constraint

$$\dot{E} = 0, \quad \int J d\sigma = 0, \quad \int \frac{J^2}{2p} d\sigma \leq C(x, t) \tag{34}$$

where

$$S(p) = - \iint p(x, \sigma, t) \log p(x, \sigma, t) d\sigma dx.$$

Using Lagrange multipliers $(\beta_p, D, \zeta) = (\beta_p(t), D(x, t), \zeta(x, t))$, we obtain

$$\delta \dot{S} - \beta_p \delta \dot{E} - \int_{\Omega} D^{-1} \left(\delta \int \frac{J^2}{2p} d\sigma \right) dx - \int_{\Omega} \zeta \left(\delta \int J d\sigma \right) dx = 0. \tag{35}$$

Since

$$\begin{aligned} \dot{E} &= \frac{d}{dt} E = \int_{\Omega} \bar{\psi} \frac{\partial \bar{\omega}}{\partial t} = \int_{\Omega} J_{\omega} \cdot \nabla \bar{\psi} = \iint \sigma J \cdot \nabla \bar{\psi} d\sigma dx \\ \dot{S} &= \frac{d}{dt} S = - \iint \frac{\partial p}{\partial t} (\log p + 1) d\sigma dx = - \iint J \cdot \frac{\nabla p}{p} d\sigma dx, \end{aligned} \tag{36}$$

Eq. (35) is reduced to

$$J = -D(\nabla p + \beta_p \sigma p \nabla \bar{\psi} + p \zeta). \tag{37}$$

From the constraint of Eq. (34), it follows that

$$0 = \int J d\sigma = - \int D(\nabla p + \beta_p \sigma p \nabla \bar{\psi} + p \zeta) d\sigma = -D(\beta_p \bar{\omega} \nabla \bar{\psi} + \zeta) \tag{38}$$

and

$$\begin{aligned} 0 &= \iint \sigma J \cdot \nabla \bar{\psi} d\sigma dx = \iint -\sigma D(\nabla p + \beta_p \sigma p \nabla \bar{\psi} + p \zeta) \cdot \nabla \bar{\psi} d\sigma dx \\ &= \iint -\sigma D(\nabla p + \beta_p (\sigma p - p \bar{\omega}) \nabla \bar{\psi}) \cdot \nabla \bar{\psi} d\sigma dx \\ &= - \int_{\Omega} D \nabla \bar{\omega} \cdot \nabla \bar{\psi} dx - \beta_p \int_{\Omega} D \left(\int \sigma^2 p d\sigma - \bar{\omega}^2 \right) |\nabla \bar{\psi}|^2 dx \end{aligned} \tag{39}$$

which implies

$$\zeta = -\beta_p \bar{\omega} \nabla \bar{\psi} \quad (40)$$

and

$$\beta_p = -\frac{\int_{\Omega} D \nabla \bar{\omega} \cdot \nabla \bar{\psi}}{\int_{\Omega} D \left(\int \sigma^2 p d\sigma - \bar{\omega}^2 \right) |\nabla \bar{\psi}|^2} \quad (41)$$

Thus, we end up with

$$\begin{aligned} \frac{\partial p}{\partial t} + \nabla \cdot (p \bar{u}) &= \nabla \cdot D \left(\nabla p + \beta_p (\sigma - \bar{\omega}) p \nabla \bar{\psi} \right), \quad \beta_p = -\frac{\int_{\Omega} D \nabla \bar{\omega} \cdot \nabla \bar{\psi}}{\int_{\Omega} D \left(\int \sigma^2 p d\sigma - \bar{\omega}^2 \right) |\nabla \bar{\psi}|^2} \\ D \left(\nabla p + \beta_p (\sigma - \bar{\omega}) p \nabla \bar{\psi} \right) \cdot \nu|_{\partial\Omega} &= 0, \quad \bar{\omega} = \int_I \sigma p d\sigma = -\Delta \bar{\psi}, \quad \bar{\psi}|_{\partial\Omega} = 0, \quad \bar{u} = \nabla^{\perp} \bar{\psi} \end{aligned} \quad (42)$$

by Eqs. (30), (37), (40) and (41), where $D = D(x, t) > 0$.

3. Point vortex model

Point vortex model is regarded as a special case of vorticity patch model, where the patch size shrinks to zero [16]. Here, we give a quantitative description of this limit process, using localization. First, we derive the equilibrium mean field equation of point vortices from that of vorticity patches. Then, we derive relaxation equation for the point vortex model. Fundamental quantities of point vortex model are circulation $\alpha \tilde{\alpha}$, probability $\rho^{\tilde{\alpha}}(x, t)$ and number density $P(d\tilde{\alpha})$. Circulation of each vortex is set to be small to preserve total energy and total circulation in the mean field limit. In the vorticity patch model, on the other hand, vorticity σ and probability $p(x, \sigma, t)$ are the fundamental quantities (**Figure 1**).

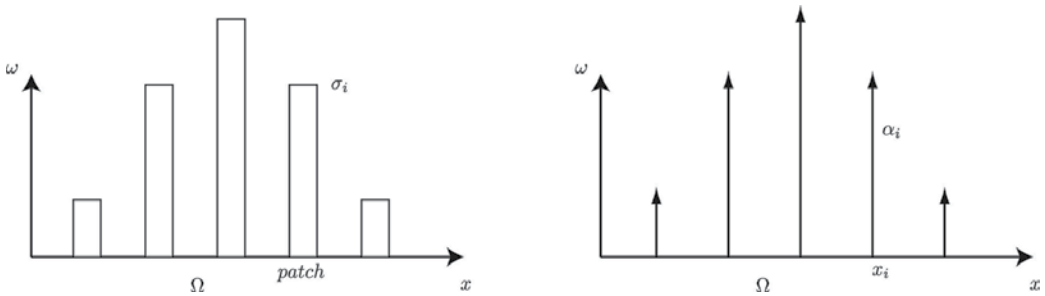


Figure 1. Vorticity distribution: vorticity patch model (left). point vortex model (right).

Here, we use the following localization in order to transform vorticity patch to point vortex (**Figure 2**):

1. Divide each patch into two patches with half area and the same vorticity.
2. Again, divide each patch into two patches with half area: one has doubled vorticity and the other has 0 vorticity.

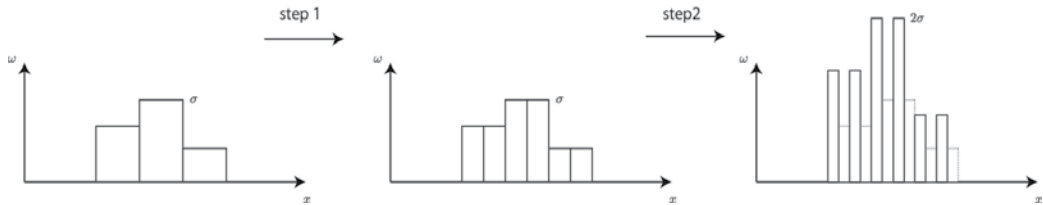


Figure 2. Sketch of localization procedure.

Under this procedure, the number of nonzero patches is doubled and their vorticities are also doubled. At the same time, the area of each patch becomes 1/4 and the number of total patches is quadrupled, while the total circulation is preserved. First, we describe the detailed process for the stationary state of Eq. (7).

Let Ω be divided into many cells with uniform size Δ and let each cell be composed of many patches. Let $N^{(k)}(x, \sigma) dx d\sigma$ be the number of patches in the cell after k -times of the above procedure centered at x of which vorticity was originally σ and let $\sigma^{(k)}$ be the vorticity of these patches after k -times localization. We assume that the number of total vorticity patches in the cell,

$$N_c^{(k)}(\Delta) = \int N^{(k)}(x, \sigma) d\sigma, \quad (43)$$

is independent of x . Then, the number of total patches in Ω , the total area of the patches and the total circulation of the patches after k -times localization procedures, with original vorticity σ , are given by

$$N^{(k)}(\sigma) d\sigma = \int_{\Omega} N^{(k)}(x, \sigma), \quad M^{(k)}(\sigma) d\sigma = |\Omega| \frac{N^{(k)}(\sigma) d\sigma}{\int N^{(k)}(\sigma) d\sigma}, \quad (44)$$

and

$$\gamma^{(k)}(\sigma) d\sigma = \sigma^{(k)} M^{(k)}(\sigma) d\sigma, \quad (45)$$

respectively.

We obtain

$$N_p = \iint N^{(0)}(x, \sigma) d\sigma dx, \quad (46)$$

recalling Eq. (7). Since

$$\sigma^{(k)} = 2^k \sigma, \quad (47)$$

it holds that

$$N^{(k)}(x, \sigma) dx d\sigma = (4^k - 2^k) N_c^{(0)}(\Delta) \delta_0(d\sigma) + 2^k N^{(0)}(x, \sigma) dx d\sigma. \quad (48)$$

From Eq. (48), the related probability

$$p^{(k)}(x, \sigma) dx d\sigma = \frac{N^{(k)}(x, \sigma) dx d\sigma}{N_c^{(k)}(\Delta)} \quad (49)$$

satisfies

$$\begin{aligned} p^{(k)}(x, \sigma) dx d\sigma &= \frac{(4^k - 2^k) N_c^{(0)}(\Delta) \delta_0(d\sigma) + 2^k N^{(0)}(x, \sigma) dx d\sigma}{(4^k - 2^k) N_c^{(0)}(\Delta) + 2^k \int N^{(0)}(x, \sigma) d\sigma} \\ &= \frac{(4^k - 2^k) N_c^{(0)}(\Delta) \delta_0(d\sigma) + 2^k N^{(0)}(x, \sigma) dx d\sigma}{4^k N_c^{(0)}(\Delta)} \end{aligned} \quad (50)$$

and hence,

$$\lim_{k \rightarrow \infty} p^{(k)}(x, \sigma) dx d\sigma = \delta_0(d\sigma). \quad (51)$$

We also have

$$M^{(k)}(\sigma) d\sigma = \int_{\Omega} p^{(k)}(x, \sigma) dx = \lim_{\Delta \rightarrow 0} \sum_{i=1}^{|\Omega|/\Delta} \frac{N^{(k)}(x_i, \sigma) dx d\sigma}{N_c^{(k)}(\Delta)} \cdot \Delta \quad (52)$$

which implies

$$\begin{aligned} M^{(k)}(\sigma) d\sigma &= \frac{|\Omega|}{4^k N_p} \lim_{\Delta \rightarrow 0} \sum_{i=1}^{|\Omega|/\Delta} N^{(k)}(x_i, \sigma) d\sigma = \frac{|\Omega|}{4^k N_p} N^{(k)}(\sigma) d\sigma \\ &= |\Omega| \left((1 - 2^{-k}) \delta_0(d\sigma) + 2^{-k} \frac{N^{(0)}(\sigma) d\sigma}{N_p} \right) \end{aligned} \quad (53)$$

by $\frac{\Delta}{N_c^{(k)}(\Delta)} = \frac{|\Omega|}{4^k N_p}$ and Eq. (48). We have, therefore,

$$\lim_{k \rightarrow \infty} M^{(k)}(\sigma) d\sigma = |\Omega| \delta_0(d\sigma). \quad (54)$$

It holds also that

$$\begin{aligned} \gamma^{(k)}(\sigma) &= \int_{\Omega} \sigma^{(k)} p^{(k)}(x, \sigma) dx = \int_{\Omega} \sigma p^{(0)}(x, \sigma) dx \\ &= \sigma^{(k)} M^{(k)}(\sigma) d\sigma = \frac{\sigma |\Omega|}{N_p} N^{(0)}(\sigma) d\sigma \end{aligned} \quad (55)$$

and

$$\bar{\omega}^{(k)}(x) = \int \sigma^{(k)} p^{(k)}(x, \sigma) d\sigma = \int \sigma p^{(0)}(x, \sigma) d\sigma. \quad (56)$$

Fundamental quantities constituting of the mean field limit of point vortex model thus arise as $k \rightarrow \infty$.

To explore the relationship between the quantities in two models, we take regards to circulation of one patch, total circulation of patches with original vorticity σ and local mean vorticity. Based on

$$\sigma^{(k)} \cdot \frac{|\Omega|}{4^k N_p} = \tilde{\alpha} \cdot \alpha, \quad k \gg 1, \tag{57}$$

and Eq. (47), we reach the ansatz $\sigma|\Omega| = \tilde{\alpha}, \frac{1}{2^k N_p} = \alpha, 2^k N_p = N$. Similarly, we use

$$\frac{\sigma|\Omega|}{N_p} N^{(0)}(\sigma) d\sigma = \tilde{\alpha} P(d\tilde{\alpha}) \tag{58}$$

to put

$$\frac{N^{(0)}(\sigma) d\sigma}{N_p} = \frac{M^{(0)}(\sigma) d\sigma}{|\Omega|} = P(d\tilde{\alpha}) \tag{59}$$

by

$$\frac{\sigma|\Omega|}{N_p} N^{(0)}(\sigma) d\sigma = \sigma|\Omega| \cdot \frac{1}{2^k N_p} \cdot 2^k N_p \cdot \frac{N^{(0)}(\sigma) d\sigma}{N_p} = \tilde{\alpha} \alpha N P(d\tilde{\alpha}) = \tilde{\alpha} P(d\tilde{\alpha}). \tag{60}$$

Finally, we use the identity on local mean vorticity

$$\int \sigma p^{(0)}(x, \sigma) d\sigma = \int \tilde{\alpha} \rho^{\tilde{\alpha}}(x) P(d\tilde{\alpha}) \tag{61}$$

to assign

$$\frac{1}{|\Omega|} p^{(0)}(x, \sigma) d\sigma = \rho^{\tilde{\alpha}}(x) P(d\tilde{\alpha}), \tag{62}$$

regarding

$$\int \sigma p^{(0)}(x, \sigma) d\sigma = \int \sigma|\Omega| \cdot \frac{p^{(0)}(x, \sigma)}{|\Omega|} d\sigma = \int \tilde{\alpha} \rho^{\tilde{\alpha}}(x) P(d\tilde{\alpha}). \tag{63}$$

These relations are summarized in the following **Table 1**:

Vorticity patch model	Point vortex model
$\sigma \Omega $	$\tilde{\alpha}$
$\frac{1}{2^k N_p}$	α
$2^k N_p$	N
$\frac{N^{(0)}(\sigma) d\sigma}{N_p}$	$P(d\tilde{\alpha})$
$\frac{1}{ \Omega } p^{(0)}(x, \sigma) d\sigma$	$\rho^{\tilde{\alpha}}(x) P(d\tilde{\alpha})$

Table 1. Relation between vorticity patch model and point vortex model for $\tilde{\alpha}$.

After k -times localization, the first equation in Eq. (29) takes the form

$$\begin{aligned}
 -\Delta\bar{\psi} &= \int \sigma^{(k)} M^{(k)}(\sigma) \frac{p^{(k)}(x, 0) e^{-\beta_p \sigma^{(k)} \bar{\psi}}}{\int_{\Omega} p^{(k)}(x, 0) e^{-\beta_p \sigma^{(k)} \bar{\psi}} d\sigma} d\sigma \\
 &= \int \frac{\sigma |\Omega|}{N_p} N^{(0)}(\sigma) \frac{p^{(k)}(x, 0) e^{-\beta_p 2^k \sigma \bar{\psi}}}{\int_{\Omega} p^{(k)}(x, 0) e^{-\beta_p 2^k \sigma \bar{\psi}} d\sigma} d\sigma \\
 &= \int \sigma |\Omega| \frac{p^{(k)}(x, 0) e^{-\beta_p \frac{2^k}{|\Omega|} \sigma |\Omega| \bar{\psi}}}{\int_{\Omega} p^{(k)}(x, 0) e^{-\beta_p \frac{2^k}{|\Omega|} \sigma |\Omega| \bar{\psi}} d\sigma} \frac{N^{(0)}(\sigma)}{N_p} d\sigma.
 \end{aligned} \tag{64}$$

From **Table 1**, the right-hand side on Eq. (64) is replaced by

$$\int \tilde{\alpha} \frac{p^{(k)}(x, 0) e^{-\frac{\beta_N}{N} \tilde{\alpha} \bar{\psi}}}{\int_{\Omega} p^{(k)}(x, 0) e^{-\frac{\beta_N}{N} \tilde{\alpha} \bar{\psi}} d\tilde{\alpha}} P(d\tilde{\alpha}) \tag{65}$$

for $\beta_N = 4^k \frac{N_p}{|\Omega|} \beta_p = N \cdot \frac{2^k \beta_p}{|\Omega|}$. Sending $k \rightarrow \infty$, we obtain the first equation of (6) with $\beta = \frac{\beta_N}{N}$ by Eq. (51). This means that the vorticity patch model is transformed to the point vortex model applied to the mean field limit by taking the localization procedure.

We can derive also relaxation equation of point vortex model from that of vorticity patch model. By Eq. (37), the value of the diffusion flux J for $\sigma = 0$ is

$$J(x, 0, t) = -D(x, t) \left(\nabla p(x, 0, t) + p(x, 0, t) \zeta(x, t) \right) \tag{66}$$

and hence

$$\zeta(x, t) = \frac{-D(x, t)^{-1} J(x, 0, t) + \nabla p(x, 0, t)}{p(x, 0, t)}. \tag{67}$$

Flux is thus given by

$$\begin{aligned}
 J(x, \sigma, t) &= \\
 &-D(x, t) \left(\nabla p(x, \sigma, t) + \beta_p(t) \sigma p(x, \sigma, t) \nabla \bar{\psi}(x, t) - p(x, \sigma, t) \frac{D(x, t)^{-1} J(x, 0, t) + \nabla p(x, 0, t)}{p(x, 0, t)} \right).
 \end{aligned} \tag{68}$$

We reach

$$\frac{\partial p}{\partial t} + \nabla \cdot (p\bar{u}) = \nabla \cdot D \left(\nabla p + \beta_p \sigma p \nabla \bar{\psi} - p \left[\frac{D^{-1} J + \nabla p}{p} \right]_{\sigma=0} \right) \tag{69}$$

with

$$\beta_p = \beta_p(t) = - \frac{\int_{\Omega} D \nabla \bar{\omega} \cdot \nabla \bar{\psi} - \int_{\Omega} D \bar{\omega} \left[\frac{D^{-1} J + \nabla p}{p} \right]_{\sigma=0} \cdot \nabla \bar{\psi}}{\iint D \sigma^2 p |\nabla \bar{\psi}|^2 d\sigma dx} \tag{70}$$

Therefore, after k -times localization procedure, it holds that

$$\begin{aligned} & \frac{\partial \sigma^{(k)} p^{(k)}}{\partial t} + \nabla \cdot \left(\sigma^{(k)} p^{(k)} \bar{u} \right) \\ &= \nabla \cdot D \left(\nabla \sigma^{(k)} p^{(k)} + \beta_p (\sigma^{(k)})^2 p^{(k)} \nabla \bar{\psi} - \sigma^{(k)} p^{(k)} \left[\frac{D^{-1} J^{(k)} + \nabla p^{(k)}}{p^{(k)}} \right]_{\sigma=0} \right). \end{aligned} \quad (71)$$

Putting $\beta_N = 4^k \frac{N_p}{|\Omega|} \beta_p$, similarly, we obtain

$$\frac{\partial}{\partial t} \left(\tilde{\alpha} \rho^{\tilde{\alpha}} P(d\tilde{\alpha}) \right) + \nabla \cdot \left(\tilde{\alpha} \rho^{\tilde{\alpha}} P(d\tilde{\alpha}) \bar{u} \right) = \nabla \cdot \left(D \left(\nabla \left(\tilde{\alpha} \rho^{\tilde{\alpha}} P(d\tilde{\alpha}) \right) + \beta \tilde{\alpha}^2 \rho^{\tilde{\alpha}} P(d\tilde{\alpha}) \nabla \bar{\psi} \right) \right), \quad (72)$$

from

$$\begin{aligned} \lim_{k \rightarrow \infty} p^{(k)}(x, \sigma, t) &= \delta_0(d\sigma), \quad \lim_{k \rightarrow \infty} J^{(k)}(x, 0, t) = 0 \\ \sigma^{(k)} p^{(k)}(x, \sigma, t) &= \sigma p^{(0)}(x, \sigma, t) = \sigma |\Omega| \cdot \frac{p^{(0)}(x, \sigma, t)}{|\Omega|} \approx \tilde{\alpha} \rho^{\tilde{\alpha}}(x, t) P(d\tilde{\alpha}) \\ (\sigma^{(k)})^2 p^{(k)}(x, \sigma, t) &= 2^k \sigma \cdot \sigma p^{(0)}(x, \sigma, t) = \frac{2^k}{|\Omega|} \cdot (\sigma |\Omega|)^2 \cdot \frac{p^{(0)}(x, \sigma, t)}{|\Omega|} \approx \frac{2^k}{|\Omega|} \tilde{\alpha}^2 \rho^{\tilde{\alpha}}(x, t) P(d\tilde{\alpha}) \end{aligned} \quad (73)$$

Here, we assume $\lim_{k \rightarrow \infty} J^{(k)}(x, 0, t) = 0$, because $\int J^{(k)}(x, \sigma, t) d\sigma = 0$ and the 0-vorticity patch becomes dominant in the system. Then, we obtain Eq. (9) by Eq. (72).

4. Relaxation dynamics

If $P(d\tilde{\alpha}) = \delta_1(d\tilde{\alpha})$, it holds that $\bar{\omega} = \bar{\omega}_2$ in Eq. (11). Then, we obtain

$$\omega_t + \nabla \cdot \omega \nabla^\perp \psi = \nabla \cdot (\nabla \omega + \beta \omega \nabla \psi), \quad \frac{\partial \omega}{\partial \nu} + \beta \omega \frac{\partial \psi}{\partial \nu} \Big|_{\partial \Omega} = 0, \quad \omega|_{t=0} = \omega_0(x) \geq 0 \quad (74)$$

$$-\Delta \psi = \omega, \quad \psi|_{\partial \Omega} = 0, \quad \beta = -\frac{\int_{\Omega} \nabla \omega \cdot \nabla \psi}{\int_{\Omega} \omega |\nabla \psi|^2} \quad (75)$$

assuming $D = 1$. Conservations of total mass and energy

$$\|\omega(\cdot, t)\|_1 = \lambda, \quad \left(\psi(\cdot, t), \omega(\cdot, t) \right) = e, \quad (76)$$

are derived from Eq. (13), while increase in entropy of Eq. (16) is reduced to

$$\frac{d}{dt} \int_{\Omega} \Phi(\omega) = - \int_{\Omega} \omega |\nabla(\log \omega - \beta \psi)|^2 \leq 0, \quad (77)$$

where $\Phi(s) = s(\log s - 1) + 1$.

In the stationary state, we obtain $\log \omega + \beta \psi = \text{constant}$ by Eq. (77). Hence, it follows that

$$-\Delta \psi = \omega, \quad \psi|_{\partial\Omega} = 0, \quad \omega = \frac{\lambda e^{-\beta\psi}}{\int_{\Omega} e^{-\beta\psi}}, \quad -\beta = \frac{\int_{\Omega} \nabla \omega \cdot \nabla \psi}{\int_{\Omega} \omega |\nabla \psi|^2}, \quad e = \int_{\Omega} \omega \psi \quad (78)$$

from Eq. (76). Here, the third equation implies the fourth equation as

$$(\nabla \omega, \nabla \psi) = -\beta \int_{\Omega} \omega |\nabla \psi|^2. \quad (79)$$

Using

$$v = \beta \psi, \quad \mu = \frac{\beta \lambda}{\int_{\Omega} e^{-\beta\psi}}, \quad (80)$$

therefore, Eq. (78) is reduced to

$$-\Delta v = \mu e^{-v}, \quad v|_{\partial\Omega} = 0, \quad \frac{e}{\lambda^2} = \frac{\int_{\Omega} |\nabla v|^2}{\left(\int_{\partial\Omega} -\frac{\partial v}{\partial \nu}\right)^2}. \quad (81)$$

In fact, to see the third equality of (81), we note

$$e = (\omega, \psi) = \beta^{-1} \frac{\lambda \int_{\Omega} e^{-v} v}{\int_{\Omega} e^{-v}} \quad (82)$$

which implies

$$\mu = \frac{\lambda}{\int_{\Omega} e^{-v}} \cdot \frac{\lambda \int_{\Omega} e^{-v} v}{e \int_{\Omega} e^{-v}} = \frac{\lambda^2}{e} \cdot \frac{\int_{\Omega} e^{-v} v}{\left(\int_{\Omega} e^{-v}\right)^2} \quad (83)$$

and hence

$$\frac{e}{\lambda^2} = \frac{1}{\mu} \cdot \frac{\int_{\Omega} e^{-v} v}{\left(\int_{\Omega} e^{-v}\right)^2} = \frac{\|\nabla v\|_2^2}{\left(\int_{\partial\Omega} -\frac{\partial v}{\partial \nu}\right)^2}. \quad (84)$$

If $\mu < 0$, system of Eq. (81) except for the third equation is equivalent to the Gel'fand problem

$$-\Delta w = \sigma e^w, \quad w|_{\partial\Omega} = 0 \quad (85)$$

with $\sigma = -\mu$. If Ω is simply connected, there is a non-compact family of solutions as $\mu \uparrow 0$, which are uniformly bounded near the boundary [8, 9]. Hence, there arises

$$\lim_{\mu \uparrow 0} \frac{e}{\lambda^2} = +\infty \quad (86)$$

for this family. For $\mu \geq 0$, on the contrary, system of Eq. (81) except for the third equation admits a unique solution $v = v_\mu(x)$. Regarding Eq. (76), therefore, it is necessary that

$$\lim_{\mu \uparrow +\infty} \frac{\|\nabla v_\mu\|_2^2}{\left(\int_{\partial\Omega} -\frac{\partial v_\mu}{\partial \nu}\right)^2} = 0 \tag{87}$$

for any orbit to Eqs. (74), (75) to be global-in-time and compact, for any $\lambda, e > 0$ in Eq. (76).

If $\Omega = B \equiv \{x \in \mathbb{R}^2 \mid |x| < 1\}$, it actually holds that Eq. (87). In this case, we have $v = v(r)$, $r = |x|$, and the result follows from an elementary calculation. More precisely, putting $u = v - \log \mu$, $s = \log r$, we obtain

$$u_{ss} + e^{-u+2s} = 0, \quad s < 0, \quad u(0) = -\log \mu, \quad \lim_{s \downarrow -\infty} u_s e^{-s} = 0, \quad \frac{\|\nabla v\|_2^2}{\left(\int_{\partial\Omega} -\frac{\partial v}{\partial \nu}\right)^2} = \frac{I}{2\pi}, \tag{88}$$

where $I = \frac{\int_0^0 u_s^2 ds}{u_s(0)^2}$. Using $w = u - 2s$, $p = \frac{1}{\sqrt{2}}(e^{-w} + 2)^{1/2}$, we have

$$p = -1 + 2(1 - ce^{2s})^{-1} \tag{89}$$

with $c \uparrow 1$ as $\mu \uparrow +\infty$. It follows that

$$I = (1-c)^2 \int_{-\infty}^0 \frac{e^{4s}}{(1 - ce^{2s})^2} ds \tag{90}$$

with

$$\int_{-\infty}^0 \frac{e^{4s}}{(1 - ce^{2s})^2} ds = \frac{1}{2c(1-c)} + \frac{1}{2c^2} \log(1-c) \tag{91}$$

and hence

$$\lim_{c \uparrow 1} I = 0. \tag{92}$$

If β is constant in Eq. (9), it is the mean field limit of Brownian vortices [15]. It is nothing but the Smoluchowski-Poisson equation [9, 17] and obeys the feature of canonical ensemble, provided with total mass conservation and decrease of free energy:

$$\frac{d\mathcal{F}}{dt} = - \int_{\Omega} \omega |\nabla(\log \omega + \beta\psi)|^2, \quad \mathcal{F}(\omega) = \int_{\Omega} \Phi(\omega) - \frac{1}{2} \left((-\Delta)^{-1} \omega, \omega \right). \tag{93}$$

Then, there arises the blowup threshold $\beta = -8\pi/\lambda$ [18]. Here, we show the following theorem, where $G = G(x, x')$ denotes the Green's function for the Poisson part,

$$-\Delta G(\cdot, x') = \delta_{x'}, \quad G(\cdot, x')|_{\partial\Omega} = 0, \quad x' \in \Omega \tag{94}$$

and

$$\rho_\varphi(x, x') = \nabla\varphi(x) \cdot \nabla_x G(x, x') + \nabla\varphi(x') \cdot \nabla_{x'} G(x, x'), \quad \varphi \in X, \tag{95}$$

where $X = \left\{ \varphi \in C^2(\overline{\Omega}) \mid \frac{\partial\varphi}{\partial\nu} \Big|_{\partial\Omega} = 0 \right\}$. It holds that $\rho_\varphi \in L^\infty(\Omega \times \Omega)$. The proof is similar as in Lemma 5.2 of [17] for the case of Neumann boundary condition.

Theorem 1: Let $\Omega = B$ and ω_0 be a smooth function in the form of $\omega_0 = \omega_0(r) > 0$ with $\omega_{0r} < 0$, $0 < r \leq 1$. Let $T \in (0, +\infty]$ be the maximal existence time of the classical solution to Eqs. (74), (75) and λ be the total mass defined by Eq. (76). Then, it follows that

$$\limsup_{t \uparrow T} \beta(t) < -\frac{8\pi}{\lambda} \Rightarrow T < +\infty \tag{96}$$

and

$$T < +\infty \Rightarrow \liminf_{t \uparrow T} \beta(t) = -\infty. \tag{97}$$

In particular, we have

$$\liminf_{t \uparrow T} \beta(t) > -\infty \Rightarrow T = +\infty, \quad \limsup_{t \uparrow T} \beta(t) \geq -\frac{8\pi}{\lambda}. \tag{98}$$

Proof: From the assumption, it follows that $(\omega, \psi) = (\omega(r, t), \psi(r, t))$ and

$$\omega_r, \psi_r < 0, \quad 0 < r \leq 1.$$

Then, we obtain

$$M \equiv \frac{\lambda}{2\pi} \geq \int_0^r r\omega dr \geq \omega(r, t) \int_0^r r dr = \frac{r^2}{2} \omega \tag{99}$$

and hence

$$\omega(r, t) \leq \frac{2M}{r^2}, \quad 0 < r \leq 1. \tag{100}$$

It holds also that

$$-\beta = \frac{\int_0^1 \omega_r \psi_r r dr}{\int_0^1 \omega \psi_r^2 r dr} > 0 \tag{101}$$

which implies

$$\omega_t = \Delta\omega + \beta \nabla\psi \cdot \nabla\omega + \beta\omega\Delta\psi = \Delta\omega + \beta \nabla\psi \cdot \nabla\omega - \beta\omega^2 \geq \Delta\omega + \beta \nabla\psi \cdot \nabla\omega \tag{102}$$

with

$$-\frac{\partial\omega}{\partial\nu} = \beta\omega \frac{\partial\psi}{\partial\nu} > 0 \quad \text{on} \quad \partial\Omega \times (0, T). \tag{103}$$

The comparison theorem now guarantees $\omega \geq \delta \equiv \min_{\Omega} \omega_0 > 0$ and hence

$$\int_{\Omega} \omega |\nabla\psi|^2 \geq \delta \int_{\Omega} |\nabla\psi|^2 = \delta e. \tag{104}$$

For Eq. (96) to prove, we use the second moment. First, the Poisson part of Eq. (75) is reduced to

$$-r\psi_r = \int_0^r r\omega dr \equiv A(r). \tag{105}$$

Second, it follows that

$$\begin{aligned} \frac{d}{dt} \int_0^1 \omega r^3 dr &= - \int_0^1 (\omega_r + \beta\omega\psi_r) 2r \cdot r dr \\ &= -2r^2 \omega|_{r=0}^{r=1} + \int_0^1 4r\omega - 2\beta\omega\psi_r r^2 dr \\ &= -2\omega|_{r=1} + 4M + 2\beta \int_0^1 A A_r dr \\ &= -2\omega|_{r=1} + 4M + \beta M^2 \leq 4M + \beta M^2 \end{aligned} \tag{106}$$

from $A(1) = M$. Under the hypothesis of Eq. (96), we have $\delta > 0$ such that

$$4M + \beta M^2 \leq -\delta, \quad t \uparrow T. \tag{107}$$

Then, $T = +\infty$ gives a contradiction.

Now, we assume $T < +\infty$. First, equality in (106) implies

$$\int_0^T -\beta(t) dt \leq C \tag{108}$$

by Eq. (100). Second, we have

$$\frac{d}{dt} \int_{\Omega} \omega \varphi = \int_{\Omega} \omega \Delta \varphi + \frac{\beta}{2} \iint_{\Omega \times \Omega} \rho_{\varphi} \omega \otimes \omega \tag{109}$$

and hence

$$\int_0^T \left| \frac{d}{dt} \int_{\Omega} \omega \varphi \right| dt \leq C_{\varphi}, \varphi \in X. \tag{110}$$

Inequality (110) takes place of the monotonicity formula used for the Smoluchowski-Poisson equation, which guarantees the continuation of $\omega(x, t)dx$ up to $t = T$ as a measure on $\overline{\Omega}$ [9, 17]. Thus, there is $\mu = \mu(dx, t) \in C_*([0, T], \mathcal{M}(\overline{\Omega}))$ such that $\mu(dx, t) = \omega(x, t)dx$ for $0 \leq t < T$. By Eq. (100), therefore, it holds that

$$\omega(x, t)dx \rightarrow c\delta_0(dx) + f(x)dx \quad \text{in } \mathcal{M}(\overline{\Omega}), \quad t \uparrow T, \tag{111}$$

with $c \geq 0$ and $0 \leq f = f(x) \in L^1(\Omega)$. From the elliptic regularity, we obtain

$$\liminf_{t \uparrow T} \psi(x, t) \geq \frac{c}{2\pi} \log \frac{1}{|x|} \quad \text{loc. unif. in } \overline{\Omega} \setminus \{0\}. \tag{112}$$

Then, $e = (\omega(\cdot, t), \psi(\cdot, t)) \geq (\omega(\cdot, t), \min\{k, \psi(\cdot, t)\})$ implies $e \geq \frac{c}{2\pi} \min\left\{k, \log \frac{1}{|x|}\right\}$ for $k = 1, 2$. Hence, it holds that $c = 0$ in Eq. (111).

If the conclusion in Eq. (97) is false, we have the ε regularity in Eqs. (74), (75) [9, 17]. Thus, there is $\varepsilon_0 = \varepsilon_0^k > 0$, such that

$$\limsup_{t \uparrow T} \|\omega(\cdot, t)\|_{L^1(\Omega \cap B(x_0, R))} < \varepsilon_0 \Rightarrow \limsup_{t \uparrow T} \|\omega(\cdot, t)\|_{L^\infty(\Omega \cap B(x_0, R/2))} < +\infty \tag{113}$$

for $0 < R \ll 1$. The hypothesis in Eq. (113) is valid for $x_0 = 0$ by Eq. (111), $c = 0$, which contradicts to $T < +\infty$.

5. Conclusion

We study the relaxation dynamics of the point vortices in the incompressible Euler fluid, using the vorticity patch which varies with uniform vorticity and constant area. The mean field limit equation is derived, which has the same form as the one derived for the Brownian point vortex model. This equation governs the last stage of self-organization, not only in the point vortices but also in the two-dimensional center guiding plasma and the rotating superfluid helium, from quasi-equilibrium to equilibrium. Mathematical analysis assures this property for radially symmetric case, provided that the inverse temperature is bounded below.

Acknowledgments

This work was supported by Grant-in-Aid for Scientific Research (A) 26247013 and Grant-in-Aid for Challenging Exploratory Research 15K13448.

Author details

Ken Sawada¹ and Takashi Suzuki^{2*}

*Address all correspondence to: suzuki@sigmath.es.osaka-u.ac.jp

1 Meteorological College, Kashiwa, Japan

2 Graduate School of Engineering Science Osaka University, Toyonaka, Japan

References

- [1] Onsager L. Statistical hydrodynamics. *Il Nuovo Cimento*. 1949;**6**(2):279–287. doi:10.1007/BF02780991
- [2] Caglioti E, Lions PL, Marchioro C, Pulvirenti M. A special class of stationary flows for two-dimensional Euler equations: A statistical mechanics description. *Communications in Mathematical Physics*. 1992;**143**(3):501–525. doi:10.1007/BF02099262
- [3] Eyink GL, Spohn H. Negative-temperature states and large-scale, long-lived vortices in two-dimensional turbulence. *Journal of Statistical Physics*. 1993;**70**(3):833–886. doi:10.1007/BF01053597
- [4] Joyce G, Montgomery D. Negative temperature states for the two-dimensional guiding-centre plasma. *Journal of Plasma Physics*. 1973;**10**(01):107–121. doi:10.1017/S0022377800007686
- [5] Kiessling MKH. Statistical mechanics of classical particles with logarithmic interactions. *Communications on Pure and Applied Mathematics*. 1993;**46**(1):27–56. doi:10.1002/cpa.3160460103
- [6] Pointin YB, Lundgren TS. Statistical mechanics of two-dimensional vortices in a bounded container. *Physics of Fluids*. 1976;**19**(10):1459–1470. doi:10.1063/1.861347
- [7] Sawada K, Suzuki T. Derivation of the equilibrium mean field equations of point vortex system and vortex filament system. *Theoretical and Applied Mechanics Japan*. 2008;**56**:285–290. doi:10.11345/nctam.56.285
- [8] Nagasaki K, Suzuki T. Asymptotic analysis for two-dimensional elliptic eigenvalue problems with exponentially dominated nonlinearities. *Asymptotic Analysis*. 1990;**3**(2):173–188. doi:10.3233/ASY-1990-3205

- [9] Suzuki T. Mean Field Theories and Dual Variation—Mathematical Structures of the Mesoscopic Model. 2nd ed. Paris: Atlantis Press; 2015. 444 p. doi:10.2991/978-94-6239-154-3
- [10] Lynden-Bell D. Statistical mechanics of violent relaxation in stellar systems. *Monthly Notices of the Royal Astronomical Society*. 1967;**136**(1):101–121. doi:10.1093/mnras/136.1.101
- [11] Robert R. A maximum-entropy principle for two-dimensional perfect fluid dynamics. *Journal of Statistical Physics*. 1991;**65**(3):531–553. doi:10.1007/BF01053743
- [12] Robert R, Sommeria J. Statistical equilibrium states for two-dimensional flows. *Journal of Fluid Mechanics*. 1991;**229**:291–310. doi:10.1017/S0022112091003038
- [13] Robert R, Sommeria J. Relaxation towards a statistical equilibrium state in two-dimensional perfect fluid dynamics. *Physical Review Letters*. 1992;**69**(19):2776–2779. doi:10.1103/PhysRevLett.69.2776
- [14] Robert R, Rosier C. The modeling of small scales in two-dimensional turbulent flows: A statistical mechanics approach. *Journal of Statistical Physics*. 1997;**86**(3):481–515. doi:10.1007/BF02199111
- [15] Chavanis PH. Two-dimensional Brownian vortices. *Physica A*. 2008;**387**(28):6917–6942. doi:10.1016/j.physa.2008.09.019
- [16] Chavanis PH, Sommeria J, Robert R. Statistical mechanics of two-dimensional vortices and collisionless stellar systems. *The Astrophysical Journal*. 1996;**1**(471):385–399. doi:10.1086/177977
- [17] Suzuki T. Free Energy and Self-Interacting Particles. 1st ed. Boston: Birkhäuser; 2005. 370 p. doi:10.1007/0-8176-4436-9
- [18] Suzuki T. Brownian point vortices and DD-model. *Discrete and Continuous Dynamical Systems—Series S*. 2014;**7**(1):161–176. doi:10.3934/dcdss.2014.7.161

Vortices in General Physical Problems

Development of Vortex Bioreactor Technology for Decentralised Water Treatment

Andrew Landels, Neil Cagney, Lisa Bauer,
Tracey A. Beacham, Stavroula Balabani and
Michael J. Allen

Additional information is available at the end of the chapter

<http://dx.doi.org/10.5772/66632>

Abstract

The vortex bioreactor (VBR) is a simple decentralised water treatment system (DeWaTS) that sits at the interface between swirl flow, biotechnology and chemical engineering. The device utilises swirl flow and suspended activated beads to achieve downstream water processing and has been tested for applications including centrifugal-driven separation, pathogen neutralisation and metal absorption. The VBR was optimised for the treatment of faecally contaminated effluents in the developing world, and the design features related to the key challenges faced by the wastewater industry are highlighted here. The VBR has two aspects that can be modified to generate different reactor conditions: the impeller, where the swirl flow is modified through alterations of rotation speed, and impeller geometry and the suspended activated beads, which facilitate mixing and alter the reactor surface area. Data from testing for some of the different applications mentioned above are presented here, and future planned developments for the technology are discussed.

Keywords: DeWaTS, swirl flow, wastewater treatment, bioreactor, remediation

1. Introduction

1.1. Water and wastewater

Water covers 70% of the surface of the planet, and yet the world currently faces a water crisis. Of this hugely abundant resource, less than 1% is available for human consumption. Two-thirds of all fresh water is locked up in glaciers and ice caps where it is typically physically separated from humans and is, therefore, not widely available for use. The remaining 97% of

the global water is saline, present within the seas and oceans. This is inappropriate for agricultural uses, industrial cleansing or human consumption without significant energy inputs and desalination efforts, although it can be employed for some limited applications, such as certain types of cooling in industrial processes. These water sources have not changed in the last 100 years, but in that time the population has undergone rapid expansion. The majority of water used by humans is either as an energy carrier in thermo-electrical power generation; where it is used for both cooling and steam production to generate the driving force for the turbines or in agricultural irrigation and cleaning [1]. The United Nations Food and Agriculture Organisation (UNFAO) estimate that 11.8% of the 3918 km³ yr⁻¹ fresh water withdrawn annually is used for municipal purposes, where it makes its way to households for drinking, washing and recreational purposes [2].

Global water volumes remain constant in a system referred to as the water cycle, and so with the exception of deserts or very densely populated areas, physical limitations of water are not usually an issue. A more significant problem, however, is the limited supply of water that is either potable (suitable for human consumption) or at a sufficient quality for other municipal and industrial applications. After water has been used in an anthropogenic process, it is referred to as wastewater. Wastewater is classified as containing output of some combination of the sources given in **Table 1**. According to the UNFAO, in 2012, the world had access to 52,600 km³ yr⁻¹ fresh water resources, which is just over thirteen times higher than the amount drawn annually; however, this resource is not evenly distributed. Asia, for example, has access to around a quarter of available world water resources, but has almost 60% of the world population [2]. The majority of people are based in global urban centres, 80% of which are located on the coast or major waterways. Many cities around the world—even in Countries which have both high annual rainfall, and are members of the Organisation for Economic Cooperation and Development (OECD countries), such as London—are considered ‘water stressed’. Being ‘water stressed’ occurs when an area requires access to more clean water than is available, or produces more wastewater than can be treated effectively. This results in a direct release of wastewater into waterways causing a reduction in water quality. This in turn has economic costs, through both work lost due to human illness and damage to the surrounding environmental resources—such as fishing stocks [3].

Name	Example contents	Risk factors
Blackwater	Excreta, urine and faecal sludge	Pathogens
Greywater	Bathing and washing water	<i>Volume increase</i>
Bluewater	Urban run-off and storm water	<i>Grit, debris</i>
Greenwater	Agricultural effluent*	Eutrophication, pesticides
Redwater	Industrial effluent	Chemical and thermal hazards

Each category has been assigned a colour to simplify reference within the text. For each, a brief summary of the category is given, and some associated risks with the wastewater are highlighted. Risks of untreated release to human health or the environment are in boldface, whilst risks that affect downstream processing are italicised.

*Agricultural effluent includes effluent from aquaculture and horticulture.

Table 1. Wastewater can be broken down into five key categories, which pose individual risks to both human health and downstream processing methods.

1.2. Water treatment

The core role of wastewater treatment is to remove waste additives from a water stream until it is at a level suitable for environmental release. These levels are set by governments in each country, for example, the Environmental Protection Agency sets recommendations for the USA that are considered safe for aquatic life [4]. Depending on the source of the wastewater, different treatment methods are required—for example, bluewater (urban run-off and storm water) can contain grit and large debris and so needs to be put through Stage 1 processing or ‘screening’; as unless removed, this debris can cause blockages and serious wear/damage to downstream machinery. This is the stage where most centrifugal type separators are employed in wastewater treatment, as swirl flow is generally not employed for transport, separation or waste processing beyond the initial latrine and grit removal stages. A general outline of the stages of centralised wastewater treatment is presented in **Figure 1**, and a brief explanation of the workflow is given below (**Figure 1**). As mentioned in the example above, Stage 1 processing is the removal of grit and debris. This is usually done using a combination of grids and baffles, however, hydrocyclones have been employed for grit removal in some cases. Stage 2 processing is an important precursor to Stage 3 water treatment, as it removes the majority of the activated sludge from suspension, typically through natural settling or through the addition of a flocculating agent such as iron chloride. This sludge can then be collected and dried, or run through anaerobic digestion to generate useful products such as methane, which can be used to power other parts of the wastewater treatment or sold to mitigate operational costs. Stage 3 processing is used to reduce phosphate and nitrate levels in the final effluent, preventing harmful downstream effects like eutrophication. The residual bacteria remaining in solution after flocculation are aerated and encouraged to grow, and in the process, the nutrients in the liquid are depleted and more sludge is produced. This sludge is then flocculated and processed as in Stage 2. Finally, the nutrient and sludge-depleted liquid will still contain some organisms that did not flocculate, so needs to be sterilised before leaving the treatment plant. This is typically done with UV sterilisation, but can also be done

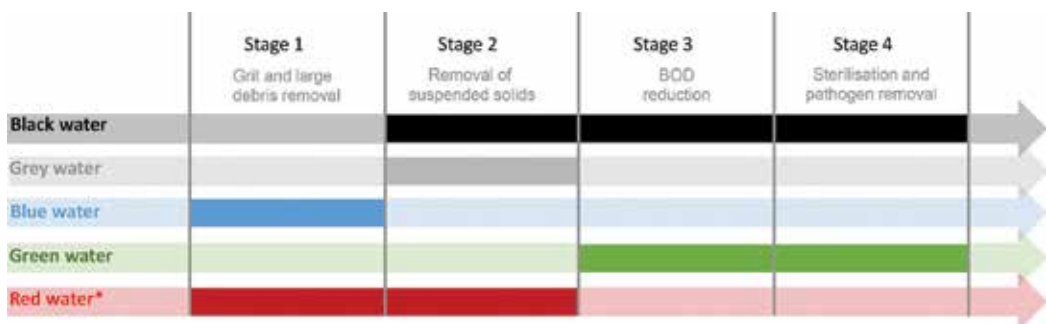


Figure 1. The different streams of wastewater described in **Table 1** as run through a classical wastewater treatment process. The stages of wastewater treatment have been grouped together into general stages to demonstrate the key aims of wastewater treatment, and shaded sections on the flow line indicate that the waste stream requires this stage of processing. These stages are (1) grit and large debris removal; (2) clarification/flocculation of suspended solids; (3) reduction of biological oxygen demand; and (4) sterilisation/pathogen removal. *Industrial effluent can vary significantly depending on the source as a result it is typically treated on-site to remove hazardous contaminants.

with chlorine or ozone dosing where the clarity of the effluent is an issue. The vortex bioreactor has applications for Stages 2–4 (clarification/flocculation of suspended solids through centrifugal-type separation, removal of nutrients by acting as a bioreactor and sterilisation/pathogen removal) of the water treatment processes. For further reading on the stages of wastewater treatment process, see Ref. [1], and for a comprehensive compendium of sanitation systems, see Ref. [5].

Large urban treatment plants are economic and highly effective at treatment of municipal wastewater, however, they are not always suitable [1]. This is particularly true in areas that lack established sewerage systems—sewerage systems have relatively high initial capital expenditure requirements and in rural environments the population density is simply too low to justify the cost. Centralised water treatment is also not a good solution for an area that suffers from intermittent power loss, as power is required for pumping the water to and from the central station and certain treatment processes. The power requirements for running wastewater treatment in the US in 1996 came to approximately 75 billion kilowatt hours (kWh), around 3% of the US annual electricity consumption that year [6]. Aside from the power costs, interruption of the electricity supply, such as from brownouts or blackouts, pose a significant risk to the fidelity of the wastewater treatment process. The large capital expenditure and operating costs involved in centralised water treatment results in public ownership or subsidies, which can be a major issue in countries experiencing political instability [3]. Finally, the water treatment industry in the developed world is incredibly resistant to innovation [7]. New large-scale technologies that could produce a step-change in processing techniques are slow to be implemented, a stance that is reinforced by effluent regulation requirements and possible fines resulting from a failure to meet water treatment standards.

Urban populations are rising faster than the average population growth rate, as more people move away from rural areas to cities [3]. Due to space limitations, growth of urban centres tends to occur in the outskirts of urban areas. These peri-urban areas, between the urban and rural zones, have a higher population density than the rural areas but, due to rapid growth, lack the key infrastructure of developed urban areas. As a result, wastewater management is a major issue for peri-urban areas; particularly municipal wastewater, which consists of grey (washing water), black (faecal contaminated) and blue (urban run-off) wastewaters. Due to the dynamic nature of these spaces, designing a suitable water treatment plan that is future-proofed, suitable and cost-effective is challenging. In these cases, decentralised treatment options are an ideal solution.

1.3. DeWaTS

Decentralised water treatment systems (DeWaTS) are small-scale water treatment systems ideally suited to operating in the urban, peri-urban and rural environments in developing countries—particularly in cases where pre-existing water infrastructure is either insufficient for requirements or unavailable [8]. A DeWaTS can be an individual unit, or a complete water treatment system, and can be utilised in either domestic or industrial water treatment. The amount of wastewater produced by an individual varies depending on environment, but typically an average person produces around 60 L of wastewater per day, with blackwater

making up around 2 L on average and the remaining coming from greywater [5]. This implies that the average person requires access to 60 L clean water each day, and so any household level water purification system should be able to accommodate this requirement for all members of an individual home.

Typically, a DeWaTS will operate in the range of $1 \text{ m}^3 \text{ day}^{-1}$ (1000 L day^{-1}) for a household unit, to $1000 \text{ m}^3 \text{ day}^{-1}$ for a community treatment system. There are a number of defining characteristics that differentiate a DeWaTS from a model or an experimental water treatment system. The system should be reliable, built to last, tolerant to fluctuating inputs, cost-effective and above all have low control and maintenance requirements [9]. A DeWaTS designed to produce a profit should aim to return the initial cost of investment through sales of cleaned water or products produced from waste within the first 1–2 years of operation, to ensure uptake of the technology [3]. The vortex bioreactor was, therefore, designed with these vital features in mind.

1.4. Summary of the VBR

The vortex bioreactor system (VBR) is a highly versatile, modular DeWaTS, which utilises suspended activated beads within a recirculating swirling flow system to facilitate downstream liquid processing and multiphase reactions. The swirl flow and accompanying vortex, for which the device is named, are induced by an impeller, which can be driven by a variety of devices such as an electric drill motor or a 3D printable hand crank. Under certain operating conditions, the device can perform liquid-liquid separation and acts as a type of centrifugal separator, where a lighter liquid phase is entrained by the precessing vortex and is siphoned into a separate flow channel. Increasing the impeller speed increases turbulence in the system, resulting in better mixing, more interaction between the contents and as a result acceleration of chemical reaction rates. Notably, this effect is also modulated by the activated beads, which can enhance, but in some cases dampen, the turbulence effect. Altering the impeller design has been shown to change the vortex characteristics, although investigations into this with the VBR system are still ongoing. To date a hydrofoil type design, a rounded blade design and a lily design have been utilised for the impeller, but so far the effects of impeller geometry have not been systematically investigated. Finally, by altering the properties of the suspended activated beads, it is possible to run a variety of different reactions or separations. For example, reducing the density of the beads by introducing sealed air microbubbles during their creation causes them to move to the core region of the VBR for easy separation and recycling, whilst sponge-like porous beads with a high surface area can be used as both a heterogeneous catalyst for multi-phase reactions and an adsorbant surface for sequestration of toxic materials, such as heavy metals.

Due to the swirl generated by the impeller, the flow within the VBR is not uniform but rather characterised by low velocities in the core region due to the formed vortex and higher velocities outside. Fluid in the core moves far more slowly than outer part, and under some regimes, the suspended beads can be held almost completely stationary within the slow-moving core region [10]. A CAD image of a prototype variant of the VBR can be seen below (**Figure 2**). This prototype consists of a closed loop, built from widely available standard plumbing

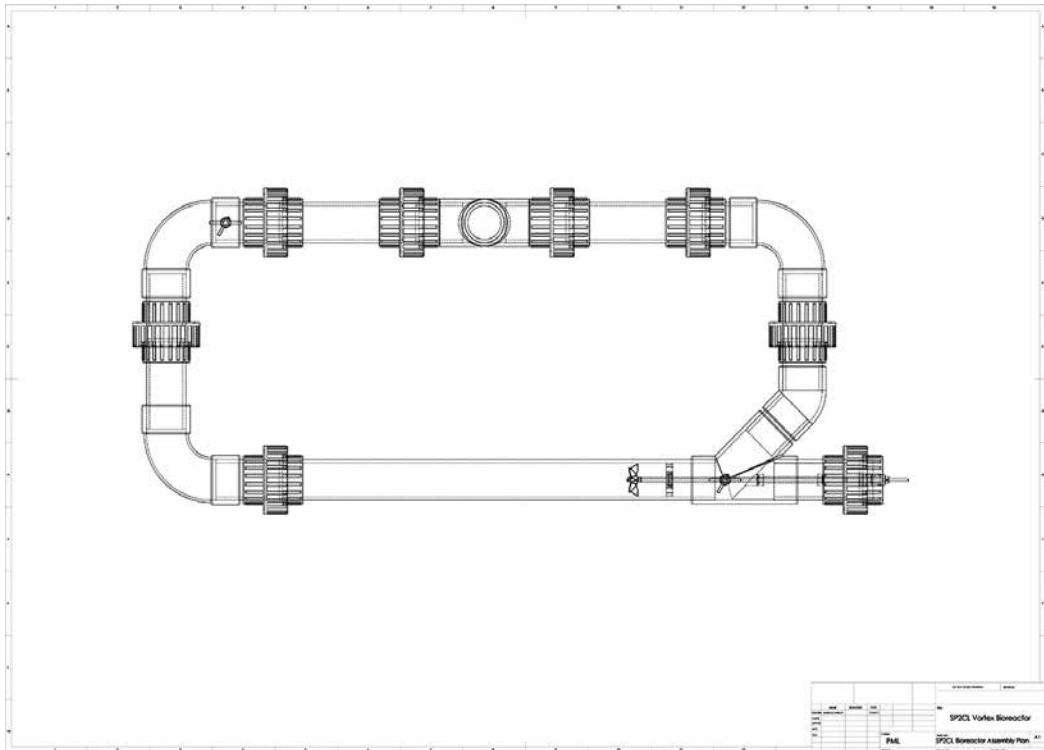


Figure 2. This CAD image shows one possible setup of the VBR system. The flow runs through a rounded quadrilateral pipe system, driven by an impeller. There is an inflow located at the top of the reactor. The prototype design also has a ball-valve controlled outflow (not shown) for emptying the system.

parts forming a rounded quadrilateral of recirculated flow. The design was constructed from 60.4 mm outside diameter and 57.4 mm inner diameter clear polycarbonate, joined with 2-acrylonitrile butadiene styrene (ABS) fittings. There is an inlet for filling the reactor at the top, and in the working prototype, a ball-valve controlled outlet was introduced at one corner for draining the VBR. Swirl flow is induced with an impeller on a shaft, which is driven by a 450 W variable speed drill motor (0–2400 RPM Bosch). This design is capable of generating a stable horizontal vortex, which entrains less dense materials, such as air or oil in water, and separates them from the carrier fluid [10].

2. Development of the VBR and case studies

2.1. Development of the VBR

The first prototype was designed and built by the Allen research group at Plymouth Marine Laboratory in 2010. It was intended for the separation of high-value oils produced by microalgae from an oil-water suspension, using centrifugal flow technology. A low-cost variant of this technique is widely employed by the oil industry in the form of hydrocyclones, but swirl

flow is not generally utilised in biological applications. Successful oil-water separation tests were performed on the device (see below), and during testing, the question of completing the whole process ‘in one box’ arose, and so investigation into upstream processing was carried out to see if the VBR could also be used for cell growth, oil production, cell rupturing for extraction of the biochemical products and ultimately separation of the functional product from the liquid media.

Microalgae are microscopic, photosynthetic organisms that are found in both marine and fresh water environments. They can be an environmental and health hazard when they bloom in waterways and are responsible for causing discolouration of standing water, but are a promising set of organisms for photosynthetic biotechnological production [11]. One of these high-value products is speciality oils, such as the omega 3 oils Eicosapentaenoic acid (EPA) and docosahexaenoic acid (DHA), which are valuable ‘nutraceuticals’ [12]. To extract these oils from microalgae, first the cells must be broken open, a process also referred to as cellular lysis. It has been documented previously that shear forces, when applied at high enough levels, can literally tear cells apart through an unevenly distributed pressure gradient against the cell membrane, or if cells are at a high enough density trigger cellular damage and death through violent collisions [13]. It is important to note that this threshold varies with different organisms and is dependent on the presence of air bubbles; when air is absent from the system, cells are much more tolerant to mechanical shear forces [13]. The large shear forces introduced into the flow system during turbulent flow were found to trigger cell death in *Escherichia coli* (a laboratory ‘model organism’) at high power inputs; however, at lower power, the shear forces actually contributed to cellular growth due to enhanced mixing and mass transfer characteristics [14]. This was when the ‘activated beads’ aspect was first introduced to the design, to encourage cell lysis at lower impeller speeds, and also where the design was first altered to be a DeWaTS, rather than just a downstream processing and separation system.

The activated beads were found to modify the VBR operation significantly. Not only did they improve the shear and mixing effects within the system, but they also opened it up to a variety of other modifications and applications far beyond the humble swirl-flow system origins. They appear to hold three key functions: they increase the reactor surface area, they appear to decrease the impeller speed needed to attain turbulent flow within the VBR in the conditions tested so far and they transform the device into a different class of reactor—from a chemical engineering point of view, it acts as a fluidised bed reactor and from a bioengineering point of view, it acts as a immobilised microcapsule perfusion bioreactor, where organisms can adhere to or be embedded within the activated beads. To estimate the increased surface area and determine how to control for it, a simple model was prepared, considering the beads as solid spheres in suspension.

$$\frac{4}{3} \pi r^3 = \text{vol of sphere} ; \frac{\pi}{3\sqrt{2}} = \text{dense sphere packing} ; 4\pi r^2 = \text{area of sphere} \quad (1)$$

$$\frac{x}{4 r^3 \sqrt{2}} = \text{number of beads} \quad (2)$$

$$4\pi r^2 \left(\frac{x}{4r^3\sqrt{2}} \right) = x \frac{\pi}{r\sqrt{2}} = \text{bead surface area} \quad (3)$$

where x is the volume of beads added to the VBR, and r is the radius of each beads. The formula indicates a linear increase in external surface area with respect to both bead radius and the volume of beads added, so if double the surface area is required, then either the volume of the beads should be doubled, or the radii of the beads halved. Here, the surface area is approximated based on the volume of beads added, an assumption of dense sphere packing – such as face centred cubic packing or hexagonal close packing, and the radius of each individual bead, as it is impractical to physically count the beads and an estimation based on volume is much more convenient.

The internal surface area of the VBR can be calculated by taking the pipe circumference and multiplying it by the length of the reactor. In the case of the 9 L VBR prototype system described above, the internal pipe circumference is 18 cm and the length is 318 cm, resulting in an internal surface area of $5.7 \times 10^3 \text{ cm}^2$. Using the model above, adding 1 L beads results in an addition of $2.22 \times 10^4 \text{ cm}^2$, raising the overall surface area to $2.79 \times 10^4 \text{ cm}^2$.

$$1000 \text{ cm}^3 \frac{\pi}{0.1 \text{ cm} \sqrt{2}} = 2.22 \times 10^4 \text{ cm}^2 \quad (4)$$

Whilst this model only accounts for the outer surface of the beads, which is a conservative estimate for increased surface area in the 9 L system, it shows that adding 1 L of 1 mm radius beads to the prototype reactor design increases the internal surface area by approximately five-fold.

2.2. Case study: oil-water separation

To characterise the ability of the system to separate oil and water effectively, a series of experiments were conducted on a model system. It was not practical to directly test algal oils throughout the experiment due to the expense and the volumes needed, so a model oil consisting of vegetable oil dyed with Nile Red so it could be observed in water was used instead. Dyed vegetable oil is a good model for algal oil, as it is cheap, available in large quantities, and has a similar density and viscosity. Algal oil has a density of 0.864 kg L^{-1} , whilst the model oil had a density of 0.93 kg L^{-1} . The dynamic viscosities are shown in **Table 2**.

Test liquid	Dynamic Viscosity at 25 °C
Test oil and dye	$\mu = 0.0562 \text{ Ns m}^{-2}$
Test oil	$\mu = 0.0625 \text{ Ns m}^{-2}$
Algal oil	$\mu = 0.0233 \text{ Ns m}^{-2}$

Table 2. The dynamic viscosities for the dyed vegetable oil was used as an affordable substitute for algal oil, the vegetable oil without the addition of the dye, and the algal oil that was being modelled.

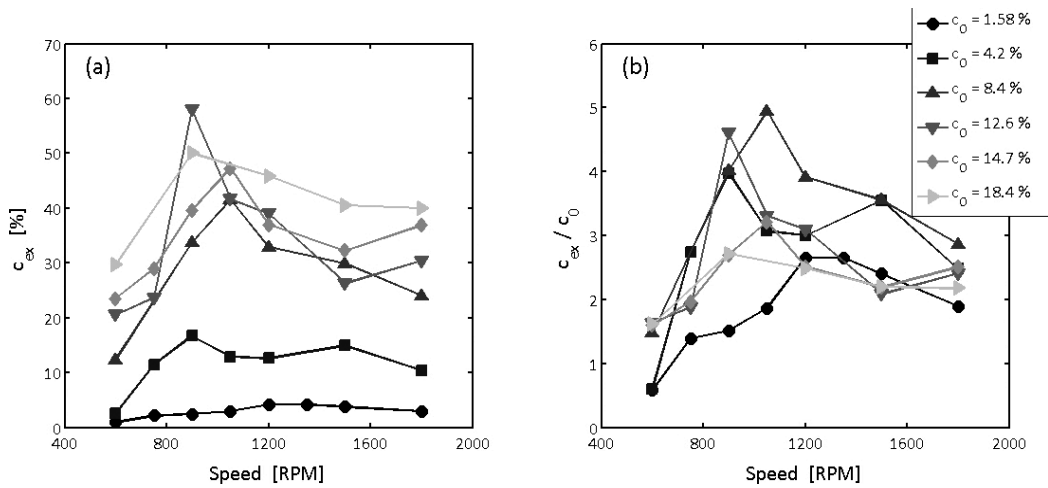


Figure 3. Variation in the oil concentration extracted from the VBR for a range of speeds and for a range of initial oil concentrations (a). The data in (b) is presented with respect to the initial oil concentration to show the efficiency of the extraction process.

An experimental series was run, beginning at an oil:water ratio of 1.58%. This ratio was modelled on a true extraction of algal oil from the growth media solution, based on the growth density of the algae and the relative quantities of oil they produce. The concentration of oil was gradually increased in the series, based on the assumption that the concentrated oil-water mix could be re-run through the system until a desired concentration had been attained or the volume limit was reached. This system was run at a number of impeller-tip speeds in order to optimise the vortex characteristics for maximum oil separation levels (**Figure 3**).

A series of experiments were run, in which the ability of the VBR to extract oil from a mixture of oil and water was tested for a range of impeller speeds and oil:water volume ratios; beginning with the expected initial value of 1.58%. The concentration of oil was gradually increased in the series, based on the assumption that the concentrated oil-water mix could be re-run through the system until a desired concentration had been attained, or the volume limit was reached. This system was run at a number of impeller-tip speeds in order to optimise the vortex characteristics for maximum oil separation levels (**Figure 3**). **Figure 3(a)** shows the concentration of oil in the mixture extracted from the syphon (c_{ex}) for a range of impeller speeds (600–1800 RPM) and a number of different initial concentrations of oil in the system ($c_0 = 1.58$ –18.4%). The same data is presented in **Figure 3(b)**, normalised with respect to the initial concentration to show the relative increase in the oil concentration at each step, i.e. the ‘efficiency’ of the system.

For most initial concentrations, the maximum concentration of oil extracted tends to occur in the range of 800–1200 RPM. At low speeds (<800 RPM), the swirling motion was too weak to entrain the oil droplets into the vortex core, and the oil remained at the top of the pipe. In contrast, when the impeller speed was high (>1200 RPM), the flow became strongly turbulent

and the oil broke into small droplets (a process known as 'emulsification') that tended to disperse throughout the fluid. This meant that fewer droplets remained in the vortex core, and the efficiency of the VBR was reduced. The data also suggest that the same efficiency may be achieved from a low initial concentration by sequential processing. For example, from an initial concentration of 1.5%, it is possible to increase the oil concentration to 4%; from 4% it is possible to increase to 12%, and so on. The maximum concentration extracted was close to 60%, although it is possible that the VBR could produce higher concentrations if the initial concentration of oil was greater.

A series of power consumption measurements were also made on the system, to determine the energy requirements and financial costs associated with operating the device at a range of rotational speeds. The measurements were initially performed when the device was filled with water, and subsequently, when it was filled with an oil-water mixture (**Figure 4**).

The measured power consumption is shown in **Figure 3**. When the motor was not moving, the controller drew approximately 4 W from the mains. As the motor speed increased, the power consumption also increased in a linear fashion. The power consumption is approximately given by

$$P = (0.064 N + 4.1) \frac{V}{9.5} \quad (5)$$

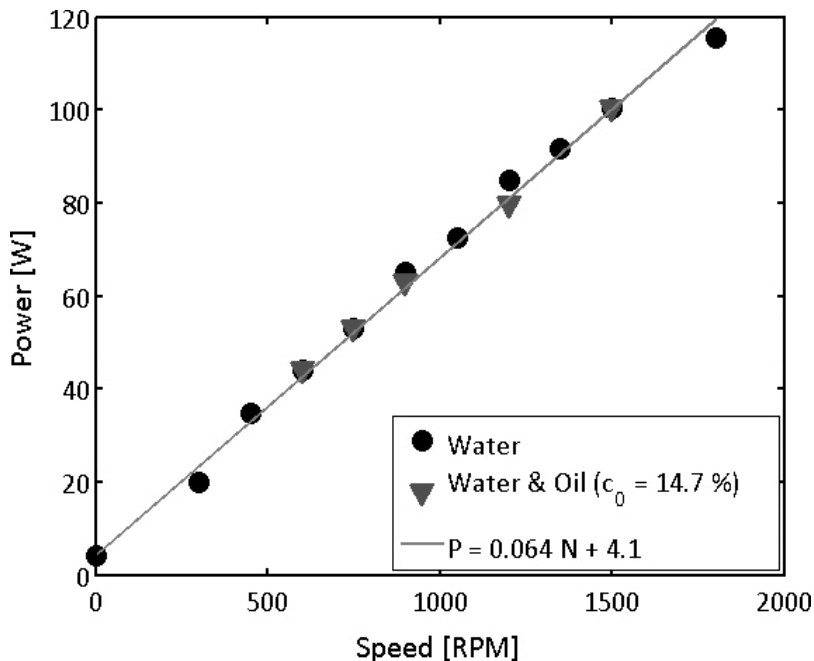


Figure 4. The variation in power consumption with increasing motor speed, measured when the SP-2 contained pure water (black circles) and a mixture of 14.7% oil (grey triangles).

where N is the motor speed, (in RPM) and V is the volume of water in the VBR ($V = 9.5$ L in the current experiments).

The presence of the oil did not affect the total power consumption of the system. This indicates that to process 1000 L of oil-water mixture at optimal motor speeds (approximately 900 RPM), using a motor with a comparable efficiency, would require 6.5 kW. Over the course of an hour, this would cost £0.65, assuming an electricity cost of approximately £0.10 per kilowatt hour based on typical rates for domestic use in the UK [15]. This indicates that (i) the VBR represents a cost-efficient method of refining the concentration of oil in an oil-water mixture, and (ii) the use of multiple steps to achieve a given concentration is not associated with a significant increase in operating costs; however, these values may change, depending on the volume being processed and the efficiency of the motor being used.

2.3. Case study: application of VBR as a pathogen-removal system

Biological disease-causing agents, or pathogens, are a major concern in wastewater treatment. Human faecal effluent is a major health risk, as the organisms living within it are already attuned to living within humans. A number of diseases have been linked to human-derived pathogens, including dysentery, typhoid and gastroenteritis [16]. In wastewater treatment, the biological quality of the water is determined by quantifying 'coliforms'. Coliforms are a subset of bacteria that are easy to culture and are present in large numbers in warm-blooded animal faeces—making them a good test for faecal contamination in wastewater [17]. The organisms are quantified by colony forming units (CFUs), referring to the number of living cells within a fixed volume. Guidelines state that to minimise risks to human health, wastewater containing blackwater should contain no measurable CFUs per 100 ml, and waste water from a known non-faecal source, such as redwater (industrial effluent), should contain no more than 10 CFUs per 100 [18].

Copper has long been known as an antimicrobial substance, given its employment in hospital door handles and work surfaces [19]. To trigger this effect within the reactor, dendritic copper micro particles were added to the system as a powder. A copper pipe was also considered; however, due to the comparably limited surface area and relatively high cost of copper within the otherwise cheap final design and the risk of corrosion over time under continuous exposure to water, it was deemed to be unsuitable [14]. The copper powder was found to be effective at triggering cell lysis; however, separating the copper from the system afterwards was considered too complicated for the design, a vital step in this case, as copper is toxic to aquatic ecosystems—and humans [20]. To aid in terminal removal from the system after processing, the copper powder was embedded within spherical, alginate matrix, hydrogel particles—referred to as the activated beads herein. A test was carried out to see if embedding copper within alginate would still trigger cell lysis; intriguingly, not only did the cells still lyse, but they did so at a more rapid rate than a comparable study with the powdered copper [20].

When the activated beads were run in the VBR system, they were found to be more effective at triggering cell lysis than the equivalent amount of free copper microparticles. Death of all the cells in the sample (initially at a concentration of 1×10^8 CFU ml⁻¹) occurred within

15 min, a rate approximately 6× faster than had previously been reported in flask experiments. In addition, this effect was observed repeatedly when additional organisms were added into the system after all the previous cells were dead. Whilst the structural integrity had been affected by the turbulent flow at particularly high speeds, the activated bead fragments could still be extracted from the system safely with minimal copper leached into the system [10]. Development of the device subsequently received financial support from the Bill and Melinda Gates Foundation, for development as a low powered, affordable alternative to UV light sterilisation of water. This resulted in testing the device on wastewater streams in a number of facilities located around the world [21]. The device demonstrated clear bactericidal effects on coliforms within seconds of exposure to the VBR—activated bead combination, and even destroyed the radiation hardy *Deinococcus radiodurans* in a direct comparison with UV treatment. To finalise the device for widespread distribution, the main feedback received from the world-wide test was that the activated beads would need to be further developed; both to increase their longevity, and to include some additional method that could sterilise the copper-resistant and shear-resistant helminth eggs—as parasitic worm infections stemming from wastewater are a major health concern in the developing world [21].

2.4. Case study: VBR as a metal-sequestering device

Embedding the copper within an alginate matrix proved extremely effective as an immobilisation technique. The low levels of measurable copper in solution—despite fragmentation of the beads during operation of the reactor—and the greater than expected rate of bactericidal action within the VBR doped with copper-alginate beads, instigated an investigation on the metal adsorption qualities of alginate in the VBR. The theory behind this application is based on alginate being a polyionic polymer that forms a hydrogel stabilised by calcium ions; it was thought that copper—or some other metal ion—could displace these calcium ions and become sequestered in the material [22]. The advantage of using alginate beads for this application is that because the bulk of the beads are composed of liquid, and as a result can be dried after use to concentrate any extracted materials for recycling and reduce volume. This is a particularly useful application when considering the VBR as a device for redwater treatment, as many industrial processes involve the use of metals and metal salts that need to be extracted from the final product due to their value, toxicity and environmental impact.

To generate hand drawn alginate beads, sodium alginate solution was added in a drop-wise fashion by hand from a syringe to cold calcium carbonate solution. The beads created by this process were approximately 2 mm diameter on average, although beads created in this fashion did show some size variation. An automated variant of this process was conducted with a syringe pump to generate a more repeatable size distribution. Features of alginate beads can be altered by changing the reagents used in their generation—for example, increasing sodium alginate concentration will create more rigid beads; whilst mixing copper-powder into the solution will create beads embedded with copper and air entrainment can create lighter beads for simpler separation from liquids such as water, as such beads are relatively more buoyant than the liquid.

The metal-absorbing properties of alginate beads were tested with metal salt solutions containing copper sulphate, nickel sulphate and chromium chloride at a high (100 mM) and low

(30 μM) concentration. The alginate beads were added to make up 50% by volume of the total volume and were tested in shaking flasks containing each of the metal salt solutions. The beads were found to have metal-absorbing properties in shake flasks, with 30–40% of the metal by concentration being extracted from solution over a period of 30 min. The samples were left for a further 60 min, although a negligible amount of additional absorption was observed. The volumes of metal being extracted were consistent with partial volume removal of a fully diffused solution. This suggests that the liquid initially sequestered in the hydrogel gradually dilutes the sample as the metals permeate the beads. The experiment was repeated with stationary flasks, producing largely similar results, suggesting that fluid motion had a limited effect on diffusion within the beads. To verify this observation, beads that had already absorbed metals were extracted and recycled into fresh metal salt solution at the initial concentration. Each additional round of extraction resulted in a diminishing rate of return, as the beads became saturated with metal approaching the initial concentration.

When the beads were tested in the VBR, the same final rate of absorption was observed, however, an interesting phenomenon was observed repeatedly through all experiments. Within the first minute of extraction, the rate at which metal salt was extracted was far more rapid in the VBR than in either shaken flasks or static flasks. The rate of absorption equalised with other experimental set ups after around 8 min; however, these data suggested that the swirl flow within the VBR has a beneficial effect on the rate of metal absorbance, at least with the outer part of the beads. This observation needs experimental verification by running the system for 1 min with a coloured metal salt and then extracting and dissecting the beads to see if the effect is limited to the outer shell or actually uniform through the bead; however, the data suggests that this is the case as all three systems eventually reach the same point. Understanding this effect has broader-reaching consequences, as alginate is a major constituent of certain medically relevant biofilms. Biofilms are a biologically derived fouling effect that utilise polymeric substances and act as a protective layer to organisms within them, conferring resistance to antibiotics [23]. If this effect could be isolated, replicated and controlled, it could provide beneficial techniques for the removal of biofilms in industrial settings—where a cleaning agent, or a medical antibiotic, could be delivered directly into the biofilm, rather than just relying on diffusion. Whilst the metal capturing hypothesis was not found to be valid with alginate, making the beads from a polymeric substance that has specific metal-binding ability—such as polyacrylamide—could provide a more effective metal absorption process, although this has not yet been tested. The alginate was tested in this case as it followed on from previous work being conducted at the time and had demonstrated a good ability to hold metallic copper in situ. It is likely that the initially observed effects are a result of the metal particles being unable to escape from the bead due to steric hindrance, rather than through a specific affinity to the alginate.

3. Future developments

As a relatively new and highly versatile piece of technology, there are a number of features of the VBR that remain to be optimised and tailored to the application to more fully understand the range of future applications it could be implemented with. The two main aspects that

affect operation are the swirl-flow regime—which is controlled by speed and impeller design, and the active beads. These are discussed in the context of remaining issues for the device as a DeWaTS and the potential applications the device has as a bioreactor. There are several other potential avenues for investigation with this technology; however, they are beyond the scope of this chapter.

3.1. Remaining challenges for the VBR as a water treatment system

There are three main potential issues with the VBR as a widespread functional DeWaTS device for water purification. The first, as mentioned earlier in this chapter, is the stability of the beads. During the process, shearing from the impeller results in the beads becoming fragmented. This is an issue, as whilst the dendritic copper powder used in the beads is relatively cheap, and can be recycled in the system, it is still the most expensive part of the fully operational system. One possible avenue for solving this is through modification of the beads. They could be modified in a number of ways, such as using the minimal amount of copper that still produces a lytic effect on pathogens to reduce the cost or by increasing the resistance of the beads to impeller shear by modifying the type or concentration of polymer. It is also possible that a different flow regime and less dense beads could be used in tandem, holding the beads static within the reactor whilst the wastewater passed around them. This would protect the beads from the impeller shear; however, it may reduce pathogen destruction efficacy, as the beads would no longer be present at the interface between the core and the turbulent outer part of the flow, and as a result may not encounter denser material or particulates within the reactor [10]. In addition, the location within the reactor where the beads have the strongest pathogen neutralising effect is not known and is also difficult to measure—if the strongest effect occurs at the site of the impeller, then this solution of keeping the beads separated from the impeller would likely be infeasible due to diminished antimicrobial activity.

The second major issue is power consumption; as highlighted earlier in this chapter, interruption of power poses a major risk to wastewater processing. The prototype VBR operating at 956 RPM has been shown to take 15 min to sterilise 10 L volume, and so needs to run for 90 min to clean 60 L pathogen-laden waste water—the average amount of waste water from all sources produced per person per day. With the energy consumption figures shown above (**Figure 4**), this equates to approximately 65 W. It can, therefore, be considered to have an annual power footprint of around $36 \text{ kW}\cdot\text{h}^{-1} \text{ yr}^{-1}$ per person, which at standard UK prices [15] comes to an average cost of £3.60 (\$4.70) per person annually. An alternative impeller design could reduce power requirements here by as much as 30% [24], and the device could be made even more efficient by selecting a motor of the minimum power required to remove pathogens. Both of these are efficiency measures, however, and do not preclude the requirement of electricity to keep the device operational.

A hand-crank was designed and 3D printed for the prototype, as a fail-safe option for this when access to electricity was limited or cut off. Whilst this option could be useful in an emergency it has a few issues. First, the obvious sociological issue—the 90 min per person per day time requirement for sterilisation is not an issue for a motor; however, an individual operating the hand-crank may have serious reservations about the technology, particularly if

they are providing water for more than one individual. In addition, whilst a motor can be run at a fixed speed for a fixed amount of time, this same regularity is not ensured with a human operator. The effects of modulating the rate of impeller rotation on the pathogen removal will need to be thoroughly investigated if this avenue is to be considered in more depth. Designs that control the rate of rotation could be implemented, but they also increase the complexity of the device, which may cause problems for operation and repair. An advantage of the mechanism of pathogen destruction using the copper-laden beads within the swirl-flow system is that due to the mechanism of action, it practically only has a minimum threshold for pathogen removal—although high speeds will cause premature degradation of the beads. The antimicrobial effect occurs as a result of extensive cell membrane damage, where the shear forces, presence of oxygen and copper all contribute towards this effect. The device will still remove pathogens passively, however, the rate at which this happens is around six-fold slower.

There is a strong argument that having a powered device, even a hand-powered device, is a less suitable solution than designing a passive swirl-flow system, such as a hydrocyclone. A gravity-driven device may be able to achieve similar effects without the need for an external power source. Whilst such a design would be favourable, it is important to keep in mind the key principals of a DeWaTS during its design. It is also important to ensure that not only is the operation of the device simple, which a passive device should be, but also that any repairs should be possible with locally available parts. If the device is too complicated for the end user to repair themselves, or if the repairs are infeasible due to the expense or scarcity of the materials used, then when an issue occurs and the device fails, it will simply no longer be used. This sociological angle needs to be considered when designing global challenge-type technologies, particularly those that will be maintained by individuals rather than by a dedicated authority.

The final key issue that needs to be considered for the VBR as a DeWaTS is a simple efficacy or a failure test. As this device is intended for use by individuals, it should also come with some form of simple, reliable and cheap test to verify that the device has performed its function. Growth assays commonly used to determine the presence of CFUs are accurate and the materials needed are cheap, but the test requires sterile conditions, as well as specific training in aseptic technique. Without these, the test will produce false positive results. Some form of this test is essential for an operator, especially in cases where the design has been modified or repaired by an individual. An attempted but failed repair could result in a seemingly operational device, which is outputting harmful pathogen-laden water that is presumed to be clean. The test would need to follow the same principals as the rest of the DeWaTS design, and be free of expensive or difficult to obtain reagents. The field of synthetic biology may be particularly useful for this. Synthetic biology is a branch of genetic engineering that differentiates itself from the rest of the field by being founded in core engineering principals, namely, those of characterised standard parts and rational design. Initiatives such as the international genetically engineered machines (iGEM) foundation have created a repository of standard parts, most of which are freely available [25]. The repository is boosted by an annual iGEM competition, where numerous teams have created parts based around wastewater treatment. The advantage of a genetically engineered 'biomarker' for this task is that once designed it can be propagated indefinitely for very low costs. Furthermore, a design like this could be utilised in ensuring functional operation in a variety of different water treatment devices beyond the VBR.

3.2. Opportunities for the VBR as a bioreactor system

The VBR was named for the cell growth aspects that were observed during operation [14]. When microalgae grow photo-autotrophically—with light as their sole source of energy—the ensuing photosynthesis results in toxic levels of oxygen being produced. One of the main advantages with the swirl flow in the VBR design is the high levels of gas exchange which occurs between the liquid and any gas present in the system. This high level of exchange results in the dissolved oxygen levels being kept at a level closer to that of ambient air, providing a free air exchange that is enabled with the outside environment. Oxygen toxicity resulting from limited gas exchange is a significant issue for impeller-driven photo-bioreactor systems, hence the widespread use of energy intensive gas-mixed systems, such as air lift reactors or bubble columns. Typically, if a gas is not used for mixing the liquid, then a dedicated degasser compartment will need to be added to the design of any photobioreactor. A vortex degasser could have wide-ranging functionality in this field, as vortex flow is both an effective gas exchange method and a scalable technology, however, tuning the shear forces to avoid killing organisms from each individual species whilst maintaining maximum oxygen exchange, likely precludes a ‘one size fits all’ passive design.

Modulating the shear forces on the VBR can provide a user controlled growth-lysis switch; however, it is also possible to grow the microalgae embedded within the beads, which provides protection during recirculation. This is already done with alginate beads in industrial bioreactors with Chinese Hamster Ovary (CHO) cells for high-value pharmaceutical production, as these mammalian cells are highly susceptible to shear-derived lysis and grow much more readily when affixed to a surface; however, it is important to note that recent research suggests that alginate is not the most suitable encapsulation polymer [26].

Within the VBR, there are three key benefits to using this growth regime. First, the mixing rate could be increased to a level that encourages maximum gas exchange but does not damage the cells, reduce growth rates or negatively impact the final product. Second, introducing a hostile, high-shear environment within the reactor reduces the movement of biological organisms between the environment and the bioreactor system. This is true in both the inward (contaminant) and outward (containment) directions. It is accepted that during microbial scale-up a certain amount of external contamination will occur, however, under a high-shear regime in the VBR, contaminating organisms will either be destroyed outright, or will have their growth diminished so that the chances of them outcompeting the encapsulated species in the reactor is lower. When working with genetically modified (GM) organisms, there is extensive concern about a GM release. The same principles mentioned above that keep the culture axenic (free from contamination) will also limit GM release. Finally, the process could be run completely continuously rather than in batch like the majority of other systems. This removes the need for expensive turnaround between cultures. With the culture confined to the beads, it also becomes trivial to separate them from the media and to recycle the media by replenishing only the nutrients that have become depleted rather than needing to replace the entire liquid volume.

Acknowledgements

This work was supported by grants awarded to MJA from the Bill & Melinda Gates Foundation (OPP1044451, OPP1095464), Innovate UK (previously Technology Strategy Board, TSB100985) and Biotechnology and Biological Sciences Research Council (BB/N010396/1). The findings and conclusions contained within are those of the author(s) and do not necessarily reflect positions or policies of the BMGF, I-UK or BBSRC. The funders had no role in study design, data collection and analysis, decision to publish or preparation of the manuscript.

Author details

Andrew Landels^{1,2*}, Neil Cagney³, Lisa Bauer², Tracey A. Beacham², Stavroula Balabani⁴ and Michael J. Allen²

*Address all correspondence to: ala@pml.ac.uk

1 Biological Chemistry and Crop Protection, Rothamsted Research, Harpenden, UK

2 Plymouth Marine Laboratory, Plymouth, UK

3 Department of Earth Sciences, University College London, London, UK

4 Department of Mechanical Engineering, University College London, London, UK

References

- [1] Spellman FR. Handbook of water and wastewater treatment plant operations. CRC Press; 2013 Oct 21. 6000 Broken Sound Parkway NW, Suite 300, Boca Raton, FL. 33487-2742, USA
- [2] United Nations Food and Agriculture Organisation water usage data. 2014. Available from: <http://www.fao.org/nr/aquastat> [Accessed 2016-06-16].
- [3] Corcoran E, editor. Sick water? The central role of wastewater management in sustainable development: a rapid response assessment. UNEP/Earthprint; 2010. Birkeland Trykkeri AS, Norway
- [4] US Environmental Protection Agency water quality criteria. 2016. Available from: <https://www.epa.gov/wqc/national-recommended-water-quality-criteria-aquatic-life-criteria-table> [Accessed 2016-09-04].
- [5] Tilley E, Ulrich L, Lüthi C, Reymond P, Zurbrügg C. Compendium of sanitation systems and technologies. Eawag; 2014. Swiss Federal Institute of Aquatic Science and Technology (Eawag), Dübendorf, Switzerland.

- [6] Burton FL. Water and wastewater industries: characteristics and energy management opportunities (Burton Engineering) Los Altos, CA, Report CR-106941. Electric power research institute report. 1996.
- [7] Molyneux-Hodgson, Susan and Balmer, Andrew S. Synthetic biology, water industry and the performance of an innovation barrier, 2013, 10.1093/scipol/sct074, <http://spp.oxfordjournals.org/content/early/2013/10/17/scipol.sct074.abstract>, <http://spp.oxfordjournals.org/content/early/2013/10/17/scipol.sct074.full.pdf+html>, Science and Public Policy
- [8] Crites R, Technobanoglous G. Small and decentralized wastewater management systems. McGraw-Hill; 1998 ISBN: 9780072890877.
- [9] Ulrich A, Reuter S, Gutterer B. Decentralised wastewater treatment system (DEWATS) and sanitation in developing countries: a practical guide. Water, Engineering and Development Centre (WEDC), Loughborough University of Technology; 2009 Loughborough, UK.
- [10] Thomas SF, Rooks P, Rudin F, Cagney N, Balabani S, Atkinson S, Goddard P, Bransgrove RM, Mason PT, Allen MJ. Swirl flow bioreactor containing dendritic copper-containing alginate beads: a potential rapid method for the eradication of *Escherichia coli* from waste water streams. Journal of Water Process Engineering. 2015 Apr 30;5:6–14.
- [11] Landels A, Evans C, Noirel J, Wright PC. Advances in proteomics for production strain analysis. Current Opinion in Biotechnology. 2015 Dec 31;35:111–7.
- [12] Usher S, Haslam RP, Ruiz-Lopez N, Sayanova O, Napier JA. Field trial evaluation of the accumulation of omega-3 long chain polyunsaturated fatty acids in transgenic *Camelina sativa*: making fish oil substitutes in plants. Metabolic Engineering Communications. 2015 Dec 31;2:93–8.
- [13] Pérez JS, Porcel ER, López JC, Sevilla JF, Chisti Y. Shear rate in stirred tank and bubble column bioreactors. Chemical Engineering Journal. 2006 Nov 1;124(1):1–5.
- [14] Thomas SF, Rooks P, Rudin F, Atkinson S, Goddard P, Bransgrove RM, Mason PT, Allen MJ. A comparison between ultraviolet disinfection and copper alginate beads within a vortex bioreactor for the deactivation of bacteria in simulated waste streams with high levels of colour, humic acid and suspended solids. PLoS One. 2014 Dec 26;9(12):e115688.
- [15] UK power energy tariffs. 2016. Available from: https://www.ukpower.co.uk/home_energy/tariffs-per-unit-kwh [Accessed: 2016-09-04].
- [16] Rose JB, Dickson LJ, Farrah SR, Carnahan RP. Removal of pathogenic and indicator microorganisms by a full-scale water reclamation facility. Water Research. 1996 Nov 30;30(11):2785–97.
- [17] American Public Health Association, American Water Works Association, Water Pollution Control Federation, Water Environment Federation. Standard methods for the examination of water and wastewater. American Public Health Association.; 1915.

- [18] Hendricks R, Pool EJ. The effectiveness of sewage treatment processes to remove faecal pathogens and antibiotic residues. *Journal of Environmental Science and Health, Part A*. 2012 Jan 15;47(2):289–97.
- [19] Dollwet HH, Sorenson JR. Historic uses of copper compounds in medicine. *Trace Elements in Medicine*. 1985;2(2):80–7.
- [20] Thomas SF, Rooks P, Rudin F, Atkinson S, Goddard P, Bransgrove R, Mason PT, Allen MJ. The bactericidal effect of dendritic copper microparticles, contained in an alginate matrix, on *Escherichia coli*. *PLoS One*. 2014 May 15;9(5):e96225.
- [21] Atkinson S, Thomas SF, Goddard P, Bransgrove RM, Mason PT, Oak A, Bansode A, Patankar R, Gleason ZD, Sim MK, Whitesell A. Swirl Flow Bioreactor coupled with Cu-alginate beads: a system for the eradication of Coliform and *Escherichia coli* from biological effluents. *Scientific Reports*. 2015;5 :9461.
- [22] Lee KY, Mooney DJ. Alginate: properties and biomedical applications. *Progress in Polymer Science*. 2012 Jan 31;37(1):106–26.
- [23] Boyd A, Chakrabarty AM. *Pseudomonas aeruginosa* biofilms: role of the alginate exopolysaccharide. *Journal of Industrial Microbiology*. 1995 Sep 1;15(3):162–8.
- [24] Walker JA, inventor. Golden ratio axial flow apparatus. United States patent US 9,328,717. 2016 May 3.
- [25] iGEM repository of standard parts. 2016. Available from: http://parts.igem.org/Main_Page [Accessed: 2016-09-04].
- [26] Demont A, Cole H, Marison IW. An understanding of potential and limitations of alginate/PLL microcapsules as a cell retention system for perfusion cultures. *Journal of Microencapsulation*. 2016 Jan 2;33(1):80–8.

Vortex Spinning System and Vortex Yarn Structure

Gizem Karakan Günaydin and Ali Serkan Soydan

Additional information is available at the end of the chapter

<http://dx.doi.org/10.5772/105882>

Abstract

Studying the yarn formation with the swirling air concept arouse of interest of the researchers for a long time because it appears to be easy to understand as a spinning principle. These kinds of systems are known as the vortex yarn spinning systems. The air-jet spinning methods have been developed since it is possible to eliminate the movable elements as the spindle and the traveler in ring spinning or the centrifuge in rotor spinning. The success of Murata vortex spinning (MVS) system which is the newest system after all studies of air-jet systems has been much acceptable especially for the spinning ability of 100% cotton in high speeds (500 m/min) and the yarn structure resembling ring yarn structure rather than rotor yarns. This study summarizes the historical background of vortex spinning, the spinning principle and the structure of the yarn spun on this system, as well as the factors influencing the yarn quality and finally the developments in vortex spinning technology.

Keywords: vortex spinning system, vortex yarn, air-jet spinning

1. Introduction

There are many different spinning systems in textile technology. Some of them are in commercial use, many are still experimental and some of them have been withdrawn from the market. Certainly, the conventional ring spinning technique is currently the most widely used, accounting for an estimated 90% of the world market spinning machines [1]. Because of ring spinning, providing all fibers to be spun into a wide range of yarn count with the lowest rate of yarn faults with the best quality, this spinning technology is still the most widely used one in the market.

Compact spinning is one of the modifications of ring spinning process by the help of better integration of fibers into the yarn structure. The fiber bundle is condensed by air suction, and

hence, this results better tensile properties for the same twist level, lower hairiness and better yarn evenness. Open-End rotor spinning is another most commonly accepted unconventional short-staple yarn spinning technology. It is a process in which the input material to the spinning system is highly drafted, ideally to the individual fiber state. The individual fibers are subsequently collected onto the tail end of a seed yarn that is rotated to twist the fibers into the yarn structure and thereby form a new length of yarn. The spinning is continuous as the input material is continuously collected onto the open end of a previously spun yarn [1].

In the early 1980s, air-jet spinning system was launched. Initially only the man-made fibers could be used as the raw material; later, it was improved for cotton yarn spinning as well. Although the developments aimed to produce 100% cotton yarns, the acceptable quality was provided with polyester/cotton blended yarns in terms of yarn strength. Today the latest development in air-jet spinning technology is the Murata vortex spinning (MVS) technology, which was firstly introduced at Osaka International Textile Machinery Show in 1997 (OTEMAS '97) by Murata Machinery Ltd [2].

2. Air-jet spinning systems

Airflows have been increasingly used in transporting, drawing, separating and deforming solid structures for the advantages with respect to high efficiency and economic benefits. Particularly in the polymer and textile processing industry, airflows have also been playing important roles in various processing methods such as melt-blowing, air-jet weft insertion, air-jet spinning and vortex spinning.

Many methods may be encountered with during the development of air-jet spinning process. But Goetzfried method is the first method where the air-jet flow is used as a twisting device. It is based on the Open-End spinning principle. The airflow is a main parameter for the control of spinning and twisting [1–3].

As a way of fascinated yarn production, there were many attempts for the air-jet spinning innovations such as “Dupont” in 1956, “Rotofil” in 1971, “Toyada” in 1983, “Toray” in 1985, etc. But these methods had little commercial success. A renaissance in the historical development of air-jet spinning started with the MJS machine of the Japanese company Murata Machinery Ltd (Murata Jet Spinner). The company introduced its first air-jet spinning machine, Murata Jet Spinner, MJS 801, at the American Textile Machinery Exhibition in 1982 (ATME '82). The machine contains a three-roll drafting system and is equipped with two air-jet nozzles that create air vortices rotating in opposite directions. In this system, the second nozzle creates false twist on the fiber bundle coming out of front roller. There is an air vortex between the front roller and the first nozzle which removes the twist and causes the edge fibers to be separated from the fiber bundle. So the edge fibers move to second nozzle in an untwisted form. However, the core fibers are directed to second nozzle in a twisted form. At the time of the second nozzle leaving, the core fibers are unwrapped and the edge fibers are twisted in the opposite direction. The system is stated to be suitable for processing man-made fibers and their

blends with cotton; however, it was not capable of spinning 100% cotton or rich blends of cotton yarn [3]. **Figure 1** displays the MJS yarn formation and the yarn structure in a detailed form.

2.1. Murata vortex spinning system

The latest concept in air-jet spinning developed by Murata Machinery Ltd. is known as the vortex spinning system which uses a modified single air nozzle. This system is claimed to be capable of producing 100% carded cotton yarns which have a ring spun-like appearance and higher tenacity due to higher number of wrapping fibers when compared with the previous air-jet spinning systems [3].

Murata has developed MVS 810, MVS 81T, MVS 851, MVS 861 and lastly the MVS 870 model spinning machines. Murata MVS 810 was the first vortex spinning machine exhibited at Osaka International Textile Machinery Show in 1997 (OTEMAS '97). The machine had a delivery speed of up to 400 m/min. The modified version of this machine, MVS 81T, was developed to produce twin vortex spun yarns. The yarns spun on two spinning units pass through the same yarn cleaning and waxing unit and are wound on the same package. These are twisted on a two-for-one twister to obtain a plied vortex yarn. Subsequently, Murata introduced the MVS 851 spinning machine. Apart from the previous machine, MVS 851 is not capable of spinning core yarns. Murata exhibited a new version of vortex spinning machine, the MVS 861, in 2003. This version allows the core yarns production with higher delivery speed of up to 450 m/min. The spinning system ensures uniform winding tension with a tension ruler with minimum energy consumption [3, 4]. **Figure 2** displays the general view of the MVS 861 machine and the yarn spinning unit.

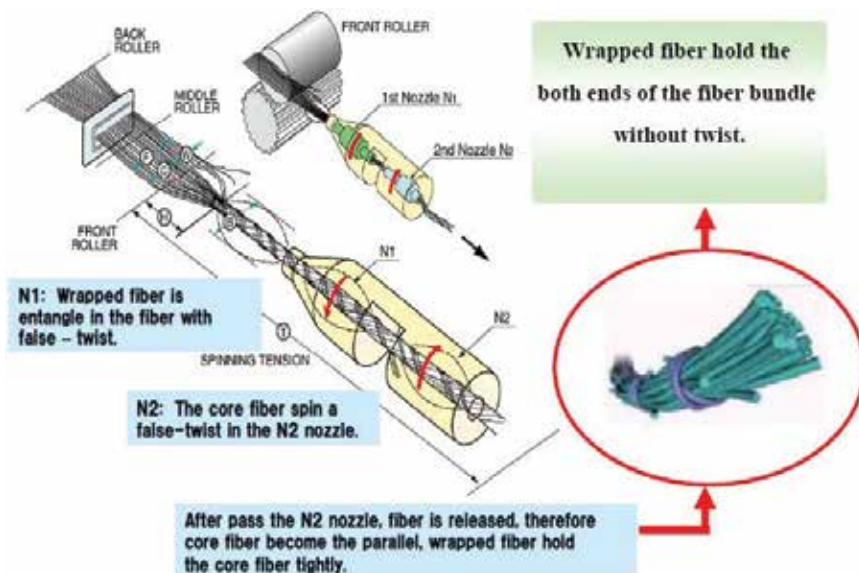


Figure 1. MJS yarn formation and the yarn structure [4].



Figure 2. MVS 861 spinning machine: (a) the general view of the machine, (b) the yarn spinning unit.

2.1.1. Principle of yarn formation in vortex spinning system

Murata vortex spinning (MVS) is based on the already existing air-jet spinning technology by Murata but essentially differs in principle from the MJS method because of the geometry of the air-jet twisting device used (US Patent 5,528, 895, 25 June 1996). This air-jet device includes a nozzle block with injectors for the generation of swirl flow, a needle holder, a hollow spindle and a guide member. **Figure 3** displays a detail view about the schematic diagram of the nozzle block of vortex spinning machine.

In MVS, a drawn sliver is fed to a four-line drafting system. After coming out of the front rollers, the fibers move to the air-jet nozzle. Although the fibers are oriented to be twisted with the pressured air effect, the twisting motion tends to flow upward toward the front rollers of the drafting unit; here, the guide member protruding from the fiber bundle passage prevents this upward during the yarn formation. The high-speed whirled air current arises in the vortex chamber into where the pressured air is injected. The preceding parts which will be core fibers later are drawn into the vortex spun yarn trail. However, the upper portions of some fibers separated from the nip point of the front rollers are kept open. After the departure of

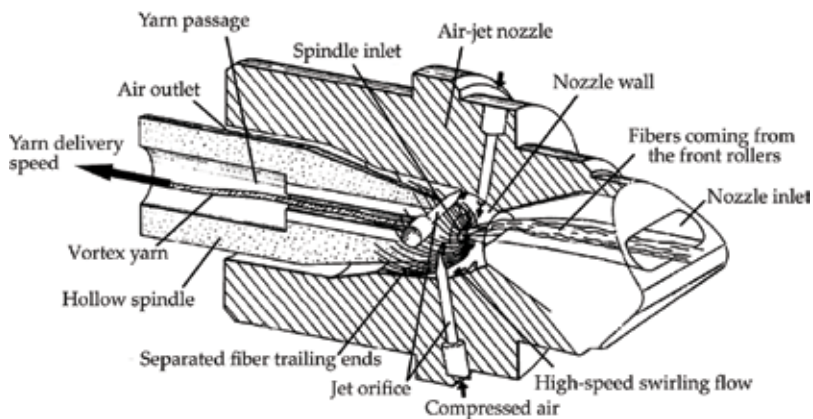


Figure 3. Schematic diagram of the nozzle block of vortex spinning machine [1].

trailing ends from the nip point, they pass through the spiral fiber passage, and they twine over the hollow stationary spindle due to the whirling force of air-jet stream and become the wrapping fibers [5]. **Figure 4** displays the yarn formation in Murata vortex spinning system.

2.1.2. Structure of vortex yarn

Vortex yarn has different yarn structure comparing the conventional yarn structures. Vortex spun yarn consists in two-segmented structure which includes core and wrapper fibers which covers the core part of the fiber grouping the yarn body. Since fiber separation occurs everywhere in the outer periphery of the fiber bundle, a higher number of wrapper fibers are obtained with jet-spun yarns. This leads to the production of a spun yarn with more of a ring-spun-type appearance and also with higher tenacity [2].

Basal (2003) studied yarn structure by using tracer fiber technique combined with the Image Analysis Application [5, 6]. The researcher captured the images of the tracer fibers which were transferred to a computer later. After evaluating the images, the researcher concluded that there were some variations along the vortex yarn length. The tracer fibers were grouped according to their configuration. It is emphasized that the percentage of straight, hooked (trailing) and hooked (both ends) is very close to each other and higher than the leading

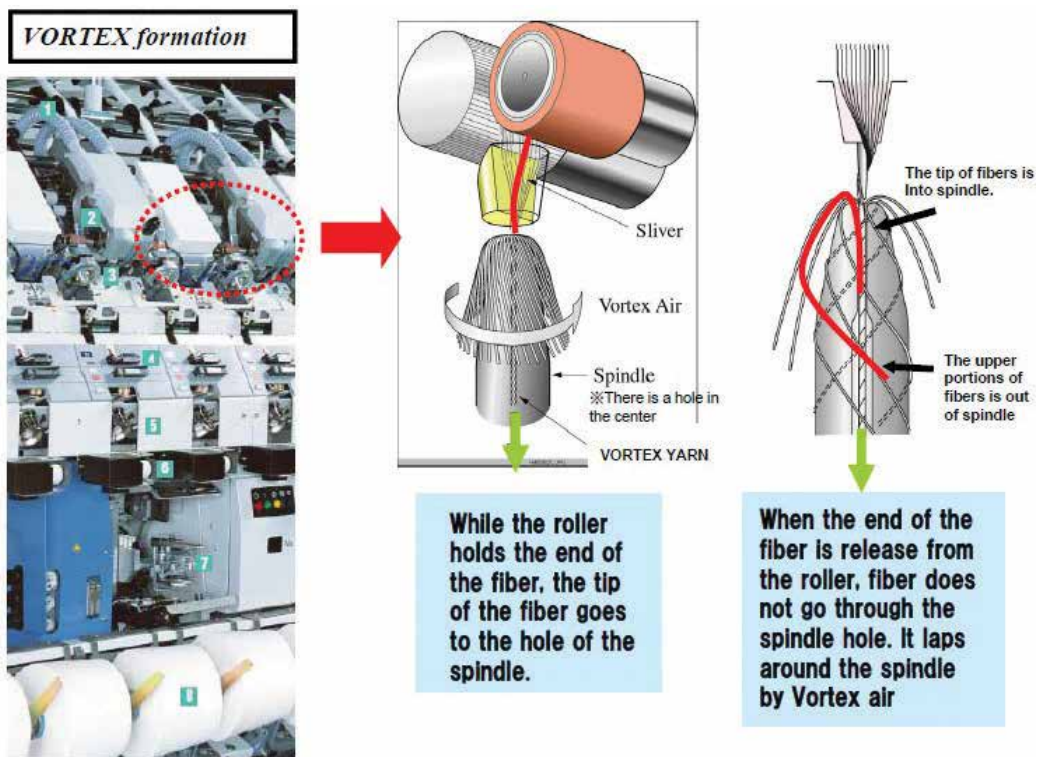


Figure 4. Yarn formation in Murata vortex spinning system [4].

hooked, entangled and looped fibers in vortex spun yarns (**Table 1**). It is concluded that the images revealed most of the tracer fibers tend to show first core fiber characteristics then wrapper fiber characteristic twining over the yarn core as described in the ideal case [5].

Soe also studied the structure of MVS Yarns and made a comparison with ring and Open-End yarns. By the help of the A Nikon SMZ 1500 microscope with a DXM 1200 digital camera, they investigated the side visual assessment of the yarn structures [7]. The fiber arrangements of the RS, OERS and MVS yarns, including the MVS yarn with the tracer fibers were observed carefully. They adopted the classification by Chasmawala et al. [8] and modified it for ring, Open-End and vortex yarns. Description of each classification depending fiber arrangement is explained below [7]:

1. **Core fibers:** These fibers may be straight or inclined. Core fibers constitute a major proportion of the yarn. Core fibers' orientation has a big impact on the stress-strain behavior of the yarn.
2. **Wild fibers:** These fiber groups randomly protrude from the main yarn body in any direction. Loops may also be observed along the yarn axis and these groups are also classified as wild fiber groups. The wild fibers increment leads to a more hairy yarn.
3. **Wrapper fibers:** The helix angle of wrapper fibers around the core fibers are considered similar. There might be some degree of inclination with respect to the yarn central axis.
4. **Wrapper-wild fibers:** These fibers wrap around the core fibers in a different direction from the regular wrapping fibers. The wrapper-wild fibers have a scattered appearance. There is no common angle for wrapper-wild fibers because of their disordered appearance.
5. **Belly-band fibers:** These fiber groups are the main body wrapping fibers composed of either core or wrapper fibers. Belly band fibers are observed in the upright position with respect to the yarn central axis.

Figure 5 also displays the schematic diagram of yarn fiber types in the yarn structure.

According to the microscopic examinations, Soe et al. concluded that the highest proportion of core fibers were observed in ring spun yarn while MVS (Murata vortex spinning) yarn had the minimum ratio of oriented core fibers. The core fibers were helically embedded into the yarn. No






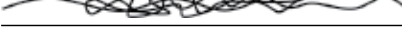
Tracer fiber configuration	Class	Percentage of fibers
	Straight	21.00
	Hooked (trailing)	20.50
	Hooked (leading)	6.4
	Hooked (both ends)	23.00
	Looped	11.50
	Entangled	10.25

Table 1. Tracer fiber configuration in MVS yarns [5].

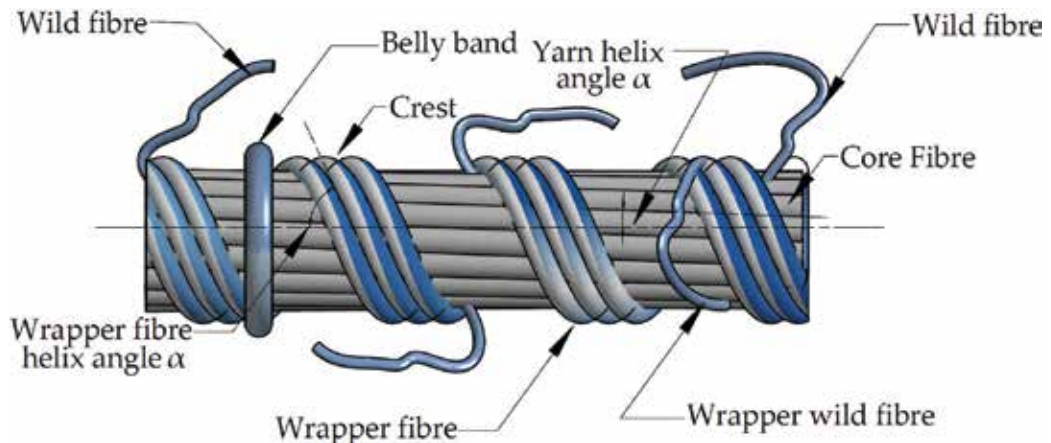


Figure 5. Schematic diagram of yarn fiber types in the yarn structure [7].

wrapper fibers were observed in the ring spun yarn structure. Belly-band fibers were mostly seen in Open-End rotor spun yarns followed by ring spun yarn. The highest wrapper fiber ratio of the three yarn types was obtained from MVS yarns. It can be emphasized that there was no twist in the core fibers of the vortex yarns which was a significant feature. The highest ratio of wild fibers in MVS yarns was observed in the wrapping fibers instead of the core fibers. This result is attributed to encirclement of the core fibers by the wrapper fibers. All forementioned fiber groups were observed in vortex spun yarn; however, belly-band fibers were hardly seen. Ideal yarn structures of ring spun, Open-End rotor and MVS yarn were illustrated in **Figure 6** [22].

There are also some studies related to comparison of air-jet spun yarns and vortex yarns. Since vortex yarn is the modified version of air-jet yarns, there are some features of vortex yarn expected to be much better. MVS spinning system uses only one air jet instead of two as in the air-jet spinning system. This directly affects the number of wrapping fibers between the vortex spinning system and air-jet spinning system. The fiber separation occurs everywhere in the outer periphery of the fiber bundle. Hence, the increasing number of wrapping fiber results with more ring-like appearance and higher tenacity [3]. **Figure 7** displays the yarn formation in MVS and MJS yarn spinning system.

Basal and Oxenham [9] produced vortex and air-jet yarns with different polyester/cotton blends as a raw material and compared the physical properties of vortex and air-jet yarns. They used variance analysis for determining the differences between the properties of the vortex yarn and the air-jet spun yarn. The results revealed that MVS yarns had fewer thick places, lower hairiness and better evenness values compared to MJS yarns. The higher tenacity values were obtained from the MVS vortex yarns for every blend ratio. But in 100% polyester yarn production, the MVS and the MJS yarn groups had the same strength. This was attributed to the higher proportion of wrap fibers because of the fiber separation from the bundle occurring everywhere in the entire outer periphery of the bundle. They also emphasized that higher proportion of wrap fibers leads to MVS yarns lower elongations because of the wrapping fibers restricting the yarn movement [9]. **Figure 8** displays the vortex and air-jet spun yarn together.

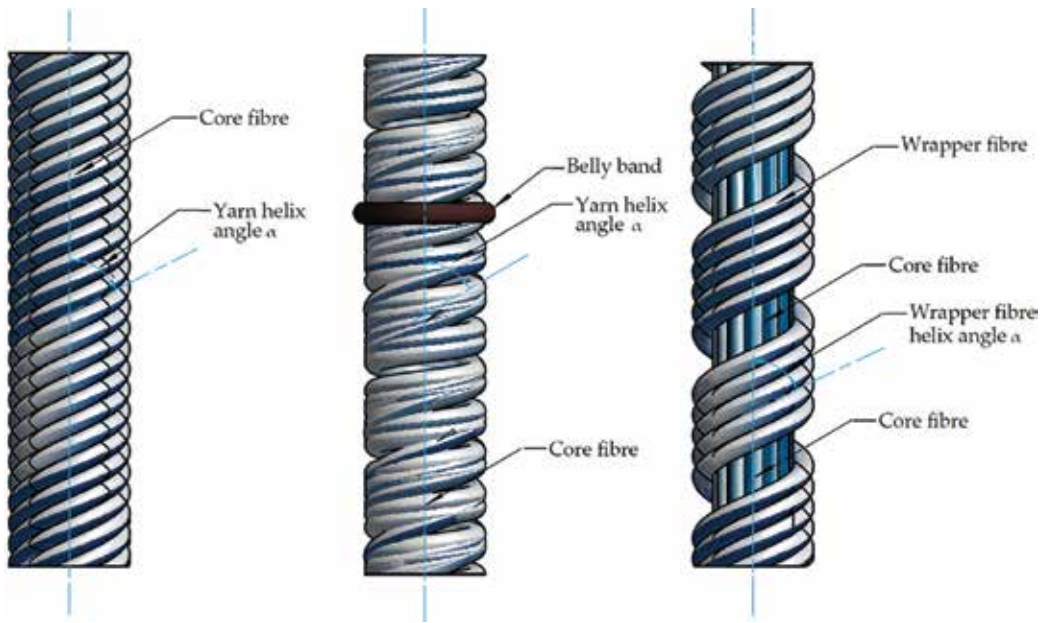


Figure 6. Ideal yarn structures of ring spun, Open-End and MVS yarn, respectively [7].

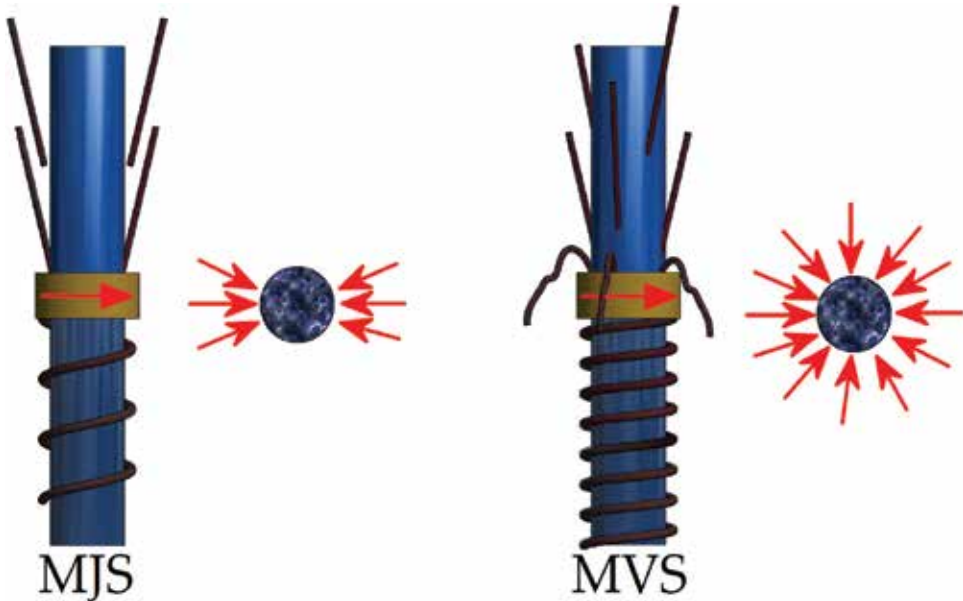


Figure 7. Comparison of yarn formation in MVS and MJS yarn spinning system [9].

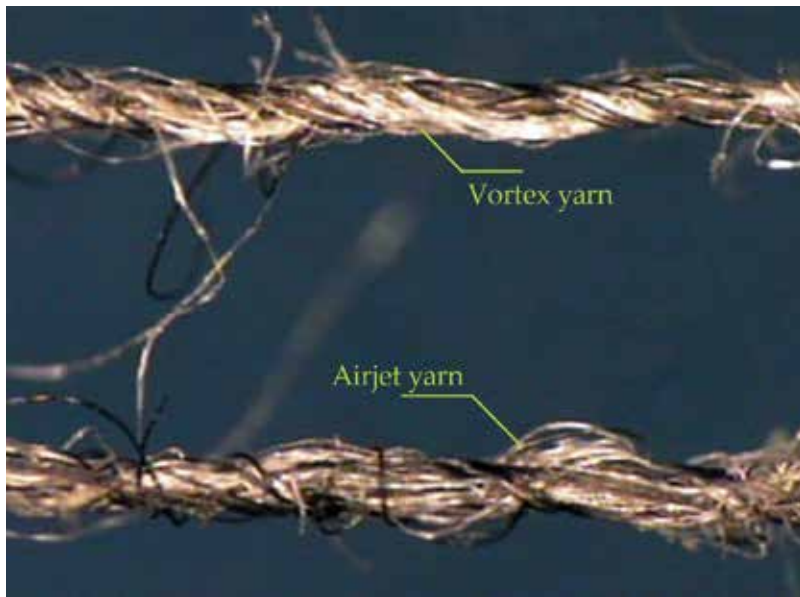


Figure 8. Vortex spun yarn versus air-jet spun yarn (28's Ne, 30/60 PES/Co) [9].

2.1.3. Effects of some parameters on structure and properties of vortex spun yarns

Previous studies proved that the structure and performance of vortex spun yarns were influenced by the effects of nozzle angle, nozzle pressure, spindle diameter, yarn delivery speed, yarn linear density, fiber composition and the distance between the front roller and the spindle [10, 11].

2.1.3.1. Nozzle pressure

There are many studies concerning the effect of nozzle pressure to the vortex spun yarn. These studies reveal that the nozzle air pressure directly influences the fiber configuration and the yarn structure. Basal and Oxenham investigated some process parameters including the nozzle pressure. It was observed that increasing the nozzle pressure led to the increment of the axial and tangential velocity. The fiber bundling receiving higher twist with the pressured air caused the yarn becoming much stronger but stiffer [10]. Tyagi et al. reported that the changes in nozzle pressure influenced the tightness of wrapping fibers along the yarn strand as well as the amount of wrapping and the proportion of unwrapped sections. In their study, they observed that the increment of the nozzle pressure resulted in high level of tight wrapping ratio. However, they were inclined to turn into irregular wrappings at very high level of nozzle air pressure [12]. In the other study of Tyagi et al., they stated that lower hairiness was provided with the high nozzle air pressure up to a certain limit. But when the nozzle pressure reached the level of 6 kgf/cm², hairiness got worse due to the formation of the wild fibers. This was attributed to the rate of change in radial position of a fiber (mean migration intensity) becoming higher at the high nozzle pressure values [13].

Another study was conducted by Zou et al. which is related to theoretical analysis of vortex yarn formation. They revealed that the high nozzle pressure values caused an increase in the mean angular velocity of the free (open) end of the fiber. This provided the wrapping fibers whirling around the yarn core with the greater force. Hence, the proportion of tight wrappings increased. They added that when the nozzle pressure was too high, the separated fibers were easily taken out of the fiber bundle by the high-speed airflow which caused more fiber loss [14].

2.1.3.2. Yarn delivery speed

In vortex spinning system, yarn delivery speed may be up to 500 m/min in the latest version of MVS 870. The yarn delivery speed is important for the time of the fibers being exposed to the whirling force. It should be noted that at high delivery speeds, the fiber loss and the yarn quality problems may probably appear.

Basal and Oxenham investigated some process parameters, and they concluded that yarn delivery speed affects the yarn diameter since lower delivery speeds lead to regular tight wrapping fiber ratio increment [10]. Ortlek and Ulku investigated some process parameters in their study, and they observed that increasing the delivery speed causes more hairiness and leads to deterioration for the tensile properties of vortex yarns. They explained this with the result of less time for the wrapper fibers wrapping the parallel core fibers properly. Especially for the finer yarns, this may be an important problem which means vortex spinning is more appropriate for the coarser yarns [11]. Koppers et al. investigated the spinning limits for the vortex spinning. They determined the ratio between the fiber guidance element and the yarn delivery speed depending on the yarn count. It is suggested that finer yarns require high ratio. At constant air speed, the delivery speed should be reduced [15].

2.1.3.3. Effect of draft ratio

Erdumlu and Ozipek investigated the effects of draft ratios on the properties of vortex spun in their study. Hundred percent viscose drawing slivers of three different counts (3.94, 3.19 and 2.68 ktex) were spun into yarns with a count of 14.76 tex while keeping all other spinning conditions constant. The yarn samples were evaluated on the basis of yarn irregularity and imperfections, as well as hairiness and tensile properties. In addition, a 3rd passage draw frame sliver with a yarn count of 3.19 ktex was spun into yarns of 14.76 tex using two different delivery speeds: 350 and 400 m/min. They concluded that while working with high levels of the total draft using a heavy sliver, the better yarn evenness and thin place values are obtained as the intermediate draft gets lower. Higher breaking elongation and work to break values were observed at the intermediate level of 2.5 with the highest total draft of 267. The results revealed that a high delivery speed deteriorated the physical properties of the yarns in terms of yarn evenness, thin places and tenacity. The lower the delivery speed, the better the yarn properties. Additionally, as the yarn delivery speed increased, hairiness also increased for both levels of intermediate draft [16].

2.1.3.4. The distance (L) between front roller nip point and the spindle

In many studies, the effect of distance between front roller nip point and the spindle was significantly important for the fiber loss and the number of wrapping fibers; Basal and Oxenham concluded that the short front roller to the spindle distance produced more even yarns with fewer imperfections and less hairiness. They also added that if the distance was short, the most of the fiber ends were tightly assembled, and there were fewer open-ended fibers. Hence, a yarn similar to MJS yarn with parallel core fibers mostly but fewer open-ended fibers was observed. In that case, yarn evenness and the imperfection results were more pleasing because of the minimum risk of losing control of fibers. Added to that in short distance between the front roller nip point and the spindle ensures less hairiness and leaner appearance [10]. Yarn formation zone in vortex spinning is shown in **Figure 9**. In that figure, L denotes the distance between front roller and the spindle.

Zou et al. [17] investigated the twisted strength acting on the vortex spun yarn by the whirled airflow by an analytical model based on simulating the flow field inside the nozzle block. The results showed that the twisted strength acting on the yarn by the vortex is also affected by the distance from the inlet of the nozzle block to the inlet of the hollow spindle. The strength twisted by the whirled airflow was weaker when the distance from the inlet of the nozzle block to the inlet of the hollow spindle was bigger. When the distance " L " increased, the number of the open-trail end fibers also increased which caused a decrease in the tangential velocity inside the nozzle block [17].

Zou et al. [18] studied the fiber spatial configuration in another research. The spatial configuration and the influenced factors were analyzed. They declared that the fiber spatial

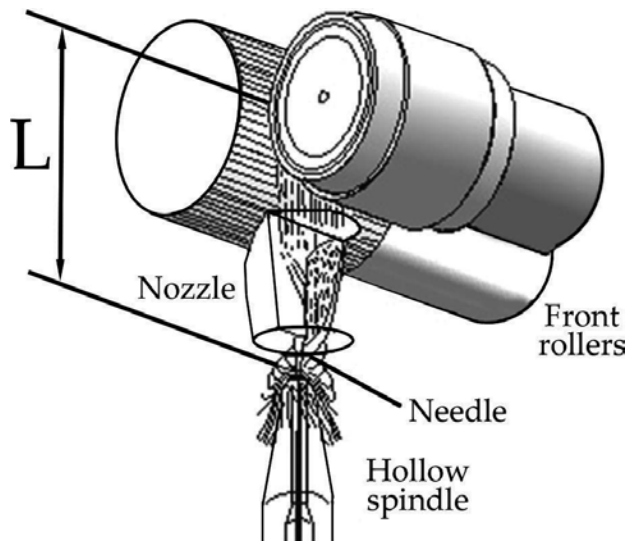


Figure 9. Yarn formation zone in vortex spinning [10].

configuration in vortex spun yarn was affected by the distance between the front roller nip point and the hollow spindle. As the distance between the front roller nip point and the inlet of the hollow spindle increased, it was observed that the open trailing ends' critical angular velocity decreased which mean the length decrease of fiber embodies into the vortex. This was explained as a risk for the leading end of the fibers to be more easily pulled out from the vortex spun yarn and for the fiber loss and more thin places in the yarn [18].

Tyagi and Sharma studied the influence of processing variables delivery speed, nozzle distance, yarn linear density and yarn composition on the structural parameters of polyester/cotton yarns spun on Murata Vortex Spinner (MVS). It is observed that MVS yarns have about 50–60% core fibers and remaining as wrapper or wild fibers. The structure of MVS yarns has been classified into four main categories: tight wrappings, long wrappings, irregular wrappings and unwrapped. They concluded that increase in nozzle distance causes an increase in long regular wrappings and number of wrapper fibers due to increase in the amount of fibers with Open-End configuration, while decrease in tight regular wrappings. And the resultant yarn was more hairy with longer hairs [12]. The tensile characteristics increased as the nozzle distance increased. But a reduction in yarn tenacity was observed at very high nozzle distances [13].

Murata Machinery Ltd. also suggests that the short front roller to the spindle is favorable for less fiber waste. The even yarns with fewer imperfections and lower hairiness are obtained. But it is also added that when the distance is too short, both ends of fibers are tightly held, and there occurs fewer fibers with open trailing ends. So the yarn is mostly composed of the parallel fibers as in the air-jet yarns [4].

2.1.3.5. Nozzle angle

There are also some investigations verifying the nozzle angle's effect on the swirling air during vortex yarn formation. Zou et al. [14] made a study concerning numerical computation of a flow field affected by the process parameters of Murata vortex spinning. They observed that the tangential, axial and radial velocities inside the nozzle block are significantly affected by the jet orifice angle and velocity at the exit of the jet orifice as well as by the diameter at the inlet of the nozzle block. They explain the effect of the jet orifice angle " θ " on the flow field inside the nozzle block is quite complex, and different " θ " values result in variations in the tangential, axial and radial velocities. Along with an increasing " θ " value, the axial velocity increases, and the tangential velocity decreases. The radial velocity influenced by the " θ " value has an expanding effect on the fiber bundle. This produces a large number of open-trail end fibers. A higher tangential velocity twists open-trail end fibers expanded by the radial velocity which enhances the strength of the MVS yarn. Static pressure distributions inside the nozzle block are significantly affected by the jet orifice angle, the velocity at the exit of the jet orifice, the outer diameter of the hollow spindle and the distance from the inlet of the nozzle block to the inlet of the hollow spindle [14]. Schematic model of nozzle block and projection of the nozzle with jet orifices at section respectively is shown in **Figure 10**.

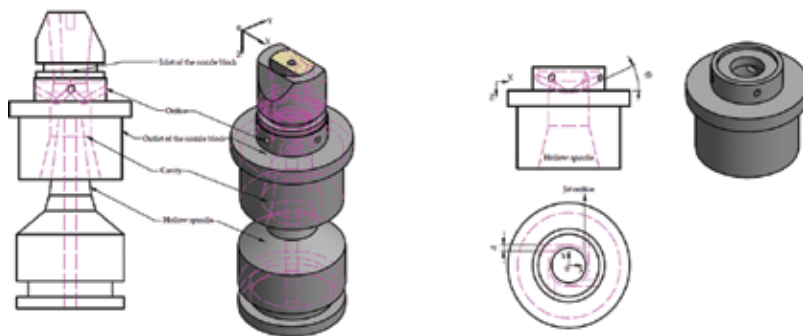


Figure 10. Schematic model of nozzle block and projection of the nozzle with jet orifices at section, respectively.

Basal and Oxenham also suggested that the nozzle angle had significant impact on yarn hairiness and evenness. They claimed that a high nozzle angle leads to higher tangential velocity, and in turn to higher twist which means more even and less hairy yarns. The interaction of a high nozzle angle and short front roller to the spindle provided better evenness.

According to the same study, low hairiness values were obtained from the high nozzle angles. It was explained with the belief that the increment of the nozzle angle and pressure caused the fibers being integrated more tightly into the yarn structure [10].

2.1.3.6. Spindle diameter and spindle working period

The studies on vortex spun yarn related to spindle diameters claim that the tightness of wrapping on vortex spun yarn is significantly affected by the spindle diameter. A smaller spindle does not give so much freedom for the fibers expanding. Hence, there occurs the tight wrapping with higher twist which means less hairy yarns. When the spindle has large diameter, the fiber bundle movement is not restricted, and wrappings become looser which means more hairy yarns.

Ortlek et al. [19] investigated the effects of various spindle diameters and the spindle working period on the properties of 100% viscose MVS yarns. MVS yarn samples produced with four levels of spindle diameter: 1.1, 1.2, 1.3, 1.4 mm and five levels of the spindle working period: 0, 1, 2, 3, 4 months were evaluated on the basis of unevenness, hairiness, elongation at break, tenacity and work-of-break (B-work) values. They concluded that a large spindle diameter resulted in high hairiness, as well as low unevenness and tenacity values. Especially, a decrease in spindle diameter from 1.3 to 1.2 mm resulted in a significant increase in the yarn unevenness value. The explanation for that was the possibility of the fibers having much more place to arrange themselves in larger spindle diameters. When it comes to spindle working period, Ortlek et al. [19] also concluded that spindle wear was a major problem as it negatively affects MVS yarn properties. The wear of the spindle increased with an increasing working period. Spindle wear mainly occurred in the tip zone and the whole surface of the spindle. The tenacity, elongation at break and B-work values of MVS yarns produced with a spindle that had 4 months working period were significantly lower than those of yarns produced with spindles which had other working periods [19]. SEM images of spindle wear versus spindle working period for different spindle diameters were shown in **Figure 11**.

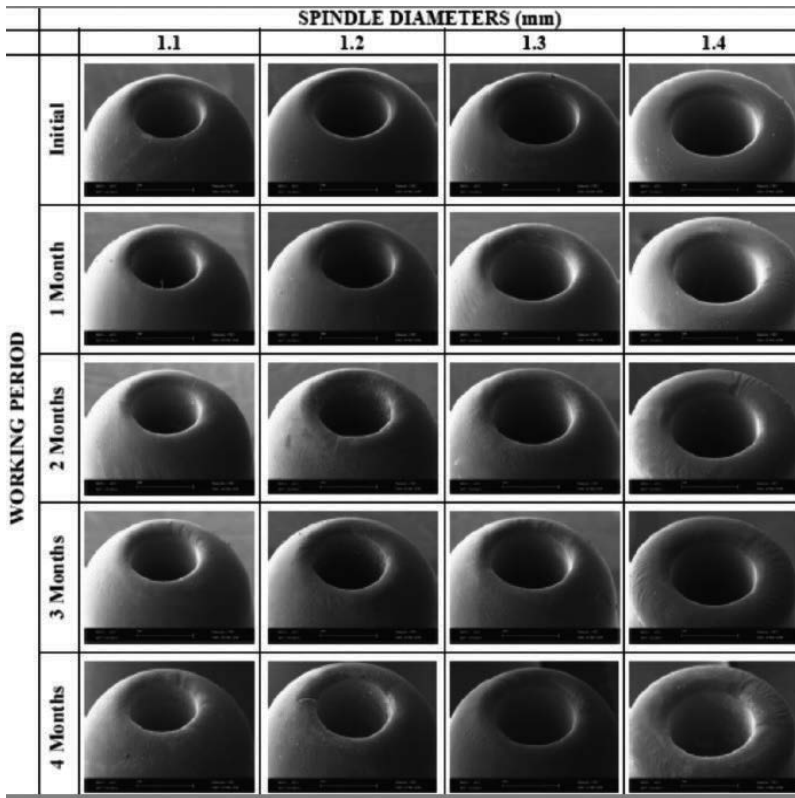


Figure 11. SEM images of spindle wear versus spindle working period for different spindle diameters [19].

2.1.3.7. Yarn count

As it is observed in the other yarn spinning systems, the yarn evenness and the imperfection results get worse also in Murata vortex spinning system. Although Murata Machinery claims, the yarn tenacity results improve as the yarn gets finer. The most studies reveal that coarser vortex spun yarns have better tenacity as well as the yarn evenness and the number of imperfections.

Ortlek and Ulku studied the some process parameters' effects on the properties of vortex yarns. The delivery speed, nozzle pressure and yarn count were the main variables on the Murata vortex spinning system. According to the experimental results, yarn evenness, imperfections, tensile properties and hairiness were all affected significantly from the parameters. They concluded yarn count was also highly correlated with the vortex yarn properties. Generally, coarser yarns yielded better yarn properties in terms of yarn evenness, imperfection values, hairiness and tensile properties [20]. Tyagi et al. also claimed that the finer MVS yarns have less proportion of core fibers than the coarser ones. So it is more difficult for the core fibers to bear the loads which results as the low tenacity [13]. In another investigation,

Leitner et al. also concluded that coarser yarns have higher tenacity and breaking elongation. In addition, they stated that there aren't major changes in tenacity and breaking elongation values of fine count vortex spun yarns [21].

2.1.3.8. Fiber Composition

Several fiber properties govern the successful application of the air-jet process in vortex spinning system. In order of importance, these properties are as follows:

- Fineness (fiber micronaire or denier).
- Cleanliness.
- Strength.
- Length and length irregularity.
- Friction coefficients: "fiber-to-fiber" and "fiber-to-nozzle".

The fiber fineness has a vital effect for the yarn quality in vortex spinning. As the number of fibers in the cross section increases, the yarn break ratio during spinning also the yarn faults will be in a decreasing tendency. On the other hand, the use of finer fibers increases the number of core fibers at the expense of the wrap fibers, which decreases the yarn strength. Generally, fibers with higher strength should be used for spinning air-jet and vortex yarns. However, the elongation of the fibers also has to be considered since the high strength fibers have very low elongation for tight wrapping of the yarn core. The fiber length and length distribution influence the fascinated structure. There will be more wrapping fibers when the fiber is longer which results as a stronger yarn [22].

There are some studies examining the vortex and air-jet yarns made from different fibers. Basal and Oxenham investigated the difference between the properties and structure of the MVS and MJS produced with different blends of cotton and black polyester. The trial of MJS yarn production of pure cotton and the polyester/cotton blend with 83% of cotton ratio was not successful. Moreover, they declared that when the blend ratio of polyester was less than 50%, many difficulties appeared during the MJS production. They succeeded to produce yarns from 100% polyester and polyester/cotton blends with the MVS system; however, MVS yarn production with the 100% cotton was not possible. They explained this with the high short fiber content of cotton slivers. They also added that there is not an apparent tendency of cotton or polyester fibers to become either wrapper or core fibers in blended yarns [9].

Kılıç and Okur investigated the properties of cotton Tencel® and cotton ProModal® blended yarns in count of 30 Ne spun in different spinning systems (conventional ring, compact and vortex spinning system). They examined the effects of different blend ratios on a yarn's structural, physical and mechanical properties by using 100% cotton, 100% regenerated cellulosic fiber and 67–33, 50–50, 33–67% cotton-regenerated cellulosic fiber blended yarns. It was observed that the increasing ratio of regenerated cellulosic fiber content increases the hairiness values of vortex spun yarn. It is obvious that as the ratio of regenerated cellulosic

fiber increases, the length of wrapping fibers will increase depending on the increased mean fiber length. So there is a dilemma here with the explanation of increasing wrapping length prevents fiber ends protruding from the yarn body. The increasement ratio of regenerated cellulosic fiber also provides better results for yarn unevenness, reduction in the number of thin-thick places and neps. They added that increasing ratio of the regenerated cellulosic fiber content has also contributes positively for the tenacity, breaking elongation values, roundness [23].

Tyagi et al. concluded that percentage of each fiber type in polyester/cotton blended vortex spun yarns has impacts on various yarn and fabric properties. Yarns with higher proportion of cotton fiber are less even and have high number of imperfections. Moreover, the yarns with higher proportion of cotton content are more hairy on account of the higher bending and torsional rigidity of cotton fiber, and flexural rigidity and abrasion resistance are considerably higher in yarns with higher polyester content [24].

Tyagi and Sharma [25] evaluated the thermal comfort characteristics air permeability, water vapor diffusion, absorbency and thermal insulation of scoured and finished fabrics made from polyester/cotton MVS yarns. Related to the fiber composition, they concluded that higher cotton content is very effective improving absorbency and thermal insulation properties but decreases the air permeability. They explained this with relation to the change in yarn bulk and hairiness, since higher cotton content results in a larger yarn diameter and more hairiness [25].

Gordon made a survey related to the short fiber content and neps on Murata vortex spinning. Darling Downs cotton was used as the raw material for the bales. But the cotton of each bale had different fiber length distributions and neps levels since different conditions with respect to moisture conditions in storage and heat conditions were applied for the each treatment. He summarized the results as dry seed cotton and hot air in the ginning increased the short fiber ratio and neps and reduced the fiber tensile. Deterioration of fiber values led to higher fiber loss in spinning, lower yarn tenacity, high hairiness, high number of imperfections and bad spinning efficiency. On the other hand, less fiber loss with high yarn quality and better spinning efficiency was obtained from the cotton fibers stored in higher moisture and treated with less heat in ginning [26].

2.2. The latest developments in vortex spinning technology

Rieter has developed Rieter J10, J20 and J26 model spinning machines working with the same principle with Murata vortex spinning system. These are double sided machines with 100 spinning units with delivery speed up to 500 m/min. The machine application range covers 100% polyester, combed cotton, cellulosic fibers, microfibers and different blends including man-made fibers in the yarn count range from Ne 20 to 70. In this spinning, system fibers that leave the drafting zone are guided through the fiber feeding element (FFE) by means of negative pressure into a spinning nozzle. The front part of the fibers enters the tube of the spinning tip and creates the core of the yarn. The four air jets in the twist element create a whirlwind air-jet stream. The air stream drifts the loose fiber ends around the yarn core. In this system, there is also a regulator connected for adjusting the compressed

air pressure to the set value. One of the distinctive features of the system from the Murata vortex spinning system is the connection of sliver condensers, nozzle and the yarn quality sensor with the traversing device. Hence, this becomes an advantage for the stable yarn quality, less wear on rollers. By this way, sliver/yarn is moved slowly over the defined range. The yarn produced by this system is called Comforjet®. Lower spinning air pressure and higher delivery speed result in soft yarns which maintain low hairiness, good pilling and high abrasion resistance. One of the decisive features from the other air-spun systems is the profiting from the minimal fiber fly. But unlike the Murata vortex spinning system, it is not possible to produce core-spun yarns in Rieter air-jet spinning [27]. Yarn formation in Rieter air-jet spinning machine and Rieter automated air-jet spinning machine is shown in **Figures 12** and **13**, respectively.

Murata Machine has also developed a new vortex spinning model MVS 870 at ITMA 2011 Barcelona. There are some little innovations compared to the previous models. The spinning speed has increased to 500 m/min, faster than before. A friction roller is adopted instead of the nip roller in the mechanism which draws the yarn from the spinning nozzle. Frictional force is generated between yarn and roller by winding a preset amount of yarn onto the friction roller. This frictional force contributes to draw the yarn from the spinning chamber with the roller rotating [28]. Eldessouki et al. made a study about the structure and comparison between Murata vortex, Reiter and Open-End rotor yarns and their mechanical behavior under dynamic stresses [29]. **Figure 14** displays scanning electron microscope pictures for the longitudinal view of Rieter, Murata vortex and Open-End rotor spinning.

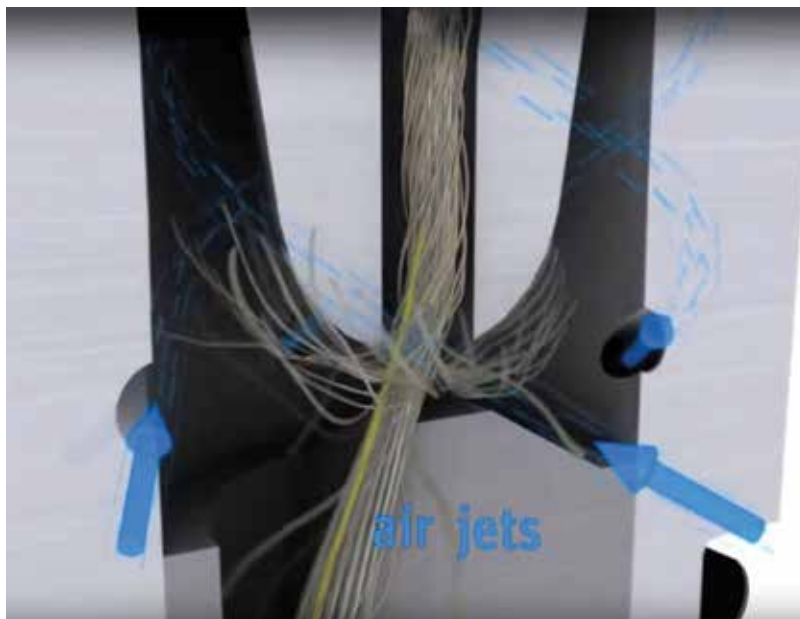


Figure 12. Yarn formation in Rieter air-jet spinning machine [27].



Figure 13. Rieter automated air-jet spinning machine [27].

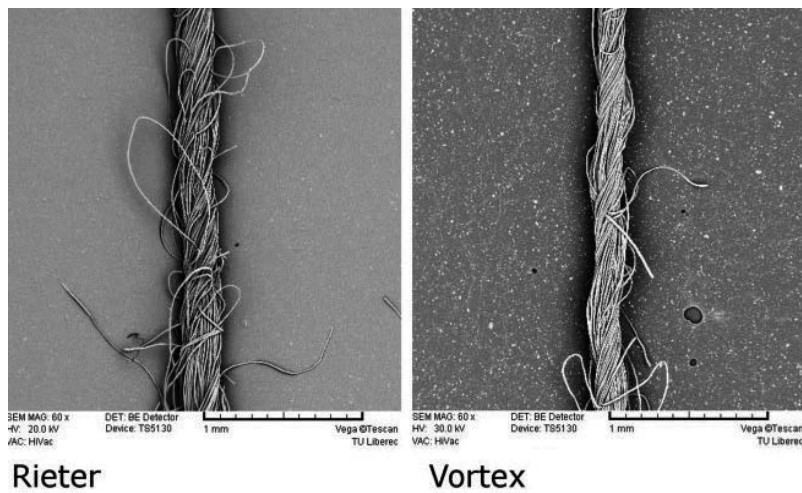


Figure 14. Scanning electron microscope pictures for the longitudinal view of Rieter, Murata vortex and Open-End spinning [29].

2.3. Numerical simulation studies concerning vortex spinning theory

Some researchers have pointed out that the dynamic behavior of the fiber in the airflow field inside the nozzle plays an important role in the twist insertion process of vortex spinning. Since the internal airflow field inside the nozzle is very complex, there aren't many studies on investigating the dynamic behavior of the fiber experimentally. With the development of computer-aided technology, computational fluid dynamics (CFD) have provided an important means of predicting the flow field under different design and operating conditions. In recent years, computational fluid dynamic approaches have been used to investigate the airflow characteristics in the vortex spinning nozzle [30–32].

Zeng and Yu [30] made a research about developing a computational fluid dynamic (CFD) to simulate the airflow patterns inside the nozzle of an air-jet spinning machine. The nozzle design parameters' effect to the flow characteristics and its reflection to the yarn was mostly discussed. The nozzle pressure increment led to the higher axial and tangential velocity in the nozzle which resulted better tensile properties of the yarn. But they emphasized that after a certain nozzle pressure, there might be some deteriorations for the yarn. The researches added that the selection of jet orifice angle which should be comprised of several factors also affected the flow characteristics. At the end of the study, they concluded that the nozzle design was a very significant factor for the vortex formation hence the yarn quality. And for further researches in order to improve vortex yarn quality, CFD can be used for optimizing the nozzle design [30].

Liu and Xu [31] studied a simple analytical formulation for the forces that determine the strength of the air vortex twist acting on the yarns during air-vortex spinning as a function of nozzle pressure, flow rate, the radius of the main nozzle in the horizontal plane, nozzle pressure, jet orifice angle, the number of the orifices, jet orifice angle, diameter of the jet orifice, and from the top of the twisting chamber to the spindle. They used FLUENT to simulate the flow fields of air vortex spinning machine. They obtained the relationship between the velocity and the radius of the main nozzle. In the study because of the high velocity and high

Reynolds number in the nozzle, airflow is accepted as a turbulent flow. The standard $k-\epsilon$ turbulence model was used to study the air stream field of the main nozzle, and the standard wall-function approach was introduced to deal with flow near the walls. The researchers focus on the yarn formation area. Considering the distance from the top of the twisting chamber to the spindle (h) and ignoring the energy loss, the momentum formulation in the horizontal direction was calculated [31].

Pei and Yu [32] discussed the principle of yarn formation mechanism in vortex spinning system by developing a three-dimensional CFD model to simulate the airflow characteristics inside the air nozzle. A three-dimensional grid and the realizable $k-\epsilon$ turbulence model are used in the simulation. A streamline starting from the nozzle inlet is also acquired. Based on the simulation, the principle of yarn formation of MVS is discussed. They stated that a negative pressure zone appears in the center of the twisting chamber causing two air currents flowing into the twisting chamber through the nozzle inlet and the yarn passage of the hollow spindle, respectively. The investigators approve the simulation results with the yarn formation theory [32].

Pei and Yu made a research about the airflow characteristics and the fiber dynamic behavior by using a two-dimensional numerical model consisting of the airflow-fiber interaction and the fiber-wall contact. The effects of nozzle structure parameters such as jet orifice angle, jet orifice diameter, the distance between the nozzle inlet and the hollow spindle were investigated to analyze the dynamic behavior of the fiber in order for a whole understand of yarn structure and tensile properties detailed. The researchers declared that the best yarn tenacity was obtained when the jet orifice angle was 70° , the jet orifice diameter was 0.4 mm, and the distance between the nozzle inlet and the hollow spindle was 14 mm [33].

In another study of Pei et al.'s [34], the fiber motion simulation under the aerodynamic effects inside the vortex spinning was investigated. The researchers made a solution of coupling between the fiber and airflow together with the fiber-wall contact. The numerical model was based on the motional characteristics of some fibers (cotton, viscose rayon, Lyocell and polyester fibers) inside the vortex spinning nozzle. The wrapping effects of different types of fibers were obtained by the numerical simulation and compared with the view of vortex yarn structure under the scanning electron microscope [34].

3. Conclusions

The swirling air has been used frequently for twisting the fibers instead of using mechanical parts in the recent years. Vortex spinning has become a modern alternative method to ring and rotor spinning. Compared to commonly used ring yarns, the vortex yarn is less hairy, which leads to less fabric pilling and high abrasion resistance, high moisture absorption, color fastness, fast drying characteristics. However, there are many parameters influencing this twisting system consequently the vortex yarn. Hence for the whole understanding of the system, each factor has to be investigated in detail.

The design of the nozzle as well as the airflow characteristics has a significant influence on the yarn character. The number of jet orifices and the diameters of orifice directly affect the vortex magnitude. The airflow characteristics depending on the nozzle pressure reflect to the ratio of the wrapping fibers to the core fibers which cause many changes in yarn properties. The ratio of wrapping fibers to core fibers is a very decisive factor for the yarn fineness. The decrease of the core fibers in the yarn structure may lead deterioration in the yarn properties as the yarn gets finer. It is thought that the possibilities of fine count vortex yarn production with newly developed fibers such as microfibers at higher speeds are good to be investigated further for softer fabric handle. Also airflow-fiber-nozzle interactions at the yarn formation area have to be analyzed carefully for the quality improvement of vortex yarn spinning.

Author details

Gizem Karakan Günaydin^{1*} and Ali Serkan Soydan²

*Address all correspondence to: ggunaydin@pau.edu.tr

1 Buldan Vocational Training School, Pamukkale University, Denizli, Turkey

2 Department of Textile Engineering, Faculty of Engineering, Pamukkale University, Denizli, Turkey

References

- [1] Lawrence C., Editor. *Fundamentals of Spun Yarn Technology*. USA: The Textile Institute, CRC Press; 2003. 523 p. ISBN:1-56676-821-7
- [2] Erdumlu N. *An Approach to Investigate Spinnability of Fine Count Yarns on Vortex Spinning System* [thesis]. Istanbul, Turkey: İstanbul Technical University; Institute Of Science And Technology. 154 p.
- [3] Erdumlu N., Ozipek B., Oxenham W. Vortex spinning technology. *Textile Progress*. 2012;**44**(3–4):141–174. doi:10.1080/00405167.2012.739345
- [4] Murata Textile Machinery. MVS 861 Catalogue [Internet]. 20.05.2006. Available from: www.muratec.net [Accessed: 10.04.2016].
- [5] Basal G. *The Structure and Properties of Vortex and Compact Spun Yarns* [thesis]. USA: North Carolina State University; 2003. 180 p.
- [6] Morton W., Yen K.C. The arrangement of fibers in fibro yarns. *Journal Textile Institute*. 1952;**43**(T60–T66).
- [7] Soe A.K., Takahashi M., Nakajima M., Matsuo T., Matsumoto T. Structure and properties of MVS yarns in comparison with ring yarns and Open-End rotor spun yarns. *Textile Research Journal*. 2004;**74**(9):819–826.

- [8] Chasmawala S.M., Jayaraman H., Jayaraman S. Structure and properties of air jet spun yarns. *Textile Research Journal*. 1990;**60**(2):61–69.
- [9] Basal G., Oxenham W. Vortex spun yarn vs air-jet spun yarn. *Autex Research Journal*. 2003;**3**(3):96–101.
- [10] Basal G., Oxenham W. Effects of some process parameters on the structure and properties of vortex spun yarns. *Textile Research Journal*. 2006;**76**(6):492–499.
- [11] Ortlek H.G., Ulku S. Effects of some variables on properties of 100% cotton vortex spun yarn. *Textile Research Journal*. 2005;**75**(6):458–461.
- [12] Tyagi G.K., Sharma D., Salhotra K.R. Process-structure-property relationship of polyester-cotton MVS yarns: Part I-influence of processing variables on the yarn structural parameters. *Indian Journal of Fiber & Textile Research*. 2004;**29**:419–428.
- [13] Tyagi G.K., Sharma D., Salhotra K.R. Process-structure property relationship of polyester-cotton MVS yarns: Part II-influence of processing variables on the yarn characteristics. *Indian Journal of Fiber & Textile Research*. 2004;**29**:429–435.
- [14] Zou Z., Liu S., Zheng S., Cheng L. Numerical computation of a flow field affected by the process parameters of Murata Vortex Spinning. *Fibers & Textiles in Eastern Europe*. 2010;**18**(2):35–39.
- [15] Kupperts S., Muller H., Ziegler K., Heitmann U., Planck H. Spinning Limits at vortex spinning at the processing of 100% cotton. *Melliand English*. 2008.
- [16] Erdumlu N., Ozipek B. Effect of draft ratio on vortex spun yarn properties. *Fibers & Textiles in Eastern Europe*. 2010;**18**(3 (80)):38–42.
- [17] Zou Z.Y., Cheng L.D., Xue W.L., Yue J.Y. A Study of the twisted strength of the whirled airflow in Murata Vortex Spinning. *Textile Research Journal*. 2008;**78**(8):682–687.
- [18] Zou Z.Y., Yu J.Y., Xue W.L., Zhu Y.D., Wu J.M., Cheng L.D. Analysis of the fiber spatial trajectory in vortex spun yarn. *Textile Research Journal*. 2009;**79**(10):924–929.
- [19] Ortlek H.G., Nair F., Kilik R., Güven K. Effect of spindle diameter and spindle working period on the properties of 100% viscose MVS yarns. *Fibers and Textiles in Eastern Europe*. 2008;**3**(68):17–20.
- [20] Ortlek H., Ulku S. Effect of some variables on properties of 100% Cotton Vortex spun yarn. *Textile Research Journal*. 2005;**75**(6):458–461.
- [21] Leitner H., Schwippl H., Baldischwieler O. Air-jet spinning-yarns & fabrics compared to established spinning systems. In: XIIth International Izmir Textile & Apparel Symposium; October 28–30; Izmir, Turkey. 2010.
- [22] Lawrence C., editor. *Advances in Yarn Spinning Technology*. Philadelphia, New Delhi: The Textile Institute Woodhead Publishing; 2010. 431 p.
- [23] Kilic M., Okur A. The properties of cotton-tencel and cotton-promodal blended yarns spun in different spinning systems. *Textile Research Journal*. 2011;**81**(2):156–172.

- [24] Tyagi G.K., Sharma D. Performance and low-stress characteristics of polyester-cotton MVS yarns. *Indian Journal of Fiber & Textile Research*. 2004;**29**(September):301–307.
- [25] Tyagi G.K., Sharma D. Thermal comfort characteristics of polyester-cotton MVS yarns fabrics. *Indian Journal of Fiber & Textile Research*. 2005;**30**:363–370.
- [26] Gordon S. The effect of short fiber and neps on Murata Vortex Spinning. *The Australian Cotton Grower*: [http://www.greenmountpress.com.au/cottongrower/Back%20 issues/231jfcot02/28 Effect.tif](http://www.greenmountpress.com.au/cottongrower/Back%20issues/231jfcot02/28%20Effect.tif). 2002;**23**(1 (January-February)):28.
- [27] RIETER. rieter.com/en/machines-systems/products/j-26-air-jet-spinning-machine [Internet]. 20.03.2015. [Accessed: 21.06.2016].
- [28] MURATEC. muratec.net/tm/products/vortex/vortex_001.html [Internet]. 02.11.2015. [Accessed: 10.05.2016].
- [29] Eldessouki M., Ibrahim S., Farag R. Dynamic properties of air jet yarns compared to rotor spinning. *Textile Research Journal*. 2015;**85**(17):1827–1837.
- [30] Zeng Y., Yu C. Numerical simulation of air flow in the nozzle of an air-jet spinning machine. *Textile Research Journal*. 2003;**73**(4):350–356.
- [31] Liu Y., Xu L. Controlling air vortex in air-vortex spinning by Zeng-He model. *International Journal of Nonlinear Sciences and Numerical Simulation*. 2006;**7**(4):389–392.
- [32] Pei Z., Yu C. Study on the principle of yarn formation of Murata vortex spinning using numerical simulation. *Textile Research Journal*. 2009;**79**(14):1274–1280.
- [33] Pei Z., Yu, C. Prediction of the vortex yarn tenacity from some process and nozzle parameters based on numericals. *Textile Research Journal*. 2011;**81**(17):1796–1807.
- [34] Pei Z., Hu B., Diao C., Chongwen Y. Investigation on the motion of different types of fibers in the vortex spinning nozzle. *Polymer Engineering & Science*. 2012;**52**(4):856–867.

Edited by Hector Perez-de-Tejada

The contents of the book cover topics on vortex dynamics in a variety of flow problems and describe observational measurements and their interpretation. The book contains 13 chapters that first include vortices in the earth and planetary sciences related to vortices in the Venus plasma wake and also on tropical cyclones and on rotating shallow water in the earth's atmosphere. Vortices in fluid problems include airplane wake vortices, vorticity evolution in free-shear flows, together with axisymmetric flows with swirl, as well as thermal conductivities in fluid layers. Vortices in relativistic fluids, in magnetic disks, solitons and vortices, and relaxation for point vortices were also examined. Other chapters describe conditions in a vortex bioreactor and in vortex yarn structures.

Photo by Xurzon / iStock

IntechOpen

